Chapter 7 *Pulse Compression*

Range resolution for a given radar can be significantly improved by using very short pulses. Unfortunately, utilizing short pulses decreases the average transmitted power, which can hinder the radar's normal modes of operation, particularly for multi-function and surveillance radars. Since the average transmitted power is directly linked to the receiver SNR, it is often desirable to increase the pulse width (i.e., increase the average transmitted power) while simultaneously maintaining adequate range resolution. This can be made possible by using pulse compression techniques. Pulse compression allows us to achieve the average transmitted power of a relatively long pulse, while obtaining the range resolution corresponding to a short pulse. In this chapter, we will analyze analog and digital pulse compression techniques.

Two analog pulse compression techniques are discussed in this chapter. The first technique is known as "correlation processing" which is dominantly used for narrow band and some medium band radar operations. The second technique is called "stretch processing" and is normally used for extremely wide band radar operations. Digital pulse compression will also be briefly presented.

7.1. Time-Bandwidth Product

Consider a radar system that employs a matched filter receiver. Let the matched filter receiver bandwidth be denoted as B. Then, the noise power available within the matched filter bandwidth is given by

$$N_i = 2 \frac{N_0}{2} B \tag{7.1}$$

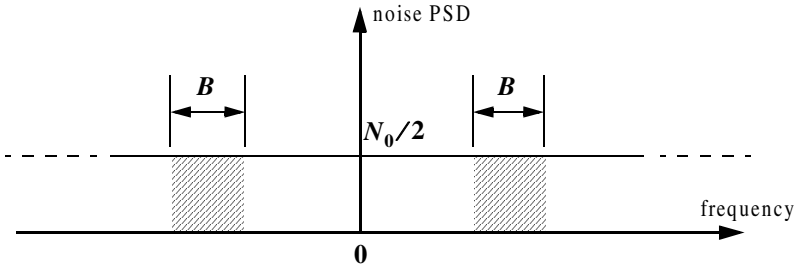

Figure 7.1. Input noise power.

where the factor of two is used to account for both negative and positive frequency bands, as illustrated in Fig. 7.1. The average input signal power over a pulse duration τ' is

$$S_i = \frac{E}{\tau'} \tag{7.2}$$

E is the signal energy. Consequently, the matched filter input SNR is given by

$$(SNR)_i = \frac{S_i}{N_i} = \frac{E}{N_0 B\tau'} \tag{7.3}$$

Using Eqs. (6.18) (from Chapter 6) and (7.3), one may compute the output peak instantaneous SNR to the input SNR ratio as

$$\frac{SNR(t_0)}{(SNR)_i} = 2B\tau' \tag{7.4}$$

The quantity $B\tau'$ is referred to as the "time-bandwidth product" for a given waveform, or its corresponding matched filter. The factor $B\tau'$ by which the output SNR is increased over that at the input is called the matched filter gain, or simply the compression gain.

In general, the time-bandwidth product of an unmodulated pulse approaches unity. The time-bandwidth product of a pulse can be made much greater than unity by using frequency or phase modulation. If the radar receiver transfer function is perfectly matched to that of the input waveform, then the compression gain is equal to $B\tau'$. Clearly, the compression gain becomes smaller than $B\tau'$ as the spectrum of the matched filter deviates from that of the input signal.

7.2. Radar Equation with Pulse Compression

The radar equation for a pulsed radar can be written as

$$SNR = \frac{P_t \tau' G^2 \lambda^2 \sigma}{(4\pi)^3 R^4 k T_e F L} \tag{7.5}$$

where P_t is peak power, τ' is pulse width, G is antenna gain, σ is target RCS, R is range, k is Boltzman's constant, T_e is effective noise temperature, F is noise figure, and L is total radar losses.

Pulse compression radars transmit relatively long pulses (with modulation) and process the radar echo into very short pulses (compressed). One can view the transmitted pulse to be composed of a series of very short subpulses (duty is 100%), where the width of each subpulse is equal to the desired compressed pulse width. Denote the compressed pulse width as τ_c. Thus, for an individual subpulse, Eq. (7.5) can be written as

$$(SNR)_{\tau_c} = \frac{P_t \tau_c G^2 \lambda^2 \sigma}{(4\pi)^3 R^4 k T_e F L} \tag{7.6}$$

The SNR for the uncompressed pulse is then derived from Eq. (7.6) as

$$SNR = \frac{P_t (\tau' = n\tau_c) G^2 \lambda^2 \sigma}{(4\pi)^3 R^4 k T_e F L} \tag{7.7}$$

where n is the number of subpulses. Equation (7.7) is denoted as the radar equation with pulse compression.

Observation of Eqs. (7.5) and (7.7) indicates the following (note that both equations have the same form): For a given set of radar parameters, and as long as the transmitted pulse remains unchanged, then the SNR is also unchanged regardless of the signal bandwidth. More precisely, when pulse compression is used, the detection range is maintained while the range resolution is drastically improved by keeping the pulse width unchanged and by increasing the bandwidth. Remember that range resolution is proportional to the inverse of the signal bandwidth,

$$\Delta R = c/2B \tag{7.8}$$

7.3. Analog Pulse Compression

Correlation and stretch pulse compression techniques are discussed in this section. Two MATLAB programs which execute digital implementation of both techniques (using the FFT) are also presented.

7.3.1. Correlation Processor

In this case, pulse compression is accomplished by adding frequency modulation to a long pulse at transmission, and by using a matched filter receiver in order to compress the received signal. As an example, we saw in Chapter 6 that using LFM within a rectangular pulse compresses the matched filter output by a factor $\xi = B\tau'$, which is directly proportional to the pulse width and bandwidth. Thus, by using long pulses and wideband LFM modulation we can achieve large compression ratios. This form of pulse compression is known as "correlation processing."

Fig. 7.2 illustrates the advantage of pulse compression. In this example, an LFM waveform is used. Two targets with RCS $\sigma_1 = 1m^2$ and $\sigma_2 = 0.5m^2$ are detected. The two targets are not separated enough in time to be resolved. Fig. 7.2a shows the composite echo signal from those targets. Clearly, the target returns overlap and, thus, they are not resolved. However, after pulse compression the two pulses are completely separated and are resolved as two targets. In fact, when using LFM, returns from neighboring targets are resolved as long as they are separated, in time, by τ_{n1}, the compressed pulse width.

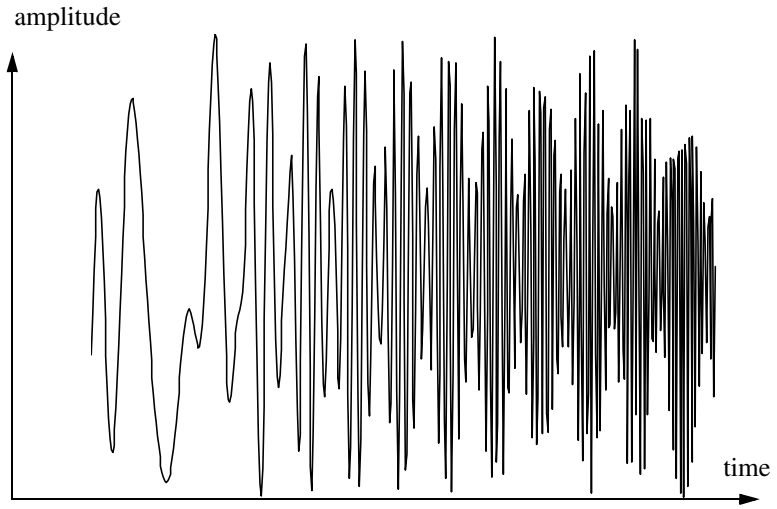

Figure 7.2a. Composite echo signal for two unresolved targets.

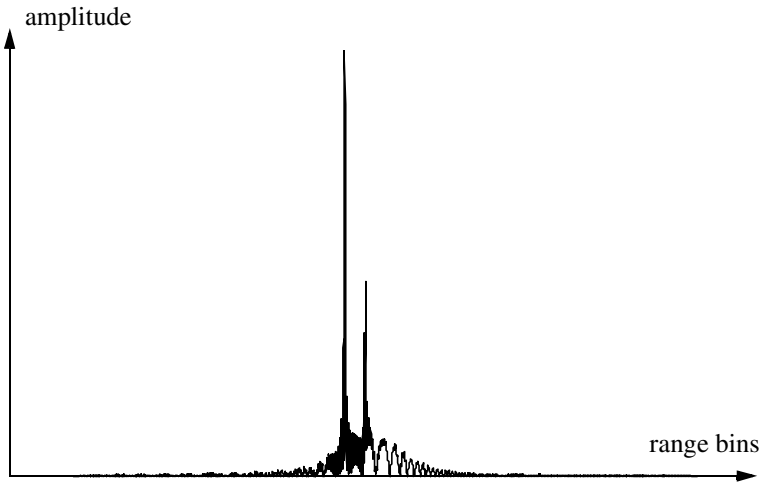

Figure 7.2b. Composite echo signal corresponding to Fig. 7.2a, after pulse compression.

Radar operations (search, track, etc.) are usually carried out over a specified range window, referred to as the receive window and defined by the difference between the radar maximum and minimum range. Returns from all targets within the receive window are collected and passed through a matched filter circuitry to perform pulse compression. One implementation of such analog processors is the Surface Acoustic Wave (SAW) devices. Because of the recent advances in digital computer development, the correlation processor is often performed digitally using the FFT. This digital implementation is called Fast Convolution Processing (FCP) and can be implemented at base-band. The fast convolution process is illustrated in Fig. 7.3

Since the matched filter is a linear time invariant system, its output can be described mathematically by the convolution between its input and its impulse response,

$$y(t) = s(t) \bullet h(t) \tag{7.9}$$

where $s(t)$ is the input signal, $h(t)$ is the matched filter impulse response (replica), and the $\bullet$ operator symbolically represents convolution. From the Fourier transform properties,

$$FFT\{s(t) \bullet h(t)\} = S(f) \cdot H(f) \tag{7.10}$$

And when both signals are sampled properly, the compressed signal $y(t)$ can be computed from

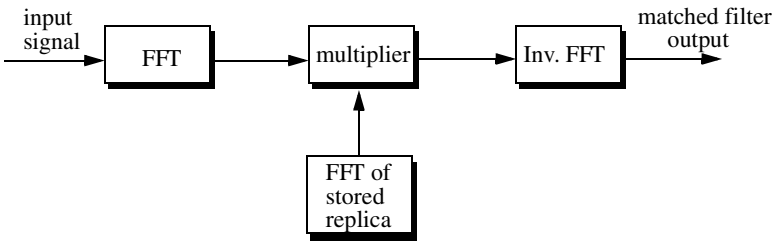

Figure 7.3. Computing the matched filter output using an FFT.

$$y = FFT^{-1}\{S \cdot H\} \tag{7.11}$$

where FFT^{-1} is the inverse FFT. When using pulse compression, it is desirable to use modulation schemes that can accomplish a maximum pulse compression ratio, and can significantly reduce the side lobe levels of the compressed waveform. For the LFM case the first side lobe is approximately $13.4dB$ below the main peak, and for most radar applications this may not be sufficient. In practice, high side lobe levels are not preferable because noise and/or jammers located at the side lobes may interfere with target returns in the main lobe.

Weighting functions (windows) can be used on the compressed pulse spectrum in order to reduce the side lobe levels. The cost associated with such an approach is a loss in the main lobe resolution, and a reduction in the peak value (i.e., loss in the SNR), as illustrated in Fig. 7.4. Weighting the time domain transmitted or received signal instead of the compressed pulse spectrum will theoretically achieve the same goal. However, this approach is rarely used, since amplitude modulating the transmitted waveform introduces extra burdens on the transmitter.

Consider a radar system that utilizes a correlation processor receiver (i.e., matched filter). The receive window in meters is defined by

$$R_{rec} = R_{max} - R_{min} \tag{7.12}$$

where R_{max} and R_{min}, respectively, define the maximum and minimum range over which the radar performs detection. Typically R_{rec} is limited to the extent of the target complex. The normalized complex transmitted signal has the form

$$s(t) = \exp\left(j2\pi\left(f_0 t + \frac{\mu}{2}t^2\right)\right) \qquad 0 \le t \le \tau' \tag{7.13}$$

τ' is the pulse width, $\mu = B/\tau'$, and B is the bandwidth. Note that this definition of the LFM pulse is different from that in Chapter 6. Earlier, f_0 denoted the chirp center frequency and in Eq. (7.13) it denotes the chirp start frequency.

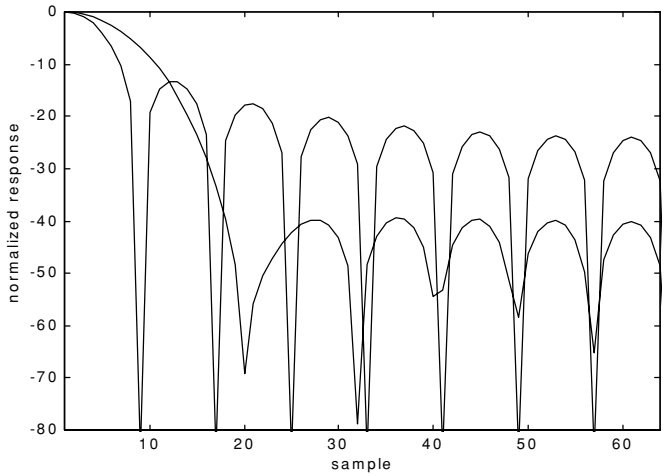

Figure 7.4. Reducing the first sidelobe to -42 dB doubles the main lobe width.

The radar echo signal is similar to the transmitted one with the exception of a time delay and an amplitude change that correspond to the target RCS. Consider a target at range R_1. The echo received by the radar from this target is

$$s_r(t) = a_1 \exp\left(j2\pi\left(f_0(t-\tau_1) + \frac{\mu}{2}(t-\tau_1)^2\right)\right) \tag{7.14}$$

where a_1 is proportional to target RCS, antenna gain, and range attenuation. The time delay τ_1 is given by

$$\tau_1 = 2R_1/c \tag{7.15}$$

The first step of the processing consists of removing the frequency f_0. This is accomplished by mixing $s_r(t)$ with a reference signal whose phase is $2\pi f_0 t$. The phase of the resultant signal, after low pass filtering, is then given by

$$\psi(t) = 2\pi\left(-f_0\tau_i + \frac{\mu}{2}(t-\tau_i)^2\right) \tag{7.16}$$

and the instantaneous frequency is

$$f_i(t) = \frac{1}{2\pi}\frac{d}{dt}\psi(t) = \mu(t-\tau_i) = \frac{B}{\tau'}\left(t - \frac{2R_1}{c}\right) \tag{7.17}$$

The quadrature components are

$$\begin{pmatrix} x_I(t) \\ x_Q(t) \end{pmatrix} = \begin{pmatrix} \cos\psi(t) \\ \sin\psi(t) \end{pmatrix} \tag{7.18}$$

Sampling the quadrature components is performed next. The number of samples, N, must be chosen so that foldover (ambiguity) in the spectrum is avoided. For this purpose, the sampling frequency, f_s (based on the Nyquist sampling rate), must be

$$f_s \geq 2B \tag{7.19}$$

and the sampling interval is

$$\Delta t \leq 1/2B \tag{7.20}$$

Using Eq. (7.17) it can be shown that (the proof is left as an exercise) the frequency resolution of the FFT is

$$\Delta f = 1/\tau' \tag{7.21}$$

The minimum required number of samples is

$$N = \frac{1}{\Delta f \Delta t} = \frac{\tau'}{\Delta t} \tag{7.22}$$

Equating Eqs. (7.20) and (7.22) yields

$$N \geq 2B\tau' \tag{7.23}$$

Consequently, a total of $2B\tau'$ real samples, or $B\tau'$ complex samples, is sufficient to completely describe an LFM waveform of duration τ' and bandwidth B. For example, an LFM signal of duration $\tau = 20\ \mu s$ and bandwidth $B = 5\ MHz$ requires 200 real samples to determine the input signal (100 samples for the I-channel and 100 samples for the Q-channel).

For better implementation of the FFT N is extended by zero padding, to the next power of two. Thus, the total number of samples, for some positive integer m, is

$$N_{FFT} = 2^m \geq N \tag{7.24}$$

The final steps of the FCP processing include: (1) taking the FFT of the sampled sequence; (2) multiplying the frequency domain sequence of the signal with the FFT of the matched filter impulse response; and (3) performing the inverse FFT of the composite frequency domain sequence in order to generate the time domain compressed pulse (HRR profile). Of course, weighting, antenna gain, and range attenuation compensation must also be performed.

Assume that I targets at ranges R_1, R_2, and so forth are within the receive window. From superposition, the phase of the down converted signal is

$$\psi(t) = \sum_{i=1}^{I} 2\pi\left(-f_0\tau_i + \frac{\mu}{2}(t-\tau_i)^2\right) \tag{7.25}$$

The times $\{\tau_i = (2R_i/c);\ i = 1, 2, \ldots, I\}$ represent the two-way time delays, where τ_1 coincides with the start of the receive window.

MATLAB Function "matched_filter.m"

The function *"matched_filter.m"* performs fast convolution processing. It is given in Listing 7.1 in Section 7.5. The syntax is as follows:

[y] = matched_filter(nscat, taup, f0, b, rmin, rrec, scat_range, scat_rcs, win)

where

Symbol	Description	Units	Status
nscat	*number of point scatterers within the received window*	*none*	*input*
rmin	*minimum range of receive window*	*Km*	*input*
rrec	*receive window size*	*m*	*input*
taup	*uncompressed pulse width*	*seconds*	*input*
f0	*chirp start frequency*	*Hz*	*input*
b	*chirp bandwidth*	*Hz*	*input*
scat_range	*vector of scatterers range*	*Km*	*input*
scat_rsc	*vector of scatterers RCS*	m^2	*input*
win	*0 = no window* *1 = Hamming* *2 = Kaiser with parameter pi* *3 = Chebychev - sidelobes at -60dB*	*none*	*input*
y	*compressed output*	*volts*	*output*

The user can access this function either by a MATLAB function call, or by executing the MATLAB program *"matched_filter_driver.m"* which utilizes MATLAB based GUI. The outputs of this function are the complex array y and plots of the uncompressed and compressed signal versus relative. This function utilizes the function "power_integer_2.m" which implements Eq. (7.24):

```
function n = power_integer_2 (x)
m = 0.;
for j = 1:30
  m = m + 1.;
  delta = x - 2.^m;
  if(delta < 0.)
    n = m;
    return
  else
  end
end
```

As an example, consider the case where

nscat	*2*	*b*	*16 MHz*
rmin	*150 Km*	*scat_range*	*rmin in Km + {0, 50} meters*
rrec	*200 m*	*scat_rsc*	*{1, 1} m^2*
taup	*0.005 ms*	*win*	*2 (Kaiser)*
f0	*14 MHz*		

Note that the compressed pulsed range resolution, without using a window, is $\Delta R = 9.3m$. Figs. 7.5 and 7.6, respectively, show the uncompressed and compressed echo signal corresponding to this example.

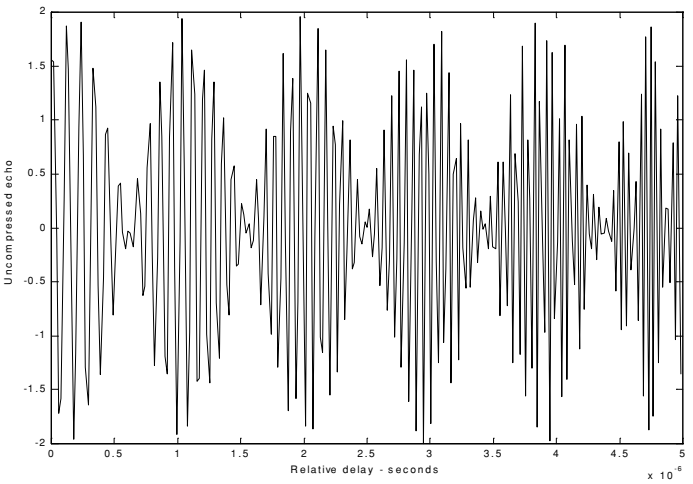

Figure 7.5. Uncompressed echo signal. Scatterers are unresolved.

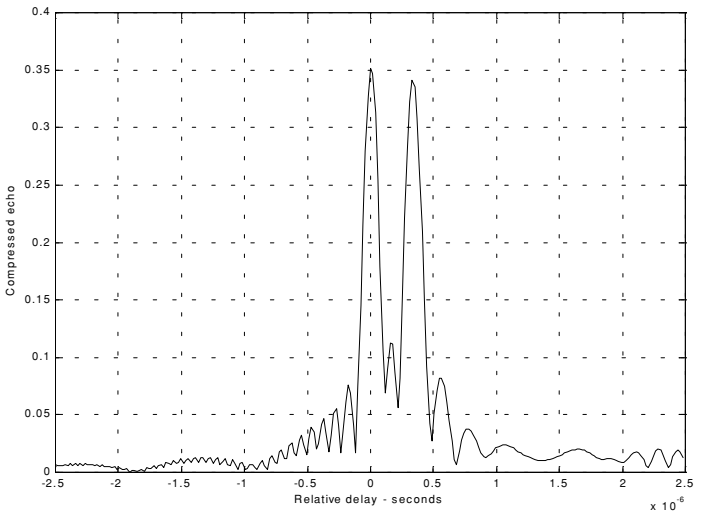

Figure 7.6. Compressed echo signal. Scatterers are resolved.

7.3.2. Stretch Processor

Stretch processing, also known as "active correlation," is normally used to process extremely high bandwidth LFM waveforms. This processing technique consists of the following steps: First, the radar returns are mixed with a replica (reference signal) of the transmitted waveform. This is followed by Low Pass Filtering (LPF) and coherent detection. Next, Analog to Digital (A/D) conversion is performed; and finally, a bank of Narrow Band Filters (NBFs) is used in order to extract the tones that are proportional to target range, since stretch processing effectively converts time delay into frequency. All returns from the same range bin produce the same constant frequency. Fig. 7.7 shows a block diagram for a stretch processing receiver. The reference signal is an LFM waveform that has the same LFM slope as the transmitted LFM signal. It exists over the duration of the radar "receive-window," which is computed from the difference between the radar maximum and minimum range. Denote the start frequency of the reference chirp as f_r.

Consider the case when the radar receives returns from a few close (in time or range) targets, as illustrated in Fig. 7.7. Mixing with the reference signal and performing low pass filtering are effectively equivalent to subtracting the return frequency chirp from the reference signal. Thus, the LPF output consists of constant tones corresponding to the targets' positions. The normalized transmitted signal can be expressed by

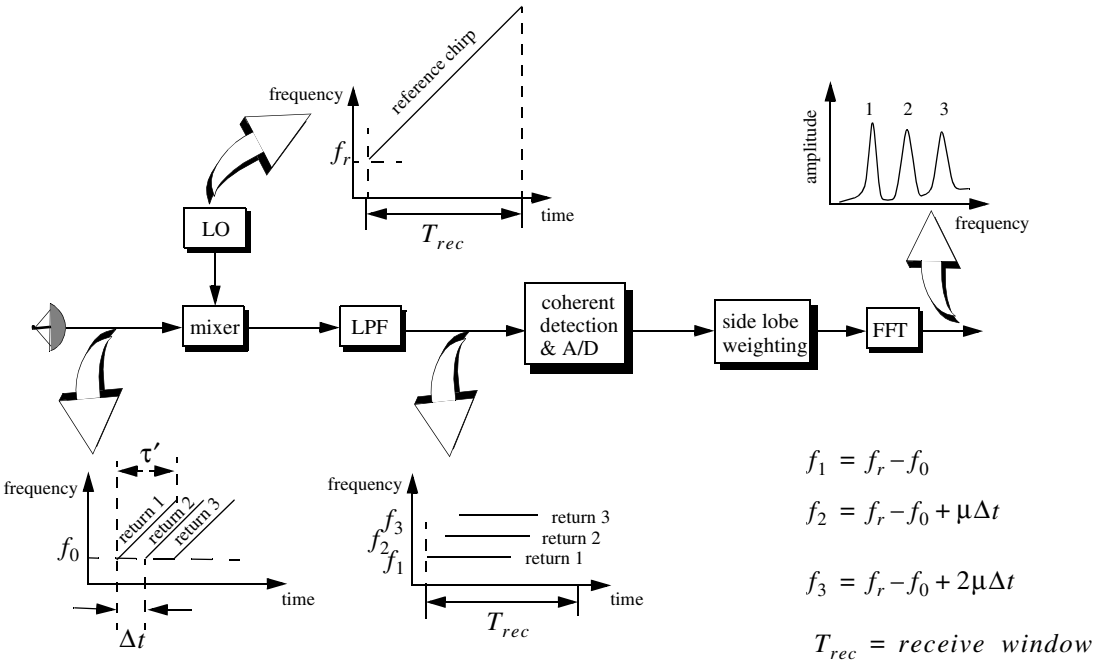

Figure 7.7. Stretch processing block diagram.

$$s_1(t) = \cos\left(2\pi\left(f_0 t + \frac{\mu}{2}t^2\right)\right) \qquad 0 \le t \le \tau' \tag{7.26}$$

where $\mu = B/\tau'$ is the LFM coefficient and f_0 is the chirp start frequency. Assume a point scatterer at range R. The received signal by the radar is

$$s_r(t) = a\cos\left[2\pi\left(f_0(t-\Delta\tau) + \frac{\mu}{2}(t-\Delta\tau)^2\right)\right] \tag{7.27}$$

where a is proportional to target RCS, antenna gain, and range attenuation. The time delay $\Delta\tau$ is

$$\Delta\tau = 2R/c \tag{7.28}$$

The reference signal is

$$s_{ref}(t) = 2\cos\left(2\pi\left(f_r t + \frac{\mu}{2}t^2\right)\right) \qquad 0 \le t \le T_{rec} \tag{7.29}$$

The received window in seconds is

$$T_{rec} = \frac{2(R_{max} - R_{min})}{c} = \frac{2R_{rec}}{c} \tag{7.30}$$

It is customary to let $f_r = f_0$. The output of the mixer is made of the product of the received and reference signals. After low pass filtering the signal is

$$s_0(t) = a\cos(2\pi f_0 t\Delta\tau + 2\pi\mu\Delta\tau t - \pi\mu(\Delta\tau)^2) \tag{7.31}$$

Substituting Eq. (7.28) into (7.31) and collecting terms yield

$$s_0(t) = a\ \cos\left[\left(\frac{4\pi BR}{c\tau'}\right)t + \frac{2R}{c}\left(2\pi f_0 - \frac{2\pi BR}{c\tau'}\right)\right] \tag{7.32}$$

and since $\tau' \gg 2R/c$, Eq. (7.32) is approximated by

$$s_0(t) \approx a\ \cos\left[\left(\frac{4\pi BR}{c\tau'}\right)t + \frac{4\pi R}{c}f_0\right] \tag{7.33}$$

The instantaneous frequency is

$$f_{inst} = \frac{1}{2\pi}\frac{d}{dt}\left(\frac{4\pi BR}{c\tau'}t + \frac{4\pi R}{c}f_0\right) = \frac{2BR}{c\tau'} \tag{7.34}$$

which clearly indicates that target range is proportional to the instantaneous frequency. Therefore, proper sampling of the LPF output and taking the FFT of

the sampled sequence lead to the following conclusion: a peak at some frequency f_1 indicates presence of a target at range

$$R_1 = f_1 c\tau'/2B \tag{7.35}$$

Assume I close targets at ranges R_1, R_2, and so forth ($R_1 < R_2 < \ldots < R_I$). From superposition, the total signal is

$$s_r(t) = \sum_{i=1}^{I} a_i(t)\cos\left[2\pi\left(f_0(t-\tau_i) + \frac{\mu}{2}(t-\tau_i)^2\right)\right] \tag{7.36}$$

where $\{a_i(t);\ i = 1, 2, \ldots, I\}$ are proportional to the targets' cross sections, antenna gain, and range. The times $\{\tau_i = (2R_i/c);\ i = 1, 2, \ldots, I\}$ represent the two-way time delays, where τ_1 coincides with the start of the receive window. Using Eq. (7.32) the overall signal at the output of the LPF can then be described by

$$s_o(t) = \sum_{i=1}^{I} a_i\cos\left[\left(\frac{4\pi BR_i}{c\tau'}\right)t + \frac{2R_i}{c}\left(2\pi f_0 - \frac{2\pi BR_i}{c\tau'}\right)\right] \tag{7.37}$$

And hence, target returns appear at constant frequency tones that can be resolved using the FFT. Consequently, determining the proper sampling rate and FFT size is very critical. The rest of this section presents a methodology for computing the proper FFT parameters required for stretch processing.

Assume a radar system using a stretch processor receiver. The pulse width is τ' and the chirp bandwidth is B. Since stretch processing is normally used in extreme bandwidth cases (i.e., very large B), the receive window over which radar returns will be processed is typically limited to few meters to possibly less than 100 meters. The compressed pulse range resolution is computed from Eq. (7.8). Declare the FFT size by N and its frequency resolution by Δf. The frequency resolution can be computed using the following procedure: consider two adjacent point scatterers at range R_1 and R_2. The minimum frequency separation, Δf, between those scatterers so that they are resolved can be computed from Eq. (7.34). More precisely,

$$\Delta f = f_2 - f_1 = \frac{2B}{c\tau'}(R_2 - R_1) = \frac{2B}{c\tau'}\Delta R \tag{7.38}$$

Substituting Eq. (7.8) into Eq. (7.38) yields

$$\Delta f = \frac{2B}{c\tau'}\ \frac{c}{2B} = \frac{1}{\tau'} \tag{7.39}$$

The maximum resolvable frequency by the FFT is limited to the region $\pm N\Delta f/2$. Thus, the maximum resolvable frequency is

$$\frac{N\Delta f}{2} > \frac{2B(R_{max} - R_{min})}{c\tau'} = \frac{2BR_{rec}}{c\tau'} \tag{7.40}$$

Using Eqs. (7.30) and (7.39) into Eq. (7.40) and collecting terms yield

$$N > 2BT_{rec} \tag{7.41}$$

For better implementation of the FFT, choose an FFT of size

$$N_{FFT} \geq N = 2^m \tag{7.42}$$

m is a nonzero positive integer. The sampling interval is then given by

$$\Delta f = \frac{1}{T_s N_{FFT}} \Rightarrow T_s = \frac{1}{\Delta f N_{FFT}} \tag{7.43}$$

MATLAB Function "stretch.m"

The function *"stretch.m"* presents a digital implementation of stretch processing. It is given in Listing 7.2 in Section 7.5. The syntax is as follows:

[y] = stretch (nscat, taup, f0, b, rmin, rrec, scat_range, scat_rcs, win)

where

Symbol	Description	Units	Status
nscat	*number of point scatterers within the received window*	*none*	*input*
rmin	*minimum range of receive window*	*Km*	*input*
rrec	*range receive window*	*m*	*input*
taup	*uncompressed pulse width*	*seconds*	*input*
f0	*chirp start frequency*	*Hz*	*input*
b	*chirp bandwidth*	*Hz*	*input*
scat_range	*vector of scatterers range*	*Km*	*input*
scat_rsc	*vector of scatterers RCS*	m^2	*input*
win	*0 = no window* *1 = Hamming* *2 = Kaiser with parameter pi* *3 = Chebychev - sidelobes at -60dB*	*none*	*input*
y	*compressed output*	*volts*	*output*

The user can access this function either by a MATLAB function call or by executing the MATLAB program *"stretch_driver.m"* which utilizes MATLAB based GUI. The outputs of this function are the complex array y and plots of the uncompressed and compressed echo signal versus time. As an example, consider the case where

nscat	*3*
rmin	*150 Km*
rrec	*30 m*
taup	*10 ms*
f0	*5.6 GHz*
b	*1 GHz*
scat_range	*rmin in Km+ {1.5, 7.5, 15.5} m*
scat_rsc	*{1, 1, 2} m^2*
win	*2 (Kaiser)*

Note that the compressed pulse range resolution, without using a window, is $\Delta R = 0.15cm$. Figs. 7.8 and 7.9, respectively, show the uncompressed and compressed echo signals corresponding to this example.

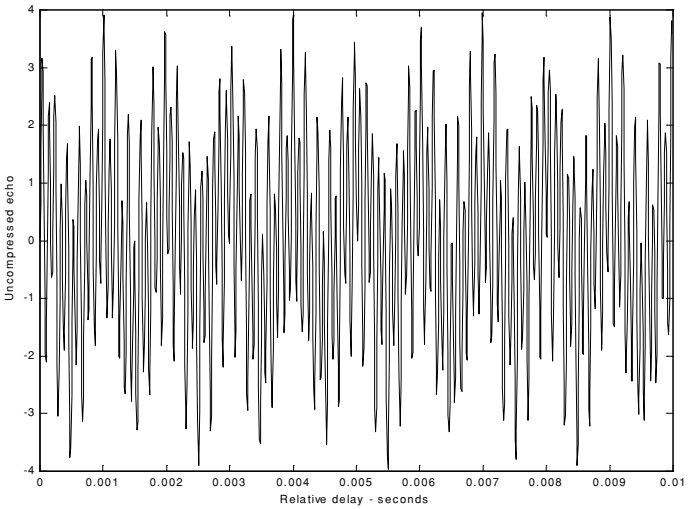

Figure 7.8. Uncompressed echo signal. Three targets are unresolved.

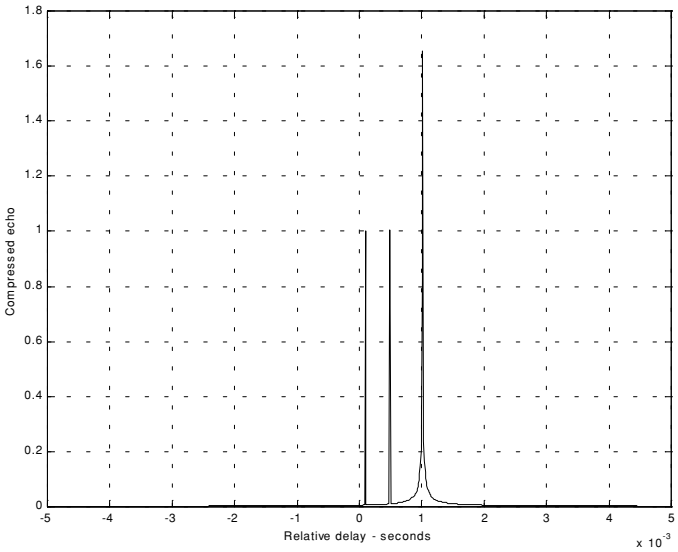

Figure 7.9. Compressed echo signal. Three targets are resolved.

7.3.3. Distortion Due to Target Velocity

Up to this point, we have analyzed pulse compression with no regards to target velocity. In fact, all analyses provided assumed stationary targets. Uncompensated target radial velocity, or equivalently Doppler shift, degrades the quality of the HRR profile generated by pulse compression. In Chapter 5, the effects of radial velocity on SFW were analyzed; similar distortion in the HRR profile is also present with LFM waveforms when target radial velocity is not compensated for.

The two effects of target radial velocity (Doppler frequency) on the radar received pulse were developed in Chapter 1. When the target radial velocity is not zero, the received pulse width is expanded (or compressed) by the time dilation factor. Additionally, the received pulse center frequency is shifted by the amount of Doppler frequency. When these effects are not compensated for, the pulse compression processor output is distorted. This is illustrated in Fig. 7.10. Fig. 7.10a shows a typical output of the pulse compression processor with no distortion. Alternatively, Figs. 7.10b, 7.10c, and 7.10d show the output of the pulse compression processor when 5% shift of the chirp center frequency and 10% time dilation are present.

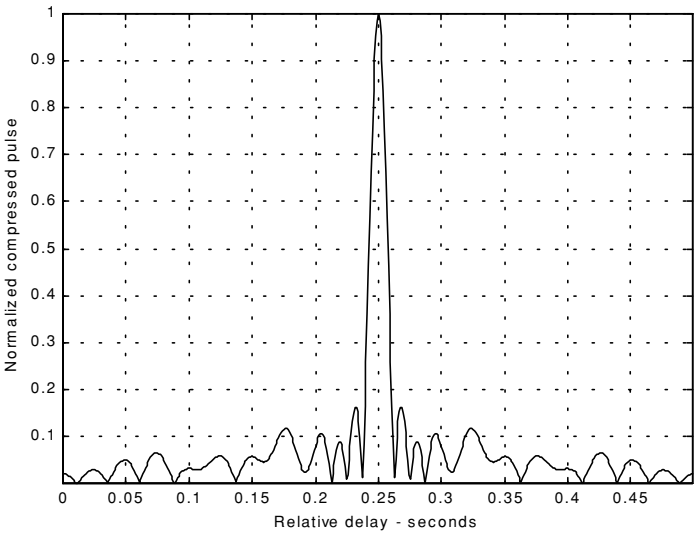

Figure 7.10a. Compressed pulse output of a pulse compression processor. No distortion is present. This figure can be reproduced using MATLAB program *"fig7_10"* given in Listing 7.3 in Section 7.5.

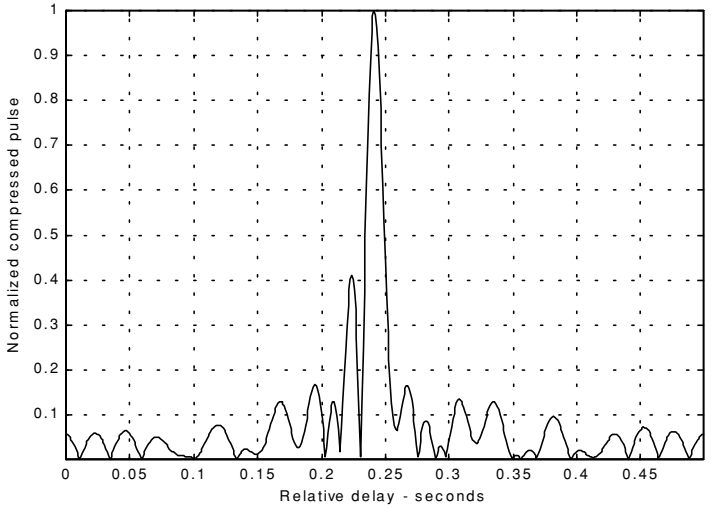

Figure 7.10b. Mismatched compressed pulse; 5% Doppler shift.

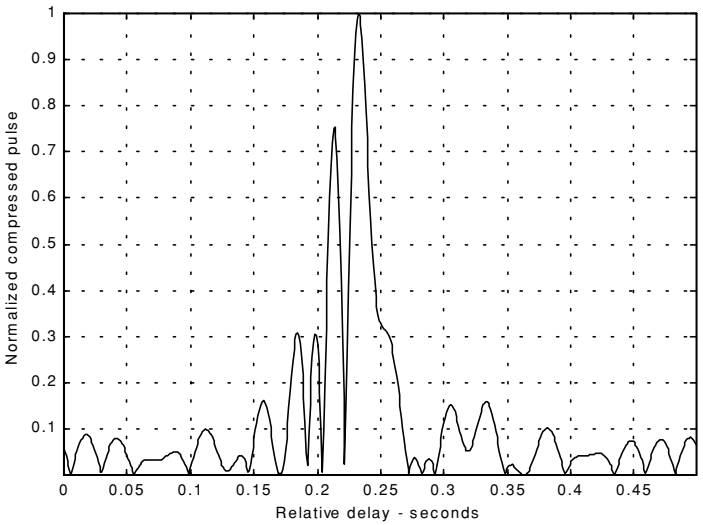

Figure 7.10c. Mismatched compressed pulse; 10% time dilation.

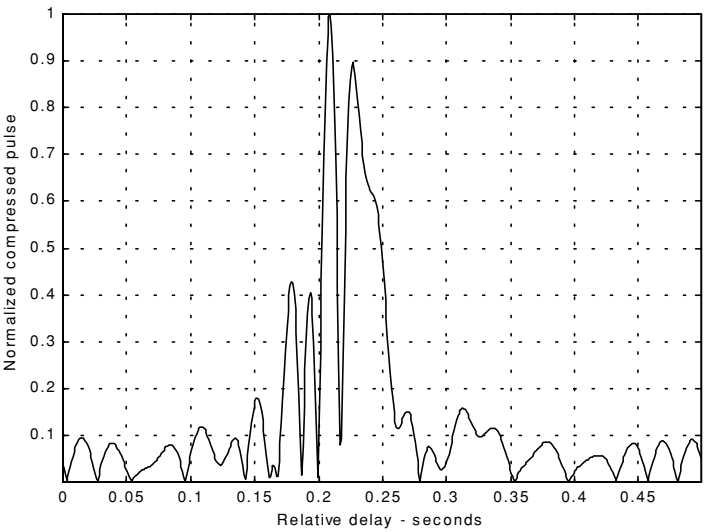

Figure 7.10d. Mismatched compressed pulse; 10% time dilation and 5% Doppler shift.

Correction for the distortion caused by the target radial velocity can be overcome by using the following approach. Over a period of few pulses, the radar data processor estimates the radial velocity of the target under track. Then, the chirp slope and pulse width of the next transmitted pulse are changed to account for the estimated Doppler frequency and time dilation.

7.3.4. Range Doppler Coupling

Plots and characteristics of the ambiguity function for an LFM waveform were presented in Chapter 6. However, the distinctive property of range Doppler coupling associated with LFM was not presented. Range Doppler coupling is a phrase used to describe the shift in the delay/range response of an LFM ambiguity function due to the presence of a Doppler shift. The nature of range Doppler coupling can be better understood by analyzing the LFM ambiguity function. An expression for an LFM ambiguity function was developed in Chapter 6, and is repeated here as Eq. (7.44):

$$\left|\chi(\tau;f_d)\right|^2 = \left|\left(1-\frac{|\tau|}{\tau'}\right)\frac{\sin\left(\pi\tau'(\mu\tau+f_d)\left(1-\frac{|\tau|}{\tau'}\right)\right)}{\pi\tau'(\mu\tau+f_d)\left(1-\frac{|\tau|}{\tau'}\right)}\right|^2 \qquad |\tau| \le \tau' \qquad \textbf{(7.44)}$$

For this purpose, consider the sketch of an LFM ambiguity function shown in Fig. 7.11.

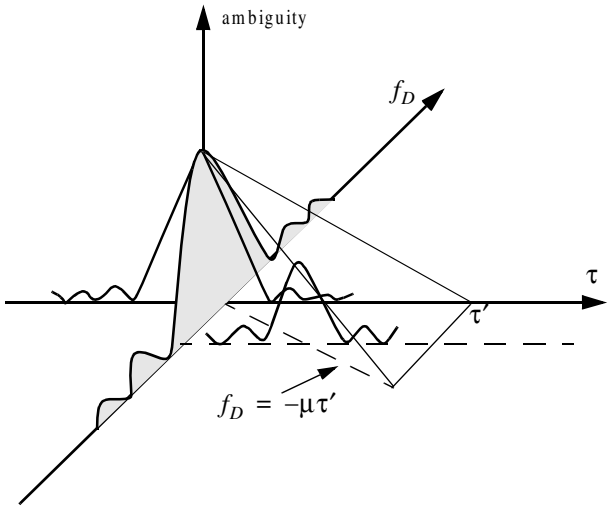

Figure 7.11. Illustration of range Doppler coupling for an LFM pulse.

The ambiguity surface extends from $-\tau'$ to τ' in range and from $-\infty$ to ∞ in Doppler. The response has a maximum at the point $(\tau, f_D) = (0, 0)$. Profiles parallel to the Doppler axis have maxima above the line $f_D = -\mu\tau$ which passes through the origin. The presence of radial velocity forces the peak of the ambiguity surface to a point that has a peak value smaller than the maximum that occurs at the origin. However, as long as the shift is less than the line $f_D = 1/\tau'$, the ambiguity function response exerts acceptable reduction in peak values, as illustrated in Fig. 7.11. This is the reason why some times LFM waveforms are called Doppler invariant.

7.4. Digital Pulse Compression

In this section we will briefly discuss three digital pulse compression techniques. They are frequency codes, binary phase codes, and poly-phase codes. Costas codes, Barker Codes, and Frank codes will be presented to illustrate, respectively, frequency, binary phase, and poly-phase coding. We will determine the pulse compression goodness of a code, based on its autocorrelation function since in the absence of noise, the output of the matched filter is proportional to the code autocorrelation. Given the autocorrelation function of a certain code, the main lobe width (compressed pulse width) and the side lobe levels are the two factors that need to be considered in order to evaluate the code's pulse compression characteristics.

7.4.1. Frequency Coding (Costas Codes)

Construction of Costas codes can be understood from the construction process of Stepped Frequency Waveforms (SFW) described in Chapter 5. In SFW, a relatively long pulse of length τ' is divided into N subpulses, each of width τ_1 ($\tau' = N\tau_1$). Each group of N subpulses is called a burst. Within each burst the frequency is increased by Δf from one subpulse to the next. The overall burst bandwidth is $N\Delta f$. More precisely,

$$\tau_1 = \tau'/N \tag{7.45}$$

and the frequency for the ith subpulse is

$$f_i = f_0 + i\Delta f \qquad ; \; i = 1, N \tag{7.46}$$

where f_0 is a constant frequency and $f_0 \gg \Delta f$. It follows that the time-bandwidth product of this waveform is

$$\Delta f\tau' = N^2 \tag{7.47}$$

Costas signals (or codes) are similar to SFW, except that the frequencies for the subpulses are selected in a random fashion, according to some predetermined rule or logic. For this purpose, consider the $N \times N$ matrix shown in Fig. 7.12. In this case, the rows are indexed from $i = 1, 2, \ldots, N$ and the columns are indexed from $j = 0, 1, 2, \ldots, (N-1)$. The rows are used to denote the subpulses and the columns are used to denote the frequency. A *"dot"* indicates the frequency value assigned to the associated subpulse. In this fashion, Fig. 7.12a shows the frequency assignment associated with a SFW. Alternatively, the frequency assignments in Fig. 7.12b are chosen randomly. For a matrix of size $N \times N$, there are a total of $N!$ possible ways of assigning the *"dots"* (i.e., $N!$ possible codes).

The sequences of *"dots"* assignment for which the corresponding ambiguity function approaches an ideal or a *"thumbtack"* response are called Costas codes. A near thumbtack response was obtained by Costas[1] by using the following logic: only one frequency per time slot (row) and per frequency slot (column). Therefore, for an $N \times N$ matrix the number of possible Costas codes is drastically less than $N!$. For example, there are $N_c = 4$ possible Costas codes for $N = 3$, and $N_c = 40$ possible codes for $N = 5$. It can be shown that the code density, defined as the ratio $N_c/N!$, significantly gets smaller as N becomes larger.

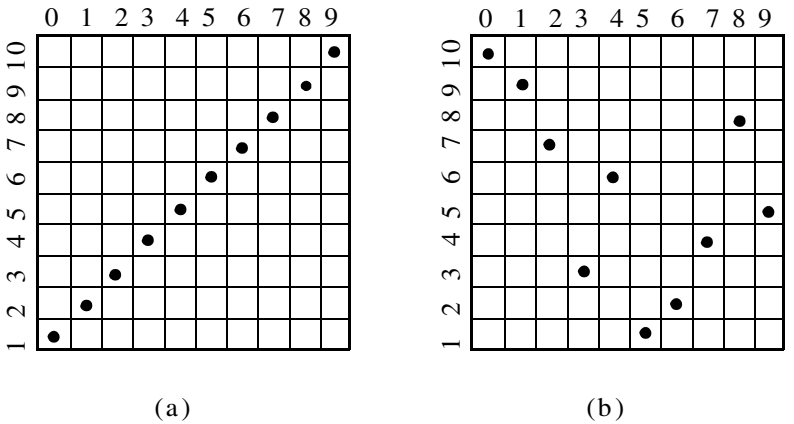

Figure 7.12. Frequency assignment for a burst of N subpulses. (a) SFW (stepped LFM); (b) Costas code of length Nc = 10.

1. Costas, J. P., A study of a Class of Detection Waveforms Having Nearly Ideal Range-Doppler Ambiguity Properties, *Proc. IEEE* ***72***, 1984, pp. 996-1009.

There are numerous analytical ways to generate Costas codes. In this section we will describe two of these methods. First, let q be an odd prime number, and choose the number of subpulses as

$$N = q - 1 \tag{7.48}$$

Define γ as the primitive root of q. A primitive root of q (an odd prime number) is defined as γ such that the powers $\gamma, \gamma^2, \gamma^3, \ldots, \gamma^{q-1}$ modulo q generate every integer from 1 to $q - 1$.

In the first method, for an $N \times N$ matrix, label the rows and columns, respectively, as

$$\begin{aligned} i &= 0, 1, 2, \ldots, (q-2) \\ j &= 1, 2, 3, \ldots, (q-1) \end{aligned} \tag{7.49}$$

Place a dot in the location (i, j) corresponding to the frequency f_i (from Eq. (7.46)) if and only if

$$i = (\gamma)^j \ \ (modulo \ \ q) \tag{7.50}$$

In the next method, Costas code is first obtained from the logic described above; then by deleting the first row and first column from the matrix a new code is generated. This method produces a Costas code of length $N = q - 2$.

Define the normalized complex envelope of the Costas signal as

$$s(t) = \frac{1}{\sqrt{N\tau_1}} \sum_{l=0}^{N-1} s_l(t - l\tau_1) \tag{7.51}$$

$$s_l(t) = \begin{pmatrix} \exp(j2\pi f_l t) & 0 \le t \le \tau_1 \\ 0 & elsewhere \end{pmatrix} \tag{7.52}$$

Costas showed that the output of the matched filter is

$$\chi(\tau, f_D) = \frac{1}{N} \sum_{l=0}^{N-1} \exp(j2\pi l f_D \tau) \left\{ \Phi_{ll}(\tau, f_D) + \sum_{\substack{q=0 \\ q \ne l}}^{N-1} \Phi_{lq}(\tau - (l-q)\tau_1, f_D) \right\} \tag{7.53}$$

$$\Phi_{lq}(\tau, f_D) = \left(\tau_1 - \frac{|\tau|}{\tau_1}\right) \frac{\sin\alpha}{\alpha} \ \exp(-j\beta - j2\pi f_q \tau) \qquad , \ |\tau| \le \tau_1 \tag{7.54}$$

$$\alpha = \pi(f_l - f_q - f_D)(\tau_1 - |\tau|) \tag{7.55}$$

$$\beta = \pi(f_l - f_q - f_D)(\tau_1 + |\tau|) \tag{7.56}$$

Three-dimensional plots for the ambiguity function of Costas signals show the near thumbtack response of the ambiguity function. All sidelobes, except for few around the origin, have amplitude $1/N$. Few sidelobes close to the origin have amplitude $2/N$, which is typical of Costas codes. The compression ratio of a Costas code is approximately N.

7.4.2. Binary Phase Codes

In this case, a relatively long pulse of width τ' is divided into N smaller pulses; each is of width $\Delta\tau = \tau'/N$. Then, the phase of each sub-pulse is randomly chosen as either 0 or π radians relative to some CW reference signal. It is customary to characterize a sub-pulse that has 0 phase (amplitude of +1 Volt) as either "1" or "+." Alternatively, a sub-pulse with phase equal to π (amplitude of -1 Volt) is characterized by either "0" or "-." The compression ratio associated with binary phase codes is equal to $\xi = \tau'/\Delta\tau$, and the peak value is N times larger than that of the long pulse. The goodness of a compressed binary phase code waveform depends heavily on the random sequence of the phase for the individual sub-pulses.

One family of binary phase codes that produce compressed waveforms with constant side lobe levels equal to unity is the Barker code. Fig. 7.13 illustrates this concept for a Barker code of length seven. A Barker code of length n is denoted as B_n. There are only seven known Barker codes that share this unique property; they are listed in Table 7.1. Note that B_2 and B_4 have complementary forms that have the same characteristics. Since there are only seven Barker codes, they are not used when radar security is an issue.

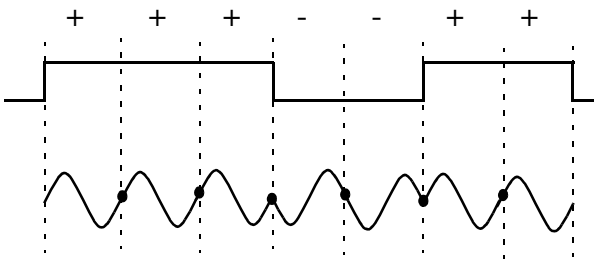

Figure 7.13. Binary phase code of length 7.

TABLE 7.1. Barker codes.

Code symbol	Code length	Code elements	Side lode reduction (dB)
B_2	2	+- ++	6.0
B_3	3	++-	9.5
B_4	4	++-+ +++-	12.0
B_5	5	+++-+	14.0
B_7	7	+++--+-	16.9
B_{11}	11	+++---+--+-	20.8
B_{13}	13	+++++--++-+-+	22.3

In general, the autocorrelation function (which is an approximation for the matched filter output) for a B_N Barker code will be $2N\Delta\tau$ wide. The main lobe is $2\Delta\tau$ wide; the peak value is equal to N. There are $(N-1)/2$ side lobes on either side of the main lobe; this is illustrated in Fig. 7.14 for a B_{13}. Notice that the main lobe is equal to 13, while all side lobes are unity.

The most side lobe reduction offered by a Barker code is $-22.3dB$, which may not be sufficient for the desired radar application. However, Barker codes can be combined to generate much longer codes. In this case, a B_m code can be used within a B_n code (m within n) to generate a code of length mn. The compression ratio for the combined B_{mn} code is equal to mn. As an example, a combined B_{54} is given by

$$B_{54} = \{11101, 11101, 00010, 11101\} \tag{7.57}$$

and is illustrated in Fig. 7.15. Unfortunately, the side lobes of a combined Barker code autocorrelation function are no longer equal to unity.

Some side lobes of a Barker code autocorrelation function can be reduced to zero if the matched filter is followed by a linear transversal filter with impulse response given by

$$h(t) = \sum_{k=-N}^{N} \beta_k \delta(t - 2k\Delta\tau) \tag{7.58}$$

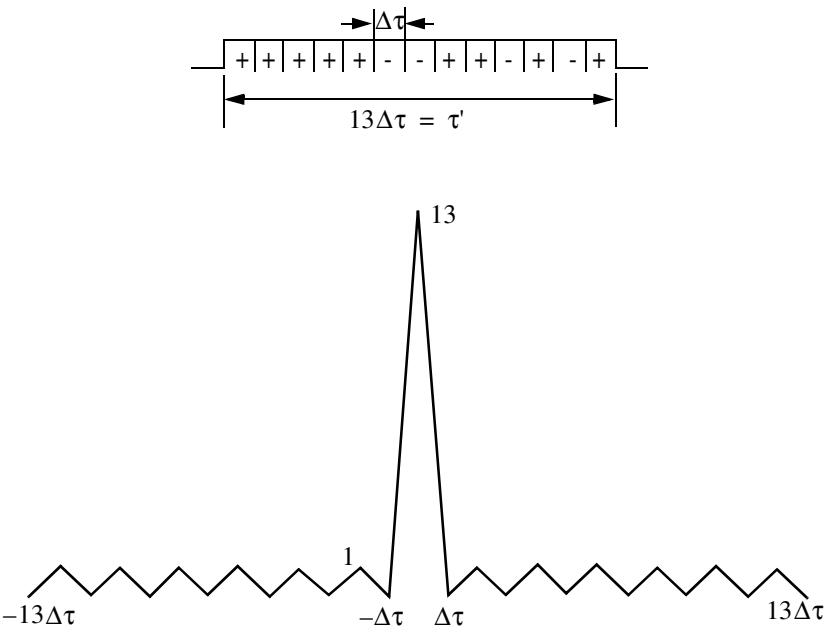

Figure 7.14. Barker code of length 13, and its corresponding autocorrelation function.

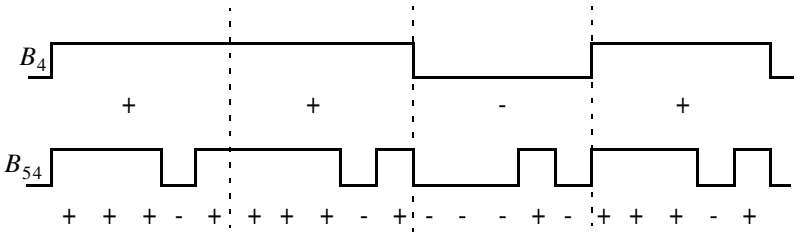

Figure 7.15. A combined B_{54} Barker code.

where N is the filter's order, the coefficients β_k ($\beta_k = \beta_{-k}$) are to be determined, $\delta(\cdot)$ is the delta function, and $\Delta\tau$ is the Barker code sub-pulse width. A filter of order N produces N zero side lobes on either side of the main lobe. The main lobe amplitude and width do not change. This is illustrated in Fig. 7.16.

In order to illustrate this approach further, consider the case where the input to the matched filter is B_{11}, and assume $N = 4$. The autocorrelation for a B_{11} code is

$$\phi_{11} = \{-1, 0, -1, 0, -1, 0, -1, 0, -1, 0, 11, \\ 0, -1, 0, -1, 0, -1, 0, -1, 0, -1\} \tag{7.59}$$

The output of the transversal filter is the discrete convolution between its impulse response and the sequence ϕ_{11}. At this point we need to compute the coefficients β_k that guarantee the desired filter output (i.e., unchanged main lobe and four zero side lobe levels). Performing the discrete convolution as defined in Eq. (7.58), and collecting equal terms ($\beta_k = \beta_{-k}$) yield the following set of five linearly independent equations:

$$\begin{bmatrix} 11 & -2 & -2 & -2 & -2 \\ -1 & 10 & -2 & -2 & -1 \\ -1 & -2 & 10 & -2 & -1 \\ -1 & -2 & -1 & 11 & -1 \\ -1 & -1 & -1 & -1 & 11 \end{bmatrix} \begin{bmatrix} \beta_0 \\ \beta_1 \\ \beta_2 \\ \beta_3 \\ \beta_4 \end{bmatrix} = \begin{bmatrix} 11 \\ 0 \\ 0 \\ 0 \\ 0 \end{bmatrix} \tag{7.60}$$

The solution of Eq. (7.60) is left as an exercise. Note that by setting the first equation equal to 11 and all other equations to 0 and then solving for β_k guarantees that the main peak remains unchanged, and that the next four side lobes are zeros. So far we have assumed that coded pulses have rectangular shapes. Using other pulses of other shapes, such as Gaussian, may produce better side lobe reduction and a larger compression ratio.

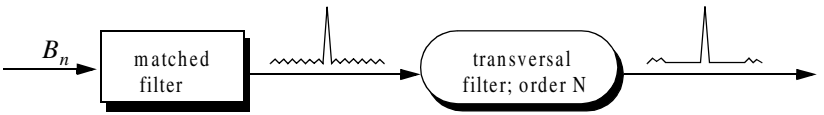

Figure 7.16. A linear transversal filter of order N can be used to produce N zero side lobes in the autocorrelation function. In this figure, N = 4.

7.4.3. Frank Codes

Codes that use any harmonically related phases based on a certain fundamental phase increment are called poly-phase codes. We will demonstrate this coding technique using Frank codes. In this case, a single pulse of width τ' is divided into N equal groups; each group is subsequently divided into other N sub-pulses each of width $\Delta\tau$. Therefore, the total number of sub-pulses within each pulse is N^2, and the compression ratio is $\xi = N^2$. As before, the phase within each sub-pulse is held constant with respect to some CW reference signal.

A Frank code of N^2 sub-pulses is referred to as an N-phase Frank code. The first step in computing a Frank code is to divide $360°$ by N, and define the result as the fundamental phase increment $\Delta\varphi$. More precisely,

$$\Delta\varphi = \frac{360°}{N} \tag{7.61}$$

Note that the size of the fundamental phase increment decreases as the number of groups is increased, and because of phase stability, this may degrade the performance of very long Frank codes. For N-phase Frank code the phase of each sub-pulse is computed from

$$\begin{pmatrix} 0 & 0 & 0 & 0 & \dots & 0 \\ 0 & 1 & 2 & 3 & \dots & N-1 \\ 0 & 2 & 4 & 6 & \dots & 2(N-1) \\ \dots & \dots & \dots & \dots & \dots & \dots \\ \dots & \dots & \dots & \dots & \dots & \dots \\ 0 & (N-1) & 2(N-1) & 3(N-1) & \dots & (N-1)^2 \end{pmatrix} \Delta\varphi \tag{7.62}$$

where each row represents a group, and a column represents the sub-pulses for that group. For example, a 4-phase Frank code has $N = 4$, and the fundamental phase increment is $\Delta\varphi = (360°/4) = 90°$. It follows that

$$\begin{pmatrix} 0 & 0 & 0 & 0 \\ 0 & 90° & 180° & 270° \\ 0 & 180° & 0 & 180° \\ 0 & 270° & 180° & 90° \end{pmatrix} \Rightarrow \begin{pmatrix} 1 & 1 & 1 & 1 \\ 1 & j & -1 & -j \\ 1 & -1 & 1 & -1 \\ 1 & -j & -1 & j \end{pmatrix} \tag{7.63}$$

Therefore, a Frank code of 16 elements is given by

$$F_{16} = \{1 \;\; 1 \;\; 1 \;\; 1 \;\; 1 \;\; j \;\; -1 \;\; -j \;\; 1 \;\; -1 \;\; 1 \;\; -1 \;\; 1 \;\; -j \;\; -1 \;\; j\} \tag{7.64}$$

The phase increments within each row represent a stepwise approximation of an up-chirp LFM waveform. The phase increments for subsequent rows increase linearly versus time. Thus, the corresponding LFM chirp slopes also increase linearly for subsequent rows. This is illustrated in Fig. 7.17, for F_{16}.

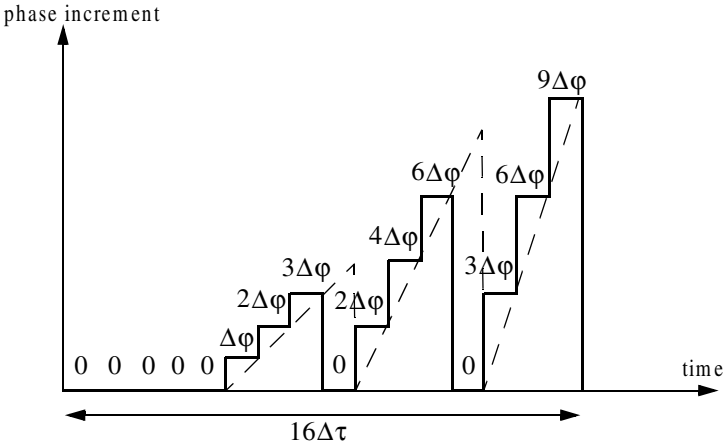

Figure 7.17. Stepwise approximation of an up-chirp waveform, using a Frank code of 16 elements.

7.4.4. Pseudo-Random (PRN) Codes

Pseudo-random (PRN) codes are also known as Maximal Length Sequences (MLS) codes. These codes are called pseudo-random because the statistics associated with their occurrence is similar to that associated with the coin-toss sequences. Maximum length sequences are periodic with period L and the code values take on two binary values (+1 and -1). The MLS correlation function is

$$\phi(n) = \begin{cases} L & n = 0, \pm L, \pm 2L, \ldots \\ -1 & elsewhere \end{cases} \qquad \textbf{(7.65)}$$

Fig. 7.18 shows a typical sketch for an MLS autocorrelation function. Clearly these codes have the advantage that the compression ratio becomes very large as the period is increased. Additionally, adjacent peaks (grating lobes) become farther apart.

Maximum length sequences exist for all integer values m, with a period equal to $2^m - 1$. They can be generated using shift register circuits with the proper feedback connections, where the sum is a modulo-2 operation. This is

illustrated in Fig. 7.19 for $m = 4$ (i.e., $L = 15$). Note that the circuit shown in Fig. 7.19 is not the only one that can produce this code.

In radar applications, long codes are very desirable. However, having very long codes presents many possibilities for the feedback connections through the modulo-2 adder. For example, for $m = 80$, the period is $L = 2^{80} - 1$, which is very huge and may take years to produce the corresponding code. Therefore, there is a need for a more systematic method for producing MLS codes.

In practice, typical MLS codes are produced by using the primitive polynomials with the proper degree that corresponds to the code, and the feedback connections are made according to the chosen polynomial, as illustrated in Fig. 7.19 for $m = 4$. In this example the primitive polynomial is $x^4 + x + 1$. Of course the initial loading for the registers must be different from all zeros. More details on primitive polynomials can be found in many sited references.

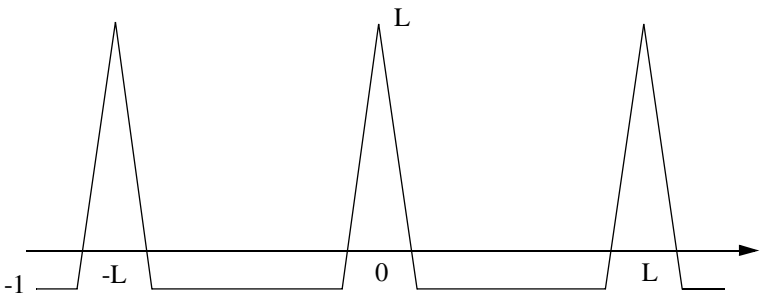

Figure 7.18. Typical autocorrelation of an MLS code of length L.

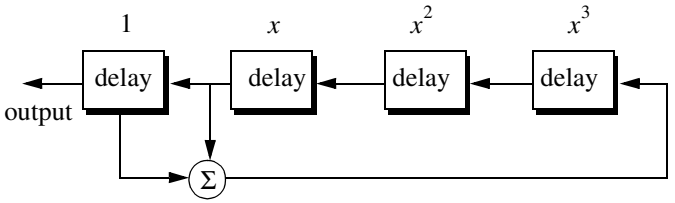

Figure 7.19. Circuit for generating an MLS sequence of length $L = 15$. The primitive polynomial is $x^4 + x + 1$.

7.5. MATLAB Listings

This section presents listings for all MATLAB programs/functions used in this chapter. The user is advised to rerun these programs with different input parameters.

Listing 7.1. MATLAB Function "matched_filter.m"

```
function [y] = matched_filter(nscat, taup, f0, b, rmin, rrec, scat_range,
scat_rcs, winid)
%
eps = 1.0e-16;
htau = taup / 2.;
c = 3.e8;
n = fix(2. * taup * b);
m = power_integer_2(n);
nfft = 2.^m;
x(nscat,1:nfft) = 0.;
y(1:nfft) = 0.;
replica(1:nfft) = 0.;
if( winid == 0.)
  win(1:nfft) = 1.;
  win =win';
else
  if(winid == 1.)
    win = hamming(nfft);
  else
    if( winid == 2.)
      win = kaiser(nfft,pi);
    else
      if(winid == 3.)
        win = chebwin(nfft,60);
      end
    end
  end
end
deltar = c / 2. / b;
max_rrec = deltar * nfft / 2.;
maxr = max(scat_range) - rmin;
if(rrec > max_rrec | maxr >= rrec )
  'Error. Receive window is too large; or scatterers fall outside window'
  break
end
trec = 2. * rrec / c;
```

```
deltat = taup / nfft;
t = 0: deltat:taup-eps;
uplimit = max(size(t));
replica(1:uplimit) = exp(i * 2.* pi * (.5 * (b/taup) .* t.^2));
figure(3)
subplot(2,1,1)
plot(real(replica))
title('Matched filter time domain response')
subplot(2,1,2)
plot(fftshift(abs(fft(replica))));
title('Matched filter frequency domain response')
for j = 1:1:nscat
   t_tgt = 2. * (scat_range(j) - rmin) / c +htau;
   x(j,1:uplimit) = scat_rcs(j) .* exp(i *  2.* pi * ...
      (.5 * (b/taup) .* (t+t_tgt).^2));
   y = y + x(j,:);
end
figure(1)
plot(t,real(y),'k')
xlabel ('Relative delay - seconds')
ylabel ('Uncompressed echo')
title ('Zero delay coincide with minimum range')
rfft = fft(replica,nfft);
yfft = fft(y,nfft);
out= abs(ifft((rfft .* conj(yfft)) .* win' )) ./ (nfft);
figure(2)
time = -htau:deltat:htau-eps;
plot(time,out,'k')
xlabel ('Relative delay - seconds')
ylabel ('Compressed echo')
title ('Zero delay coincide with minimum range')
grid
```

Listing 7.2. MATLAB Function "stretch.m"

```
function [y] = stretch(nscat,taup,f0,b,rmin,rrec,scat_range,scat_rcs,winid)
eps = 1.0e-16;
htau = taup / 2.;
c = 3.e8;
trec = 2. * rrec / c;
n = fix(2. * trec * b);
m = power_integer_2(n);
nfft = 2.^m;
x(nscat,1:nfft) = 0.;
```

```
y(1:nfft) = 0.;
if( winid == 0.)
  win(1:nfft) = 1.;
  win =win';
else
  if(winid == 1.)
    win = hamming(nfft);
  else
    if( winid == 2.)
      win = kaiser(nfft,pi);
    else
      if(winid == 3.)
        win = chebwin(nfft,60);
      end
    end
  end
end
deltar = c / 2. / b;
max_rrec = deltar * nfft / 2.;
maxr = max(scat_range) - rmin;
if(rrec > max_rrec | maxr >= rrec )
  'Error. Receive window is too large; or scatterers fall outside window'
  break
end
deltat = taup / nfft;
t = 0: deltat:taup-eps;
uplimit = max(size(t));
for j = 1:1:nscat
  psi1 = 4. * pi * scat_range(j) * f0 / c - ...
    4. * pi * b * scat_range(j) * scat_range(j) / c / c/ taup;
  psi2 = (4. * pi * b * scat_range(j) / c / taup) .* t;
  x(j,1:uplimit) = scat_rcs(j) .* exp(i * psi1 + i .* psi2);
  y = y + x(j,:);
end
figure(1)
plot(t,real(y),'k')
xlabel ('Relative delay - seconds')
ylabel ('Uncompressed echo')
title ('Zero delay coincide with minimum range')
ywin = y .* win';
yfft = fft(y,nfft) ./ nfft;
out= fftshift(abs(yfft));
figure(2)
time = -htau:deltat:htau-eps;
```

```
plot(time,out,'k')
xlabel ('Relative delay - seconds')
ylabel ('Compressed echo')
title ('Zero delay coincide with minimum range')
grid
```

Listing 7.3. MATLAB Program "fig7_10.m'

```
clear all
eps = 1.5e-5;
t = 0:0.001:.5;
y = chirp(t,0,.25,20);
figure(1)
plot(t,y);
yfft = fft(y,512) ;
ycomp = fftshift(abs(ifft(yfft .* conj(yfft))));
maxval = max (ycomp);
ycomp = eps + ycomp ./ maxval;
figure(1)
del = .5 /512.;
tt = 0:del:.5-eps;
plot (tt,ycomp,'k')
xlabel ('Relative delay - seconds');
ylabel('Normalized compressed pulse')
grid
%change center frequency
y1 = chirp (t,0,.25,21);
y1fft = fft(y1,512);
y1comp = fftshift(abs(ifft(y1fft .* conj(yfft))));
maxval = max (y1comp);
y1comp = eps + y1comp ./ maxval;
figure(2)
plot (tt,y1comp,'k')
xlabel ('Relative delay - seconds');
ylabel('Normalized compressed pulse')
grid
%change pulse width
t = 0:0.001:.45;
y2 = chirp (t,0,.225,20);
y2fft = fft(y2,512);
y2comp = fftshift(abs(ifft(y2fft .* conj(yfft))));
maxval = max (y2comp);
y2comp = eps + y2comp ./ maxval;
figure(3)
```

```
plot (tt,y2comp,'k')
xlabel ('Relative delay - seconds');
ylabel('Normalized compressed pulse')
grid
```

Problems

7.1. Starting with Eq. (7.17), prove Eq. (7.21).

7.2. The smallest positive primitive root of $q = 11$ is $\gamma = 2$; for $N = 10$ generate the corresponding Costas matrix.

7.3. Develop a MATLAB program to plot the ambiguity function associated with Costas codes. Use Eqs. (7.53) through (7.56). Your program should generate 3-D plots, contour plots, and zero delay/Doppler cuts. Verify the side lobe behaviour and the compression ratio of Costas codes.

7.4. Consider the 7-bit Barker code, designated by the sequence $x(n)$. (a) Compute and plot the autocorrelation of this code. (b) A radar uses binary phase coded pulses of the form $s(t) = r(t)\cos(2\pi f_0 t)$, where $r(t) = x(0),\ for\ \ 0 < t < \Delta t$, $r(t) = x(n),\ for\ \ n\Delta t < t < (n+1)\Delta t$, and $r(t) = 0,\ \ for\ \ t > 7\Delta t$. Assume $\Delta t = 0.5\mu s$. (a) Give an expression for the autocorrelation of the signal $s(t)$, and for the output of the matched filter when the input is $s(t - 10\Delta t)$; (b) compute the time bandwidth product, the increase in the peak SNR, and the compression ratio.

7.5. (a) Perform the discrete convolution between the sequence ϕ_{11} defined in Eq. (7.59), and the transversal filter impulse response (i.e., derive Eq. (7.60). (b) Solve Eq. (7.60), and sketch the corresponding transversal filter output.

7.6. Repeat the previous problem for $N = 13$ and $k = 6$. Use Barker code of length 13.

7.7. Develop a Barker code of length 35. Consider both B_{75} and B_{57}.

7.8. Write a computer program to calculate the discrete correlation between any two finite length sequences. Verify your code by comparing your results to the output of the MATLAB function *"xcorr"*.

7.9. Compute the discrete autocorrelation for an F_{16} Frank code.

7.10. Generate a Frank code of length 8, F_8.

Chapter 8 *Radar Wave Propagation*

In the earlier chapters, radar systems were analyzed with the assumption that the radar waves which traveled to and from targets are in free space. Signal interference due to the earth and its atmosphere was not considered. Despite the fact that *"free space analysis"* may be adequate to provide a general understanding of radar systems, it is only an approximation. In order to accurately predict radar performance, we must modify free space analysis to include the effects of the earth and its atmosphere. This modification should account for ground reflections from the surface of the earth, diffraction of electromagnetic waves, bending or refraction of radar waves due to the earth atmosphere, and attenuation or absorption of radar energy by the gases constituting the atmosphere.

8.1. Earth Atmosphere

The earth atmosphere is compromised of several layers, as illustrated in Fig. 8.1. The first layer which extends in altitude to about 20 Km is known as the troposphere. Electromagnetic waves refract (bend downward) as they travel in the troposphere. The troposphere refractive effect is related to its dielectric constant which is a function of the pressure, temperature, water vapor, and gaseous content. Additionally, due to gases and water vapor in the atmosphere radar energy suffers a loss. This loss is known as the atmospheric attenuation. Atmospheric attenuation increases significantly in the presence of rain, fog, dust, and clouds.

The region above the troposphere (altitude from 20 to 50 Km) behaves like free space, and thus little refraction occurs in this region. This region is known as the interference zone.

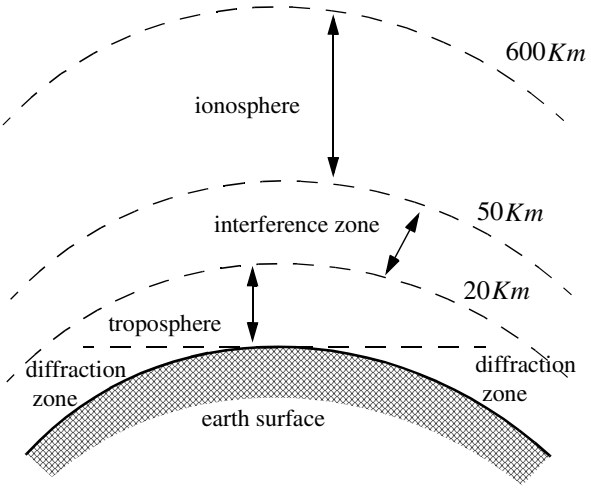

Figure 8.1. Earth atmosphere geometry.

The ionosphere extends from about 50 Km to about 600 Km. It has very low gas density compared to the troposphere. It contains a significant amount of ionized free electrons. The ionization is primarily caused by the sun's ultraviolet and X-rays. This presence of free electrons in the ionosphere affects electromagnetic wave propagation in different ways. These effects include refraction, absorption, noise emission, and polarization rotation. The degree of degradation depends heavily on the frequency of the incident waves. For example, frequencies lower than about 4 to 6 MHz are completely reflected from the lower region of the ionosphere. Frequencies higher than 30 MHz may penetrate the ionosphere with some level of attenuation. In general, as the frequency is increased the ionosphere's effects become less prominent.

The region below the horizon, close to the earth's surface, is called the diffraction region. Diffraction is a term used to describe the bending of radar waves around physical objects. Two types of diffraction are common. They are knife edge and cylinder edge diffraction.

8.2. Refraction

In free space, electromagnetic waves travel in straight lines. However, in the presence of the earth atmosphere, they bend (refract). Refraction is a term used

to describe the deviation of radar wave propagation from straight lines. The deviation from straight line propagation is caused by the variation of the index of refraction. The index of refraction is defined as

$$n = c/v \tag{8.1}$$

where c is the velocity of electromagnetic waves in free space and v is the wave velocity in the medium. Close to the earth's surface the index of refraction is almost unity; however, with increasing altitude the index of refraction decreases gradually. The discussion presented in this chapter assumes a well mixed atmosphere, where the index of refraction decreases in a smooth monotonic fashion with height. The rate of change of the earth's index of refraction n with altitude h is normally referred to as the refractivity gradient, dn/dh. As a result of the negative rate of change in dn/dh, electromagnetic waves travel at slightly higher velocities in the upper troposphere than the lower part. As a result of this, waves traveling horizontally in the troposphere gradually bend downward. In general, since the rate of change in the refractivity index is very slight, waves do not curve downward appreciably unless they travel very long distances through the troposphere.

Refraction affects radar waves in two different ways depending on height. For targets that have altitudes, typically above 100 meters, the effect of refraction is illustrated in Fig. 8.2. In this case, refraction imposes limitations on the radar's capability to measure target position. Refraction introduces an error in measuring the elevation angle.

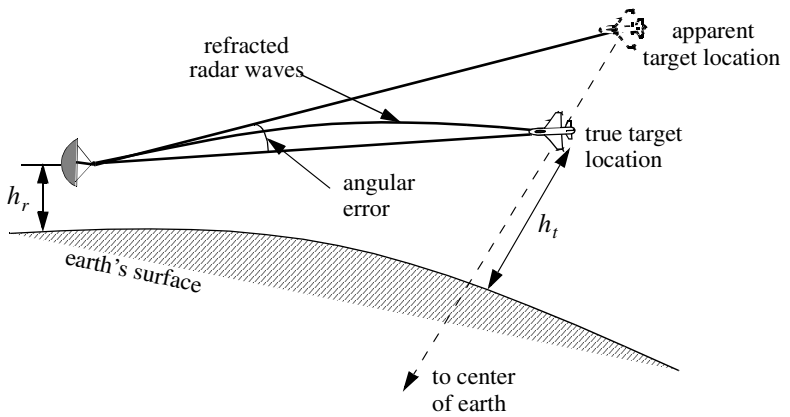

Figure 8.2. Refraction high altitude effect on electromagnetic waves.

In a well mixed atmosphere, the refractivity gradient close to the earth's surface is almost constant. However, temperature changes and humidity lapses close to the earth's surface may cause serious changes in the refractivity profile. When the refractivity index becomes large enough electromagnetic waves bend around the curve of the earth. Consequently, the radar's range to the horizon is extended. This phenomenon is called ducting, and is illustrated in Fig. 8.3. Ducting can be serious over the sea surface, particularly during the hot summertime.

Using ray tracing (geometric optics) an integral-relating range-to-target height with the elevation angle as a parameter can be derived and calculated. However, such computations are complex and numerically intensive. Thus, in practice, radar systems deal with refraction in two different ways, depending on height. For altitudes higher than 3 Km, actual target heights are estimated from look-up tables or from charts of target height versus range for different elevation angles.

Simpler methods that are valid for altitude less than 3 Km, for calculating target height, can also be employed. In this case, the most common way of dealing with refraction is to replace the actual earth with an imaginary earth whose effective radius is $r_e = kr_0$, where r_0 is the actual earth radius, and k is

$$k = \frac{1}{1 + r_0(dn/dh)} \tag{8.2}$$

When the refractivity gradient is assumed to be constant with altitude and is equal to 39×10^{-9} per meter, then $k = 4/3$. Using an effective earth radius $r_e = (4/3)r_0$ produces what is known as the *"four third earth model."* In general, choosing

$$r_e = r_0(1 + 6.37 \times 10^{-3}(dn/dh)) \tag{8.3}$$

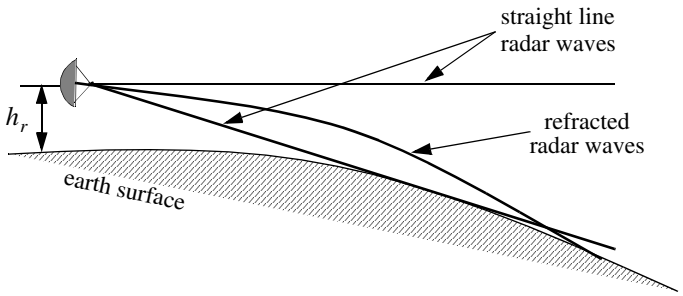

Figure 8.3. Refraction low altitude effect on electromagnetic waves.

produces a propagation model where waves travel in straight lines. Selecting the correct value for k depends heavily on the region's meteorological conditions. Blake[1] derives the *"height-finding equation"* for the 4/3 earth. It is

$$h = h_r + 6076R\sin\theta + 0.6625R^2(\cos\theta)^2 \tag{8.4}$$

where h and h_r are in feet and R is nautical miles. All variables are defined in Fig. 8.4.

The distance to the horizon for a radar located at height h_r can be calculated with the help of Fig. 8.5. For the right-angle triangle OBA we get

$$r_h = \sqrt{(r_0 + h_r)^2 - r_0^2} \tag{8.5}$$

where r_h is the distance to the horizon. By expanding Eq. (8.5) and collecting terms we can derive the expression for the distance to the horizon as

$$r_h^2 = 2r_0h_r + h_r^2 \tag{8.6}$$

Finally, since $r_0 \gg h_r$ Eq. (8.6) is approximated by

$$r_h \approx \sqrt{2r_0h_r} \tag{8.7}$$

and when refraction is accounted for, Eq. (8.7) becomes

$$r_h \approx \sqrt{2r_eh_r} \tag{8.8}$$

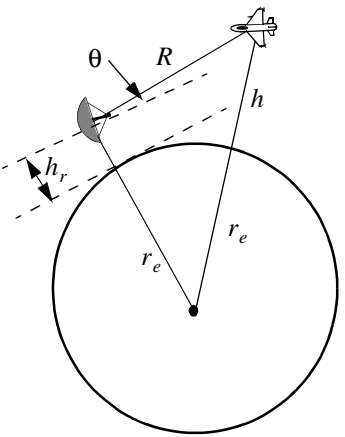

Figure 8.4. Measuring target height for 4/3 earth.

1. Blake, L. V., *Radar Range-Performance Analysis*, Artech House, 1986.

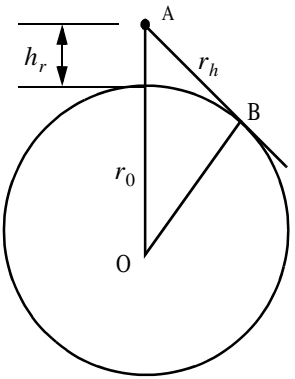

Figure 8.5. Measuring the distance to the horizon.

8.3. Ground Reflection

When radar waves are reflected from the earth's surface, they suffer a loss in amplitude and a change in phase. Three factors that contribute to these changes that are the overall ground reflection coefficient are the reflection coefficient for a flat surface, the divergence factor due to earth curvature, and the surface roughness.

8.3.1. Smooth Surface Reflection Coefficient

The smooth surface reflection coefficient depends on the frequency, on the surface dielectric coefficient, and on the radar grazing angle. The vertical polarization and the horizontal polarization reflection coefficients are

$$\Gamma_v = \frac{\varepsilon \sin\psi_g - \sqrt{\varepsilon - (\cos\psi_g)^2}}{\varepsilon \sin\psi_g + \sqrt{\varepsilon - (\cos\psi_g)^2}} \tag{8.9}$$

$$\Gamma_h = \frac{\sin\psi_g - \sqrt{\varepsilon - (\cos\psi_g)^2}}{\sin\psi_g + \sqrt{\varepsilon - (\cos\psi_g)^2}} \tag{8.10}$$

where ψ_g is the grazing angle (incident angle) and ε is the complex dielectric constant of the surface, and are given by

$$\varepsilon = \varepsilon' - j\varepsilon'' \tag{8.11}$$

Typical values of ε' and ε" can be found tabulated in the literature. For example, seawater at $28°C$ has ε' = 65 and ε" = 30.7 at X-band. Fig. 8.6 shows the corresponding magnitude plots for Γ_h and Γ_v, while Fig. 8.7 shows the phase plots. The plots shown in those figures show the general typical behavior of the reflection coefficient.

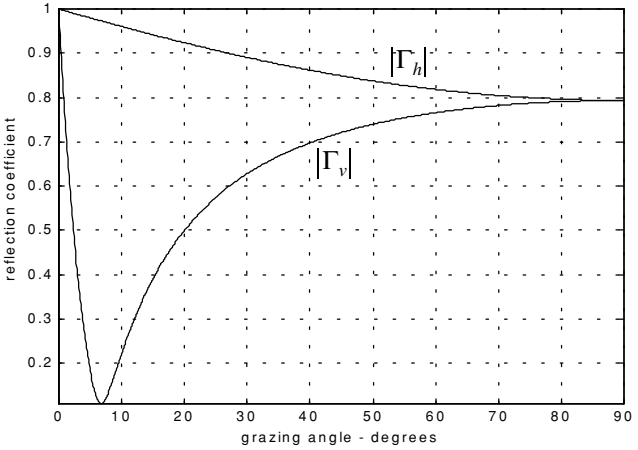

Figure 8.6. Reflection coefficient magnitude.

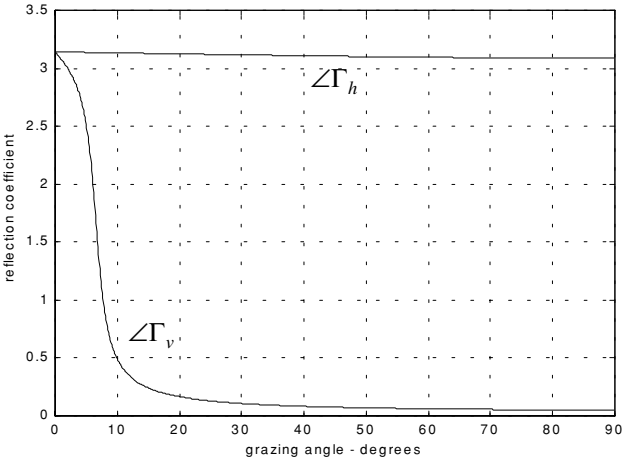

Figure 8.7. Reflection coefficient phase.

Note that when $\psi_g = 90°$ we get

$$\Gamma_h = \frac{1-\sqrt{\varepsilon}}{1+\sqrt{\varepsilon}} = -\frac{\varepsilon-\sqrt{\varepsilon}}{\varepsilon+\sqrt{\varepsilon}} = -\Gamma_v \tag{8.12}$$

while when the grazing angle is very small ($\psi_g \approx 0$), we have

$$\Gamma_h = -1 = \Gamma_v \tag{8.13}$$

Observation of Figs. 8.6 and 8.7 yield the following conclusions: (1) The magnitude of the reflection coefficient with horizontal polarization is equal to unity at very small grazing angles and it decreases monotonically as the angle is increased. (2) The magnitude of the vertical polarization has a well defined minimum. The angle that corresponds to this condition is called Brewster's polarization angle. For this reason, airborne radars in the look-down mode utilize mainly vertical polarization to significantly reduce the terrain bounce reflections. (3) For horizontal polarization the phase is almost π; however, for vertical polarization the phase changes to zero around the Brewster's angle. (4) For very small angles (less than $2°$) both $|\Gamma_h|$ and $|\Gamma_v|$ are nearly one; $\angle\Gamma_h$ and $\angle\Gamma_v$ are nearly π. Thus, little difference in the propagation of horizontally or vertically polarized waves exists at low grazing angles.

MATLAB Function "ref_coef.m"

The function *"ref_coef.m"* calculates and plots the horizontal and vertical magnitude and phase response of the reflection coefficient. It is given in Section 8.7. The syntax is as follows

[rh,rv,ph,pv] = ref_coef (epsp,epspp)

where

Symbol	Description	Status
epsp	ε'	*input*
epspp	ε''	*input*
rh	*vector of* $\|\Gamma_h\|$	*output*
rv	*vector of* $\|\Gamma_v\|$	*output*
ph	*vector of* $\angle\Gamma_h$	*output*
vh	*vector of* $\angle\Gamma_v$	*output*

8.3.2. Divergence

The overall reflection coefficient is also affected by the round earth divergence factor, D. When an electromagnetic wave is incident on a round earth surface, the reflected wave diverges because of the earth's curvature. This is illustrated in Fig. 8.8a. Due to divergence the reflected energy is defocused, and the radar power density is reduced. The divergence factor can be derived using geometrical considerations. A widely accepted approximation for the divergence factor is given by

$$D \approx \frac{1}{\sqrt{1 + \dfrac{2r_1 r_2}{r_e r \sin\psi_g}}} \tag{8.14}$$

where all variables in Eq. (8.14) are defined in Fig. 8.8b.

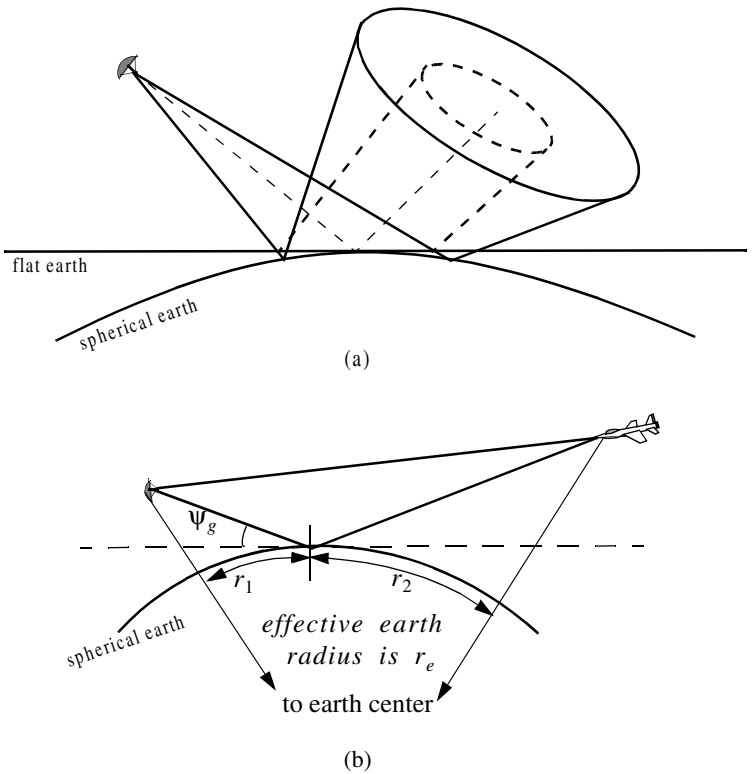

Figure 8.8. Illustration of divergence. (a) Solid line: Ray perimeter for spherical earth. Dashed line: Ray perimeter for flat earth. (b) Definition of variables in Eq. (8.14)

8.3.3. Rough Surface Reflection

In addition to divergence, surface roughness also affects the reflection coefficient. Surface roughness is given by

$$S_r = e^{-2\left(\frac{2\pi h_{rms}\sin\psi_g}{\lambda}\right)^2} \tag{8.15}$$

where h_{rms} is the rms surface height irregularity. In general, rays reflected from rough surfaces undergo changes in phase and amplitude, which results in the diffused (non-coherent) portion of the reflected signal. Combining the above three factors, we can express the total reflection coefficient Γ_t as

$$\Gamma_t = \Gamma_{(h,v)} D S_r \tag{8.16}$$

$\Gamma_{(h,v)}$ is the horizontal or vertical smoothed surface reflection coefficient.

8.4. The Pattern Propagation Factor

In general, the pattern propagation factor is a term used to describe the wave propagation when free space conditions are not met. This factor is defined separately for the transmitting and receiving paths. The propagation factor also accounts for the radar antenna pattern effects. The basic definition of the propagation factor is

$$F = \left|E/E_0\right| \tag{8.17}$$

where E is the electric field in the medium and E_0 is the free space electric field.

Near the surface of the earth, multipath propagation effects dominate the formation of the propagation factor. In this section, a general expression for the propagation factor due to multipath will be developed. In this sense, the propagation factor describes the constructive/destructive interference of the electromagnetic waves diffracted from the earth surface (which can be either flat or curved). The subsequent sections derive the specific forms of the propagation factor due to flat and curved earth.

Consider the geometry shown in Fig. 8.9. The radar is located at height h_r. The target is at range R, and is located at a height h_t. The grazing angle is ψ_g. The radar energy emanating from its antenna will reach the target via two paths: the "direct path" AB and the "indirect path" ACB. The lengths of the paths AB and ACB are normally very close to one another and thus, the difference between the two paths is very small. Denote the direct path as R_d, the indirect path as R_i, and the difference as $\Delta R = R_i - R_d$. It follows that the phase difference between the two paths is given by

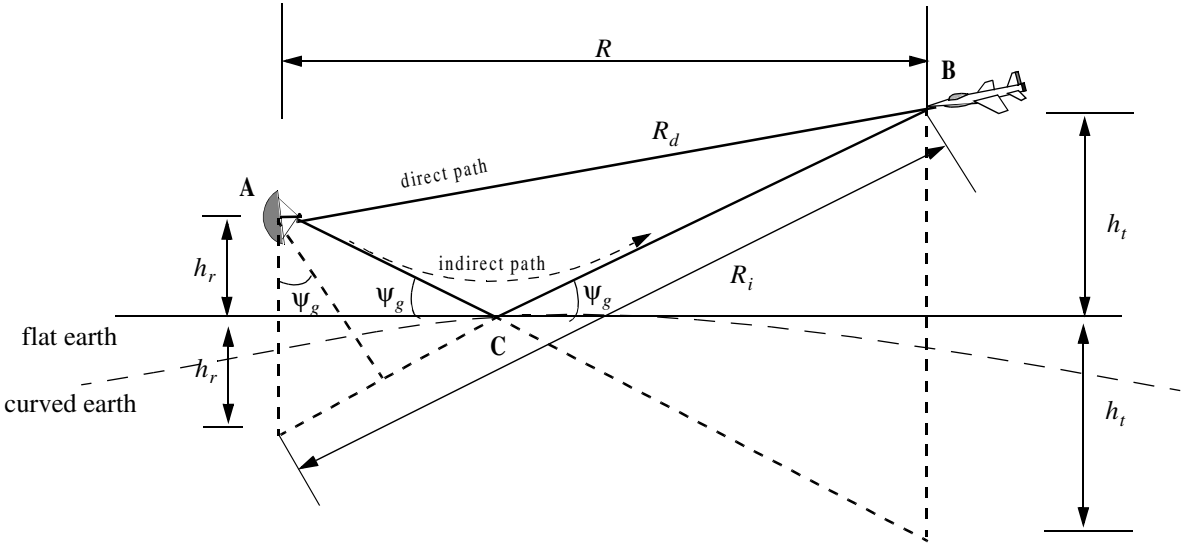

Figure 8.9. Geometry for multipath propagation.

$$\Delta\Phi = \frac{2\pi}{\lambda}\Delta R \tag{8.18}$$

where λ is the radar wavelength.

The indirect signal amplitude arriving at the target is less than the signal amplitude arriving via the direct path. This is because the antenna gain in the direction of the indirect path is less than that along the direct path, and because the signal reflected from the earth surface at point C is modified in amplitude and phase in accordance to the earth's reflection coefficient, Γ. The earth reflection coefficient is given by

$$\Gamma = \rho e^{j\varphi} \tag{8.19}$$

where ρ is less than unity and φ describes the phase shift induced on the indirect path signal due to surface roughness.

The direct signal (in volts) arriving at the target via the direct path can be written as

$$E_d = e^{j\omega_0 t} e^{j\frac{2\pi}{\lambda}R_d} \tag{8.20}$$

where the time harmonic term $\exp(j\omega_0 t)$ represents the signal's time dependency, and the exponential term $\exp(j(2\pi/\lambda)R_d)$ represents the signal spatial phase. The indirect signal at the target is

$$E_i = \rho e^{j\varphi} e^{j\omega_0 t} e^{j\frac{2\pi}{\lambda}R_i} \tag{8.21}$$

where $\rho\exp(j\varphi)$ is the surface reflection coefficient. Therefore, the overall signal arriving at the target is

$$E = E_d + E_i = e^{j\omega_0 t} e^{j\frac{2\pi}{\lambda}R_d}\left(1 + \rho e^{j\left(\varphi + \frac{2\pi}{\lambda}(R_i - R_d)\right)}\right) \tag{8.22}$$

Due to reflections from the earth surface, the overall signal strength is then modified at the target by the ratio of the signal strength in the presence of earth to the signal strength at the target in free space. From Eq. (8.17) the modulus of this ratio is the propagation factor. By using Eqs. (8.20) and (8.22) the propagation factor is computed as

$$F = \left|\frac{E_d}{E_d + E_i}\right| = \left|1 + \rho e^{j\varphi} e^{j\Delta\Phi}\right| \tag{8.23}$$

which can be rewritten as

$$F = \left|1 + \rho e^{j\alpha}\right| \tag{8.24}$$

where $\alpha = \Delta\Phi + \varphi$. Using Euler's identity ($e^{j\alpha} = \cos\alpha + j\sin\alpha$), Eq. (8.24) can be written as

$$F = \sqrt{1 + \rho^2 + 2\rho\cos\alpha} \tag{8.25}$$

It follows that the signal power at the target is modified by the factor F^2. By using reciprocity, the signal power at the radar is computed by multiplying the radar equation by the factor F^4. In the following two sections we will develop exact expressions for the propagation factor for flat and curved earth.

The propagation factor for free space and no multipath is $F = 1$. Denote the radar detection range in free space (i.e., $F = 1$) as R_0. It follows that the detection range in the presence of the atmosphere and multipath interference is

$$R = \frac{R_0 F}{(L_a)^{1/4}} \tag{8.26}$$

where L_a is the two-way atmospheric loss at range R. Atmospheric attenuation will be discussed in a later section. Thus, for the purpose of illustrating the effect of multipath interference on the propagation factor, assume that $L_a = 1$. In this case, Eq. (8.26) is modified to

$$R = R_0 F \tag{8.27}$$

Fig. 8.10 shows the general effects of multipath interference on the propagation factor. Note that, due to the presence of surface reflections, the antenna elevation coverage is transformed into a lobed pattern structure. The lobe widths are directly proportional to λ, and inversely proportional to h_r. A target located at a maxima will be detected at twice its free space range. Alternatively, at other angles, the detection range will be less than that in free space.

8.4.1. Flat Earth

Using the geometry of Fig. 8.9, the direct and indirect paths are computed as

$$R_d = \sqrt{R^2 + (h_t - h_r)^2} \tag{8.28}$$

$$R_i = \sqrt{R^2 + (h_t + h_r)^2} \tag{8.29}$$

Eqs. (8.28) and (8.29) can be approximated using the truncated binomial series expansion as

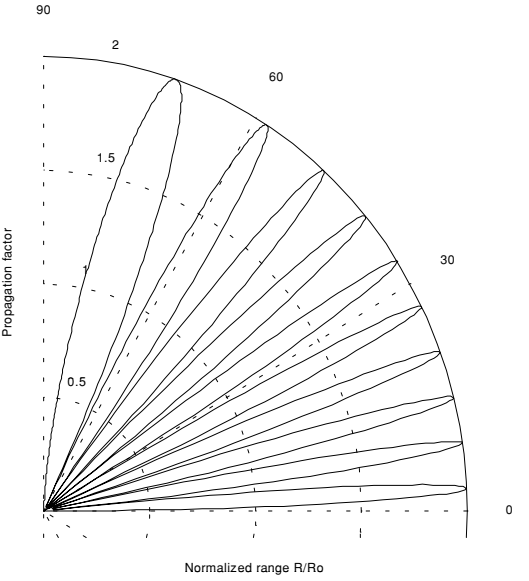

Figure 8.10. Vertical lobe structure due to the reflecting surface as a function of the elevation angle.

$$R_d \approx R + \frac{(h_t - h_r)^2}{2R} \tag{8.30}$$

$$R_i \approx R + \frac{(h_t + h_r)^2}{2R} \tag{8.31}$$

This approximation is valid for low grazing angles, where $R \gg h_t, h_r$. It follows that

$$\Delta R = R_i - R_d \approx \frac{2h_t h_r}{R} \tag{8.32}$$

Substituting Eq. (8.32) into Eq. (8.18) yields the phase difference due to multipath propagation between the two signals (direct and indirect) arriving at the target. More precisely,

$$\Delta\Phi = \frac{2\pi}{\lambda}\Delta R \approx \frac{4\pi h_t h_r}{\lambda R} \tag{8.33}$$

At this point assume smooth surface with reflection coefficient $\Gamma = -1$. This assumption means that waves reflected from the surface suffer no amplitude loss, and that the induced surface phase shift is equal to 180°. Using Eq. (8.18) and Eq. (8.25) along with these assumptions yield

$$F^2 = 2 - 2\cos\Delta\Phi = 4(\sin(\Delta\Phi/2))^2 \tag{8.34}$$

Substituting Eq. (8.33) into Eq. (8.34) yields

$$F^2 = 4\left(\sin\frac{2\pi h_t h_r}{\lambda R}\right)^2 \tag{8.35}$$

By using reciprocity, the expression for the propagation factor at the radar is then given by

$$F^4 = 16\left(\sin\frac{2\pi h_t h_r}{\lambda R}\right)^4 \tag{8.36}$$

Finally, the signal power at the radar is computed by multiplying the radar equation by the factor F^4,

$$P_r = \frac{P_t G^2 \lambda^2 \sigma}{(4\pi)^3 R^4} \; 16\left(\sin\frac{2\pi h_t h_r}{\lambda R}\right)^4 \tag{8.37}$$

Since the sine function varies between 0 and 1, the signal power will then vary between 0 and 16. Therefore, the fourth power relation between signal power and the target range results in varying the target range from 0 to twice the actual range in free space. In addition to that, the field strength at the radar will now have holes that correspond to the nulls of the propagation factor.

The nulls of the propagation factor occur when the sine is equal to zero. More precisely,

$$\frac{2h_r h_t}{\lambda R} = n \tag{8.38}$$

where $n = \{0, 1, 2, \ldots\}$. The maxima occur at

$$\frac{4h_r h_t}{\lambda R} = n + 1 \tag{8.39}$$

The target heights that produce nulls in the propagation factor are $\{h_t = n(\lambda R/2h_r); n = 0, 1, 2, \ldots\}$, and the peaks are produced from target heights $\{h_t = n(\lambda R/4h_r); n = 1, 2, \ldots\}$. Therefore, due to the presence of surface reflections, the antenna elevation coverage is transformed into a lobed pattern structure as illustrated by Fig. 8.10. A target located at a maxima will be detected at twice its free space range. Alternatively, at other angles, the

detection range will be less than that in free space. At angles defined by Eq. (8.38) there would be no measurable target returns.

For small angles, Eq. (8.37) can be approximated by

$$P_r \approx \frac{4\pi P_t G^2 \sigma}{\lambda^2 R^8} (h_t h_r)^4 \tag{8.40}$$

Thus, the received signal power varies as the eighth power of the range instead of the fourth power. Also, the factor $G\lambda$ is now replaced by G/λ.

8.4.2. Spherical Earth

In order to model the effects of multipath propagation on radar performance more accurately, we need to remove the flat earth condition and account for the earth's curvature. When considering round earth, electromagnetic waves travel in curved paths because of the atmospheric refraction. And as mentioned earlier, the most commonly used approach to mitigating the effects of atmospheric refraction is to replace the actual earth by an imaginary earth such that electromagnetic waves travel in straight lines. The effective radius of the imaginary earth is

$$r_e = kr_0 \tag{8.41}$$

where k is a constant and r_0 is the actual earth radius ($6371 Km$). Using the geometry in Fig. 8.11, the direct and indirect path difference is

$$\Delta R = R_1 + R_2 - R_d \tag{8.42}$$

The propagation factor is computed by using ΔR from Eq. (8.42) in Eq. (8.18) and substituting the result in Eq. (8.25). To compute (R_1, R_2, and R_d) the following cubic equation must first be solved for r_1:

$$2r_1^3 - 3rr_1^2 + (r^2 - 2r_e(h_r + h_t))r_1 + 2r_e h_r r = 0 \tag{8.43}$$

The solution is

$$r_1 = \frac{r}{2} - p\sin\frac{\xi}{3} \tag{8.44}$$

where

$$p = \frac{2}{\sqrt{3}}\sqrt{r_e(h_t + h_r) + \frac{r^2}{4}} \tag{8.45}$$

$$\xi = \operatorname{asin}\left(\frac{2r_e r(h_t - h_r)}{p^3}\right) \tag{8.46}$$

Next, we solve for R_1, R_2, and R_d. From Fig. 8.11,

$$\phi_1 = r_1 / r_e \tag{8.47}$$

$$\phi_2 = r_2 / r_e \tag{8.48}$$

Using the law of cosines to the triangles ABO and BOC yields

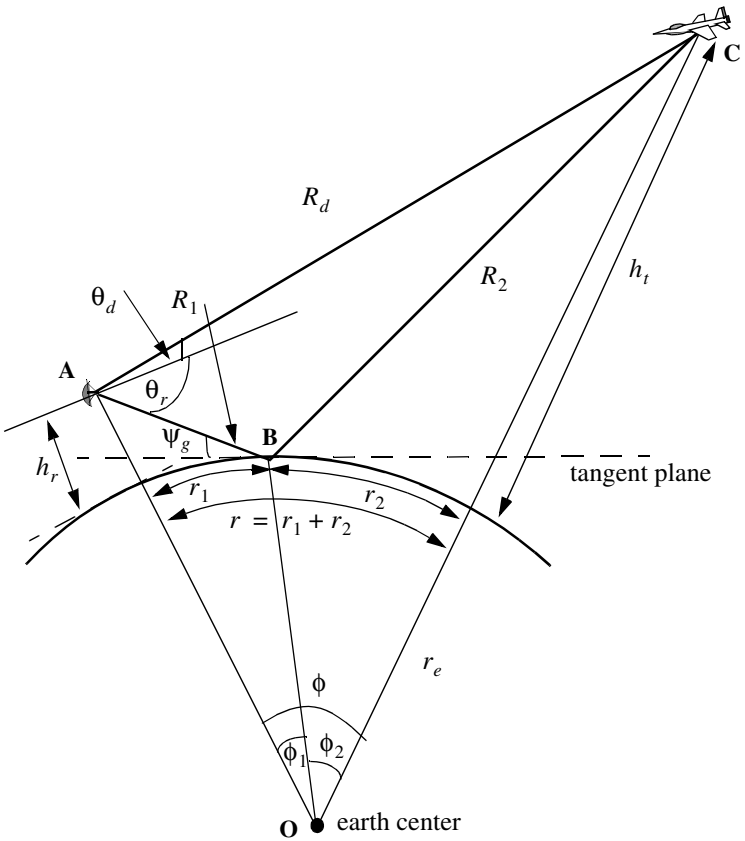

Figure 8.11. Geometry associated with multipath propagation over round earth.

$$R_1 = \sqrt{r_e^2 + (r_e + h_r)^2 - 2r_e(r_e + h_r)\cos\phi_1} \tag{8.49}$$

$$R_2 = \sqrt{r_e^2 + (r_e + h_t)^2 - 2r_e(r_e + h_t)\cos\phi_2} \tag{8.50}$$

Eqs. (8.49) and (8.50) can be written in the following simpler forms:

$$R_1 = \sqrt{h_r^2 + 4r_e(r_e + h_r)(\sin(\phi_1/2))^2} \tag{8.51}$$

$$R_2 = \sqrt{h_t^2 + 4r_e(r_e + h_t)(\sin(\phi_2/2))^2} \tag{8.52}$$

Using the law of cosines on the triangle AOC yields

$$R_d = \sqrt{(h_t - h_r)^2 + 4(r_e + h_t)(r_e + h_r)\left(\sin\left(\frac{\phi_1 + \phi_2}{2}\right)\right)^2} \tag{8.53}$$

Substituting Eqs. (8.51) through (8.53) directly into Eq. (8.42) may not be conducive to numerical accuracy. A more suitable form for the computation of ΔR is then derived. The detailed derivation is in Blake. The results are listed below. For better numerical accuracy use the following expression to compute ΔR:

$$\Delta R = \frac{4R_1R_2(\sin\psi_g)^2}{R_1 + R_2 + R_d} \tag{8.54}$$

where

$$\psi_g \approx \operatorname{asin}\left(\frac{h_t}{R_1} - \frac{R_1}{2r_e}\right) \tag{8.55}$$

8.5. Diffraction

Diffraction is a term used to describe the phenomenon of electromagnetic waves bending around obstacles. It is of major importance to radar systems operating at very low altitudes. Hills and ridges diffract radio energy and make it possible to perform detection in regions that are physically shadowed. In practice, experimental data measurements provide the dominant source of information available on this phenomenon. Some theoretical analyses of diffraction are also available. However, in these cases many assumptions are made, and perhaps the most important assumption is that obstacles are chosen to be perfect conductors.

The problem of propagation over a knife edge on a plane can be described with help of Fig. 8.12. The target and radar heights are denoted, respectively,

by h_t and h_r. The edge height is h_e. Denote the distance by which the radar rays clear (or do not clear) the tip of the edge by δ. As a matter of notation δ is assumed to be positive when the direct rays clear the edge, and is negative otherwise. Because of the fact that ground reflection occurs on both sides of the edge, then the propagation factor is composed of four distinct rays, as illustrated in Fig. 8.13. An expression for the propagation factor corresponding to the four rays is reported in Meeks (see Bibliography).

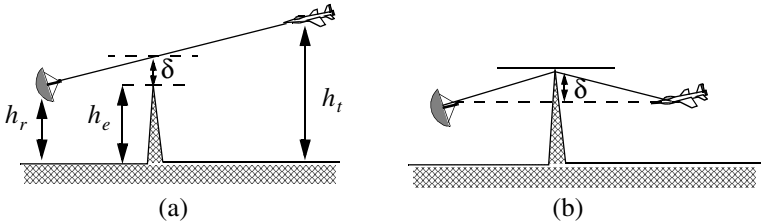

Figure 8.12. Diffraction over a knife edge. (a) Positive δ. (b) Negative δ.

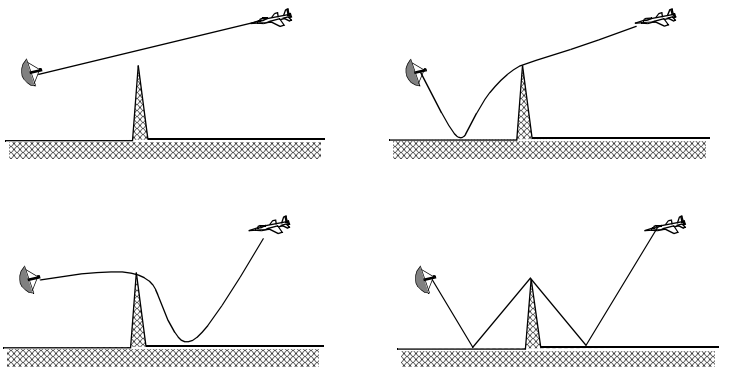

Figure 8.13. Four ray formation.

8.6. Atmospheric Attenuation

Electromagnetic waves travel in free space without suffering any energy loss. Alternatively, due to gases and water vapor in the atmosphere radar

energy suffers a loss. This loss is known as the atmospheric attenuation. Atmospheric attenuation increases significantly in the presence of rain, fog, dust, and clouds. Most of the lost radar energy is normally absorbed by gases and water vapor and transformed into heat, while a small portion of this lost energy is used in molecular transformation of the atmosphere particles.

The two-way atmospheric attenuation over a range R can be expressed as

$$L_{atmosphere} = e^{-2\alpha R} \tag{8.56}$$

where α is the one-way attenuation coefficient. Water vapor attenuation peaks at about $22.3 GHz$, while attenuation due to oxygen peaks at between 60 and $118 GHz$. Atmospheric attenuation is severe for frequencies higher than $35 GHz$. This is the reason why ground-based radars rarely use frequencies higher than $35 GHz$.

Atmospheric attenuation is a function range, frequency, and elevation angle. Fig. 8.14 shows a typical two-way atmospheric attenuation plot versus range at $3 GHz$, with the elevation angle as a parameter. Fig. 8.15 is similar to Fig. 8.14, except it is for $10 GHz$. For further details on this subject the reader is advised to visit Blake.

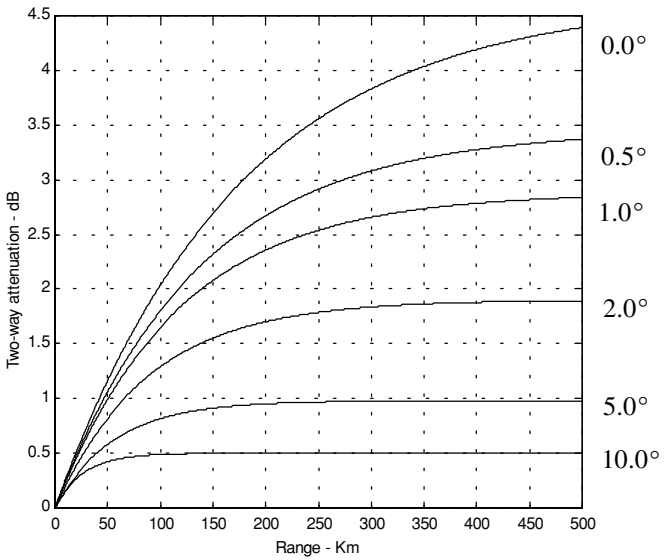

Figure 8.14. Attenuation versus range; frequency is *3 GHz*.

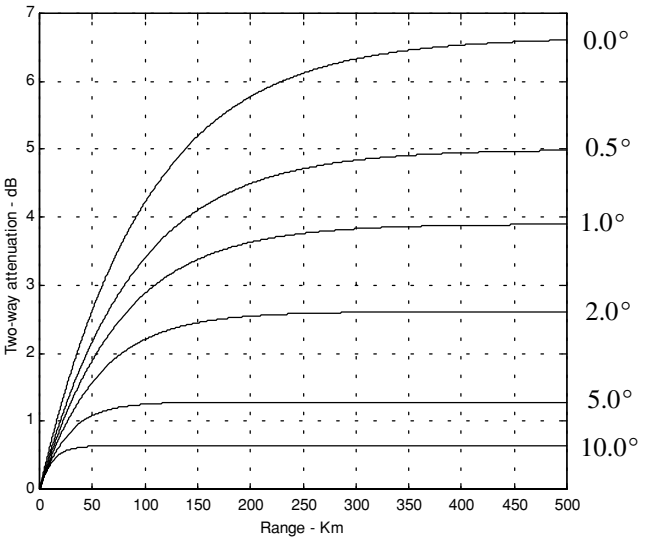

Figure 8.15. Attenuation versus range; frequency is *10 GHz.*

8.7. MATLAB Program "ref_coef.m"

```
function [rh,rv,ph,pv] = ref_coef (epsp,epspp)
eps = epsp - i * epspp; %65.0-30.7i;
psi = 0:0.1:90;
psirad = psi.*(pi/180.);
arg1 = eps-(cos(psirad).^2);
arg2 = sqrt(arg1);
arg3 = sin(psirad);
arg4 = eps.*arg3;
rv = (arg4-arg2)./(arg4+arg2);
rh = (arg3-arg2)./(arg3+arg2);
gamamodv = abs(rv);
gamamodh = abs(rh);
figure(1)
plot(psi,gamamodv,'k',psi,gamamodh,'k -.');
axis tight
grid
xlabel('grazing angle - degrees');
ylabel('reflection coefficient - amplitude')
```

```
legend ('Vertical Polarization','Horizontal Polarization')
pv = -angle(rv);
ph = angle(rh);
figure(2)
plot(psi,pv,'k',psi,ph,'k -.');
grid
xlabel('grazing angle - degrees');
ylabel('reflection coefficient - phase')
legend ('Vertical Polarization','Horizontal Polarization')
```

Problems

8.1. Using Eq. (8.4), determine h when $h_r = 15m$ and $R = 35Km$.

8.2. An exponential expression for the index of refraction is given by

$$n = 1 + 315 \times 10^{-6} \exp(-0.136h)$$

where the altitude h is in Km. Calculate the index of refraction for a well mixed atmosphere at 10% and 50% of the troposphere.

8.3. Rederive Eq. (8.34) assuming vertical polarization.

8.4. Reproduce Figs. 8.6 and 8.7 by using $f = 8GHz$ and (a) $\varepsilon' = 2.8$ and $\varepsilon'' = 0.032$ (dry soil); (b) $\varepsilon' = 47$ and $\varepsilon'' = 19$ (sea water at $0°C$); (c) $\varepsilon' = 50.3$ and $\varepsilon'' = 18$ (lake water at $0°C$).

8.5. In reference to Fig. 8.9, assume a radar height of $h_r = 100m$ and a target height of $h_t = 500m$. The range is $R = 20Km$. (a) Calculate the lengths of the direct and indirect paths. (b) Calculate how long it will take a pulse to reach the target via the direct and indirect paths.

8.6. In the previous problem, assuming that you may be able to use the small grazing angle approximation: (a) Calculate the ratio of the direct to the indirect signal strengths at the target. (b) If the target is closing on the radar with velocity $v = 300m/s$, calculate the Doppler shift along the direct and indirect paths. Assume $\lambda = 3cm$.

8.7. Utilizing the plots generated in solving Problem 8.4, derive an emperical expression for the Brewster's angle.

8.8. A radar at altitude $h_r = 10m$ and a target at altitude $h_t = 300m$, and assuming a spherical earth, calculate r_1, r_2, and ψ_g.

8.9. Derive an asymptotic form for Γ_h and Γ_v when the grazing angle is very small.

8.10. In reference to Fig. 8.8, assume a radar height of $h_r = 100m$ and a target height of $h_t = 500m$. The range is $R = 20Km$. (a) Calculate the lengths of the direct and indirect paths. (b) Calculate how long it will take a pulse to reach the target via the direct and indirect paths.

8.11. Using the law of cosines, derive Eqs. (8.51) through (8.53).

8.12. In the previous problem, assuming that you may be able to use the small grazing angle approximation: (a) Calculate the ratio of the direct to the indirect signal strengths at the target. (b) If the target is closing on the radar with velocity $v = 300m/s$, calculate the Doppler shift along the direct and indirect paths. Assume $\lambda = 3cm$.

8.13. In the previous problem, assuming that you may be able to use the small grazing angle approximation: (a) Calculate the ratio of the direct to the indirect signal strengths at the target. (b) If the target is closing on the radar with velocity $v = 300m/s$, calculate the Doppler shift along the direct and indirect paths. Assume $\lambda = 3cm$.

8.14. Calculate the range to the horizon corresponding to a radar at $5Km$ and $10Km$ of altitude. Assume 4/3 earth.

8.15. Develop a mathematical expression that can be used to reproduce Figs. 8.14 and 8.15.

Chapter 9

Clutter and Moving Target Indicator (MTI)

9.1. Clutter Definition

Clutter is a term used to describe any object that may generate unwanted radar returns that may interfere with normal radar operations. Parasitic returns that enter the radar through the antenna's main lobe are called main lobe clutter; otherwise they are called side lobe clutter. Clutter can be classified in two main categories: surface clutter and airborne or volume clutter. Surface clutter includes trees, vegetation, ground terrain, man-made structures, and sea surface (sea clutter). Volume clutter normally has large extent (size) and includes chaff, rain, birds, and insects. Chaff consists of a large number of small dipole reflectors that have large RCS values. It is released by hostile aircaft or missiles as a means of ECM in an attempt to confuse the defense. Surface clutter changes from one area to another, while volume clutter may be more predictable.

Clutter echoes are random and have thermal noise-like characteristics because the individual clutter components (scatterers) have random phases and amplitudes. In many cases, the clutter signal level is much higher than the receiver noise level. Thus, the radar's ability to detect targets embedded in high clutter background depends on the Signal-to-Clutter Ratio (SCR) rather than the SNR.

White noise normally introduces the same amount of noise power across all radar range bins, while clutter power may vary within a single range bin. And since clutter returns are target-like echoes, the only way a radar can distinguish target returns from clutter echoes is based on the target RCS σ_t, and the anticipated clutter RCS σ_c (via clutter map). Clutter RCS can be defined as the equivalent radar cross section attributed to reflections from a clutter area, A_c. The average clutter RCS is given by

$$\sigma_c = \sigma^0 A_c \tag{9.1}$$

where $\sigma^0 (m^2/m^2)$ is the clutter scattering coefficient, a dimensionless quantity that is often expressed in dB. Some radar engineers express σ^0 in terms of squared centimeters per squared meter. In these cases, σ^0 is $40dB$ higher than normal.

The term that describes the constructive/destructive interference of the electromagnetic waves diffracted from an object (target or clutter) is called the propagation factor (see Chapter 8 for more details). Since target and clutter returns have different angles of arrival (different propagation factors), we can define the SCR as

$$SCR = \frac{\sigma_t F_t^2 F_r^2}{\sigma_c F_c^2} \tag{9.2}$$

where F_c is the clutter propagation factor, F_t and F_r are, respectively, the transmit and receive propagation factors for the target. In many cases $F_t = F_r$.

9.2. Surface Clutter

Surface clutter includes both land and sea clutter, and is often called area clutter. Area clutter manifests itself in airborne radars in the look-down mode. It is also a major concern for ground-based radars when searching for targets at low grazing angles. The grazing angle ψ_g is the angle from the surface of the earth to the main axis of the illuminating beam, as illustrated in Fig. 9.1.

Three factors affect the amount of clutter in the radar beam. They are the grazing angle, surface roughness, and the radar wavelength. Typically, the clutter scattering coefficient σ^0 is larger for smaller wavelengths. Fig. 9.2 shows a sketch describing the dependency of σ^0 on the grazing angle. Three regions are identified; they are the low grazing angle region, flat or plateau region, and the high grazing angle region.

The low grazing angle region extends from zero to about the critical angle. The critical angle is defined by Rayleigh as the angle below which a surface is considered to be smooth, and above which a surface is considered to be rough. Denote the root mean square (rms) of a surface height irregularity as h_{rms}, then according to the Rayleigh critera the surface is considered to be smooth if

$$\frac{4\pi h_{rms}}{\lambda} \sin\psi_g < \frac{\pi}{2} \tag{9.3}$$

Consider a wave incident on a rough surface, as shown in Fig. 9.3. Due to surface height irregularity (surface roughness), the "rough path" is longer than the "smooth path" by a distance $2h_{rms}\sin\psi_g$. This path difference translates into a phase differential $\Delta\psi$:

$$\Delta\psi = \frac{2\pi}{\lambda}\ 2h_{rms}\sin\psi_g \tag{9.4}$$

The critical angle ψ_{gc} is then computed when $\Delta\psi = \pi$ (first null), thus

$$\frac{4\pi h_{rms}}{\lambda}\ \sin\psi_{gc} = \pi \tag{9.5}$$

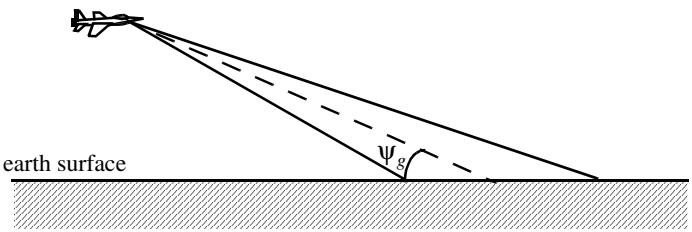

Figure 9.1. Definition of grazing angle.

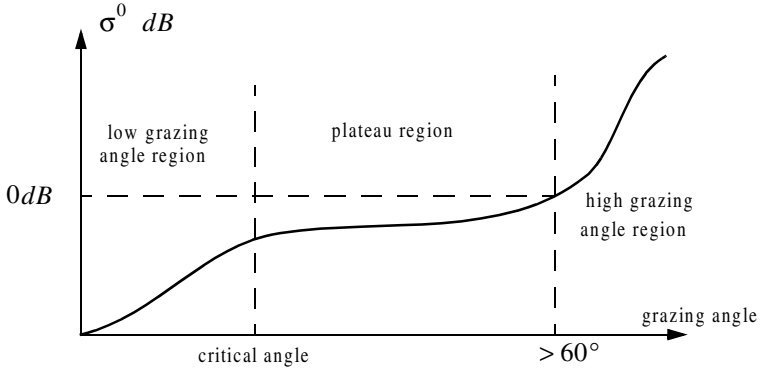

Figure 9.2. Clutter regions.

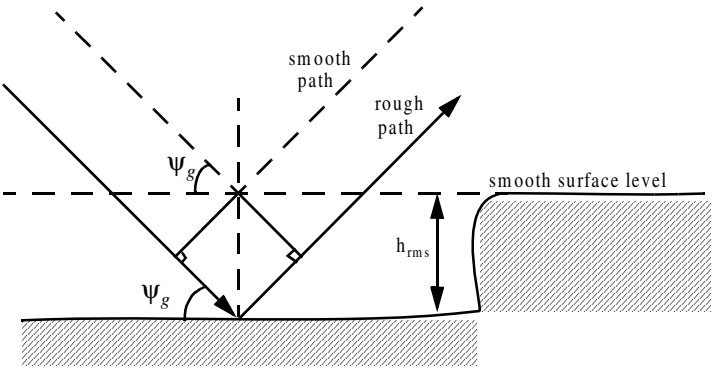

Figure 9.3. Rough surface definition.

or equivalently,

$$\psi_{gc} = \text{asin}\frac{\lambda}{4h_{rms}} \tag{9.6}$$

In the case of sea clutter, for example, the rms surface height irregularity is

$$h_{rms} \approx 0.025 + 0.046 \;\; S_{state}^{1.72} \tag{9.7}$$

where S_{state} is the sea state, which is tabulated in several cited references. The sea state is characterized by the wave height, period, length, particle velocity, and wind velocity. For example, $S_{state} = 3$ refers to a moderate sea state, where in this case the wave height is approximately equal to between $0.9144 \;\; to \;\; 1.2192 \;\; m$, the wave period 3.5 to 4.5 seconds, wave length $1.9812 \;\; to \;\; 33.528 \;\; m$, wave velocity $20.372 \;\; to \;\; 25.928 \;\; Km/hr$, and wind velocity $22.224 \;\; to \;\; 29.632 \;\; Km/hr$.

Clutter at low grazing angles is often referred to as diffused clutter, where there are a large number of clutter returns in the radar beam (non-coherent reflections). In the flat region the dependency of σ^0 on the grazing angle is minimal. Clutter in the high grazing angle region is more specular (coherent reflections) and the diffuse clutter components disappear. In this region the smooth surfaces have larger σ^0 than rough surfaces, opposite of the low grazing angle region.

9.2.1. *Radar Equation for Area Clutter*

Consider an airborne radar in the look-down mode shown in Fig. 9.4. The intersection of the antenna beam with ground defines an elliptically shaped footprint. The size of the footprint is a function of the grazing angle and the antenna 3dB beam width θ_{3dB}, as illustrated in Fig. 9.5. The footprint is divided into many ground range bins each of size $(c\tau/2)\sec\psi_g$, where τ is the pulse width.

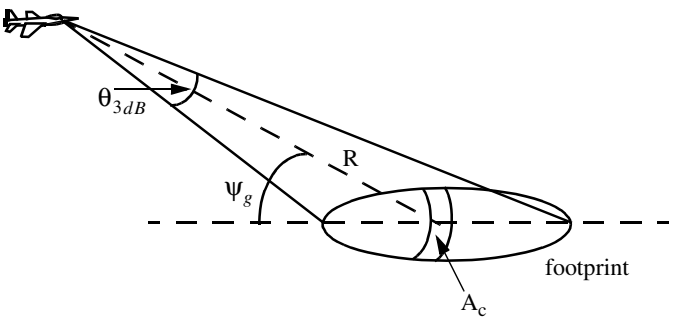

Figure 9.4. Airborne radar in the look-down mode.

From Fig. 9.5, the clutter area A_c is

$$A_c \approx R\theta_{3dB}\frac{c\tau}{2}\sec\psi_g \tag{9.8}$$

The power received by the radar from a scatterer within A_c is given by the radar equation as

$$S_t = \frac{P_t G^2 \lambda^2 \sigma_t}{(4\pi)^3 R^4} \tag{9.9}$$

where as usual, P_t is the peak transmitted power, G is the antenna gain, λ is the wavelength, and σ_t is the target RCS. Similarly, the received power from clutter is

$$S_{Ac} = \frac{P_t G^2 \lambda^2 \sigma_c}{(4\pi)^3 R^4} \tag{9.10}$$

where the subscript A_c is used for area clutter. Substituting Eq. (9.1) for σ_c into Eq. (9.10), we can then obtain the SCR for area clutter by dividing Eq. (9.9) by Eq. (9.10). More precisely,

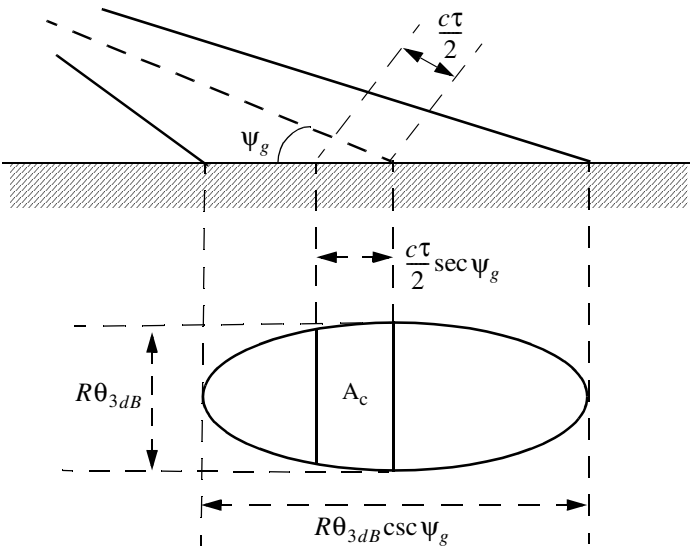

Figure 9.5. Footprint definition.

$$(SCR)_{Ac} = \frac{2\sigma_t \cos\psi_g}{\sigma^0 \theta_{3dB} R c\tau} \tag{9.11}$$

Example 9.1: Consider an airborne radar shown in Fig. 9.4. Let the antenna 3dB beam width be $\theta_{3dB} = 0.02rad$, *the pulse width* $\tau = 2\mu s$, *range* $R = 20Km$, *and grazing angle* $\psi_g = 20°$. *Assume target RCS* $\sigma_t = 1m^2$, *and clutter reflection coefficient* $\sigma^0{}_g = 0.0136m^2/m^2$. *Compute the SCR.*

Solution: The SCR is given by Eq. (9.11) as

$$(SCR)_{Ac} = \frac{2\sigma_t \cos\psi_g}{\sigma^0 \theta_{3dB} R c\tau} \Rightarrow$$

$$(SCR)_{AC} = \frac{(2)(1)(\cos 20)}{(0.0136)(0.02)(20000)(3\times 10^8)(2\times 10^{-6})} = 2.48\times 10^{-4}$$

It follows that

$$(SCR)_{Ac} = -36.06dB$$

Thus, for reliable detection the radar must somehow increase its SCR by at least $(36 + X)dB$, *where* X *is on the order of* $10dB$ *or better.*

9.3. Volume Clutter

Volume clutter has large extents and includes rain (weather), chaff, birds, and insects. The volume clutter coefficient is normally expressed in squared meters (RCS per resolution volume). Birds, insects, and other flying particles are often referred to as angel clutter or biological clutter. The average RCS for individual birds or insects as a function of the weight of the bird or insect is reported in the literature[1] as

$$(\sigma_b)_{dBsm} \approx -46 + 5.8 \log W_b \tag{9.12}$$

where W_b is the individual bird or insect weight in grams. Bird and insect RCSs are also a function of frequency; for example, a pigeon's average RCS is $-26 dBsm$ at S-band, and is equal to $-27 dBsm$ at X-band.

As mentioned earlier, chaff is used as an ECM technique by hostile forces. It consists of a large number of dipole reflectors with large RCS values. Historically, chaff was made of aluminum foil; however, in recent years most chaff is made of the more rigid fiber glass with conductive coating. The maximum chaff RCS occurs when the dipole length L is one half the radar wavelength. The average RCS for a single dipole when viewed broadside is

$$\sigma_{chaff1} \approx 0.88\lambda^2 \tag{9.13}$$

and for an average aspect angle, it drops to

$$\sigma_{chaff1} \approx 0.15\lambda^2 \tag{9.14}$$

where the subscript $chaff1$ is used to indicate a single dipole, and λ is the radar wavelength. The total chaff RCS within a radar resolution volume is

$$\sigma_{chaff} \approx 0.15\lambda^2 N_D \tag{9.15}$$

where N_D is the total number of dipoles in the resolution volume.

Weather or rain clutter is easier to suppress than chaff, since rain droplets can be viewed as perfect small spheres. We can use the Rayleigh approximation of perfect sphere to estimate the rain droplets' RCS. The Rayleigh approximation, without regard to the propagation medium index of refraction, is given in Eq. (2.30) and is repeated here as Eq. (9.16):

$$\sigma = 9\pi r^2 (kr)^4 \qquad r \ll \lambda \tag{9.16}$$

where $k = 2\pi/\lambda$, and r is radius of a rain droplet.

1. Edde, B., *Radar - Principles, Technology, Applications*, Prentice-Hall, 1993.

Electromagnetic waves when reflected from a perfect sphere become strongly co-polarized (have the same polarization as the incident waves). Consequently, if the radar transmits, say, a right-hand-circularly (RHC) polarized wave, then the received waves are left-hand-circularly (LHC) polarized, because it is propagating in the opposite direction. Therefore, the back-scattered energy from rain droplets retains the same wave rotation (polarization) as the incident wave, but has a reversed direction of propagation. It follows that radars can suppress rain clutter by co-polarizing the radar transmit and receive antennas.

Defining η as RCS per unit resolution volume V_W, it is computed as the sum of all individual scatterers RCS within the volume,

$$\eta = \sum_{i=1}^{N} \sigma_i \tag{9.17}$$

where N is the total number of scatterers within the resolution volume. Thus, the total RCS of a single resolution volume is

$$\sigma_W = \sum_{i=1}^{N} \sigma_i V_W \tag{9.18}$$

A resolution volume is shown in Fig. 9.6, and is approximated by

$$V_W \approx \frac{\pi}{8} \theta_a \theta_e R^2 c\tau \tag{9.19}$$

where θ_a, θ_e are, respectively, the antenna beam width in azimuth and elevation, τ is the pulse width in seconds, c is speed of light, and R is range.

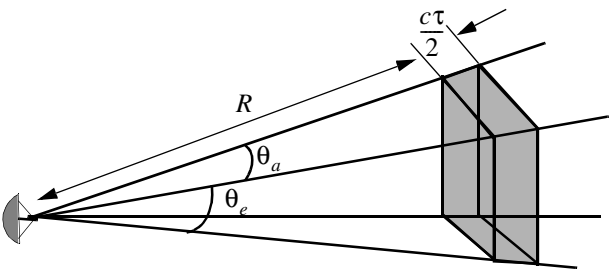

Figure 9.6. Definition of a resolution volume.

Consider a propagation medium with an index of refraction m. The ith rain droplet RCS approximation in this medium is

$$\sigma_i \approx \frac{\pi^5}{\lambda^4} K^2 D_i^6 \tag{9.20}$$

where

$$K^2 = \left| \frac{m^2 - 1}{m^2 + 2} \right|^2 \tag{9.21}$$

and D_i is the ith droplet diameter. For example, temperatures between $32°F$ and $68°F$ yield

$$\sigma_i \approx 0.93 \frac{\pi^5}{\lambda^4} D_i^6 \tag{9.22}$$

and for ice Eq. (9.20) can be approximated by

$$\sigma_i \approx 0.2 \frac{\pi^5}{\lambda^4} D_i^6 \tag{9.23}$$

Substituting Eq. (9.20) into Eq. (9.17) yields

$$\eta = \frac{\pi^5}{\lambda^4} K^2 Z \tag{9.24}$$

where the weather clutter coefficient Z is defined as

$$Z = \sum_{i=1}^{N} D_i^6 \tag{9.25}$$

In general, a rain droplet diameter is given in millimeters and the radar resolution volume in expressed in cubic meters, thus the units of Z are often expressed in $milliemeter^6/m^3$.

9.3.1. Radar Equation for Volume Clutter

The radar equation gives the total power received by the radar from a σ_t target at range R as

$$S_t = \frac{P_t G^2 \lambda^2 \sigma_t}{(4\pi)^3 R^4} \tag{9.26}$$

where all parameters in Eq. (9.26) have been defined earlier. The weather clutter power received by the radar is

$$S_W = \frac{P_t G^2 \lambda^2 \sigma_W}{(4\pi)^3 R^4} \tag{9.27}$$

Using Eq. (9.18) and Eq. (9.19) into Eq. (9.27) and collecting terms yield

$$S_W = \frac{P_t G^2 \lambda^2}{(4\pi)^3 R^4} \frac{\pi}{8} R^2 \theta_a \theta_e c\tau \sum_{i=1}^{N} \sigma_i \tag{9.28}$$

The SCR for weather clutter is then computed by dividing Eq. (9.26) by Eq. (9.28). More precisely,

$$(SCR)_V = \frac{S_t}{S_W} = \frac{8\sigma_t}{\pi \theta_a \theta_e c\tau R^2 \sum_{i=1}^{N} \sigma_i} \tag{9.29}$$

where the subscript V is used to denote volume clutter.

Example 9.2: A certain radar has target RCS $\sigma_t = 0.1 m^2$, *pulse width* $\tau = 0.2 \mu s$, *antenna beam width* $\theta_a = \theta_e = 0.02 radians$. *Assume the detection range to be* $R = 50 Km$, *and compute the SCR if* $\sum \sigma_i = 1.6 \times 10^{-8} (m^2/m^3)$.

Solution: From Eq. (9.29) we have

$$(SCR)_V = \frac{8\sigma_t}{\pi \theta_a \theta_e c\tau R^2 \sum_{i=1}^{N} \sigma_i}$$

substituting the proper values we get

$$(SCR)_V = \frac{(8)(0.1)}{\pi (0.02)^2 (3 \times 10^8)(0.2 \times 10^{-6})(50 \times 10^3)^2 (1.6 \times 10^{-8})} = 0.265$$

$$(SCR)_V = -5.768 dB.$$

9.4. Clutter Statistical Models

Since clutter within a resolution cell (or volume) is composed of a large number of scatterers with random phases and amplitudes, it is statistically described by a probability distribution function. The type of distribution depends on the nature of clutter itself (sea, land, volume), the radar operating frequency, and the grazing angle.

If sea or land clutter is composed of many small scatterers when the probability of receiving an echo from one scatterer is statistically independent of the echo received from another scatterer, then the clutter may be modeled using a Rayleigh distribution,

$$f(x) = \frac{2x}{x_0}\exp\left(\frac{-x^2}{x_0}\right) \;;\; x \geq 0 \qquad \textbf{(9.30)}$$

where x_0 is the mean squared value of x.

The log-normal distribution best describes land clutter at low grazing angles. It also fits sea clutter in the plateau region. It is given by

$$f(x) = \frac{1}{\sigma\sqrt{2\pi}\;x}\;\exp\left(-\frac{(\ln x - \ln x_m)^2}{2\sigma^2}\right) \;;\; x > 0 \qquad \textbf{(9.31)}$$

where x_m is the median of the random variable x, and σ is the standard deviation of the random variable $\ln(x)$.

The Weibull distribution is used to model clutter at low grazing angles (less than five degrees) for frequencies between 1 and $10GHz$. The Weibull probability density function is determined by the Weibull slope parameter a (often tabulated) and a median scatter coefficient $\bar{\sigma}_0$, and is given by

$$f(x) = \frac{bx^{b-1}}{\bar{\sigma}_0}\;\exp\left(-\frac{x^b}{\bar{\sigma}_0}\right) \;;\; x \geq 0 \qquad \textbf{(9.32)}$$

where $b = 1/a$ is known as the shape parameter. Note that when $b = 2$ the Weibull distribution becomes a Rayleigh distribution.

9.5. Clutter Spectrum

The power spectrum of stationary clutter (zero Doppler) can be represented by a delta function. However, clutter is not always stationary; it actually exhibits some Doppler frequency spread because of wind speed and motion of the radar scanning antenna. In general, the clutter spectrum is concentrated around

$f = 0$ and integer multiples of the radar PRF f_r, and may exhibit some small spreading.

The clutter power spectrum can be written as the sum of fixed (stationary) and random (due to frequency spreading) components. For most cases, the random component is Gaussian. If we denote the fixed to the random power ratio by W^2, then we can write the clutter spectrum as

$$S_c(\omega) = \bar{\sigma}_0 \left(\frac{W^2}{1+W^2} \right) \delta(\omega_0) + \frac{\bar{\sigma}_0}{(1+W^2)\sqrt{2\pi\sigma_\omega^2}} \exp\left(-\frac{(\omega-\omega_0)^2}{2\sigma_\omega^2} \right) \quad \textbf{(9.33)}$$

where $\omega_0 = 2\pi f_0$ is the radar operating frequency in radians per second, σ_ω is the rms frequency spread component (determines the Doppler frequency spread), and $\bar{\sigma}_0$ is the Weibull parameter.

The first term of the right-hand side of Eq. (9.33) represents the PSD for stationary clutter, while the second term accounts for the frequency spreading. Nevertheless, since most of the clutter power is concentrated around zero Doppler with some spreading (typically less than 100 Hz), it is customary to model clutter using a Gaussian-shaped power spectrum (which is easier to analyze than Eq. (9.33)). More precisely,

$$S_c(\omega) = \frac{P_c}{\sqrt{2\pi\sigma_\omega^2}} \exp\left(-\frac{(\omega-\omega_0)^2}{2\sigma_\omega^2} \right) \quad \textbf{(9.34)}$$

where P_c is the total clutter power; σ_ω^2 and ω_0 were defined earlier. Fig. 9.7 shows a typical PSD sketch of radar returns when both target and clutter are present. Note that the clutter power is concentrated around DC and integer multiples of the PRF.

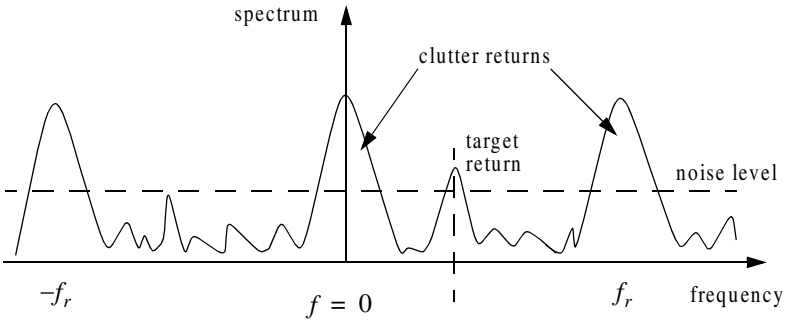

Figure 9.7. Typical radar return PSD when clutter and target are present.

9.6. Moving Target Indicator (MTI)

Clutter spectrum is normally concentrated around DC ($f = 0$) and multiple integers of the radar PRF f_r, as illustrated in Fig. 9.8a. In CW radars, clutter is avoided or suppressed by ignoring the receiver output around DC, since most of the clutter power is concentrated about the zero frequency band. Pulsed radar systems may utilize special filters that can distinguish between slowly moving or stationary targets and fast moving ones. This class of filters is known as the Moving Target Indicator (MTI). In simple words, the purpose of an MTI filter is to suppress target-like returns produced by clutter, and allow returns from moving targets to pass through with little or no degradation. In order to effectively suppress clutter returns, an MTI filter needs to have a deep stop-band at DC and at integer multiples of the PRF. Fig. 9.8b shows a typical sketch of an MTI filter response, while Fig. 9.8c shows its output when the PSD shown in Fig. 9.8a is the input.

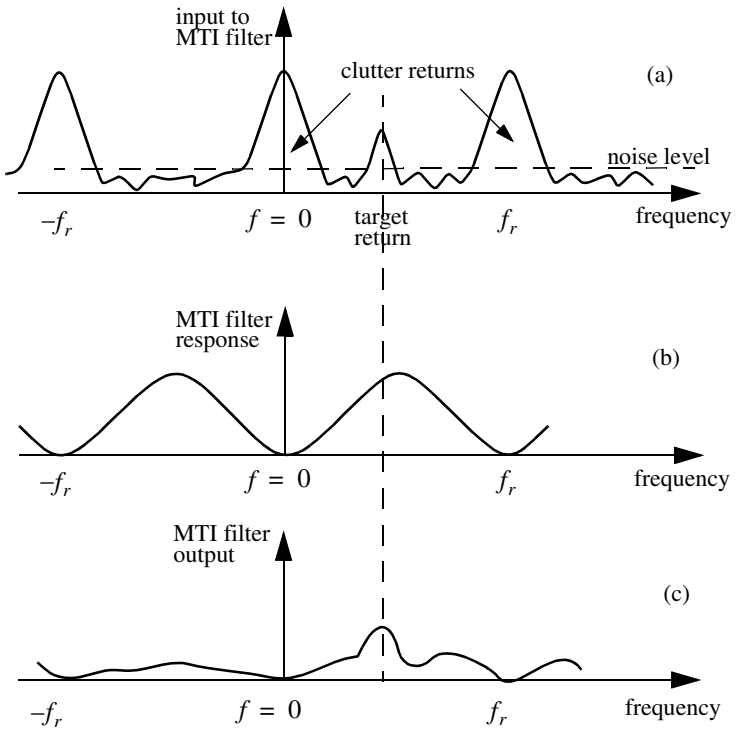

Figure 9.8. (a) Typical radar return PSD when clutter and target are present. (b) MTI filter frequency response. (c) Output from an MTI filter.

MTI filters can be implemented using delay line cancelers. As we will show later in this chapter, the frequency response of this class of MTI filters is periodic, with nulls at integer multiples of the PRF. Thus, targets with Doppler frequencies equal to nf_r are severely attenuated. And since Doppler is proportional to target velocity ($f_d = 2v/\lambda$), target speeds that produce Doppler frequencies equal to integer multiples of f_r are known as blind speeds. More precisely,

$$v_{blind} = \frac{\lambda f_r}{2} \;\; ; \;\; n \geq 0 \tag{9.35}$$

Radar systems can minimize the occurrence of blind speeds by either employing multiple PRF schemes (PRF staggering) or by using high PRFs where in this case the radar may become range ambiguous. The main difference between PRF staggering and PRF agility is that the pulse repetition interval (within an integration interval) can be changed between consecutive pulses for the case of PRF staggering.

Fig. 9.9 shows a block diagram of a coherent MTI radar. Coherent transmission is controlled by the STAble Local Oscillator (STALO). The outputs of the STALO, f_{LO}, and the COHerent Oscillator (COHO), f_C, are mixed to produce the transmission frequency, $f_{LO} + f_C$. The Intermediate Frequency (IF), $f_C \pm f_d$, is produced by mixing the received signal with f_{LO}. After the IF amplifier, the signal is passed through a phase detector and is converted into a base band. Finally, the video signal is inputted into an MTI filter.

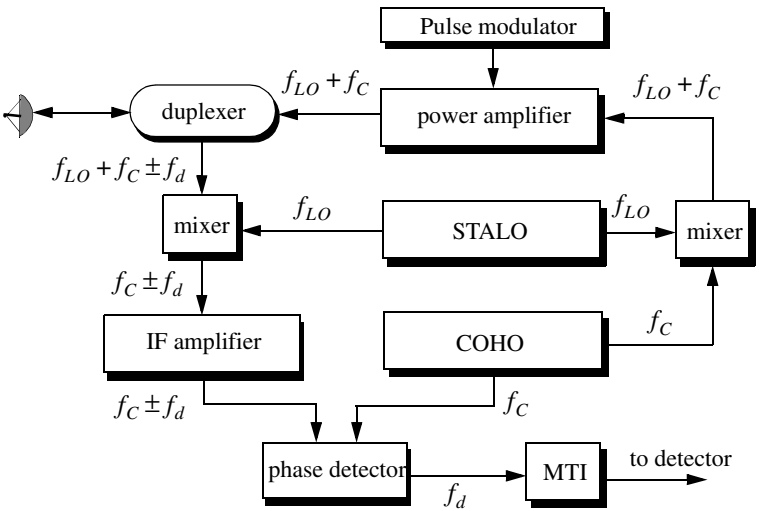

Figure 9.9. Coherent MTI radar block diagram.

9.7. Single Delay Line Canceler

A single delay line canceler can be implemented as shown in Fig. 9.10. The canceler's impulse response is denoted as $h(t)$. The output $y(t)$ is equal to the convolution between the impulse response $h(t)$ and the input $x(t)$. The single delay canceler is often called a "two-pulse canceler" since it requires two distinct input pulses before an output can be read.

The delay T is equal to the PRI of the radar $(1/f_r)$. The output signal $y(t)$ is

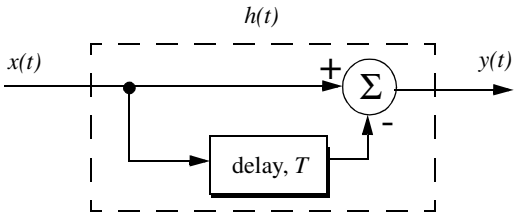

Figure 9.10. Single delay line canceler.

$$y(t) = x(t) - x(t-T) \tag{9.36}$$

The impulse response of the canceler is given by

$$h(t) = \delta(t) - \delta(t-T) \tag{9.37}$$

where $\delta(\cdot)$ is the delta function. It follows that the Fourier transform (FT) of $h(t)$ is

$$H(\omega) = 1 - e^{-j\omega T} \tag{9.38}$$

where $\omega = 2\pi f$.

In the z-domain, the single delay line canceler response is

$$H(z) = 1 - z^{-1} \tag{9.39}$$

The power gain for the single delay line canceler is given by

$$|H(\omega)|^2 = H(\omega)H^*(\omega) = (1 - e^{-j\omega T})(1 - e^{j\omega T}) \tag{9.40}$$

It follows that

$$|H(\omega)|^2 = 1 + 1 - (e^{j\omega T} + e^{-j\omega T}) = 2(1 - \cos\omega T) \tag{9.41}$$

and using the trigonometric identity $(2 - 2\cos 2\vartheta) = 4(\sin\vartheta)^2$ yields

$$|H(\omega)|^2 = 4(\sin(\omega T/2))^2 \quad \textbf{(9.42)}$$

MATLAB Function "single_canceler.m"

The function *"single_canceler.m"* computes and plots (as a function of f/f_r) the amplitude response for a single delay line canceler. It is given in Listing 9.1 in Section 9.14. The syntax is as follows:

[resp] = single_canceler (fofr)

where *fofr* is the number of periods desired. Typical output of the function "single_canceler.m" is shown in Fig. 9.11. Clearly, the frequency response of a single canceler is periodic with a period equal to f_r. The peaks occur at $f = (2n+1)/(2f_r)$, and the nulls are at $f = nf_r$, where $n \geq 0$.

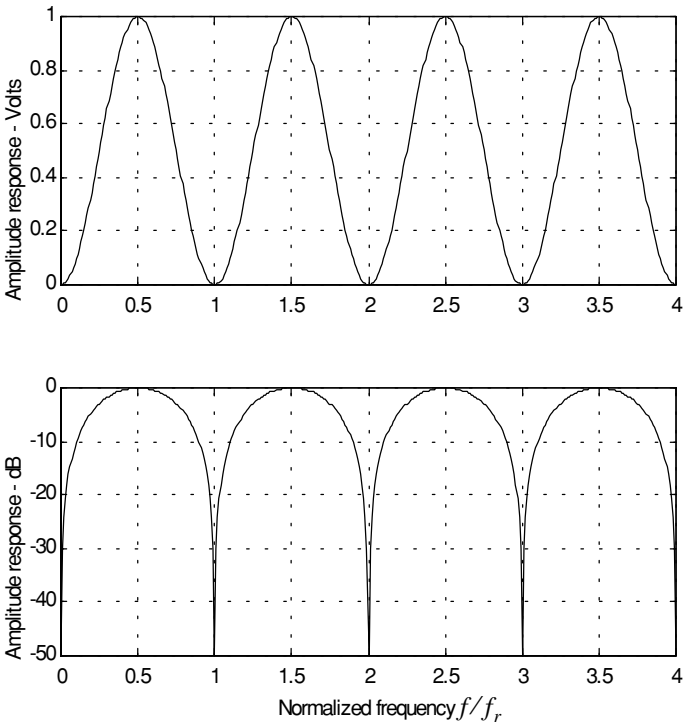

Figure 9.11. Single canceler frequency response.

In most radar applications the response of a single canceler is not acceptable since it does not have a wide notch in the stop-band. A double delay line canceler has better response in both the stop- and pass-bands, and thus it is more frequently used than a single canceler. In this book, we will use the names "single delay line canceler" and "single canceler" interchangeably.

9.8. Double Delay Line Canceler

Two basic configurations of a double delay line canceler are shown in Fig. 9.12. Double cancelers are often called "three-pulse cancelers" since they require three distinct input pulses before an output can be read. The double line canceler impulse response is given by

$$h(t) = \delta(t) - 2\delta(t-T) + \delta(t-2T) \tag{9.43}$$

Again, the names "double delay line" canceler and "double canceler" will be used interchangeably. The power gain for the double delay line canceler is

$$|H(\omega)|^2 = |H_1(\omega)|^2 |H_1(\omega)|^2 \tag{9.44}$$

where $|H_1(\omega)|^2$ is the single line canceler power gain given in Eq. (9.42). It follows that

$$|H(\omega)|^2 = 16\left(\sin\left(\omega\frac{T}{2}\right)\right)^4 \tag{9.45}$$

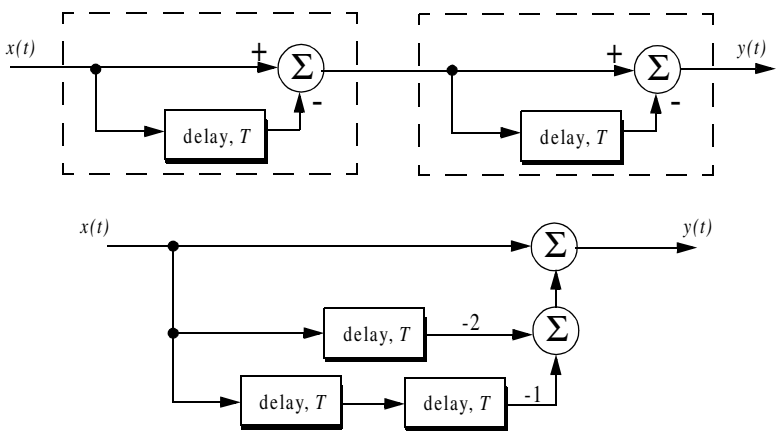

Figure 9.12. Two configurations for a double delay line canceler.

And in the z-domain, we have

$$H(z) = (1 - z^{-1})^2 = 1 - 2z^{-1} + z^{-2} \tag{9.46}$$

MATLAB Function "double_canceler.m"

The function *"single_canceler.m"* computes and plots (as a function of f/f_r) the amplitude response for a single delay line canceler. It is given in Listing 9.2 in Section 9.14. The syntax is as follows:

[resp] = double_canceler (fofr)

where *fofr* is the number of periods desired.

Fig. 9.13 shows typical output from this function. Note that the double canceler has a better response than the single canceler (deeper notch and flatter pass-band response).

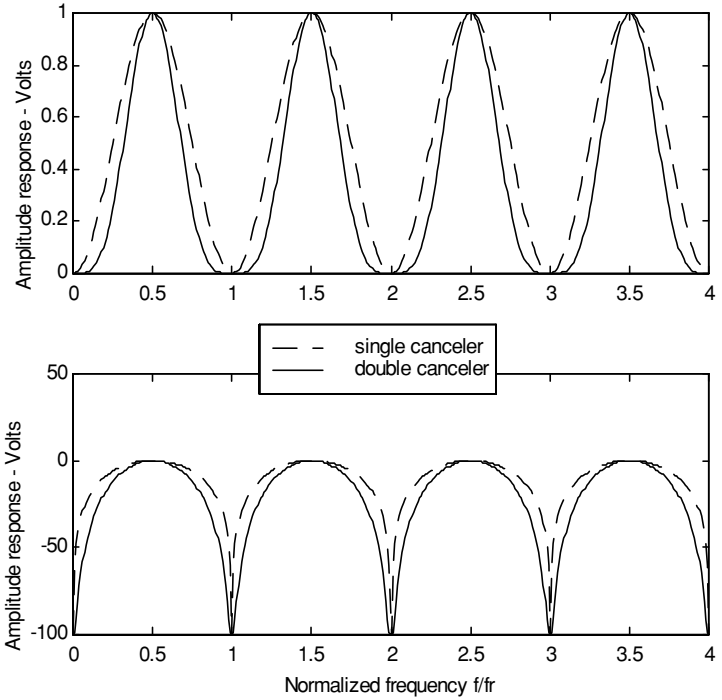

Figure 9.13. Normalized frequency responses for single and double cancelers.

9.9. Delay Lines with Feedback (Recursive Filters)

Delay line cancelers with feedback loops are known as recursive filters. The advantage of a recursive filter is that through a feedback loop we will be able to shape the frequency response of the filter. As an example, consider the single canceler shown in Fig. 9.14. From the figure we can write

$$y(t) = x(t) - (1-K)w(t) \tag{9.47}$$

$$v(t) = y(t) + w(t) \tag{9.48}$$

$$w(t) = v(t-T) \tag{9.49}$$

Applying the z-transform to the above three equations yields

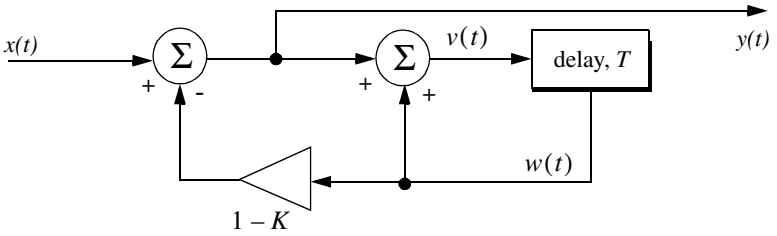

Figure 9.14. MTI recursive filter.

$$Y(z) = X(z) - (1-K)W(z) \tag{9.50}$$

$$V(z) = Y(z) + W(z) \tag{9.51}$$

$$W(z) = z^{-1}V(z) \tag{9.52}$$

Solving for the transfer function $H(z) = Y(z)/X(z)$ yields

$$H(z) = \frac{1-z^{-1}}{1-Kz^{-1}} \tag{9.53}$$

The modulus square of $H(z)$ is then equal to

$$|H(z)|^2 = \frac{(1-z^{-1})(1-z)}{(1-Kz^{-1})(1-Kz)} = \frac{2-(z+z^{-1})}{(1+K^2)-K(z+z^{-1})} \tag{9.54}$$

Using the transformation $z = e^{j\omega T}$ yields

$$z + z^{-1} = 2\cos\omega T \tag{9.55}$$

Thus, Eq. (54) can now be rewritten as

$$\left|H(e^{j\omega T})\right|^2 = \frac{2(1-\cos\omega T)}{(1+K^2)-2K\cos(\omega T)} \tag{9.56}$$

Note that when $K = 0$, Eq. (9.56) collapses to Eq. (9.42) (single line canceler). Fig. 9.15 shows a plot of Eq. (9.56) for $K = 0.25, 0.7, 0.9$. Clearly, by changing the gain factor K one can control of the filter response.

In order to avoid oscillation due to the positive feedback, the value of K should be less than unity. The value $(1-K)^{-1}$ is normally equal to the number of pulses received from the target. For example, $K = 0.9$ corresponds to ten pulses, while $K = 0.98$ corresponds to about fifty pulses.

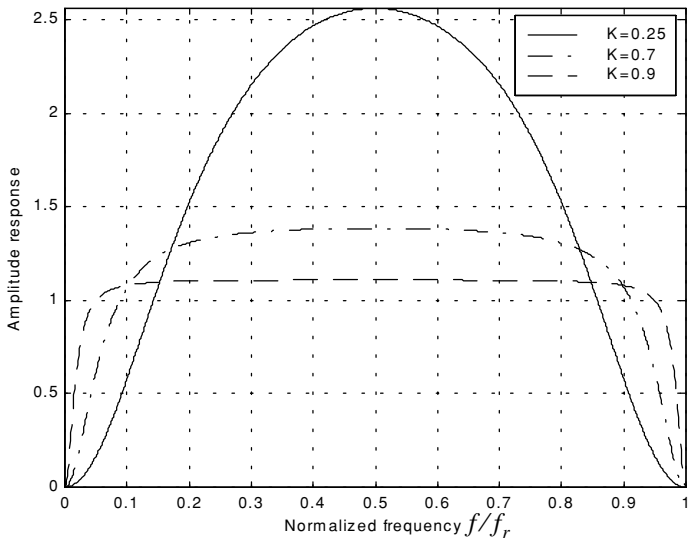

Figure 9.15. Frequency response corresponding to Eq. (9.56). This plot can be reproduced using MATLAB program *"fig9_15.m"* given in Listing 9.3 in Section 9.14.

9.10. PRF Staggering

Blind speeds can pose serious limitations on the performance of MTI radars and their ability to perform adequate target detection. Using PRF agility by changing the pulse repetition interval between consecutive pulses can extend

the first blind speed to tolerable values. In order to show how PRF staggering can alleviate the problem of blind speeds, let us first assume that two radars with distinct PRFs are utilized for detection. Since blind speeds are proportional to the PRF, the blind speeds of the two radars would be different. However, using two radars to alleviate the problem of blind speeds is a very costly option. A more practical solution is to use a single radar with two or more different PRFs.

For example, consider a radar system with two interpulse periods T_1 and T_2, such that

$$\frac{T_1}{T_2} = \frac{n_1}{n_2} \tag{9.57}$$

where n_1 and n_2 are integers. The first true blind speed occurs when

$$\frac{n_1}{T_1} = \frac{n_2}{T_2} \tag{9.58}$$

This is illustrated in Fig. 9.16 for $n_1 = 4$ and $n_2 = 5$. Note that if $n_2 = n_1 + 1$, then the process of PRF staggering is similar to that discussed in Chapter 3.

The ratio

$$k_s = \frac{n_1}{n_2} \tag{9.59}$$

is known as the stagger ratio. Using staggering ratios closer to unity pushes the first true blind speed farther out. However, the dip in the vicinity of $1/T_1$ becomes deeper, as illustrated in Fig. 9.17 for stagger ratio $k_s = 63/64$. In general, if there are N PRFs related by

$$\frac{n_1}{T_1} = \frac{n_2}{T_2} = \ldots = \frac{n_N}{T_N} \tag{9.60}$$

and if the first blind speed to occur for any of the individual PRFs is v_{blind1}, then the first true blind speed for the staggered waveform is

$$v_{blind} = \frac{n_1 + n_2 + \ldots + n_N}{N} \, v_{blind1} \tag{9.61}$$

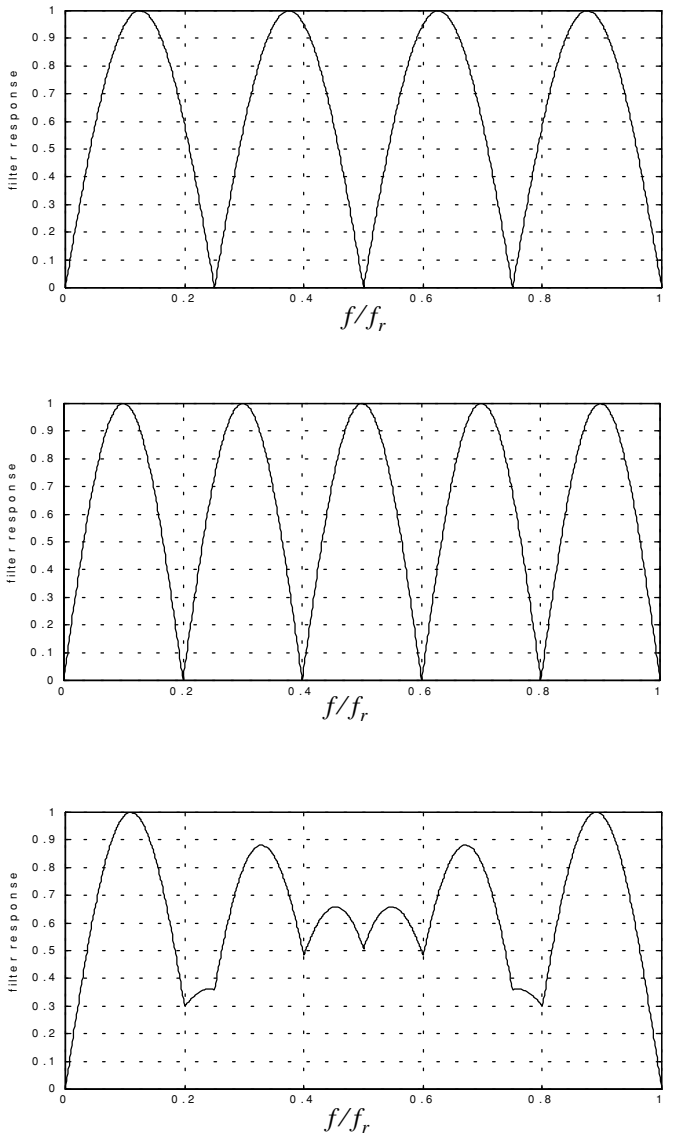

Figure 9.16. Frequency responses of a single canceler. Top plot corresponds to T_1, middle plot corresponds to T_2, bottom plot corresponds to stagger ratio $T_1/T_2 = 4/3$. This plot can be reproduced using MATLAB program *"fig9_16.m"* given in Listing 9.4 in Section 9.14.

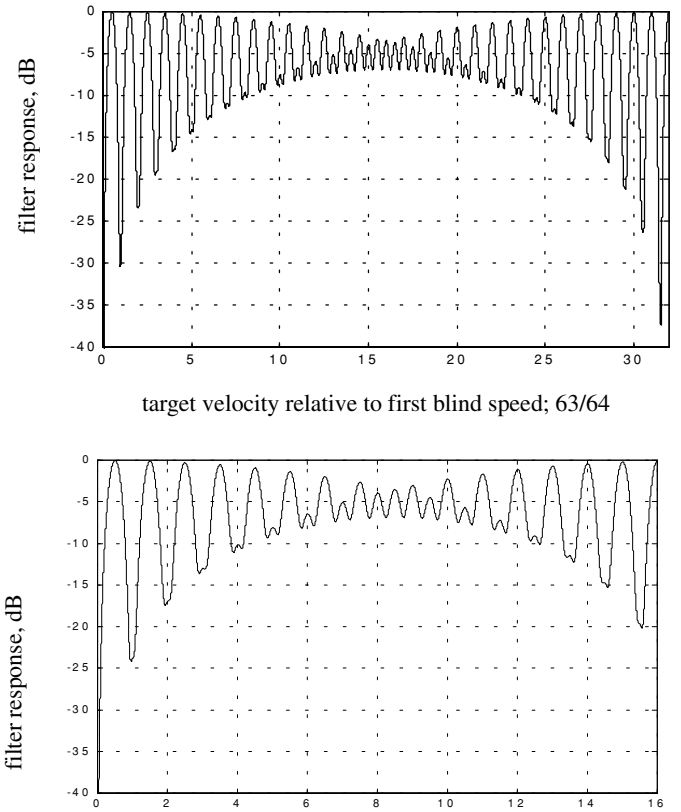

Figure 9.17. MTI responses, staggering ratio 63/64. This plot can be reproduced using MATLAB program *"fig9_17.m"* given in Listing 9.5 in Section 9.14.

9.11. MTI Improvement Factor

In this section two quantities that are normally used to define the performance of MTI systems are introduced. They are "Clutter Attenuation (CA)" and the MTI "Improvement Factor." The MTI CA is defined as the ratio between the MTI filter input clutter power C_i to the output clutter power C_o,

$$CA = C_i / C_o \tag{9.62}$$

The MTI improvement factor is defined as the ratio of the Signal to Clutter (SCR) at the output to the SCR at the input,

$$I = \left(\frac{S_o}{C_o}\right) \Big/ \left(\frac{S_i}{C_i}\right) \tag{9.63}$$

which can be rewritten as

$$I = \frac{S_o}{S_i} CA \tag{9.64}$$

The ratio S_o/S_i is the average power gain of the MTI filter, and it is equal to $|H(\omega)|^2$. In this section, a closed form expression for the improvement factor using a Gaussian-shaped power spectrum is developed. A Gaussian-shaped clutter power spectrum is given by

$$W(f) = \frac{P_c}{\sqrt{2\pi}\ \sigma_c} \exp(-f^2/2\sigma_c^2) \tag{9.65}$$

where P_c is the clutter power (constant), and σ_c is the clutter rms frequency and is given by

$$\sigma_c = 2\sigma_v/\lambda \tag{9.66}$$

where λ is the wavelength, and σ_v is the rms wind velocity, since wind is the main reason for clutter frequency spreading. Substituting Eq. (9.66) into Eq. (9.65) yields

$$W(f) = \frac{\lambda P_c}{2\sqrt{2\pi}\ \sigma_v} \exp\left(-\frac{f^2\lambda^2}{8\sigma_v^2}\right) \tag{9.67}$$

The clutter power at the input of an MTI filter is

$$C_i = \int_{-\infty}^{\infty} \frac{P_c}{\sqrt{2\pi}\ \sigma_c} \exp\left(-\frac{f^2}{2\sigma_c^2}\right) df \tag{9.68}$$

Factoring out the constant P_c yields

$$C_i = P_c \int_{-\infty}^{\infty} \frac{1}{\sqrt{2\pi}\sigma_c} \exp\left(-\frac{f^2}{2\sigma_c^2}\right) df \tag{9.69}$$

It follows that (Why?)

$$C_i = P_c \tag{9.70}$$

The clutter power at the output of an MTI is

$$C_o = \int_{-\infty}^{\infty} W(f)|H(f)|^2 \, df \tag{9.71}$$

We will continue the analysis using a single delay line canceler. The frequency response for a single delay line canceler is given by Eq. (9.38). The single canceler power gain is given in Eq. (9.42), which will be repeated here, in terms of f rather than ω, as Eq. (9.72),

$$|H(f)|^2 = 4\left(\sin\left(\frac{\pi f}{f_r}\right)\right)^2 \tag{9.72}$$

It follows that

$$C_o = \int_{-\infty}^{\infty} \frac{P_c}{\sqrt{2\pi}\ \sigma_c} \exp\left(-\frac{f^2}{2\sigma_c^2}\right) 4\left(\sin\left(\frac{\pi f}{f_r}\right)\right)^2 \, df \tag{9.73}$$

Now, since clutter power will only be significant for small f, then the ratio f/f_r is very small (i.e., $\sigma_c \ll f_r$). Consequently, by using the small angle approximation Eq. (9.73) is approximated by

$$C_o \approx \int_{-\infty}^{\infty} \frac{P_c}{\sqrt{2\pi}\ \sigma_c} \exp\left(-\frac{f^2}{2\sigma_c^2}\right) 4\left(\frac{\pi f}{f_r}\right)^2 \, df \tag{9.74}$$

which can be rewritten as

$$C_o = \frac{4P_c\pi^2}{f_r^2} \int_{-\infty}^{\infty} \frac{1}{\sqrt{2\pi\sigma_c^2}} \exp\left(-\frac{f^2}{2\sigma_c^2}\right) f^2 \, df \tag{9.75}$$

The integral part in Eq. (9.75) is the second moment of a zero mean Gaussian distribution with variance σ_c^2. Replacing the integral in Eq. (9.75) by σ_c^2 yields

$$C_o = \frac{4P_c\pi^2}{f_r^2}\ \sigma_c^2 \tag{9.76}$$

Substituting Eqs. (9.76) and (9.70) into Eq. (9.62) produces

$$CA = \frac{C_i}{C_o} = \left(\frac{f_r}{2\pi\sigma_c}\right)^2 \tag{9.77}$$

It follows that the improvement factor for a single canceler is

$$I = \left(\frac{f_r}{2\pi\sigma_c}\right)^2 \frac{S_o}{S_i} \tag{9.78}$$

The power gain ratio for a single canceler is (remember that $|H(f)|$ is periodic with period f_r)

$$\frac{S_o}{S_i} = |H(f)|^2 = \frac{1}{f_r}\int_{-f_r/2}^{f_r/2} 4\left(\sin\frac{\pi f}{f_r}\right)^2 df \tag{9.79}$$

Using the trigonometric identity $(2 - 2\cos 2\vartheta) = 4(\sin\vartheta)^2$ yields

$$|H(f)|^2 = \frac{1}{f_r}\int_{-f_r/2}^{f_r/2} \left(2 - 2\cos\frac{2\pi f}{f_r}\right) df = 2 \tag{9.80}$$

It follows that

$$I = 2(f_r/(2\pi\sigma_c))^2 \tag{9.81}$$

The expression given in Eq. (9.81) is an approximation valid only for $\sigma_c \ll f_r$. When the condition $\sigma_c \ll f_r$ is not true, then the autocorrelation function needs to be used in order to develop an exact expression for the improvement factor.

Example 9.3: A certain radar has $f_r = 800Hz$. If the clutter rms is $\sigma_c = 6.4Hz$ (wooded hills with $\sigma_v = 1.16311Km/hr$), find the improvement factor when a single delay line canceler is used.

Solution: The clutter attenuation CA is

$$CA = \left(\frac{f_r}{2\pi\sigma_c}\right)^2 = \left(\frac{800}{(2\pi)(6.4)}\right)^2 = 395.771 = 25.974dB$$

and since $S_o/S_i = 2 = 3dB$ we get

$$I_{dB} = (CA + S_o/S_i)_{dB} = 3 + 25.97 = 28.974dB.$$

9.12. Subclutter Visibiliy (SCV)

The phrase Subclutter Visibility (SCV) describes the radar's ability to detect non-stationary targets embedded in a strong clutter background, for some

probabilities of detection and false alarm. It is often used as a measure of MTI performance. For example, a radar with $10dB$ subclutter visibility will be able to detect moving targets whose returns are ten times smaller than those of clutter. A sketch illustrating the concept of SCV is shown in Fig. 9.18.

If a radar system can resolve the areas of strong and weak clutter within its field of view, then the phrase Interclutter Visibility (ICV) describes the radar's ability to detect non-stationary targets between strong clutter points. The subclutter visibility is expressed as the ratio of the improvement factor to the minimum MTI output SCR required for proper detection for a given probability of detection. More precisely,

$$SCV = I/(SCR)_o \tag{9.82}$$

When comparing different radar systems' performances on the basis of SCV, one should use caution since the amount of clutter power is dependent on the radar resolution cell (or volume), which may be different from one radar to another. Thus, only if the different radars have the same beam widths and the same pulse widths can SCV be used as a basis of performance comparison.

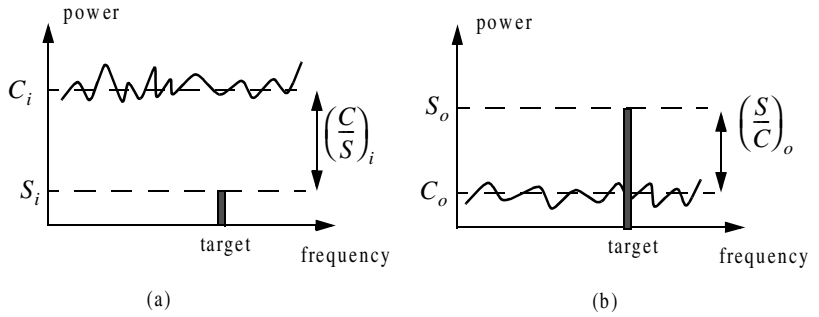

Figure 9.18. Illustration of SCV. (a) MTI input. (b) MTI output.

9.13. Delay Line Cancelers with Optimal Weights

The delay line cancelers discussed in this chapter belong to a family of transversal Finite Impulse Response (FIR) filters widely known as the "tapped delay line" filters. Fig. 9.19 shows an N-stage tapped delay line implementation.

When the weights are chosen such that they are the binomial coefficients (coefficients of the expansion $(1-x)^N$) with alternating signs, then the resultant MTI filter is equivalent to N-stage cascaded single line cancelers. This is illustrated in Fig. 9.20 for $N = 4$. In general, the binomial coefficients are given by

$$w_i = (-1)^{i-1} \frac{N!}{(N-i+1)!(i-1)!} \quad ; \; i = 1, \ldots, N+1 \tag{9.83}$$

Using the binomial coefficients with alternating signs produces an MTI filter that closely approximates the optimal filter in the sense that it maximizes the improvement factor, as well as the probability of detection. In fact, the difference between an optimal filter and one with binomial coefficients is so small that the latter one is considered to be optimal by most radar designers. However, being optimal in the sense of the improvement factor does not guarantee a deep notch, nor a flat pass-band in the MTI filter response. Consequently, many researchers have been investigating other weights that can produce a deeper notch around DC, as well as a better pass-band response.

In general, the average power gain for an N-stage delay line canceler is

$$\frac{S_o}{S_i} = \prod_{i=1}^{N} |H_1(f)|^2 = \prod_{i=1}^{N} 4\left(\sin\left(\frac{\pi f}{f_r}\right)\right)^2 \tag{9.84}$$

where $|H_1(f)|^2$ is given in Eq. (9.72). For example, $N = 2$ (double delay line canceler) gives

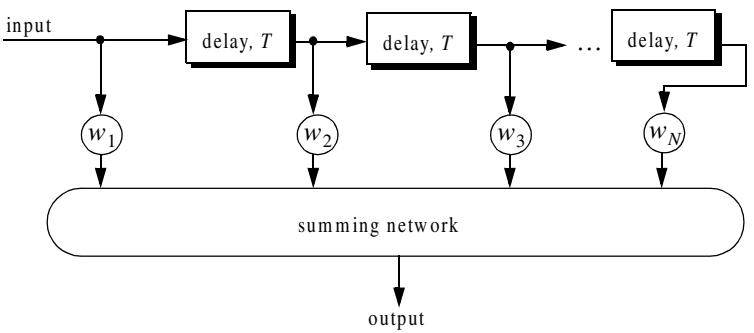

Figure 9.19. N-stage tapped delay line filter.

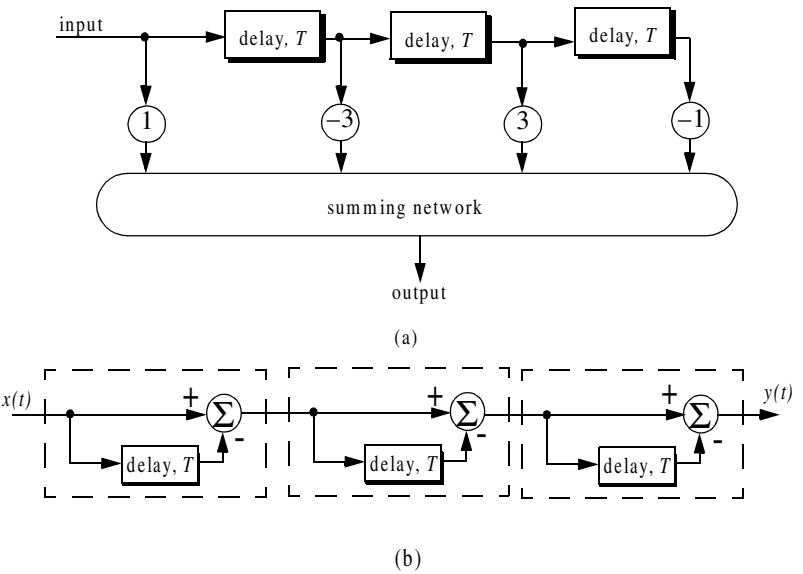

Figure 9.20. Two equivalent three delay line cancelers.
(a) Tapped delay line.
(b) Three cascaded single line cancelers.

$$\frac{S_o}{S_i} = 16\left(\sin\left(\frac{\pi f}{f_r}\right)\right)^4 \tag{9.85}$$

Equation (9.84) can be rewritten as

$$\frac{S_o}{S_i} = \left|H_1(f)\right|^{2N} = 2^{2N}\left(\sin\left(\frac{\pi f}{f_r}\right)\right)^{2N} \tag{9.86}$$

As indicated by Eq. (9.86), blind speeds for an N-stage delay canceler are identical to those of a single canceler. It follows that blind speeds are independent from the number of cancelers used. It is possible to show that Eq. (9.86) can be written as

$$\frac{S_o}{S_i} = 1 + N^2 + \left(\frac{N(N-1)}{2!}\right)^2 + \left(\frac{N(N-1)(N-2)}{3!}\right)^2 + \ldots \tag{9.87}$$

A general expression for the improvement factor of an N-stage tapped delay line canceler is reported by Nathanson[1] to be

1. Nathanson, F. E., *Radar Design Principles*, second edition, McGraw-Hill, Inc., 1991.

$$I = \frac{(S_o/S_i)}{\sum_{k=1}^{N}\sum_{j=1}^{N} w_k w_j^* \rho\left(\frac{(k-j)}{f_r}\right)} \tag{9.88}$$

where the weights w_k and w_j are those of a tapped delay line canceler, and $\rho((k-j)/f_r)$ is the correlation coefficient between the kth and jth samples. For example, $N = 2$ produces

$$I = \frac{1}{1 - \frac{4}{3}\rho T + \frac{1}{3}\rho 2T} \tag{9.89}$$

9.14. MATLAB Program/Function Listings

This section contains listings of all MATLAB programs and functions used in this chapter. Users are encouraged to rerun these codes with different inputs in order to enhance their understanding of the theory.

Listing 9.1. MATLAB Function "single_canceler.m"

```
function [resp] = single_canceler (fofr1)
eps = 0.00001;
fofr = 0:0.01:fofr1;
arg1 = pi .* fofr;
resp = 4.0 .*((sin(arg1)).^2);
max1 = max(resp);
resp = resp ./ max1;
subplot(2,1,1)
plot(fofr,resp,'k')
xlabel ('Normalized frequency - f/fr')
ylabel( 'Amplitude response - Volts')
grid
subplot(2,1,2)
resp=10.*log10(resp+eps);
plot(fofr,resp,'k');
axis tight
grid
xlabel ('Normalized frequency - f/fr')
ylabel( 'Amplitude response - dB')
```

Listing 9.2. MATLAB Function "double_canceler.m"

```
function [resp] = double_canceler(fofr1)
eps = 0.00001;
fofr = 0:0.01:fofr1;
arg1 = pi .* fofr;
resp = 4.0 .* ((sin(arg1)).^2);
max1 = max(resp);
resp = resp ./ max1;
resp2 = resp .* resp;
subplot(2,1,1);
plot(fofr,resp,'k--',fofr, resp2,'k');
ylabel ('Amplitude response - Volts')
resp2 = 20. .* log10(resp2+eps);
resp1 = 20. .* log10(resp+eps);
subplot(2,1,2)
plot(fofr,resp1,'k--',fofr,resp2,'k');
legend ('single canceler','double canceler')
xlabel ('Normalized frequency f/fr')
ylabel ('Amplitude response - Volts')
```

Listing 9.3. MATLAB Program "fig9_15.m"

```
clear all
fofr = 0:0.001:1;
arg = 2.*pi.*fofr;
nume = 2.*(1.-cos(arg));
den11 = (1. + 0.25 * 0.25);
den12 = (2. * 0.25) .* cos(arg);
den1 = den11 - den12;
den21 = 1.0 + 0.7 * 0.7;
den22 = (2. * 0.7) .* cos(arg);
den2 = den21 - den22;
den31 = (1.0 + 0.9 * 0.9);
den32 = ((2. * 0.9) .* cos(arg));
den3 = den31 - den32;
resp1 = nume ./ den1;
resp2 = nume ./ den2;
resp3 = nume ./ den3;
plot(fofr,resp1,'k',fofr,resp2,'k-.',fofr,resp3,'k--');
xlabel('Normalized frequency')
ylabel('Amplitude response')
legend('K=0.25','K=0.7','K=0.9')
grid
axis tight
```

Listing 9.4. MATLAB Program "fig9_16.m"

```
clear all
fofr = 0:0.001:1;
f1 = 4.0 .* fofr;
f2 = 5.0 .* fofr;
arg1 = pi .* f1;
arg2 = pi .* f2;
resp1 = abs(sin(arg1));
resp2 = abs(sin(arg2));
resp = resp1+resp2;
max1 = max(resp);
resp = resp./max1;
plot(fofr,resp1,fofr,resp2,fofr,resp);
xlabel('Normalized frequency f/fr')
ylabel('Filter response')
```

Listing 9.5. MATLAB Program "fig9_17.m"

```
clear all
fofr = 0.01:0.001:32;
a = 63.0 / 64.0;
term1 = (1. - 2.0 .* cos(a*2*pi*fofr) + cos(4*pi*fofr)).^2;
term2 = (-2. .* sin(a*2*pi*fofr) + sin(4*pi*fofr)).^2;
resp = 0.25 .* sqrt(term1 + term2);
resp = 10. .* log(resp);
plot(fofr,resp);
axis([0 32 -40 0]);
grid
```

Problems

9.1. Compute the signal-to-clutter ratio (SCR) for the radar described in Example 9.1. In this case, assume antenna 3dB beam width $\theta_{3dB} = 0.03 rad$, pulse width $\tau = 10 \mu s$, range $R = 50 Km$, grazing angle $\psi_g = 15°$, target RCS $\sigma_t = 0.1 m^2$, and clutter reflection coefficient $\sigma^0 = 0.02 (m^2/m^2)$.

9.2. Repeat Example 9.2 for target RCS $\sigma_t = 0.15 m^2$, pulse width $\tau = 0.1 \mu s$, antenna beam width $\theta_a = \theta_e = 0.03 radians$; the detection range is $R = 100 Km$, and $\sum \sigma_i = 1.6 \times 10^{-9} (m^2/m^3)$.

9.3. The quadrature components of the clutter power spectrum are, respectively, given by

$$\bar{S}_I(f) = \delta(f) + \frac{C}{\sqrt{2\pi}\sigma_c}\exp(-f^2/2\sigma_c^2)$$

$$\overline{S_Q}(f) = \frac{C}{\sqrt{2\pi}\sigma_c}\exp(-f^2/2\sigma_c^2)$$

Compute the D.C. and A.C. power of the clutter. Let $\sigma_c = 10Hz$.

9.4. A certain radar has the following specifications: pulse width $\tau' = 1\mu s$, antenna beam width $\Omega = 1.5°$, and wavelength $\lambda = 3cm$. The radar antenna is $7.5m$ high. A certain target is simulated by two point targets (scatterers). The first scatterer is $4m$ high and has RCS $\sigma_1 = 20m^2$. The second scatterer is $12m$ high and has RCS $\sigma_2 = 1m^2$. If the target is detected at $10Km$, compute (a) SCR when both scatterers are observed by the radar; (b) the SCR when only the first scatterer is observed by the radar. Assume a reflection coefficient of -1, and $\sigma^0 = -30dB$.

9.5. A certain radar has range resolution of $300m$ and is observing a target somewhere in a line of high towers each having RCS $\sigma_{tower} = 10^6 m^2$. If the target has RCS $\sigma_t = 1m^2$, (a) How much signal-to-clutter ratio should the radar have? (b) Repeat part a for range resolution of $30m$.

9.6. (a) Derive an expression for the impulse response of a single delay line canceler. (b) Repeat for a double delay line canceler.

9.7. One implementation of a single delay line canceler with feedback is shown below:

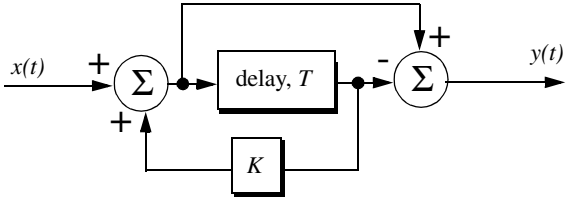

(a) What is the transfer function, $H(z)$? (b) If the clutter power spectrum is $W(f) = w_0\exp(-f^2/2\sigma_c^2)$, find an exact expression for the filter power gain. (c) Repeat part b for small values of frequency, f. (d) Compute the clutter attenuation and the improvement factor in terms of K and σ_c.

9.8. Plot the frequency response for the filter described in the previous problem for $K = -0.5, 0, and\ 0.5$.

9.9. An implementation of a double delay line canceler with feedback is shown below:

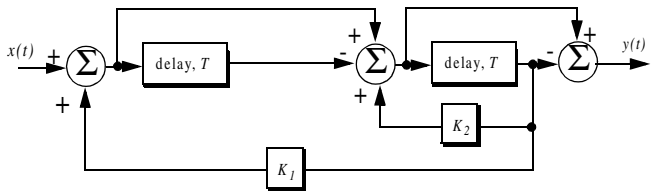

(a) What is the transfer function, $H(z)$? (b) Plot the frequency response for $K_1 = 0 = K_2$, and $K_1 = 0.2, K_2 = 0.5$.

9.10. Consider a single delay line canceler. Calculate the clutter attenuation and the improvement factor. Assume that $\sigma_c = 4Hz$ and a PRF $f_r = 450Hz$.

9.11. Develop an expression for the improvement factor of a double delay line canceler.

9.12. Repeat Problem 9.10 for a double delay line canceler.

9.13. An experimental expression for the clutter power spectrum density is $W(f) = w_0 \exp(-f^2/2\sigma_c^2)$, where w_0 is a constant. Show that using this expression leads to the same result obtained for the improvement factor as developed in Section 9.11.

9.14. Repeat Problem 9.13 for a double delay line canceler.

9.15. A certain radar uses two PRFs with stagger ratio 63/64. If the first PRF is $f_{r1} = 500Hz$, compute the blind speeds for both PRFs and for the resultant composite PRF. Assume $\lambda = 3cm$.

9.16. A certain filter used for clutter rejection has an impulse response $h(n) = \delta(n) - 3\delta(n-1) + 3\delta(n-2) - \delta(n-3)$. (a) Show an implementation of this filter using delay lines and adders. (b) What is the transfer function? (c) Plot the frequency response of this filter. (d) Calculate the output when the input is the unit step sequence.

9.17. The quadrature components of the clutter power spectrum are given in Problem 9.3. Let $\sigma_c = 10Hz$ and $f_r = 500Hz$. Compute the improvement of the signal-to-clutter ratio when a double delay line canceler is utilized.

9.18. Develop an expression for the clutter improvement factor for single and double line cancelers using the clutter autocorrelation function. Assume that the clutter power spectrum is as defined in Eq. (9.65).

Chapter 10 *Radar Antennas*

An antenna is a radiating element which acts as a transducer between an electrical signal in a system and a propagating wave. The Institute of Electrical and Electronic Engineers (IEEE)'s Standard Definition of Terms for Antennas (IEEE std. 145-1973) defines an antenna as "a mean for radiating or receiving radio power."

10.1. Directivity, Power Gain, and Effective Aperture

Radar antennas can be characterized by the directive gain G_D, power gain G, and effective aperture A_e. Antenna gain is term used to describe the ability of an antenna to concentrate the transmitted energy in a certain direction. Directive gain, or simply directivity, is more representative of the antenna radiation pattern, while power gain is normally used in the radar equation. Plots of the power gain and directivity, when normalized to unity, are called *antenna radiation pattern*. The directivity of a transmitting antenna can be defined by

$$G_D = \frac{maximum\ \ radiation\ \ intensity}{average\ \ radiation\ \ intensity} \tag{10.1}$$

The radiation intensity is the power per unit solid angle in the direction (θ, ϕ) and denoted by $P(\theta, \phi)$. The average radiation intensity over 4π radians (solid angle) is the total power divided by 4π. Hence, Eq. (10.1) can be written as

$$G_D = \frac{4\pi(maximum\ \ radiated\ \ power/unit\ \ solid\ \ angle)}{total\ \ radiated\ \ power} \tag{10.2}$$

It follows that

$$G_D = \frac{4\pi P(\beta, \phi)_{max}}{\iint P(\beta, \phi)\ d\beta d\phi} \tag{10.3}$$

As an approximation, it is customary to rewrite Eq. (10.3) as

$$G_D \approx \frac{4\pi}{\beta_3 \phi_3} \tag{10.4}$$

where β_3 and ϕ_3 are the antenna half-power (3-dB) beamwidths in either direction.

The antenna power gain and its directivity are related by

$$G = \rho_r G_D \tag{10.5}$$

where ρ_r is the radiation efficiency factor. In this book, the antenna power gain will be denoted as *gain*. The radiation efficiency factor accounts for the ohmic losses associated with the antenna. Therefore, the definition for the antenna gain is also given in Eq. (10.1). The antenna effective aperture A_e is related to gain by

$$A_e = \frac{G\lambda^2}{4\pi} \tag{10.6}$$

where λ is the wavelength. The relationship between the antenna's effective aperture A_e and the physical aperture A is

$$\begin{aligned} A_e &= \rho A \\ 0 \le \rho &\le 1 \end{aligned} \tag{10.7}$$

ρ is referred to as the aperture efficiency, and good antennas require $\rho \to 1$ (in this book $\rho = 1$ is always assumed, i.e., $A_e = A$).

Using simple algebraic manipulations of Eqs. (10.4) through (10.6) (assuming that $\rho_r = 1$) yields

$$G = \frac{4\pi A_e}{\lambda^2} \approx \frac{4\pi}{\beta_3 \phi_3} \tag{10.8}$$

Consequently, the angular cross section of the beam is

$$\beta_3 \phi_3 \approx \frac{\lambda^2}{A_e} \tag{10.9}$$

Eq. (10.9) indicates that the antenna beamwidth decreases as $\sqrt{A_e}$ increases. It follows that, in surveillance operations, the number of beam positions an antenna will take on to cover a volume V is

$$N_{Beams} > \frac{V}{\beta_3 \phi_3} \tag{10.10}$$

and when V represents the entire hemisphere, Eq. (10.10) is modified to

$$N_{Beams} > \frac{2\pi}{\beta_3 \phi_3} \approx \frac{2\pi A_e}{\lambda^2} \approx \frac{G}{2} \tag{10.11}$$

10.2. Near and Far Fields

The electric field intensity generated from the energy emitted by an antenna is a function of the antenna physical aperture shape and the electric current amplitude and phase distribution across the aperture. Plots of the modulus of the electric field intensity of the emitted radiation, $|E(\beta, \phi)|$, are referred to as the *intensity pattern* of the antenna. Alternatively, plots of $|E(\beta, \phi)|^2$ are called the *power radiation pattern* (the same as $P(\beta, \phi)$).

Based on the distance away from the face of the antenna, where the radiated electric field is measured, three distinct regions are identified. They are the near field, Fresnel, and the Fraunhofer regions. In the near field and the Fresnel regions, rays emitted from the antenna have spherical wavefronts (equi-phase fronts). In the Fraunhofer regions the wavefronts can be locally represented by plane waves. The near field and the Fresnel regions are normally of little interest to most radar applications. Most radar systems operate in the Fraunhofer region, which is also known as the far field region. In the far field region, the electric field intensity can be computed from the aperture Fourier transform.

Construction of the far criterion can be developed with the help of Fig. 10.1. Consider a radiating source at point O that emits spherical waves. A receiving antenna of length d is at distance r away from the source. The phase difference between a spherical wave and a locally plane wave at the receiving antenna can be expressed in terms of the distance δr. The distance δr is given by

$$\delta r = \overline{AO} - \overline{OB} = \sqrt{r^2 + \left(\frac{d}{2}\right)^2} - r \tag{10.12}$$

and since in the far field $d \ll r$, Eq. (10.12) is approximated via binomial expansion by

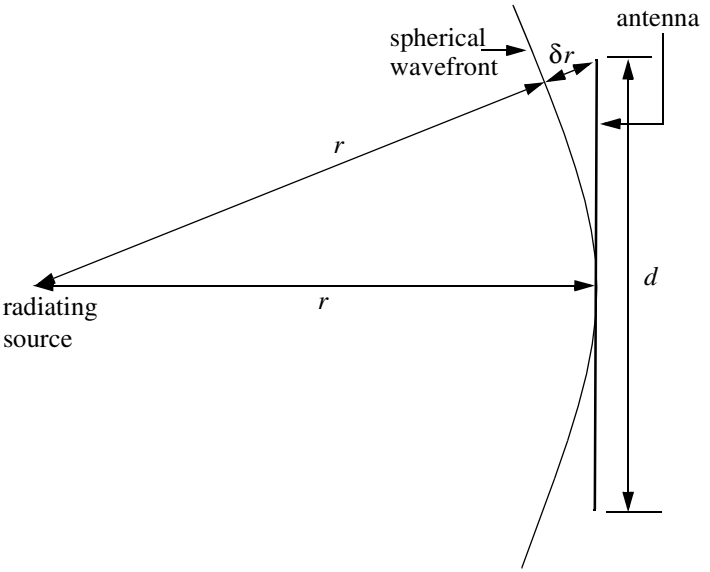

Figure 10.1. Construction for far field criterion.

$$\delta r = r\left(\sqrt{1+\left(\frac{d}{2r}\right)^2}-1\right)\approx \frac{d^2}{8r} \tag{10.13}$$

It is customary to assume far field when the distance δr corresponds to less than $1/16$ of a wavelength (i.e., $22.5°$). More precisely, if

$$\delta r = d^2/8r \le \lambda/16 \tag{10.14}$$

then a useful expression for far field is

$$r \ge 2d^2/\lambda \tag{10.15}$$

Note that far field is a function of both the antenna size and the operating wavelength.

10.3. Circular Dish Antenna Pattern

Circular dish reflectors are widely used in microwave and radar applications because of their simplicity in design and fabrication. Additionally, closed form far field expressions can be easily computed for all existing modes over the

circular aperture. Fig. 10.2 shows the geometry associated with a circular aperture. Denote the aperture radius as r. A far field observation point P is defined by range R and angular position (β, ϕ). The aperture factor at P is given by

$$E(\beta, \phi) = \int_{aperture} \int D(x', y') e^{j\psi(x', y')} dx' dy' \tag{10.16}$$

$$\psi(x', y') = k(x' \sin\beta\cos\phi + y' \sin\beta\sin\phi) \tag{10.17}$$

where $k = (2\pi)/\lambda$, λ is the wavelength, and $D(x', y')$ is the current distribution over the aperture. Due to the circular nature of the aperture, it is more convenient to adopt cylindrical coordinates. It follows that

$$\begin{aligned} x' &= \rho\cos\phi' \\ y' &= \rho\sin\phi' \end{aligned} \tag{10.18}$$

$$x' \sin\beta\cos\phi + y' \sin\beta\sin\phi = \rho\sin\beta\cos(\phi - \phi') \tag{10.19}$$

$$dx'dy' = \rho d\rho d\phi' \tag{10.20}$$

$$E(\beta, \phi) = \int_0^r \rho d\rho \int_0^{2\pi} e^{jk\rho\sin\beta\cos(\phi - \phi')} d\phi' \tag{10.21}$$

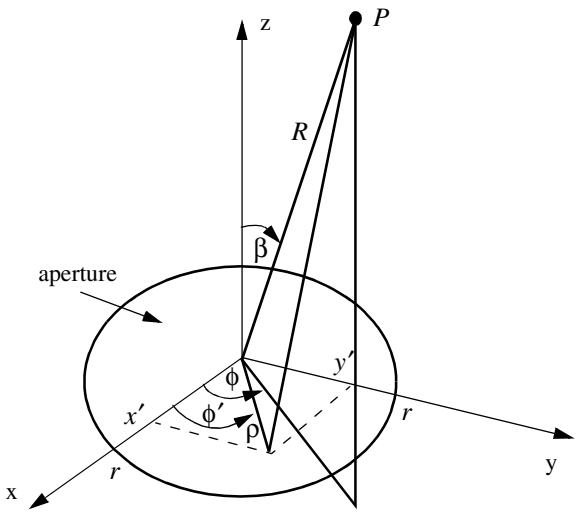

Figure 10.2. Circular aperture geometry.

where the current distribution over the aperture is assumed to be unity. The second integral in Eq. (10.21) is of the form

$$\int_0^{2\pi} e^{jz\cos\zeta} d\zeta = 2\pi J_0(z) \tag{10.22}$$

where J_0 is the Bessel function of the first kind of order zero. Because of the circular symmetry over the aperture, the electric field is independent of ϕ. Hence, $E(\beta, \phi) = E(\beta)$, and Eq. (10.21) can now be rewritten as

$$E(\beta) = 2\pi \int_0^r \rho J_0(k\rho \sin\beta) d\rho \tag{10.23}$$

Using the Bessel function identity

$$\int_0^r \rho J_0(q\rho) d\rho = \frac{r}{q} J_1(qr) \tag{10.24}$$

leads to the following expression for the aperture factor

$$E(\beta) = \pi r^2 \frac{2J_1(kr\sin\beta)}{kr\sin\beta} \tag{10.25}$$

The far field circular dish antenna pattern is computed as the modulus of the aperture factor defined in Eq. (10.25). The first null occurs when the Bessel function is zero. More precisely,

$$\frac{2\pi r}{\lambda}\sin\beta_{n1} = 1.22\pi \Rightarrow \beta_{n1} \approx 1.22\frac{\lambda}{2r} \tag{10.26}$$

Through tapering (windowing) the current distribution across the aperture, one can significantly reduce the side lobe levels.

MATLAB Function "circ_aperture.m"

The function *"circ_aperture.m"* computes and plots the antenna patter for a circular aperture of diameter d. It is given in Listing 10.1 in Section 10.9. The syntax is as follows:

[emod] = circ_aperture (lambda, d)

where *lambda* is the wavelength and *d* is the aperture diameter; both parameters should be in meters. Fig. 10.3 shows typical outputs produced using this function. In this example, $d = 0.3m$ and $\lambda = 0.1m$.

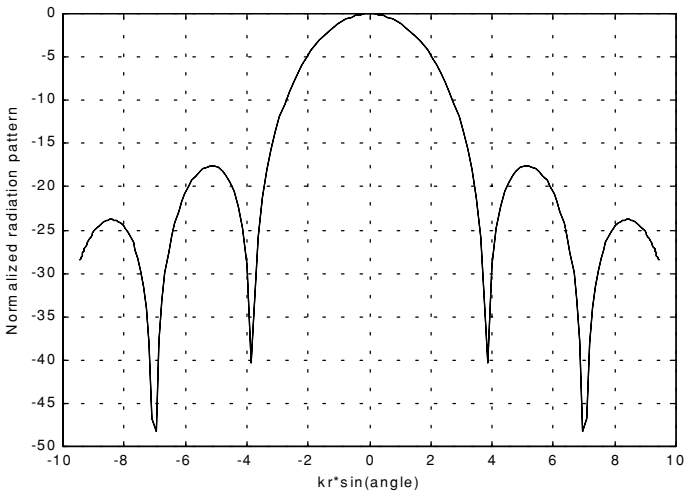

Figure 10.3a. Circular aperture radiation pattern. Typical output produced by *"circ_aperture.m"*. $d = 0.3m;\ \lambda = 0.1m$.

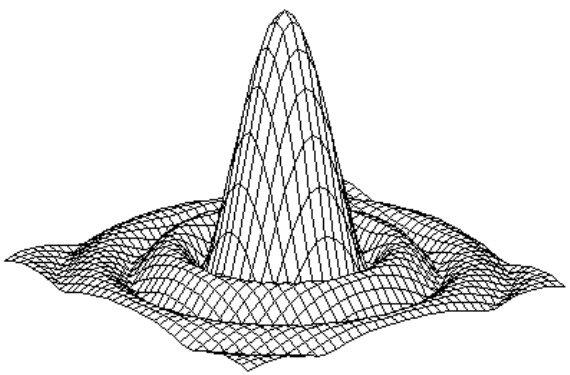

Figure 10.3b. Three-dimensional array pattern corresponding to Fig. 10.3a. Typical output produced by *"circ_aperture.m"*.
$d = 0.3m;\ \lambda = 0.1m$.

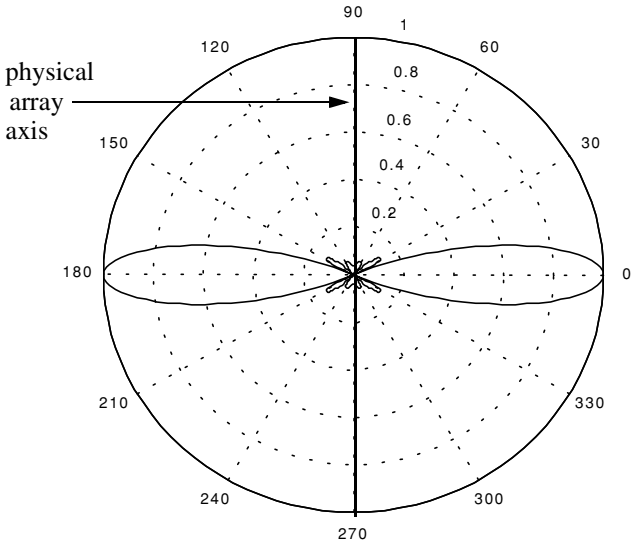

Figure 10.3c. Polar plot for a circular aperture. Typical output produced by *"circ_aperture.m"*. $d = 0.3m;\ \lambda = 0.1m$.

10.4. Array Antennas

An array is a composite antenna formed from two or more basic radiators. Each radiator is denoted as an element. The elements forming an array could be dipoles, dish reflectors, slots in a wave guide, or any other type of radiator. Array antennas synthesize narrow directive beams that may be steered, mechanically or electronically, in many directions. Electronic steering is achieved by controlling the phase of the current feeding the array elements. Arrays with electronic beam steering capability are called phased arrays. Phased array antennas when compared to other simple antennas such as dish reflectors, are costly and complicated to design. However, the inherent flexibility of phased array antennas to steer the beam electronically and also the need for specialized multi-function radar systems have made phased array antennas attractive for radar applications.

10.4.1. Linear Array Antennas

Fig.10.4 shows a linear array antenna consisting of N identical elements. The element spacing is d (normally measured in wavelength units). The combined electric field measured at a far field observation point P is computed as the product between the array factor and the element pattern,

$$E(P) = E(one\ \ element)(array\ \ factor) \tag{10.27}$$

The array factor is a general function of the number of elements, their spacing, and their relative phases and magnitudes.

Consider the linear array shown in Fig. 10.4. Let element #1 serve as a phase reference for the array. From the geometry, it is clear that an outgoing wave at the nth element leads the phase at the $(n+1)th$ element by $kd\sin\beta$, where $k = 2\pi/\lambda$. The electric field at a far field observation point with direction-sine equal to $\sin\beta$ (assuming isotropic elements) is

$$E(\sin\beta) = \sum_{i=1}^{N} e^{j(i-1)(kd\sin\beta)} \tag{10.28}$$

Expanding the summation in Eq. (10.28) yields

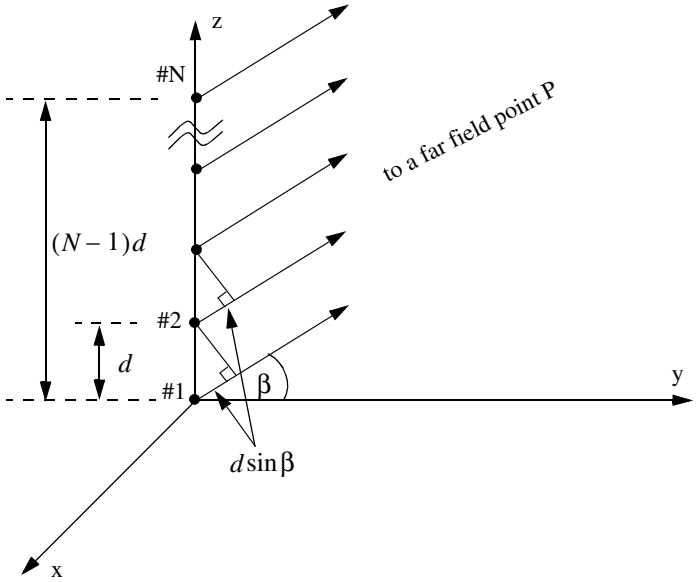

Figure 10.4. Linear array of equally spaced elements.

$$E(\sin\beta) = 1 + e^{jkd\sin\beta} + \ldots + e^{j(N-1)(kd\sin\beta)} \tag{10.29}$$

The right-hand side of Eq. (10.29) is a geometric series, which can be expressed in the form

$$1 + a + a^2 + a^3 + \ldots + a^{(N-1)} = \frac{1 - a^N}{1 - a} \tag{10.30}$$

Replacing a by $e^{jkd\sin\beta}$ yields

$$E(\sin\beta) = \frac{1 - e^{jNkd\sin\beta}}{1 - e^{jkd\sin\beta}} = \frac{1 - \cos Nkd\sin\beta - j\sin Nkd\sin\beta}{1 - \cos kd\sin\beta - j\sin kd\sin\beta} \tag{10.31}$$

The far field array intensity pattern is then given by

$$|E(\sin\beta)| = \sqrt{E(\sin\beta)E^*(\sin\beta)} \tag{10.32}$$

Substituting Eq. (10.31) into Eq. (10.32) and collecting terms yield

$$\begin{aligned} |E(\sin\beta)| &= \sqrt{\frac{(1 - \cos Nkd\sin\beta)^2 + (\sin Nkd\sin\beta)^2}{(1 - \cos kd\sin\beta)^2 + (\sin kd\sin\beta^2)}} \\ &= \sqrt{\frac{1 - \cos Nkd\sin\beta}{1 - \cos kd\sin\beta}} \end{aligned} \tag{10.33}$$

and using the trigonometric identity $1 - \cos\theta = 2(\sin\theta/2)^2$ yields

$$|E(\sin\beta)| = \left|\frac{\sin(Nkd\sin\beta/2)}{\sin(kd\sin\beta/2)}\right| \tag{10.34}$$

which is a periodic function of $kd\sin\beta$, and its period is equal to 2π.

The maximum value of $|E(\sin\beta)|$ occurs at $\beta = 0$, and it is equal to N. It follows that the normalized intensity pattern is equal to

$$|E_n(\sin\beta)| = \frac{1}{N}\left|\frac{\sin((Nkd\sin\beta)/2)}{\sin((kd\sin\beta)/2)}\right| \tag{10.35}$$

The normalized two-way array pattern (radiation pattern) is given by

$$G(\sin\beta) = |E_n(\sin\beta)|^2 = \frac{1}{N^2}\left(\frac{\sin((Nkd\sin\beta)/2)}{\sin((kd\sin\beta)/2)}\right)^2 \tag{10.36}$$

Fig. 10.5 shows a plot of Eq. (10.36) versus $\sin\beta$ for $N = 8$. The radiation pattern $G(\sin\beta)$ has cylindrical symmetry about its axis $(\sin\beta = 0)$, and it is independent of the azimuth angle. Thus, it is completely determined by its values within the interval $(0 < \beta < \pi)$. This plot can be reproduced using MATLAB program *"fig10_5.m"* given in Listing 10.2 in Section 10.9.

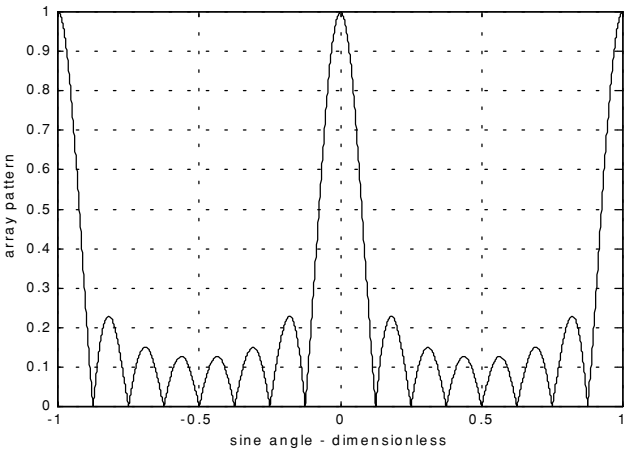

Figure 10.5a. Normalized radiation pattern for a linear array; $N = 8$ and $d = \lambda$.

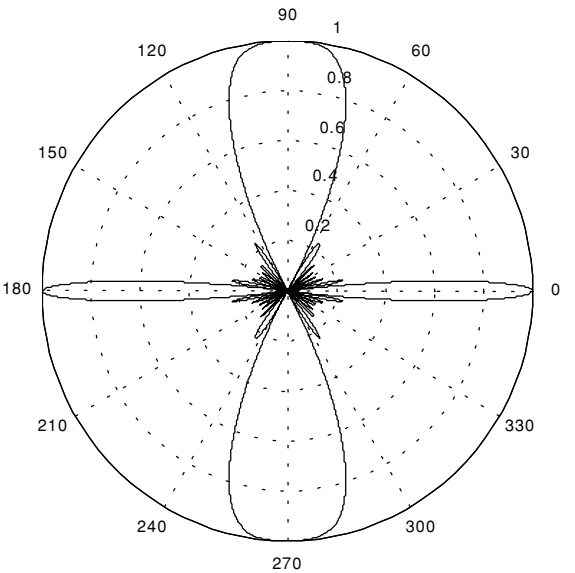

Figure 10.5b. Polar plot for the radiation pattern in Fig. 10.5a.

The main beam of an array can be steered electronically by varying the phase of the current applied to each array element. Steering the main beam into the direction-sine $\sin\beta_0$ is accomplished by making the phase difference between any two adjacent elements equal to $kd\sin\beta_0$. In this case, the normalized radiation pattern can be written as

$$G(\sin\beta) = \frac{1}{N^2}\left(\frac{\sin[(Nkd/2)(\sin\beta - \sin\beta_0)]}{\sin[(kd/2)(\sin\beta - \sin\beta_0)]}\right)^2 \qquad \textbf{(10.37)}$$

If $\beta_0 = 0$ then the main beam is perpendicular to the array axis, and the array is said to be a broadside array. Alternatively, the array is called an endfire array when the main beam points along the array axis.

The radiation pattern maxima are computed using L'Hopital's rule when both the denominator and numerator of Eq. (10.36) are zeros. More precisely,

$$\frac{kd\sin\beta}{2} = \pm m\pi \qquad ;\ m = 0, 1, 2, \ldots \qquad \textbf{(10.38)}$$

Solving for β yields

$$\beta_m = \text{asin}\left(\pm\frac{\lambda m}{d}\right) \qquad ;\ m = 0, 1, 2, \ldots \qquad \textbf{(10.39)}$$

where the subscript m is used as a maxima indicator. The first maximum occurs at $\beta_0 = 0$, and is denoted as the main beam (lobe). Other maxima occurring at $|m| \geq 1$ are called grating lobes. Grating lobes are undesirable and must be suppressed. The grating lobes occur at non-real angles when the absolute value of the arc-sine argument in Eq. (10.39) is greater than unity; it follows that $d < \lambda$. Under this condition, the main lobe is assumed to be at $\beta = 0$ (broadside array). Alternatively, when electronic beam steering is considered, the grating lobes occur at

$$|\sin\beta - \sin\beta_0| = \pm\frac{\lambda n}{d} \qquad ;\ n = 1, 2, \ldots \qquad \textbf{(10.40)}$$

Thus, in order to prevent the grating lobes from occurring between $\pm 90°$, the element spacing should be $d < \lambda/2$.

The radiation pattern attains secondary maxima (side lobes). These secondary maxima occur when the numerator of Eq. (10.36) is maximum, or equivalently

$$\frac{Nkd\sin\beta}{2} = \pm(2l+1)\frac{\pi}{2} \qquad ;\ l = 1, 2, \ldots \qquad \textbf{(10.41)}$$

Solving for β yields

$$\beta_l = \text{asin}\left(\pm\frac{\lambda}{2d}\frac{2l+1}{N}\right) \quad ; \; l = 1, 2, \ldots \tag{10.42}$$

where the subscript l is used as an indication of side lobe maxima. The nulls of the radiation pattern occur when only the numerator of Eq. (10.36) is zero. More precisely,

$$\frac{N}{2}kd\sin\beta = \pm n\pi \quad ; \; \begin{matrix} n = 1, 2, \ldots \\ n \neq N, 2N, \ldots \end{matrix} \tag{10.43}$$

Again solving for β yields

$$\beta_n = \text{asin}\left(\pm\frac{\lambda}{d}\frac{n}{N}\right) \quad ; \; \begin{matrix} n = 1, 2, \ldots \\ n \neq N, 2N, \ldots \end{matrix} \tag{10.44}$$

where the subscript n is used as a null indicator. Define the angle which corresponds to the half power point as β_h. It follows that the half power (3 dB) beam width is $2|\beta_m - \beta_h|$. This occurs when

$$\frac{N}{2}kd\sin\beta_h = 1.391 \;\; radians \Rightarrow \beta_h = \text{asin}\left(\frac{\lambda}{2\pi d}\frac{2.782}{N}\right) \tag{10.45}$$

MATLAB Function "linear_array.m"

The function *"linear_array.m"* computes and plots the linear array radiation pattern, in linear and polar coordinates. This function is given in Listing 10.3 in Section 10.9. The syntax is as follows:

[emod] = linear_array (ne, d, beta0)

where

Symbol	Description	Units	Status
ne	*number of elements in array*	*none*	*input*
d	*element spacing (e.g., $d = \lambda$; $d = \lambda/2$)*	*wavelengths*	*input*
beta0	*steering angle*	*degrees*	*input*
emod	*radiation pattern vector*	*dB*	*output*

Fig. 10.6 shows typical outputs produced using this function. In this example, $ne = 8$, $d = \lambda/2$, and $beta0 = 30°$. The array axis is assumed to be aligned with the line passing through the 90-to-270 degrees line. Fig. 10.7 is similar to Fig. 10.6 except in this case $d = \lambda$ and $beta0 = 0°$. Note how the grating lobes get closer to the main beam as the element spacing is increased, thus, limiting the electronic steering capability of the array to within the first pair of grating lobes.

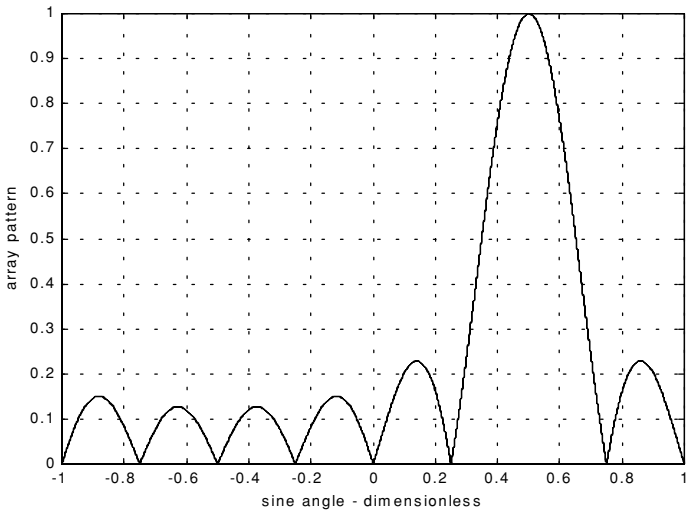

Figure 10.6a. Normalized radiation pattern for a linear array. $N = 8$, $d = \lambda/2$, **and** $\beta_0 = 30°$.

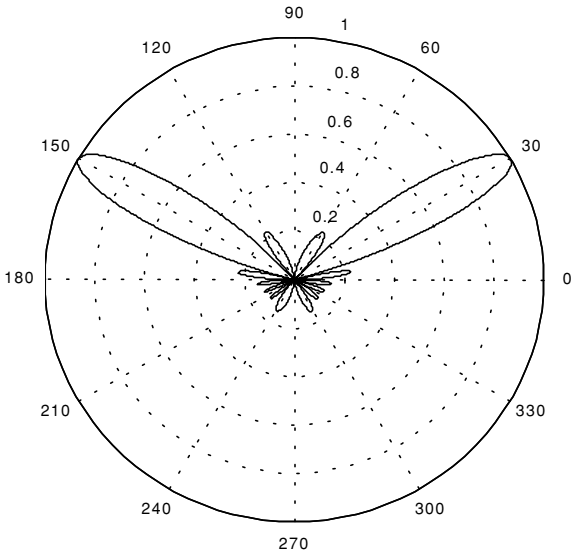

Figure 10.6b. Polar plot corresponding to Fig. 10.6a.

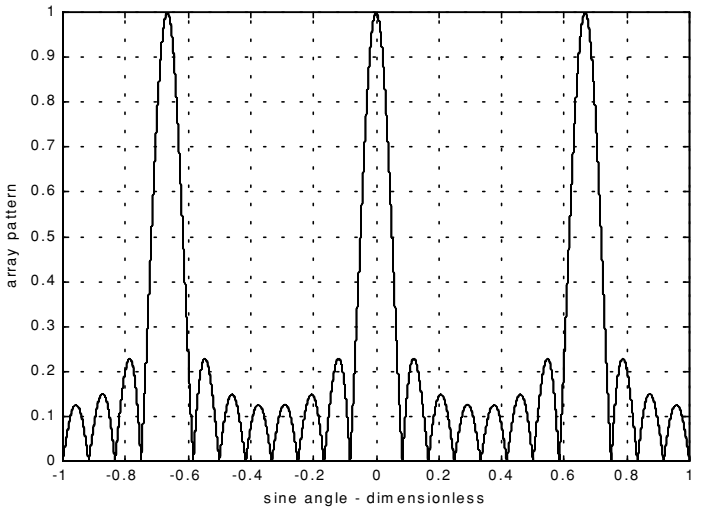

Figure 10.7a. Normalized radiation pattern for a linear array. $N = 8$, $d = 1.5\lambda$, **and** $\beta_0 = 0°$.

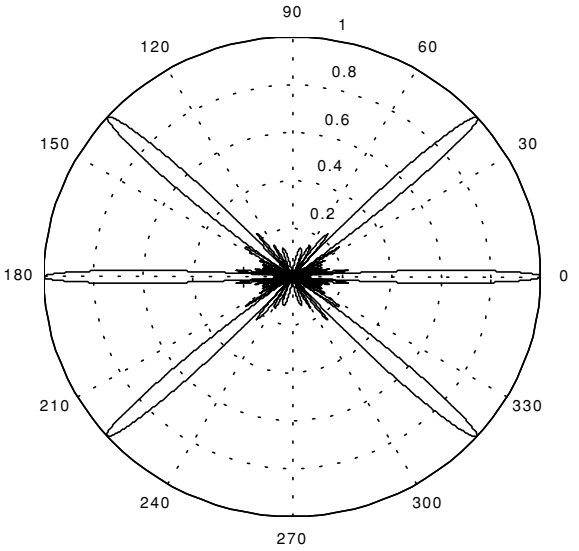

Figure 10.7b. Polar plot corresponding to Fig. 10.7a.

10.5. Array Tapering

Fig. 10.8 shows a normalized two-way radiation pattern of a uniformly excited linear array of size $N = 8$, element spacing $d = \lambda/2$. The first side lobe is about $13.46\ dB$ below the main lobe, and for most radar applications this may not be sufficient.

In order to reduce the side lobe levels, the array must be designed to radiate more power towards the center, and much less at the edges. This can be achieved through tapering (windowing) the current distribution over the face of the array. There are many possible tapering sequences that can be used for this purpose. However, as known from spectral analysis, windowing reduces side lobe levels at the expense of widening the main beam. Thus, for a given radar application, the choice of the tapering sequence must be based on the trade-off between side lobe reduction and main beam widening.

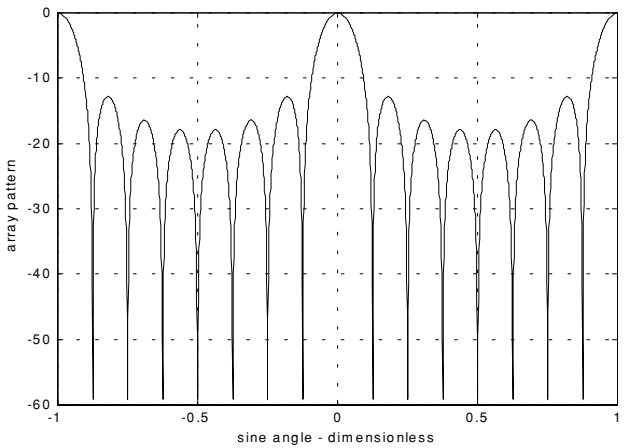

Figure 10.8. Normalized radiation pattern for a linear array. $N = 8$ and $d = \lambda/2$.

10.6. Computation of the Radiation Pattern via the DFT

Fig. 10.9 shows a linear array of size N, element spacing d, and wavelength λ. The radiators are circular dishes of diameter $D = d$. Let $w(n)$ and $\psi(n)$, respectively, denote the tapering and phase shifting sequences. The normalized electric field at a far field point in the direction-sine $\sin\beta$ is

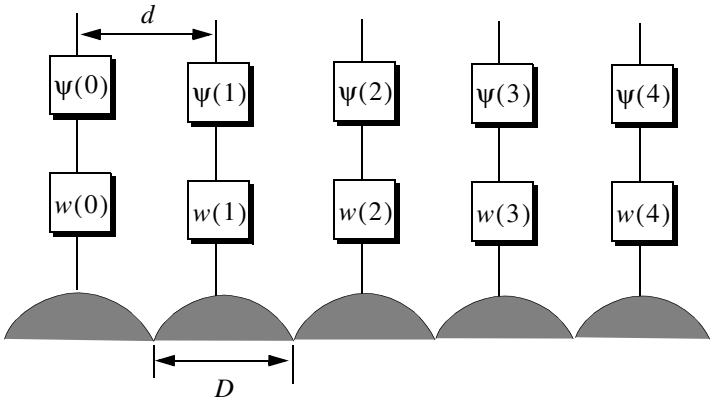

Figure 10.9. Linear array of size 5, with tapering and phase shifting hardware.

$$E(\sin\beta) = \sum_{n=0}^{N-1} w(n) e^{j\Delta\phi\left(n-\left(\frac{N-1}{2}\right)\right)} \tag{10.46}$$

where in this case the phase reference is taken as the physical center of the array, and

$$\Delta\phi = \frac{2\pi d}{\lambda}\sin\beta \tag{10.47}$$

Expanding Eq. (10.46) and factoring the common phase term $\exp[j(N-1)\Delta\phi/2]$ yield

$$E(\sin\beta) = e^{j(N-1)\Delta\phi/2}\{w(0)e^{-j(N-1)\Delta\phi} + w(1)e^{-j(N-2)\Delta\phi} + \ldots + w(N-1)\} \tag{10.48}$$

By using the symmetry property of a window sequence (remember that a window must be symmetrical about its central point), we can rewrite Eq. (10.48) as

$$E(\sin\beta) = e^{j\phi_0}\{w(N-1)e^{-j(N-1)\Delta\phi} + w(N-2)e^{-j(N-2)\Delta\phi} + \ldots + w(0)\} \tag{10.49}$$

where $\phi_0 = (N-1)\Delta\phi/2$.

Define $\{V_1^n = \exp(-j\Delta\phi n); n = 0, 1, \ldots, N-1\}$. It follows that

$$E(\sin\beta) = e^{j\phi_0}[w(0) + w(1)V_1^1 + \ldots + w(N-1)V_1^{N-1}] \tag{10.50}$$

$$= e^{j\phi_0}\sum_{}^{N-1} w(n)V_1^n$$

The discrete Fourier transform of the sequence $w(n)$ is defined as

$$W(k) = \sum_{n=0}^{N-1} w(n)e^{-\frac{(j2\pi nk)}{N}} \quad ; \; k = 0, 1, \ldots, N-1 \tag{10.51}$$

The set $\{\sin\beta_k\}$ which makes V_1 equal to the DFT kernel is

$$\sin\beta_k = \frac{\lambda k}{Nd} \quad ; \; k = 0, 1, \ldots, N-1 \tag{10.52}$$

Then by using Eq. (10.52) in Eq. (10.51) yields

$$E(\sin\beta) = e^{j\phi_0}W(k) \tag{10.53}$$

The one-way array pattern is computed as the modulus of Eq. (10.53). It follows that the one-way radiation pattern of a tapered linear array of circular dishes is

$$G(\sin\beta) = G_e\left(\frac{\lambda k}{Nd}\right)|W(k)| \tag{10.54}$$

where G_e is the element pattern. Fig. 10.10 shows the one-way array pattern for a linear array of size $N = 16$, element spacing $d = \lambda/2$, and the elements being circular dishes of diameter $D = d$; no tapering is utilized.

10.7. Array Pattern for Rectangular Planar Array

Fig. 10.11 shows a sketch of an $N \times N$ planar array formed from a rectangular grid. Other planar array configurations may be composed using a circular or hexagonal grid. Planar arrays can be steered electronically in both azimuth and elevation (β, ϕ).

If the array were composed of only one line of elements distributed along the x-axis, then the electric field at a far field observation point defined by (β, ϕ) is

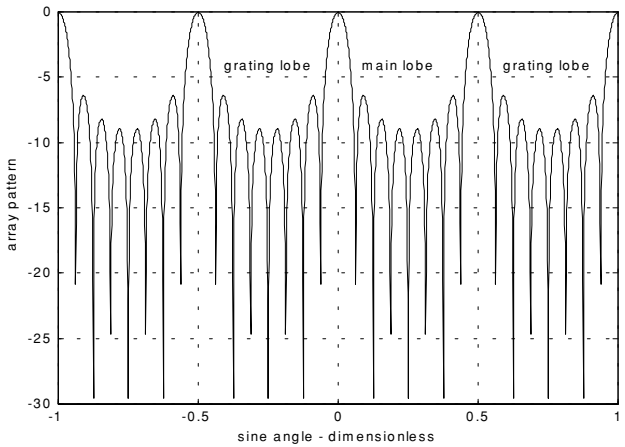

isotropic elements

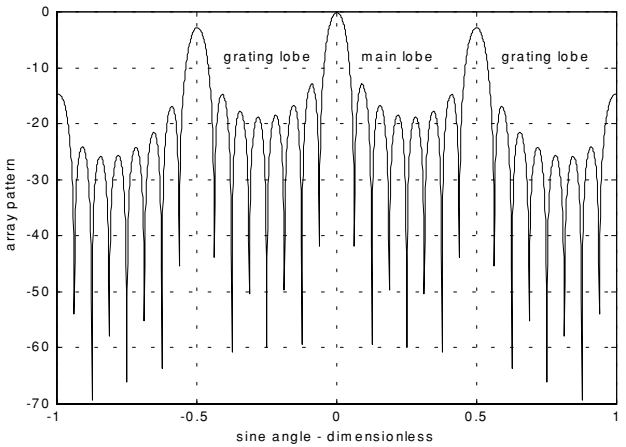

circular dishes

Figure 10.10. Normalized one-way pattern for linear array of size 8, isotropic elements, and circular dishes. This plot can be reproduced using MATLAB program "fig10_10.m" given in Listing 10.4 in Section 10.9.

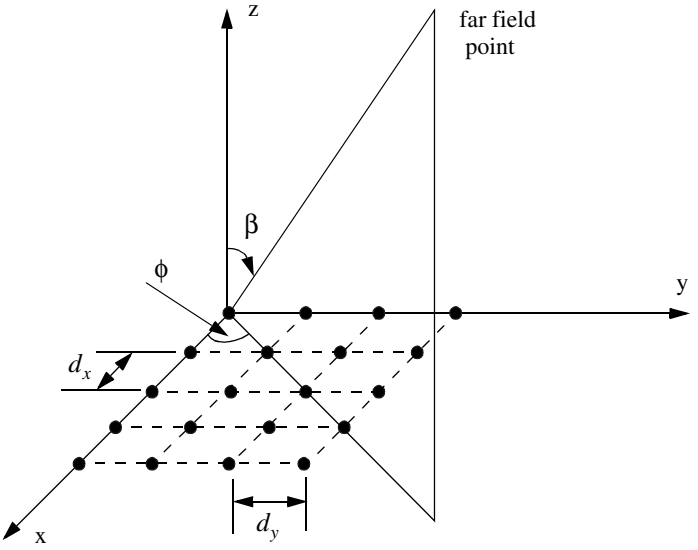

Figure 10.11. Planar array geometry.

$$E_x(\beta, \phi) = \sum_{n=1}^{N} e^{j(n-1)kd_x \sin\beta \cos\phi} \tag{10.55}$$

where d_x is the element spacing along the x-axis. Now, if N of these linear arrays are placed next to one another along the y-axis, a rectangular array would be formed. In this case, the total electric field at a far field observation point is computed as

$$E(\beta, \phi) = E_x(\beta, \phi)E_y(\beta, \phi) = \sum_{m=1}^{N} E_x(\beta, \phi)e^{j(m-1)kd_y \sin\beta \sin\phi} \tag{10.56}$$

where

$$E_y(\beta, \phi) = \sum_{m=1}^{N} e^{j(m-1)kd_y \sin\beta \sin\phi} \tag{10.57}$$

and d_y is the element spacing along the y-axis.

The rectangular array one-way intensity pattern is then equal to the product of the individual patterns. More precisely,

$$E(\beta, \phi) = \left| \frac{\sin((Nkd_x \sin\beta\cos\phi)/2)}{\sin((kd_x \sin\beta\cos\phi)/2)} \right| \left| \frac{\sin((Nkd_y \sin\beta\sin\phi)/2)}{\sin((kd_y \sin\beta\sin\phi)/2)} \right| \quad \textbf{(10.58)}$$

The radiation pattern maxima, nulls, side lobes, and grating lobes in both the x- and y-axis are computed in a similar fashion to the linear array case. Additionally, the same conditions for grating lobes control are applicable.

MATLAB Function "rect_array.m"

The function *"rect_array.m"* computes and plots the linear array radiation pattern, in linear and polar coordinates. This function is given in Listing 10.5 in Section 10.9. The syntax is as follows:

[emod] = rect_array (nex, ney, dx, dy)

where

Symbol	Description	Units	Status
nex	*number of elements in x-direction*	*none*	*input*
ney	*number of elements in y-direction*	*none*	*input*
dx	*element spacing in x-direction (e.g. $d = \lambda$; $d = \lambda/2$)*	*wavelengths*	*input*
dy	*element spacing in y-direction (e.g. $d = \lambda$; $d = \lambda/2$)*	*wavelengths*	*input*
emod	*radiation pattern vector*	*dB*	*output*

Fig. 10.12 shows a three-dimensional radiation pattern for a rectangular array of size 5×5, element spacing $d_x = d_y = \lambda/2$, and isotropic elements.

10.8. Conventional Beamforming

Adaptive arrays are phased array antennas that are normally used to automatically sense and eliminate unwanted signals entering the radar's Field of View (FOV), while enhancing reception about the desired target returns. For this purpose, adaptive arrays utilize a rather complicated combination of hardware and require demanding levels of software implementation. Through feedback networks, a proper set of complex weights is computed and applied to each channel of the array. Adaptive array operation can be considered a special case of beamforming, where the basic idea is to enhance the signal in a certain direction while attenuating noise in all other directions.

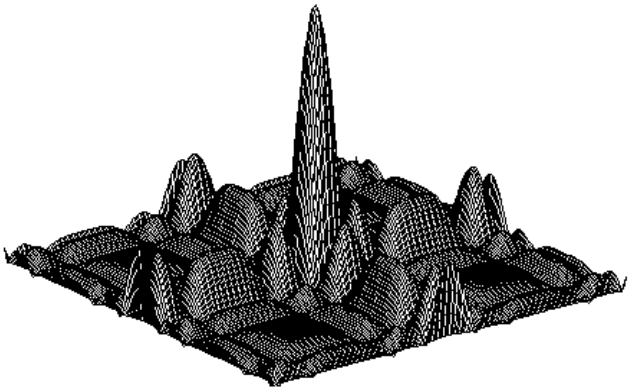

Figure 10.12a. Three-dimensional pattern for a rectangular array of size 5x5, and uniform element spacing.

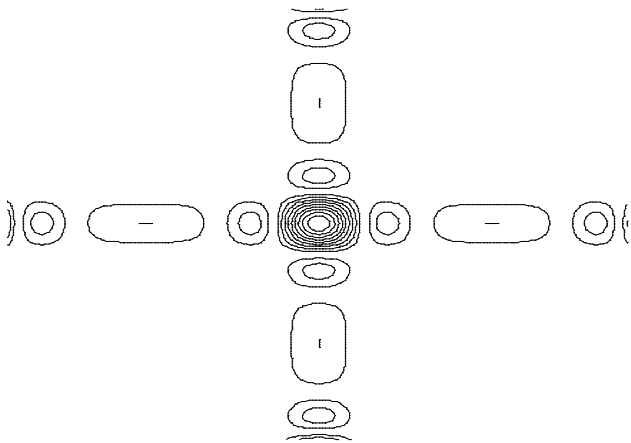

Figure 10.12b. Contour plot corresponding to Fig. 10.12a.

Multiple beams can be formed at the transmitting or receiving modes. Also, it can be carried out at the RF, IF, base band, or digital levels. RF beamforming is the simplest and most common technique. In this case, multiple narrow beams are formed through the use of phase shifters. IF and base band beamforming require complex coherent hardware. However, the system is operated at lower frequencies where tolerance is not as critical. Digital beamforming is more flexible than RF, IF, or base band techniques, but it requires a demanding level of parallel VLSI processing hardware.

A successful implementation of adaptive arrays depends heavily on two factors: first, a proper choice of the reference signal, which is used for comparison against the received target/jammer returns. A good estimate of the reference signal makes the computation of the weights systematic and effective. On the other hand, a bad estimate of the reference signal increases the array's adapting time and limits the system to impractical (non-real time) situations. Second, a fast (real time) computation of the optimum weights is essential. There have been many algorithms developed for this purpose. Nevertheless, they all share a common problem, that is the computation of the inverse of a complex matrix. This drawback has limited the implementation of adaptive arrays to experimental systems or small arrays.

Consider a linear array of N equally spaced elements, and a plane wave incident on the aperture with direction-sine $\sin\beta$, as shown in Fig. 10.13. Conventional beamformers appropriately delay the outputs of each sensor to form a beam steered at angle β. The output of the beamformer is

$$y(t) = \sum_{n=0}^{N-1} x_n(t-\tau_n) \tag{10.59}$$

$$\tau_n = (N-1-n)\frac{d}{c}\sin\beta;\ n = N-1 \tag{10.60}$$

where d is the element spacing and c is the speed of light. Fourier transformation of Eq. (10.59) yields

$$Y(\omega) = \sum_{n=0}^{N-1} X_n(\omega)exp(-j\omega\tau_n) \tag{10.61}$$

which can be written in vector form as

$$\vec{Y} = \vec{a}^{\dagger}\vec{X} \tag{10.62}$$

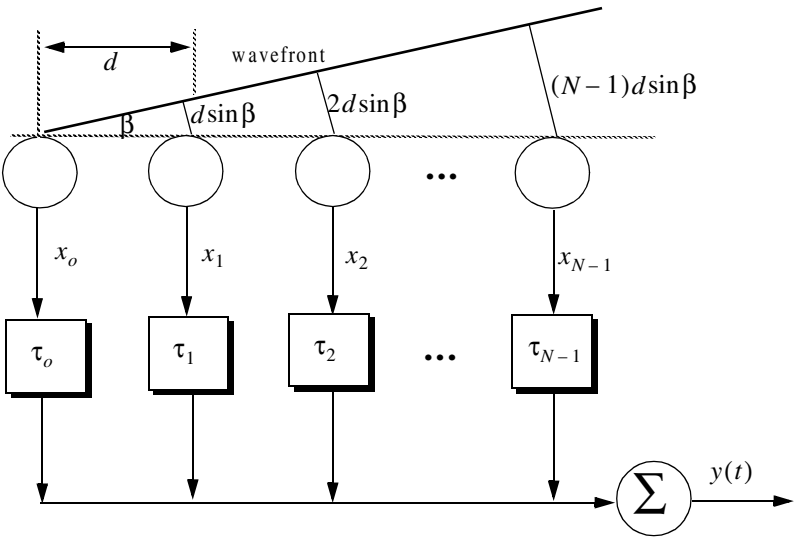

Figure 10.13. A linear array of size N, element spacing d, and an incident plane wave defined by $\sin\beta$.

$$\vec{a}^{\dagger} = [exp(j\omega\tau_o) \;\; exp(j\omega\tau_1)\ldots exp(j\omega\tau_{N-1})] \tag{10.63}$$

$$\vec{X}^{\dagger} = [X_o(\omega) \;\; X_1(\omega)\ldots X_{N-1}(\omega)]^* \tag{10.64}$$

where the superscript † indicates complex conjugate transpose.

Let A_1 be the amplitude of the wavefront defined by $\sin\beta_1$; it follows that the vector $\vec{X}$ is given by

$$\vec{X} = A_1 \vec{s}_{k1}^{\,*} \tag{10.65}$$

where $\vec{s}_{k1}$ is a steering vector, and in general $\vec{s}_k$ is given by

$$\vec{s}_k^{\,\dagger} = [1 \cdot exp(-jk) \cdot \ldots \cdot exp(-j(N-1)k)]; \;\; k = \frac{2\pi d}{\lambda} \cdot \sin\beta \tag{10.66}$$

Ignoring the phase term $exp(-j(N-1)k)$, we can write Eq. (10.63) as

$$\vec{a} = \vec{s}_k \tag{10.67}$$

and the beamformer output will be

$$\vec{Y} = \vec{a}^{\dagger}\vec{X} = A_1 \vec{s}_{k1}^{\dagger} \vec{s}_k \tag{10.68}$$

The array pattern of the beam steered at k_1 is computed as the expected value of $\vec{Y}$. In other words,

$$S(k) = E\left[\vec{Y}\vec{Y}^{\dagger}\right] = P_1 \vec{s}_k^{\dagger} \Re \vec{s}_k \tag{10.69}$$

where $P_1 = E[|A_1|^2]$ and $\Re$ is the correlation matrix. If $\vec{X} = A_1 \vec{s}_{k1}^{*}$, then the power spectrum is

$$S(k) = P_1 \vec{s}_k^{\dagger} \vec{s}_{k1} \vec{s}_{k1}^{\dagger} \vec{s}_k \tag{10.70}$$

Consider L incident plane waves with directions of arrival defined by

$$k_i = \frac{2\pi d}{\lambda} \sin\beta_i; \; i = 1, L \tag{10.71}$$

The n^{th} sample at the output of the m^{th} sensor is

$$y_m(n) = \upsilon(n) + \sum_{i=1}^{L} A_i(n) exp(-jmk_i); \; m = 0, N-1 \tag{10.72}$$

where $A_i(n)$ is the amplitude of the i^{th} plane wave, and $\upsilon(n)$ is white, zero-mean noise with variance σ_υ^2, and it is assumed to be uncorrelated with the signals. Eq. (10.72) can be written in vector notation as

$$\vec{y}(n) = \vec{\upsilon}(n) + \sum_{i=1}^{L} A_i(n) \vec{s}_{ki}^{*} \tag{10.73}$$

A set of L steering vectors is needed to simultaneously form L beams. Define the steering matrix $\aleph$ as

$$\aleph = \left[\vec{s}_{k1} \; \vec{s}_{k2} \; \ldots \; \vec{s}_{kL}\right] \tag{10.74}$$

Then the autocorrelation matrix of the field measured by the array is

$$\Re = E\{\vec{y}_m(n)\vec{y}_m^{\dagger}(n)\} = \sigma_\upsilon^2 \boldsymbol{I} + \aleph \boldsymbol{C} \aleph^{\dagger} \tag{10.75}$$

where $\boldsymbol{C} = dig\left[P_1 \; P_2 \; \ldots \; P_L\right]$, and $\boldsymbol{I}$ is the identity matrix.

The array pattern can now be computed using standard spectral estimators. For example, using the Bartlett beamformer yields

$$\widehat{S}(k) = \vec{s}_k^{\,\dagger} \Re \vec{s}_k \tag{10.76}$$

The spectrum defined by Eq. (10.76) generates spectral peaks at angles β_i for each wavefront defined by k_i. Assuming the i^{th} wavefront, then the SNR is

$$SNR = N\left(\frac{P_i}{\sigma_\upsilon^2}\right) \tag{10.77}$$

10.9. MATLAB Programs and Functions

This section contains listings of all MATLAB programs and functions used in this chapter. Users are encouraged to rerun these codes with different inputs in order to enhance their understanding of the theory.

Listing 10.1. MATLAB Function "circ_aperture.m"

```
function [emod] = circ_aperture (lambda, d)
eps = 0.000001;
k = 2. * pi / lambda;
r = d /2.;
beta = -pi:pi/200.:pi;
sinbet = sin(beta);
var = k * r .* sinbet; %2.0 * pi * (-2:0.001:2);
pattern = (2. * r^2)  .* besselj(1,var) ./ (var);
maxval = max(abs(pattern));
pattern = pattern ./ maxval;
emod = 20. * log10(abs(pattern));
figure(1)
plot(var,emod,'k')
grid;
xlabel('kr*sin(angle)')
ylabel('Normalized radiation pattern');
minval = fix(min(var));
maxval = fix(max(var));
var3d = minval:.5:maxval;
[X,Y] = meshgrid(var3d,var3d);
U = sqrt(X.^2 + Y.^2) + eps;
z = 2. * besselj(1,U) ./ U;
figure (2)
mesh(abs(z))
axis off
figure(3)
```

```
polar(beta,pattern,'k')
```

Listing 10.2. MATLAB Program "fig10_5.m"

```
clear all
eps = 0.0000001;
beta = -pi : pi / 10791 : pi;
var = sin(beta);
%var = -1.:0.00101:1.;
num = sin((8. * 2. * pi * 0.5) .* var);
if(abs(num) <= eps)
  num = eps;
end
den = sin((2. * pi * 0.5) .* var);
if(abs(den) <= eps)
  den = eps;
end
pattern = num ./ den;
maxval = max(abs(pattern));
pattern = abs(pattern ./ maxval);
i=0;
mod=abs(pattern);
figure (1)
plot(var,mod,'k');
grid;
xlabel('sine angle - dimensionless')
ylabel('array pattern')
figure(2)
polar(beta,abs(pattern),'k')
```

Listing 10.3. MATLAB Function "linear_array.m"

```
function [emod] = linear_array (ne, d, beta0)
eps = 0.0000001;
beta = 0 : pi / 10791 : 2.*pi;
beta0 = beta0 * pi /180.;
var = sin(beta) - sin(beta0);
num = sin((0.5 * ne * 2. * pi * d) .* var);
if(abs(num) <= eps)
  num = eps;
end
den = sin((0.5 * 2. * pi * d) .* var);
if(abs(den) <= eps)
  den = eps;
```

```
end
pattern = num ./ den;
maxval = max(abs(pattern));
pattern = abs(pattern ./ maxval);
emod=abs(pattern);
figure(1)
plot(sin(beta),emod,'k');
grid;
xlabel('sine angle - dimensionless')
ylabel('array pattern')
figure(2)
polar(beta,abs(pattern),'k')
```

Listing 10.4. MATLAB Program "fig10_10.m"

```
pattern = num ./ den;
maxval = max(abs(pattern));
pattern = abs(pattern ./ maxval);
i = 0.;
for ii=-1:0.001:1
i = i + 1.;
if(pattern(i) < 0.001)
  pattern(i) = 0.0011;
end
end
mod = abs(pattern);
subplot(2,1,1);
plot(var,20.0 .* log10(mod),'k');
grid;
xlabel('sine angle - dimensionless')
ylabel('array pattern')
gtext('main lobe');
gtext('grating lobe');
gtext('grating lobe');
var1 = 1. * pi .* var;
patternj = 2. .* besselj(1,var1) ./ var1;
mod = abs(pattern) .* abs(patternj);
subplot(2,1,2);
plot(var,20.0 .* log10(mod),'k');
grid;
xlabel('sine angle - dimensionless')
ylabel('array pattern')
gtext('main lobe');
gtext('grating lobe');
```

```
gtext('grating lobe');
```

Listing 10.5. MATLAB Function "rect_array.m"

```
function emod = rect_array(nex,ney,dx,dy)
eps = 0.0000001;
factx = nex * 2. * pi * 0.5 * dx ;
facty = ney * 2. * pi * 0.5 * dy ;
ii = 0.;
delpi = pi / 10.;
for betax = 0.+delpi : pi/101 : 2.*pi-delpi
  ii = ii + 1.;
  numx = sin(factx * sin(betax));
    if(abs(numx) <= eps)
      numx = eps;
    end
    denx = sin(factx * sin(betax) / nex);
    if(abs(denx) <= eps)
      denx = eps;
    end
  jj = 0.;
  for betay = 0.+delpi : pi/101 : 2.*pi-delpi
    jj = jj + 1.;
    numy = sin(facty * sin(betay));
    if(abs(numy) <= eps)
      numy = eps;
    end
    deny = sin(facty * sin(betay) / ney);
    if(abs(deny) <= eps)
      deny = eps;
    end
    emod(ii,jj) = abs(numx / denx) * abs(numy / deny);
  end
end
maxval = max(max(emod));
emod = emod ./ maxval;
figure(1)
mesh(emod)
figure(2)
contour(emod)
```

Problems

10.1. Consider an antenna whose diameter is $d = 3m$. What is the far field requirement for an X-band or an L-band radar that is using this antenna?

10.2. Consider an antenna with electric field intensity in the *xy*-plane $E(\varsigma)$. This electric field is generated by a current distribution $D(y)$ in the *yz*-plane. The electric field intensity is computed using the integral

$$E(\varsigma) = \int_{-r/2}^{r/2} D(y)\exp\left(2\pi j\frac{y}{\lambda}\sin\varsigma\right)dy$$

where λ is the wavelength and r is the aperture. (a) Write an expression for $E(\varsigma)$ when $D(Y) = d_0$ (a constant). (b) Write an expression for the normalized power radiation pattern and plot it in dB.

10.3. A linear phased array consists of 50 elements with $\lambda/2$ element spacing. (a) Compute the 3dB beam width when the main beam steering angle is $0°$ and $45°$. (b) Compute the electronic phase difference for any two consecutive elements for steering angle $60°$.

10.4. A linear phased array antenna consists of eight elements spaced with $d = \lambda$ element spacing. (a) Give an expression for the antenna gain pattern (assume no steering and uniform aperture weighting). (b) Sketch the gain pattern versus sine of the off boresight angle β. What problems do you see is using $d = \lambda$ rather than $d = \lambda/2$?

10.5. In Section 10.6 we showed how a DFT can be used to compute the radiation pattern of a linear phased array. Consider a linear of 64 elements at half wavelength spacing, where an FFT of size 512 is used to compute the pattern. What are the FFT bins that correspond to steering angles $\beta = 30°, 45°$?

Chapter 11 *Target Tracking*

Part I: Single Target Tracking

Tracking radar systems are used to measure the target's relative position in range, azimuth angle, elevation angle, and velocity. Then, by using and keeping track of these measured parameters the radar can predict their future values. Target tracking is important to military radars as well as to most civilian radars. In military radars, tracking is responsible for fire control and missile guidance; in fact, missile guidance is almost impossible without proper target tracking. Commercial radar systems, such as civilian airport traffic control radars, may utilize tracking as a means of controlling incoming and departing airplanes.

Tracking techniques can be divided into range/velocity tracking and angle tracking. It is also customary to distinguish between continuous single-target tracking radars and multi-target track-while-scan (TWS) radars. Tracking radars utilize pencil beam (very narrow) antenna patterns. It is for this reason that a separate search radar is needed to facilitate target acquisition by the tracker. Still, the tracking radar has to search the volume where the target's presence is suspected. For this purpose, tracking radars use special search patterns, such as helical, T.V. raster, cluster, and spiral patterns, to name a few.

11.1. Angle Tracking

Angle tracking is concerned with generating continuous measurements of the target's angular position in the azimuth and elevation coordinates. The accuracy of early generation angle tracking radars depended heavily on the size of the pencil beam employed. Most modern radar systems achieve very fine angular measurements by utilizing monopulse tracking techniques.

Tracking radars use the angular deviation from the antenna main axis of the target within the beam to generate an error signal. This deviation is normally measured from the antenna's main axis. The resultant error signal describes how much the target has deviated from the beam main axis. Then, the beam position is continuously changed in an attempt to produce a zero error signal. If the radar beam is normal to the target (maximum gain), then the target angular position would be the same as that of the beam. In practice, this is rarely the case.

In order to be able to quickly achieve changing the beam position, the error signal needs to be a linear function of the deviation angle. It can be shown that this condition requires the beam's axis to be squinted by some angle (squint angle) off the antenna's main axis.

11.1.1. Sequential Lobing

Sequential lobing is one of the first tracking techniques that was utilized by the early generation of radar systems. Sequential lobing is often referred to as lobe switching or sequential switching. It has a tracking accuracy that is limited by the pencil beam width used and by the noise caused by either mechanical or electronic switching mechanisms. However, it is very simple to implement. The pencil beam used in sequential lobing must be symmetrical (equal azimuth and elevation beam widths).

Tracking is achieved (in one coordinate) by continuously switching the pencil beam between two pre-determined symmetrical positions around the antenna's Line of Sight (LOS) axis. Hence, the name sequential lobing is adopted. The LOS is called the radar tracking axis, as illustrated in Fig. 11.1.

As the beam is switched between the two positions, the radar measures the returned signal levels. The difference between the two measured signal levels is used to compute the angular error signal. For example, when the target is tracked on the tracking axis, as the case in Fig. 11.1a, the voltage difference is zero and, hence, is also the error signal. However, when the target is off the tracking axis, as in Fig. 11.1b, a nonzero error signal is produced. The sign of the voltage difference determines the direction in which the antenna must be moved. Keep in mind, the goal here is to make the voltage difference be equal to zero.

In order to obtain the angular error in the orthogonal coordinate, two more switching positions are required for that coordinate. Thus, tracking in two coordinates can be accomplished by using a cluster of four antennas (two for each coordinate) or by a cluster of five antennas. In the latter case, the middle antenna is used to transmit, while the other four are used to receive.

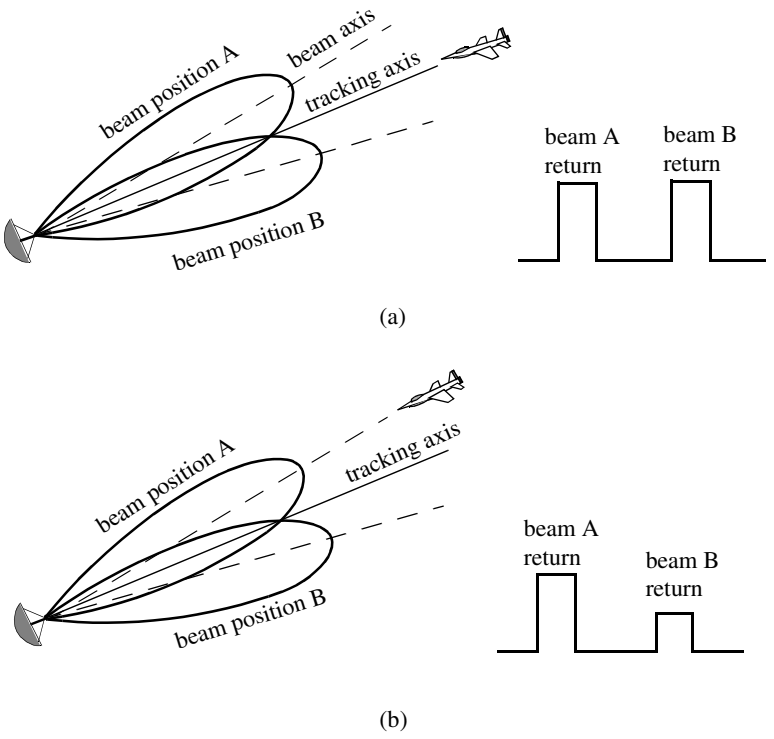

Figure 11.1. Sequential lobing. (a) Target is located on track axis. (b) Target is off track axis.

11.1.2. Conical Scan

Conical scan is a logical extension of sequential lobing where, in this case, the antenna is continuously rotated at an offset angle, or has a feed that is rotated about the antenna's main axis. Fig. 11.2 shows a typical conical scan beam. The beam scan frequency, in radians per second, is denoted as ω_s. The angle between the antenna's LOS and the rotation axis is the squint angle φ. The antenna's beam position is continuously changed so that the target will always be on the tracking axis.

Fig. 11.3 shows a simplified conical scan radar system. The envelope detector is used to extract the return signal amplitude and the Automatic Gain Control (AGC) tries to hold the receiver output to a constant value. Since the AGC operates on large time constants, it can hold the average signal level constant and still preserve the signal rapid scan variation. It follows that the tracking

error signals (azimuth and elevation) are functions of the target's RCS; they are functions of its angular position with the main beam axis.

In order to illustrate how conical scan tracking is achieved, we will first consider the case shown in Fig. 11.4. In this case, as the antenna rotates around the tracking axis all target returns have the same amplitude (zero error signal). Thus, no further action is required.

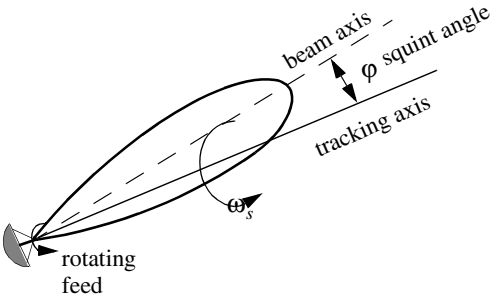

Figure 11.2. Conical scan beam.

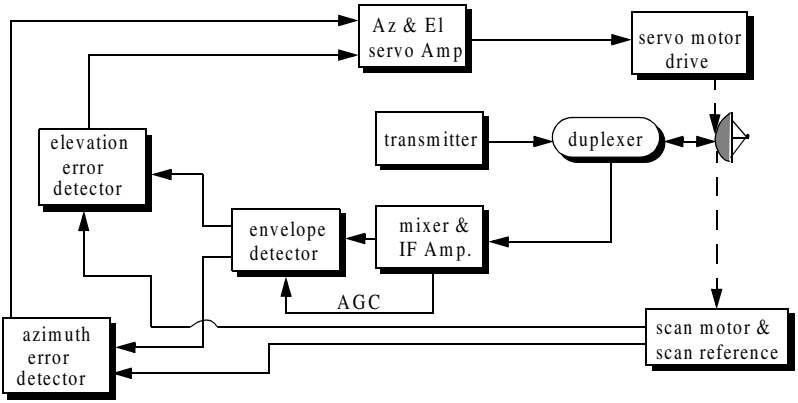

Figure 11.3. Simplified conical scan radar system.

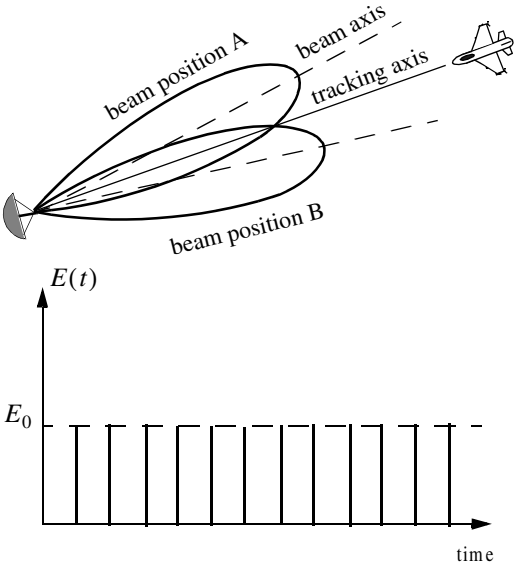

Figure 11.4. Error signal produced when the target is on the tracking axis for conical scan.

Next, consider the case depicted by Fig. 11.5. Here, when the beam is at position B, returns from the target will have maximum amplitude. And when the antenna is at position A, returns from the target have minimum amplitude. Between those two positions, the amplitude of the target returns will vary between the maximum value at position B, and the minimum value at position A. In other words, Amplitude Modulation (AM) exists on top of the returned signal. This AM envelope corresponds to the relative position of the target within the beam. Thus, the extracted AM envelope can be used to derive a servo-control system in order to position the target on the tracking axis.

Now, let us derive the error signal expression that is used to drive the servo-control system. Consider the top view of the beam axis location shown in Fig. 11.6. Assume that $t = 0$ is the starting beam position. The locations for maximum and minimum target returns are also identified. The quantity ε defines the distance between the target location and the antenna's tracking axis. It follows that the azimuth and elevation errors are, respectively, given by

$$\varepsilon_a = \varepsilon \sin\varphi \tag{11.1}$$

$$\varepsilon_e = \varepsilon \cos\varphi \tag{11.2}$$

These are the error signals that the radar uses to align the tracking axis on the target.

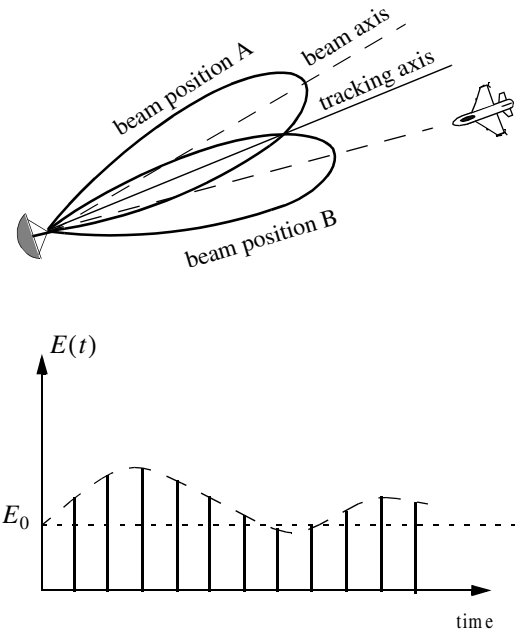

Figure 11.5. Error signal produced when the target is off the tracking axis for conical scan.

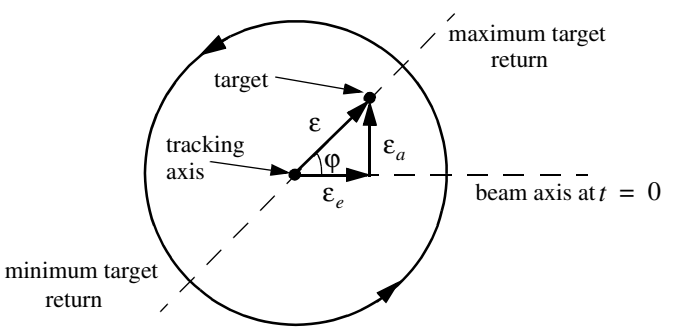

Figure 11.6. Top view of beam axis for a complete scan.

The AM signal $E(t)$ can then be written as

$$E(t) = E_0 \cos(\omega_s t - \varphi) = E_0 \varepsilon_e \cos\omega_s t + E_0 \varepsilon_a \sin\omega_s t \quad (11.3)$$

where E_0 is a constant called the error slope, ω_s is the scan frequency in radians per seconds, and φ is the angle already defined. The scan reference is the signal that the radar generates to keep track of the antenna's position around a complete path (scan). The elevation error signal is obtained by mixing the signal $E(t)$ with $\cos\omega_s t$ (the reference signal) followed by low pass filtering. More precisely,

$$E_e(t) = E_0 \cos(\omega_s t - \varphi)\cos\omega_s t = -\frac{1}{2}E_0 \cos\varphi + \frac{1}{2}\cos(2\omega_s t - \varphi) \quad (11.4)$$

and after low pass filtering we get

$$E_e(t) = -\frac{1}{2}E_0 \cos\varphi \quad (11.5)$$

Negative elevation error drives the antenna beam downward, while positive elevation error drives the antenna beam upward. Similarly, the azimuth error signal is obtained by multiplying $E(t)$ by $\sin\omega_s t$ followed by low pass filtering. It follows that

$$E_a(t) = \frac{1}{2}E_0 \sin\varphi \quad (11.6)$$

The antenna scan rate is limited by the scanning mechanism (mechanical or electronic), where electronic scanning is much faster and more accurate than mechanical scan. In either case, the radar needs at least four target returns to be able to determine the target azimuth and elevation coordinates (two returns per coordinate). Therefore, the maximum conical scan rate is equal to one fourth of the PRF. Rates as high as 30 scans per seconds are commonly used.

The conical scan squint angle needs to be large enough so that a good error signal can be measured. However, due to the squint angle, the antenna gain in the direction of the tracking axis is less than maximum. Thus, when the target is in track (located on the tracking axis), the SNR suffers a loss equal to the drop in the antenna gain. This loss is known as the squint or crossover loss. The squint angle is normally chosen such that the two-way (transmit and receive) crossover loss is less than a few decibels.

11.2. Amplitude Comparison Monopulse

Amplitude comparison monopulse tracking is similar to lobing in the sense that four squinted beams are required to measure the target's angular position. The difference is that the four beams are generated simultaneously rather than

sequentially. For this purpose, a special antenna feed is utilized such that the four beams are produced using a single pulse, hence the name "monopulse." Additionally, monopulse tracking is more accurate and is not susceptible to lobing anomalies, such as AM jamming and gain inversion ECM. Finally, in sequential and conical lobing variations in the radar echoes degrade the tracking accuracy; however, this is not a problem for monopulse techniques since a single pulse is used to produce the error signals. Monopulse tracking radars can employ both antenna reflectors as well as phased array antennas.

Fig. 11.7 show a typical monopulse antenna pattern. The four beams A, B, C, and D represent the four conical scan beam positions. Four feeds, mainly horns, are used to produce the monopulse antenna pattern. Amplitude monopulse processing requires that the four signals have the same phase and different amplitudes.

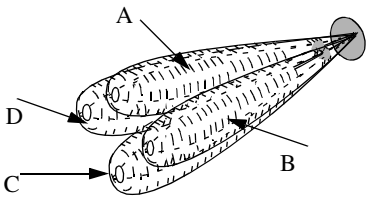

Figure 11.7. Monopulse antenna pattern.

A good way to explain the concept of amplitude monopulse technique is to represent the target echo signal by a circle centered at the antenna's tracking axis, as illustrated by Fig. 11.8a, where the four quadrants represent the four beams. In this case, the four horns receive an equal amount of energy, which indicates that the target is located on the antenna's tracking axis. However, when the target is off the tracking axis (Figs. 11.8b-d), an unbalance of energy occurs in the different beams. This unbalance of energy is used to generate an error signal that drives the servo-control system. Monopulse processing consists of computing a sum Σ and two difference Δ (azimuth and elevation) antenna patterns. Then by dividing a Δ channel voltage by the Σ channel voltage, the angle of the signal can be determined.

The radar continuously compares the amplitudes and phases of all beam returns to sense the amount of target displacement off the tracking axis. It is critical that the phases of the four signals be constant in both transmit and receive modes. For this purpose, either digital networks or microwave comparator circuitry are utilized. Fig. 11.9 shows a block diagram for a typical microwave comparator, where the three receiver channels are declared as the sum channel, elevation angle difference channel, and azimuth angle difference channel.

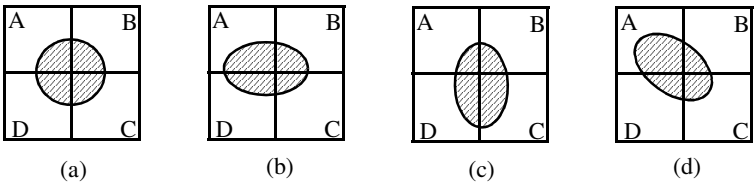

Figure 11.8. Illustration of monopulse concept. (a) Target is on the tracking axis. (b) - (d) Target is off the tracking axis.

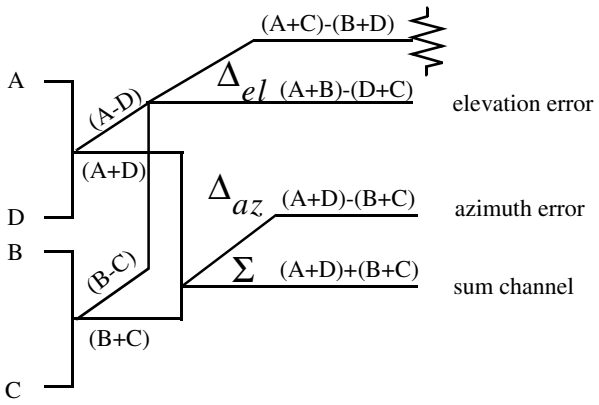

Figure 11.9. Monopulse comparator.

To generate the elevation difference beam, one can use the beam difference (A−D) or (B−C). However, by first forming the sum patterns (A+B) and (D+C) and then computing the difference (A+B)−(D+C), we achieve a stronger elevation difference signal, Δ_{el}. Similarly, by first forming the sum patterns (A+D) and (B+C) and then computing the difference (A+D)−(B+C), a stronger azimuth difference signal, Δ_{az}, is produced.

A simplified monopulse radar block diagram is shown in Fig. 11.10. The sum channel is used for both transmit and receive. In the receiving mode the sum channel provides the phase reference for the other two difference channels. Range measurements can also be obtained from the sum channel. In order to illustrate how the sum and difference antenna patterns are formed, we will assume a $\sin\varphi/\varphi$ single element antenna pattern and squint angle φ_0. The sum signal in one coordinate (azimuth or elevation) is then given by

$$\Sigma(\varphi) = \frac{\sin(\varphi - \varphi_0)}{(\varphi - \varphi_0)} + \frac{\sin(\varphi + \varphi_0)}{(\varphi + \varphi_0)} \qquad (11.7)$$

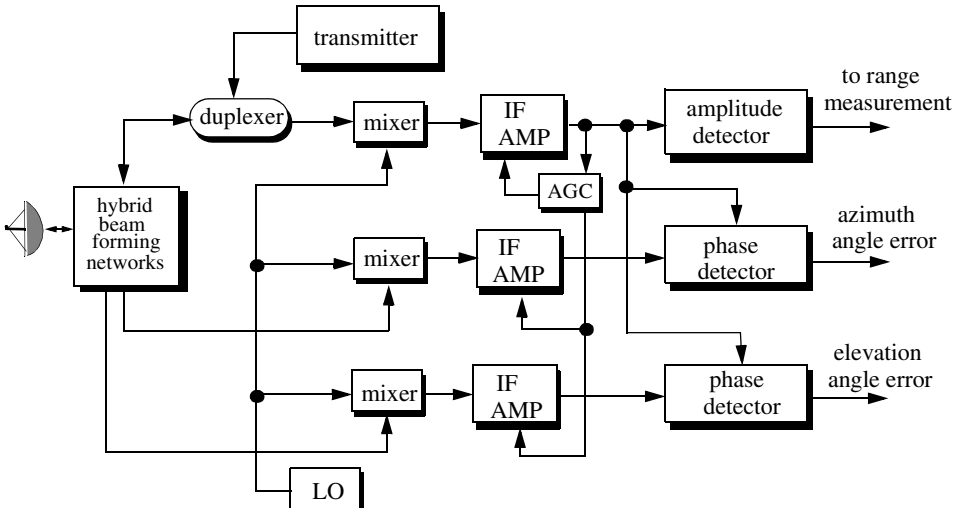

Figure 11.10. Simplified amplitude comparison monopulse radar block diagram.

and a difference signal in the same coordinate is

$$\Delta(\varphi) = \frac{\sin(\varphi - \varphi_0)}{(\varphi - \varphi_0)} - \frac{\sin(\varphi + \varphi_0)}{(\varphi + \varphi_0)} \tag{11.8}$$

MATLAB Function "mono_pulse.m"

The function "mono_pulse.m" implements Eqs. (11.7) and (11.8). Its output includes plots of the sum and difference antenna patterns as well as the difference-to-sum ratio. It is given in Listing 11.1 in Section 11.10. The syntax is as follows:

mono_pulse (phi0)

where *phi0* is the squint angle in radians.

Fig. 11.11 (a-c) shows the corresponding plots for the sum and difference patterns for $\varphi_0 = 0.15$ radians. Fig. 11.12 (a-c) is similar to Fig. 11.11, except in this case $\varphi_0 = 0.75$ radians. Clearly, the sum and difference patterns depend heavily on the squint angle. Using a relatively small squint angle produces a better sum pattern than that resulting from a larger angle. Additionally, the difference pattern slope is steeper for the small squint angle.

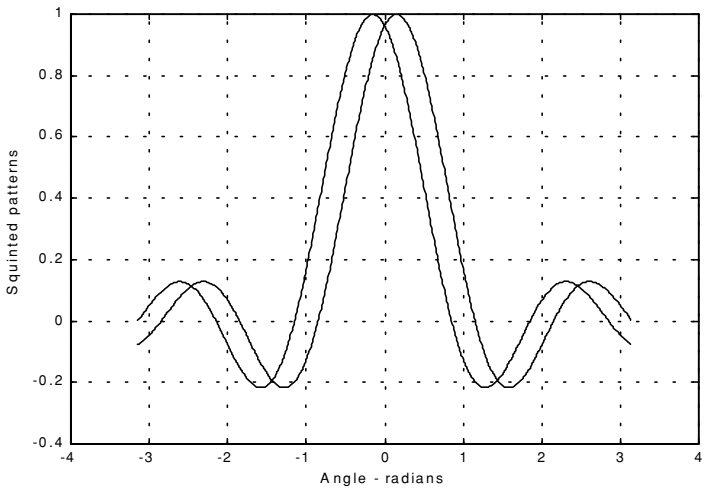

Figure 11.11a. Two squinted patterns. Squint angle is $\varphi_0 = 0.15$ radians.

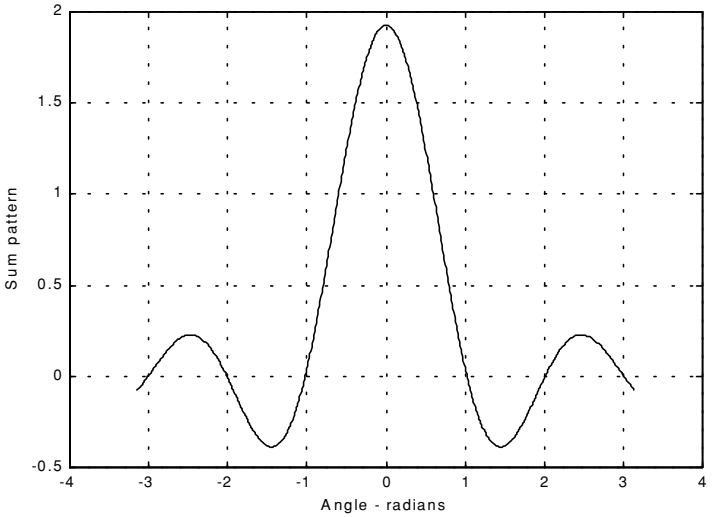

Figure 11.11b. Sum pattern corresponding to Fig. 11.11a.

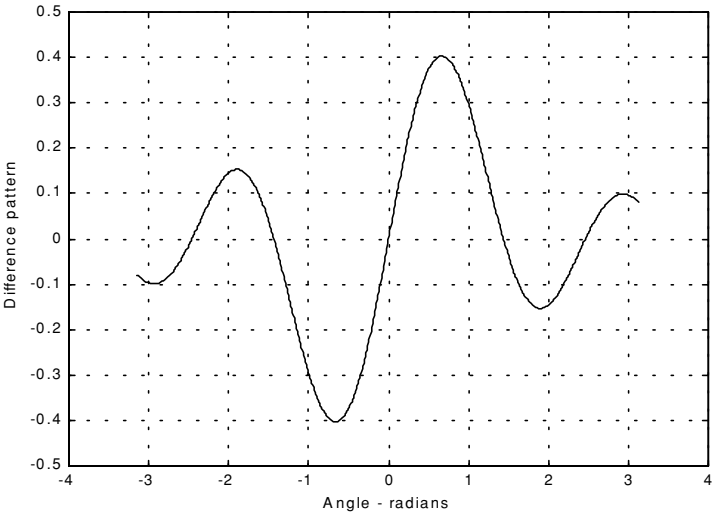

Figure 11.11c. Difference pattern corresponding to Fig. 11.11a.

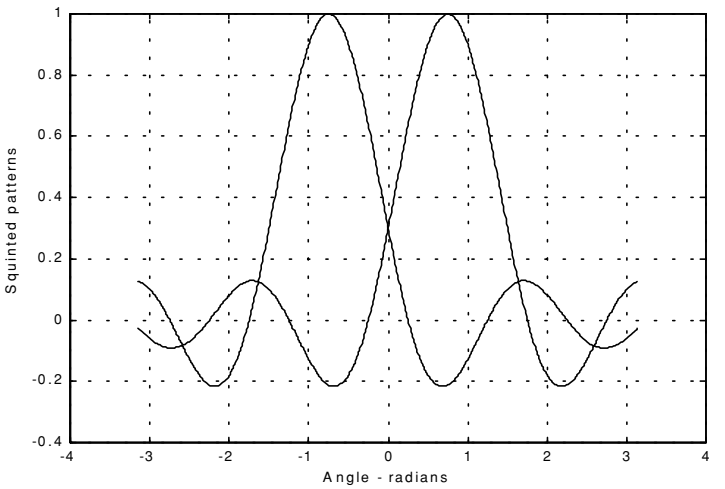

Figure 11.12a. Two squinted patterns. Squint angle is $\varphi_0 = 0.75$ radians.

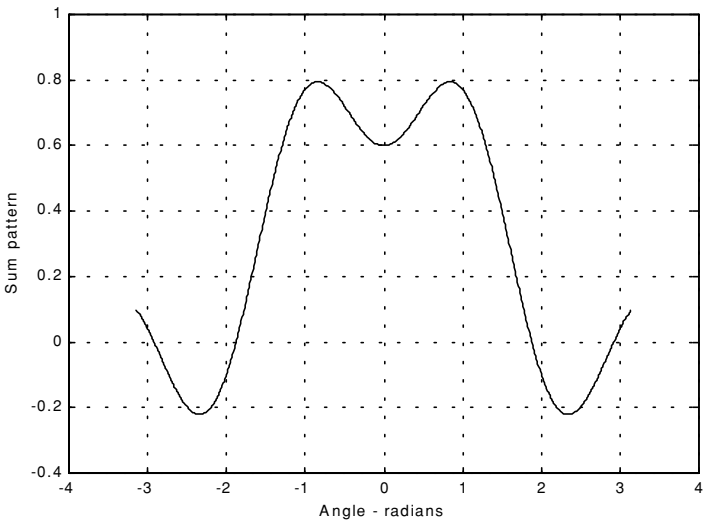

Figure 11.12b. Sum pattern corresponding to Fig. 11.12a.

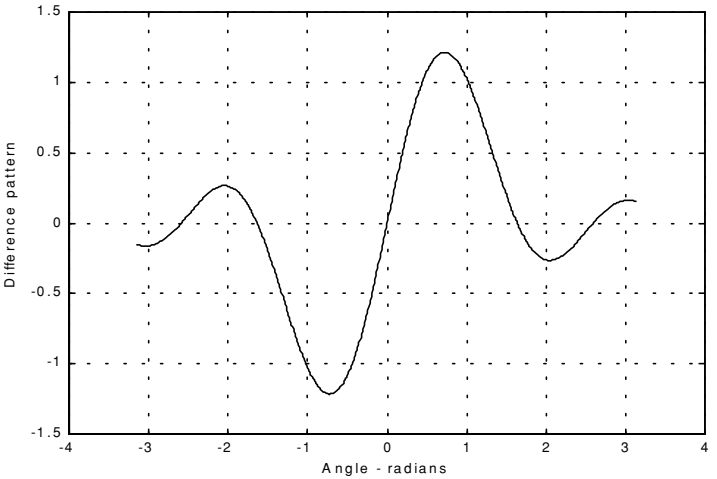

Figure 11.12c. Difference pattern corresponding to Fig. 11.12a.

The difference channels give us an indication of whether the target is on or off the tracking axis. However, this signal amplitude depends not only on the target angular position, but also on the target's range and RCS. For this reason the ratio Δ/Σ (delta over sum) can be used to accurately estimate the error angle that only depends on the target's angular position.

Let us now address how the error signals are computed. First, consider the azimuth error signal. Define the signals S_1 and S_2 as

$$S_1 = A + D \tag{11.9}$$

$$S_2 = B + C \tag{11.10}$$

The sum signal is $\Sigma = S_1 + S_2$, and the azimuth difference signal is $\Delta_{az} = S_1 - S_2$. If $S_1 \geq S_2$, then both channels have the same phase $0°$ (since the sum channel is used for phase reference). Alternatively, if $S_1 < S_2$, then the two channels are $180°$ out of phase. Similar analysis can be done for the elevation channel, where in this case $S_1 = A + B$ and $S_2 = D + C$. Thus, the error signal output is

$$\varepsilon_\varphi = \frac{|\Delta|}{|\Sigma|} \cos\xi \tag{11.11}$$

where ξ is the phase angle between the sum and difference channels and it is equal to $0°$ or $180°$. More precisely, if $\xi = 0$, then the target is on the tracking axis; otherwise it is off the tracking axis. Fig. 11.13 (a,b) shows a plot for the ratio Δ/Σ for the monopulse radar whose sum and difference patterns are in Figs. 11.11 and 11.12.

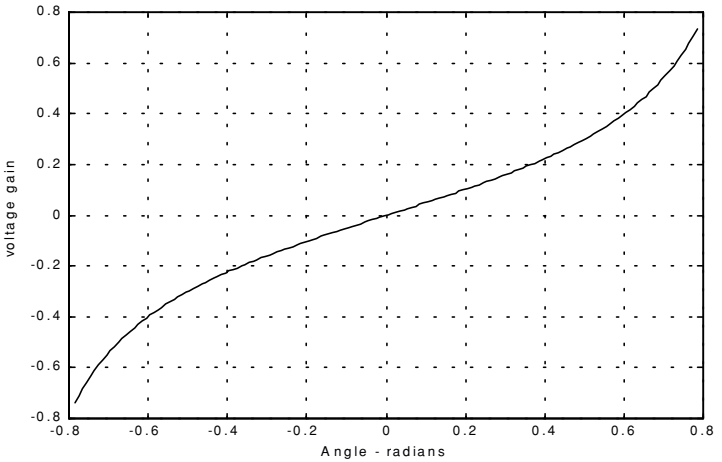

Figure 11.13a. Difference-to-sum ratio corresponding to Fig. 11.11a.

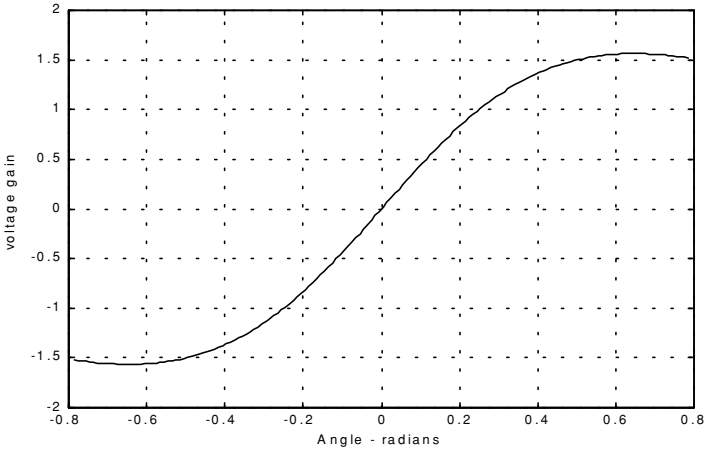

Figure 11.13b. Difference-to-sum ratio corresponding to Fig. 11.12a.

11.3. Phase Comparison Monopulse

Phase comparison monopulse is similar to amplitude comparison monopulse in the sense that the target angular coordinates are extracted from one sum and two difference channels. The main difference is that the four signals produced in amplitude comparison monopulse will have similar phases but different amplitudes; however, in phase comparison monopulse the signals have the same amplitude and different phases. Phase comparison monopulse tracking radars use a minimum of a two-element array antenna for each coordinate (azimuth and elevation), as illustrated in Fig. 11.14. A phase error signal (for each coordinate) is computed from the phase difference between the signals generated in the antenna elements.

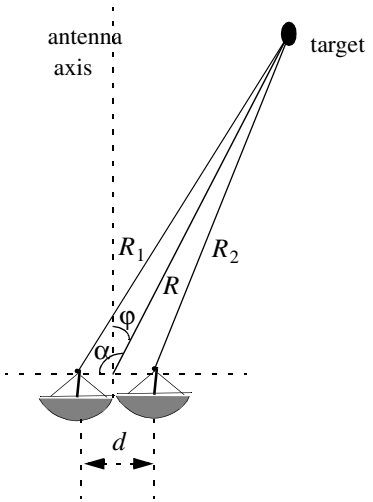

Figure 11.14. Single coordinate phase comparison monopulse antenna.

Consider Fig. 11.14; since the angle α is equal to $\varphi + \pi/2$, it follows that

$$R_1^2 = R^2 + \left(\frac{d}{2}\right)^2 - 2\frac{d}{2}R\cos\left(\varphi + \frac{\pi}{2}\right) \qquad (11.12)$$
$$= R^2 + \frac{d^2}{4} - dR\sin\varphi$$

and since $d \ll R$ we can use the binomial series expansion to get

$$R_1 \approx R\left(1 + \frac{d}{2R}\sin\varphi\right) \tag{11.13}$$

Similarly,

$$R_2 \approx R\left(1 - \frac{d}{2R}\sin\varphi\right) \tag{11.14}$$

The phase difference between the two elements is then given by

$$\phi = \frac{2\pi}{\lambda}(R_1 - R_2) = \frac{2\pi}{\lambda} d\sin\varphi \tag{11.15}$$

where λ is the wavelength. The phase difference ϕ is used to determine the angular target location. Note that if $\phi = 0$, then the target would be on the antenna's main axis. The problem with this phase comparison monopulse technique is that it is quite difficult to maintain a stable measurement of the off boresight angle φ, which causes serious performance degradation. This problem can be overcome by implementing a phase comparison monopulse system as illustrated in Fig. 11.15.

The (single coordinate) sum and difference signals are, respectively, given by

$$\Sigma(\varphi) = S_1 + S_2 \tag{11.16}$$

$$\Delta(\varphi) = S_1 - S_2 \tag{11.17}$$

where the S_1 and S_2 are the signals in the two elements. Now, since S_1 and S_2 have similar amplitude and are different in phase by ϕ, we can write

$$S_1 = S_2 e^{-j\phi} \tag{11.18}$$

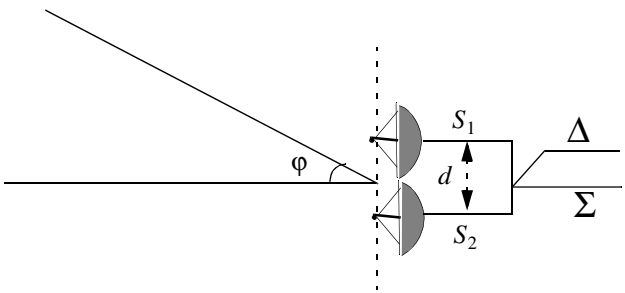

Figure 11.15. Single coordinate phase monopulse antenna, with sum and difference channels.

It follows that

$$\Delta(\varphi) = S_2(1 - e^{-j\phi}) \tag{11.19}$$

$$\Sigma(\varphi) = S_2(1 + e^{-j\phi}) \tag{11.20}$$

The phase error signal is computed from the ratio Δ/Σ. More precisely,

$$\frac{\Delta}{\Sigma} = \frac{1 - e^{-j\phi}}{1 + e^{-j\phi}} = j\tan\left(\frac{\phi}{2}\right) \tag{11.21}$$

which is purely imaginary. The modulus of the error signal is then given by

$$\frac{|\Delta|}{|\Sigma|} = \tan\left(\frac{\phi}{2}\right) \tag{11.22}$$

This kind of phase comparison monopulse tracker is often called the half-angle tracker.

11.4. Range Tracking

Target range is measured by estimating the round-trip delay of the transmitted pulses. The process of continuously estimating the range of a moving target is known as range tracking. Since the range to a moving target is changing with time, the range tracker must be constantly adjusted to keep the target locked in range. This can be accomplished using a split gate system, where two range gates (early and late) are utilized. The concept of split gate tracking is illustrated in Fig. 11.16, where a sketch of a typical pulsed radar echo is shown in the figure. The early gate opens at the anticipated starting time of the radar echo and lasts for half its duration. The late gate opens at the center and closes at the end of the echo signal. For this purpose, good estimates of the echo duration and the pulse centertime must be reported to the range tracker so that the early and late gates can be placed properly at the start and center times of the expected echo. This reporting process is widely known as the "designation process."

The early gate produces positive voltage output while the late gate produces negative voltage output. The outputs of the early and late gates are subtracted, and the difference signal is fed into an integrator to generate an error signal. If both gates are placed properly in time, the integrator output will be equal to zero. Alternatively, when the gates are not timed properly, the integrator output is not zero, which gives an indication that the gates must be moved in time, left or right depending on the sign of the integrator output.

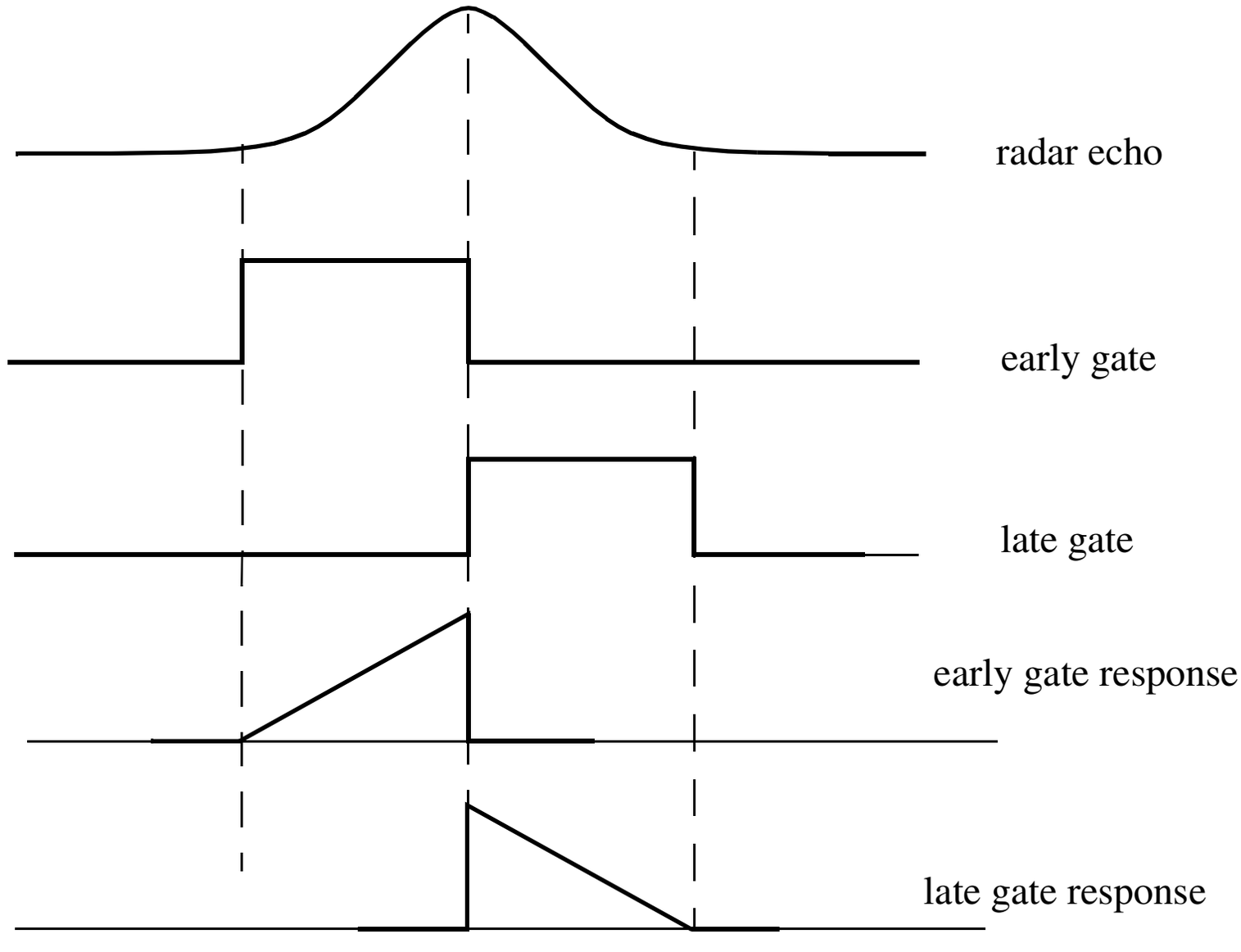

Figure 11.16. Illustration of split-range gate.

Part II: Multiple Target Tracking

Track-while-scan radar systems sample each target once per scan interval, and use sophisticated smoothing and prediction filters to estimate the target parameters between scans. To this end, the Kalman filter and the Alpha-Beta-Gamma ($\alpha\beta\gamma$) filter are commonly used. Once a particular target is detected, the radar may transmit up to a few pulses to verify the target parameters, before it establishes a track file for that target. Target position, velocity, and acceleration comprise the major components of the data maintained by a track file.

The principles of recursive tracking and prediction filters are presented in this part. First, an overview of state representation for Linear Time Invariant (LTI) systems is discussed. Then, second and third order one-dimensional fixed gain polynomial filter trackers are developed. These filters are, respectively, known as the $\alpha\beta$ and $\alpha\beta\gamma$ filters (also known as the g-h and g-h-k filters). Finally, the equations for an n-dimensional multi-state Kalman filter is introduced and analyzed. As a matter of notation, small case letters, with an underneath bar, are used.

11.5. Track-While-Scan (TWS)

Modern radar systems are designed to perform multi-function operations, such as detection, tracking, and discrimination. With the aid of sophisticated computer systems, multi-function radars are capable of simultaneously tracking many targets. In this case, each target is sampled once (mainly range and angular position) during a dwell interval (scan). Then, by using smoothing and prediction techniques future samples can be estimated. Radar systems that can perform multi-tasking and multi-target tracking are known as Track-While-Scan (TWS) radars.

Once a TWS radar detects a new target it initiates a separate track file for that detection; this ensures that sequential detections from that target are processed together to estimate the target's future parameters. Position, velocity, and acceleration comprise the main components of the track file. Typically, at least one other confirmation detection (verify detection) is required before the track file is established.

Unlike single target tracking systems, TWS radars must decide whether each detection (observation) belongs to a new target or belongs to a target that has been detected in earlier scans. And in order to accomplish this task, TWS radar systems utilize correlation and association algorithms. In the correlation process each new detection is correlated with all previous detections in order to avoid establishing redundant tracks. If a certain detection correlates with more than one track, then a pre-determined set of association rules are exercised so

that the detection is assigned to the proper track. A simplified TWS data processing block diagram is shown in Fig. 11.17.

Choosing a suitable tracking coordinate system is the first problem a TWS radar has to confront. It is desirable that a fixed reference of an inertial coordinate system be adopted. The radar measurements consist of target range, velocity, azimuth angle, and elevation angle. The TWS system places a gate around the target position and attempts to track the signal within this gate. The gate dimensions are normally azimuth, elevation, and range. Because of the uncertainty associated with the exact target position during the initial detections, a gate has to be large enough so that targets do not move appreciably from scan to scan; more precisely, targets must stay within the gate boundary during successive scans. After the target has been observed for several scans the size of the gate is reduced considerably.

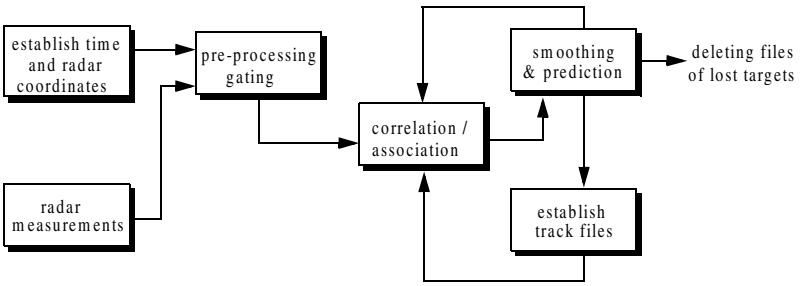

Figure. 11.17. Simplified block diagram of TWS data processing.

Gating is used to decide whether an observation is assigned to an existing track file, or to a new track file (new detection). Gating algorithms are normally based on computing a statistical error distance between a measured and an estimated radar observation. For each track file, an upper bound for this error distance is normally set. If the computed difference for a certain radar observation is less than the maximum error distance of a given track file, then the observation is assigned to that track.

All observations that have an error distance less than the maximum distance of a given track are said to correlate with that track. For each observation that does not correlate with any existing tracks, a new track file is established accordingly. Since new detections (measurements) are compared to all existing track files, a track file may then correlate with no observations or with one or more observations. The correlation between observations and all existing track files is identified using a correlation matrix. Rows of the correlation matrix

represent radar observations, while columns represent track files. In cases where several observations correlate with more than one track file, a set of predetermined association rules can be utilized so that a single observation is assigned to a single track file.

11.6. State Variable Representation of an LTI System

Linear time invariant system (continuous or discrete) can be describe mathematically using three variables. They are the input, output, and the state variables. In this representation, any LTI system has observable or measurable objects (abstracts). For example, in the case of a radar system, range may be an object measured or observed by the radar tracking filter. States can be derived in many different ways. For the scope of this book, states of an object or an abstract are the components of the vector that contains the object and its time derivatives. For example, a third-order one-dimensional (in this case range) state vector representing range can be given by

$$\underline{x} = \begin{bmatrix} R \\ \dot{R} \\ \ddot{R} \end{bmatrix} \tag{11.23}$$

where R, $\dot{R}$, and $\ddot{R}$ are, respectively, the range measurement, range rate (velocity), and acceleration. The state vector defined in Eq. (11.23) can be representative of continuous or discrete states. In this book, the emphasis is on discrete time representation, since most radar signal processing is executed using digital computers. For this purpose, an n-dimensional state vector has the following form:

$$\underline{x} = \left[x_1 \; \dot{x}_1 \; \ldots \; x_2 \; \dot{x}_2 \; \ldots \; x_n \; \dot{x}_n \; \ldots \right]^t \tag{11.24}$$

where the superscript indicates the transpose operation.

The LTI system of interest can be represented using the following state equations:

$$\dot{\underline{x}}(t) = \underline{A} \; \underline{x}(t) + \underline{B}\underline{w}(t) \tag{11.25}$$

$$\underline{y}(t) = \underline{C} \; \underline{x}(t) + \underline{D}\underline{w}(t) \tag{11.26}$$

where: $\dot{\underline{x}}$ is the value of the $n \times 1$ state vector; $\underline{y}$ is the value of the $p \times 1$ output vector; $\underline{w}$ is the value of the $m \times 1$ input vector; $\underline{A}$ is an $n \times n$ matrix; $\underline{B}$ is an $n \times m$ matrix; $\underline{C}$ is $p \times n$ matrix; and $\underline{D}$ is an $p \times m$ matrix. The

homogeneous solution (i.e., $\underline{w} = \underline{0}$) to this linear system, assuming known initial condition $\underline{x}(0)$ at time t_0, has the form

$$\underline{x}(t) = \underline{\Phi}(t - t_0)\underline{x}(t - t_0) \tag{11.27}$$

The matrix Φ is known as the state transition matrix, or fundamental matrix, and is equal to

$$\underline{\Phi}(t - t_0) = e^{\underline{A}(t - t_0)} \tag{11.28}$$

Eq. (11.28) can be expressed in series format as

$$\underline{\Phi}(t - t_0)\big|_{t_0 = 0} = e^{\underline{A}(t)} = \underline{I} + \underline{A}t + \underline{A}^2\frac{t^2}{2!} + \ldots = \sum_{k=0} \underline{A}^k \frac{t^k}{k!} \tag{11.29}$$

Example 11.1: Compute the state transition matrix for an LTI system when

$$\underline{A} = \begin{bmatrix} 0 & 1 \\ -0.5 & -1 \end{bmatrix}$$

Solution:

The state transition matrix can be computed using Eq. (11.29). For this purpose, compute $\underline{A}^2$ *and* $\underline{A}^3$ *.... It follows*

$$\underline{A}^2 = \begin{bmatrix} -\frac{1}{2} & -1 \\ \frac{1}{2} & \frac{1}{2} \end{bmatrix} \qquad \underline{A}^3 = \begin{bmatrix} \frac{1}{2} & \frac{1}{2} \\ -\frac{1}{4} & 0 \end{bmatrix} \qquad \ldots$$

Therefore,

$$\underline{\Phi} = \begin{bmatrix} 1 + 0t - \frac{\frac{1}{2}t^2}{2!} + \frac{\frac{1}{2}t^3}{3!} + \ldots & 0 + t - \frac{t^2}{2!} + \frac{\frac{1}{2}t^3}{3!} + \ldots \\ 0 - \frac{1}{2}t + \frac{\frac{1}{2}t^2}{2!} - \frac{\frac{1}{4}t^3}{3!} + \ldots & 1 - t + \frac{\frac{1}{2}t^2}{2!} + \frac{0t^3}{3!} + \ldots \end{bmatrix}$$

The state transition matrix has the following properties (the proof is left as an exercise):

1. *Derivative property*

$$\frac{\partial}{\partial t}\underline{\Phi}(t-t_0) = \underline{A}\,\underline{\Phi}(t-t_0) \tag{11.30}$$

2. *Identity property*

$$\underline{\Phi}(t_0-t_0) = \underline{\Phi}(0) = \underline{I} \tag{11.31}$$

3. *Initial value property*

$$\left.\frac{\partial}{\partial t}\underline{\Phi}(t-t_0)\right|_{t=t_0} = \underline{A} \tag{11.32}$$

4. *Transition property*

$$\underline{\Phi}(t_2-t_0) = \underline{\Phi}(t_2-t_1)\underline{\Phi}(t_1-t_0) \qquad ;\ t_0 \le t_1 \le t_2 \tag{11.33}$$

5. *Inverse property*

$$\underline{\Phi}(t_0-t_1) = \underline{\Phi}^{-1}(t_1-t_0) \tag{11.34}$$

6. *Separation property*

$$\underline{\Phi}(t_1-t_0) = \underline{\Phi}(t_1)\underline{\Phi}^{-1}(t_0) \tag{11.35}$$

The general solution to the system defined in Eq. (11.25) can be written as

$$\underline{x}(t) = \underline{\Phi}(t-t_0)\underline{x}(t_0) + \int_{t_0}^{t}\underline{\Phi}(t-\tau)\underline{B}\,\underline{w}(\tau)d\tau \tag{11.36}$$

The first term of the right-hand side of Eq. (11.36) represents the contribution from the system response to the initial condition. The second term is the contribution due to the driving force $\underline{w}$. By combining Eqs. (11.26) and (11.36) an expression for the output is computed as

$$\underline{y}(t) = \underline{C}e^{\underline{A}(t-t_0)}\underline{x}(t_0) + \int_{t_0}^{t}[\underline{C}e^{\underline{A}(t-\tau)}\underline{B} - \underline{D}\delta(t-\tau)]\underline{w}(\tau)d\tau \tag{11.37}$$

Note that the system impulse response is equal to $\underline{C}e^{\underline{A}t}\underline{B} - \underline{D}\delta(t)$.

The difference equations describing a discrete time system, equivalent to Eqs. (11.25) and (11.26), are

$$\underline{x}(n+1) = \underline{A}\ \underline{x}(n) + \underline{B}\underline{w}(n) \tag{11.38}$$

$$\underline{y}(n) = \underline{C}\ \underline{x}(n) + \underline{D}\underline{w}(n) \tag{11.39}$$

where n defines the discrete time nT and T is the sampling interval. All other vectors and matrices were defined earlier. The homogeneous solution to the system defined in Eq. (11.38), with initial condition $\underline{x}(n_0)$, is

$$\underline{x}(n) = \underline{A}^{n-n_0}\underline{x}(n_0) \tag{11.40}$$

In this case the state transition matrix is an $n \times n$ matrix given by

$$\underline{\Phi}(n, n_0) = \underline{\Phi}(n-n_0) = \underline{A}^{n-n_0} \tag{11.41}$$

The following is the list of properties associated with the discrete transition matrix

$$\underline{\Phi}(n+1-n_0) = \underline{A}\underline{\Phi}(n-n_0) \tag{11.42}$$

$$\underline{\Phi}(n_0-n_0) = \underline{\Phi}(0) = \underline{I} \tag{11.43}$$

$$\underline{\Phi}(n_0+1-n_0) = \underline{\Phi}(1) = \underline{A} \tag{11.44}$$

$$\underline{\Phi}(n_2-n_0) = \underline{\Phi}(n_2-n_1)\underline{\Phi}(n_1-n_0) \tag{11.45}$$

$$\underline{\Phi}(n_0-n_1) = \underline{\Phi}^{-1}(n_1-n_0) \tag{11.46}$$

$$\underline{\Phi}(n_1-n_0) = \underline{\Phi}(n_1)\underline{\Phi}^{-1}(n_0) \tag{11.47}$$

The solution to the general case (i.e., non-homogeneous system) is given by

$$\underline{x}(n) = \underline{\Phi}(n-n_0)\underline{x}(n_0) + \sum_{m=n_0}^{n-1} \underline{\Phi}(n-m-1)\underline{B}\underline{w}(m) \tag{11.48}$$

It follows that the output is given by

$$\underline{y}(n) = \underline{C}\underline{\Phi}(n-n_0)\underline{x}(n_0) + \sum_{m=n_0}^{n-1} \underline{C}\ \underline{\Phi}(n-m-1)\underline{B}\underline{w}(m) + \underline{D}\underline{w}(n) \tag{11.49}$$

where the system impulse response is given by

$$\underline{h}(n) = \sum_{m=n_0}^{n-1} \underline{C}\ \underline{\Phi}(n-m-1)\underline{B}\delta(m) + \underline{D}\delta(n) \tag{11.50}$$

Taking the Z-transform for Eqs. (11.38) and (11.39) yields

$$z\underline{x}(z) = \underline{A}\underline{x}(z) + \underline{B}\underline{w}(z) + z\underline{x}(0) \tag{11.51}$$

$$\underline{y}(z) = \underline{C}\underline{x}(z) + \underline{D}\underline{w}(z) \tag{11.52}$$

Manipulating Eqs. (11.51) and (11.52) yields

$$\underline{x}(z) = [z\underline{I} - \underline{A}]^{-1}\underline{B}\underline{w}(z) + [z\underline{I} - \underline{A}]^{-1}z\underline{x}(0) \tag{11.53}$$

$$\underline{y}(z) = \{\underline{C}[z\underline{I} - \underline{A}]^{-1}\underline{B} + \underline{D}\}\underline{w}(z) + \underline{C}[z\underline{I} - \underline{A}]^{-1}z\underline{x}(0) \tag{11.54}$$

It follows that the state transition matrix is

$$\underline{\Phi}(z) = z[z\underline{I} - \underline{A}]^{-1} = [\underline{I} - z^{-1}\underline{A}]^{-1} \tag{11.55}$$

and the system impulse response in the z-domain is

$$\underline{h}(z) = \underline{C}\underline{\Phi}(z)z^{-1}\underline{B} + \underline{D} \tag{11.56}$$

11.7. The LTI System of Interest

For the purpose of establishing the framework necessary for the Kalman filter development, consider the LTI system shown in Fig. 11.18. This system (which is a special case of the system described in the previous section) can be described by the following first order differential vector equations

$$\dot{\underline{x}}(t) = \underline{A}\ \underline{x}(t) + \underline{u}(t) \tag{11.57}$$

$$\underline{y}(t) = \underline{G}\ \underline{x}(t) + \underline{v}(t) \tag{11.58}$$

where $\underline{y}$ is the observable part of the system (i.e., output), $\underline{u}$ is a driving force, and $\underline{v}$ is the measurement noise. The matrices $\underline{A}$ and $\underline{G}$ vary depending on the system. The noise observation $\underline{v}$ is assumed to be uncorrelated. If the initial condition vector is $\underline{x}(t_0)$, then from Eq. (11.36) we get

$$\underline{x}(t) = \underline{\Phi}(t-t_0)\underline{x}(t_0) + \int_{t_0}^{t} \underline{\Phi}(t-\tau)\underline{u}(\tau)d\tau \tag{11.59}$$

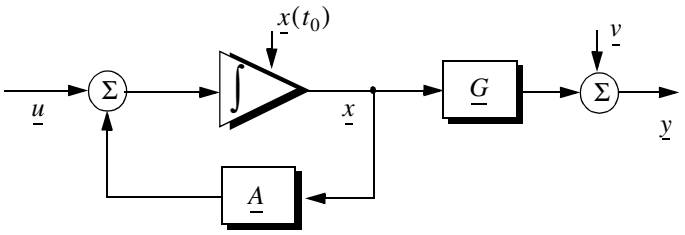

Figure 11.18. An LTI system.

The object (abstract) is observed only at discrete times determined by the system. These observation times are declared by discrete time nT where T is the sampling interval. Using the same notation adopted in the previous section, the discrete time representations of Eqs. (11.57) and (11.58) are

$$\underline{x}(n) = \underline{A}\ \underline{x}(n-1) + \underline{u}(n) \tag{11.60}$$

$$\underline{y}(n) = \underline{G}\ \underline{x}(n) + \underline{v}(n) \tag{11.61}$$

The homogeneous solution to this system is given in Eq. (11.27) for continuous time, and in Eq. (11.40) for discrete time.

The state transition matrix corresponding to this system can be obtained using Taylor series expansion of the vector $\underline{x}$. More precisely,

$$\begin{aligned} x &= x + T\dot{x} + \frac{T^2}{2!}\ddot{x} + \ldots \\ \dot{x} &= \dot{x} + T\ddot{x} + \ldots \\ \ddot{x} &= \ddot{x} + \ldots \end{aligned} \tag{11.62}$$

It follows that the elements of the state transition matrix are defined by

$$\underline{\Phi}[ij] = \begin{cases} T^{j-i} \div (j-i)! & 1 \le i, j \le n \\ 0 & j < i \end{cases} \tag{11.63}$$

Using matrix notation, the state transition matrix is then given by

$$\underline{\Phi} = \begin{bmatrix} 1 & T & \frac{T^2}{2!} & \cdots \\ 0 & 1 & T & \cdots \\ 0 & 0 & 1 & \cdots \\ \cdots & \cdots & \cdots & \cdots \end{bmatrix} \tag{11.64}$$

The matrix given in Eq. (11.64) is often called the Newtonian matrix.

11.8. Fixed-Gain Tracking Filters

This class of filters (or estimators) is also known as "Fixed-Coefficient" filters. The most common examples of this class of filters are the $\alpha\beta$ and $\alpha\beta\gamma$ filters and their variations. The $\alpha\beta$ and $\alpha\beta\gamma$ trackers are one-dimensional second and third order filters, respectively. They are equivalent to special cases of the one-dimensional Kalman filter. The general structure of this class of estimators is similar to that of the Kalman filter.

The standard $\alpha\beta\gamma$ filter provides smoothed and predicted data for target position, velocity (Doppler), and acceleration. It is a polynomial predictor/corrector linear recursive filter. This filter can reconstruct position, velocity, and constant acceleration based on position measurements. The $\alpha\beta\gamma$ filter can also provide a smoothed (corrected) estimate of the present position which can be used in guidance and fire control operations.

Notation:

For the purpose of the discussion presented in the remainder of this chapter, the following notation is adopted: $x(n|m)$ represents the estimate during the nth sampling interval, using all data up to and including the mth sampling interval; y_n is the nth measured value; and e_n is the nth residual (error).

The fixed-gain filter equation is given by

$$\underline{x}(n|n) = \underline{\Phi}\underline{x}(n-1|n-1) + \underline{K}[y_n - \underline{G}\underline{\Phi}\underline{x}(n-1|n-1)] \tag{11.65}$$

Since the transition matrix assists in predicting the next state,

$$\underline{x}(n+1|n) = \underline{\Phi}\underline{x}(n|n) \tag{11.66}$$

Substituting Eq. (11.66) into Eq. (11.65) yields

$$\underline{x}(n|n) = \underline{x}(n|n-1) + \underline{K}[y_n - \underline{G}\underline{x}(n|n-1)] \tag{11.67}$$

The term enclosed within the brackets on the right hand side of Eq. (11.67) is often called the residual (error) which is the difference between the measured input and predicted output. Eq. (11.67) means that the estimate of $\underline{x}(n)$ is the sum of the prediction and the weighted residual. The term $\underline{G}\underline{x}(n|n-1)$ represents the prediction state. In the case of the $\alpha\beta\gamma$ estimator, $\underline{G}$ is row vector given by

$$\underline{G} = \begin{bmatrix} 1 & 0 & 0 & \ldots \end{bmatrix} \tag{11.68}$$

and the gain matrix $\underline{K}$ is given by

$$\underline{K} = \begin{bmatrix} \alpha \\ \beta/T \\ \gamma/T^2 \end{bmatrix} \tag{11.69}$$

One of the main objectives of a tracking filter is to decrease the effect of the noise observation on the measurement. For this purpose the noise covariance matrix is calculated. More precisely, the noise covariance matrix is

$$\underline{C}(n|n) = E\{(\underline{x}(n|n)\ )\underline{x}^t(n|n)\} \qquad ;\ y_n = v_n \tag{11.70}$$

where E indicates the expected value operator. Noise is assumed to be a zero mean random process with variance equal to σ_v^2. Additionally, noise measurements are also assumed to be uncorrelated,

$$E\{v_n v_m\} = \begin{cases} \delta\sigma_v^2 & n = m \\ 0 & n \neq m \end{cases} \tag{11.71}$$

Eq. (11.65) can be written as

$$\underline{x}(n|n) = \underline{A}\underline{x}(n-1|n-1) + \underline{K}y_n \tag{11.72}$$

where

$$\underline{A} = (\underline{I} - \underline{K}\underline{G})\underline{\Phi} \tag{11.73}$$

Substituting Eqs. (11.72) and (11.73) into Eq. (11.70) yields

$$\underline{C}(n|n) = E\{(\underline{A}\underline{x}(n-1|n-1) + \underline{K}y_n)(\underline{A}\underline{x}(n-1|n-1) + \underline{K}y_n)^t\} \tag{11.74}$$

Expanding the right hand side of Eq. (11.74) and using Eq. (11.71) give

$$\underline{C}(n|n) = \underline{A}\,\underline{C}(n-1|n-1)\underline{A}^t + \underline{K}\sigma_v^2\underline{K}^t \tag{11.75}$$

Under the steady state condition, Eq. (11.75) collapses to

$$\underline{C}(n|n) = \underline{A}\,\underline{C}\,\underline{A}^t + \underline{K}\sigma_v^2\underline{K}^t \tag{11.76}$$

where $\underline{C}$ is the steady state noise covariance matrix. In the steady state,

$$\underline{C}(n|n) = \underline{C}(n-1|n-1) = \underline{C} \qquad for\ any\ n \tag{11.77}$$

Several criteria can be used to establish the performance of fixed-gain tracking filter. The most commonly used technique is to compute the Variance Reduction Ratio (VRR). The VRR is defined only when the input to the tracker is noise measurements. It follows that in the steady state case, the VRR is the steady state ratio of the output variance (auto-covariance) to the input measurement variance.

In order to determine the stability of the tracker under consideration, consider the Z-transform for Eq. (11.72),

$$\underline{x}(z) = \underline{A}z^{-1}\underline{x}(z) + \underline{K}y_n(z) \tag{11.78}$$

Rearranging Eq. (11.78) yields the following system transfer functions:

$$\underline{h}(z) = \frac{\underline{x}(z)}{y_n(z)} = (\underline{I} - \underline{A}z^{-1})^{-1}\underline{K} \tag{11.79}$$

where $(\underline{I} - \underline{A}z^{-1})$ is called the characteristic matrix. Note that the system transfer functions can exist only when the characteristic matrix is a non-singular matrix. Additionally, the system is stable if and only if the roots of the characteristic equation are within the unit circle in the z-plane,

$$\left|(\underline{I} - \underline{A}z^{-1})\right| = 0 \tag{11.80}$$

The filter's steady state errors can be determined with the help of Fig. 11.19. The error transfer function is

$$\underline{e}(z) = \frac{\underline{y}(z)}{1 + \underline{h}(z)} \tag{11.81}$$

and by using Abel's theorem, the steady state error is

$$\underline{e}_\infty = \lim_{t\to\infty} \underline{e}(t) = \lim_{z\to 1}\left(\frac{z-1}{z}\right)\underline{e}(z) \tag{11.82}$$

Substituting Eq. (11.82) into (11.81) yields

$$\underline{e}_{\infty} = \lim_{z \to 1} \frac{z-1}{z} \frac{\underline{y}(z)}{1+\underline{h}(z)} \tag{11.83}$$

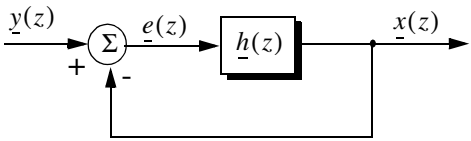

Figure 11.19. Steady state errors computation.

11.8.1. The αβ Filter

The αβ tracker produces, on the nth observation, smoothed estimates for position and velocity, and a predicted position for the $(n+1)th$ observation. Fig. 11.20 shows an implementation of this filter. Note that the subscripts "p" and "s" are used to indicate, respectively, the predicated and smoothed values. The αβ tracker can follow an input ramp (constant velocity) with no steady state errors. However, a steady state error will accumulate when constant acceleration is present in the input. Smoothing is done to reduce errors in the predicted position through adding a weighted difference between the measured and predicted values to the predicted position, as follows:

$$x_s(n) = x(n|n) = x_p(n) + \alpha(x_0(n) - x_p(n)) \tag{11.84}$$

$$\dot{x}_s(n) = x'(n|n) = \dot{x}_s(n-1) + \frac{\beta}{T}(x_0(n) - x_p(n)) \tag{11.85}$$

x_0 is the position input samples. The predicted position is given by

$$x_p(n) = x_s(n|n-1) = x_s(n-1) + T\dot{x}_s(n-1) \tag{11.86}$$

The initialization process is defined by

$$x_s(1) = x_p(2) = x_0(1)$$

$$\dot{x}_s(1) = 0$$

$$\dot{x}_s(2) = \frac{x_0(2) - x_0(1)}{T}$$

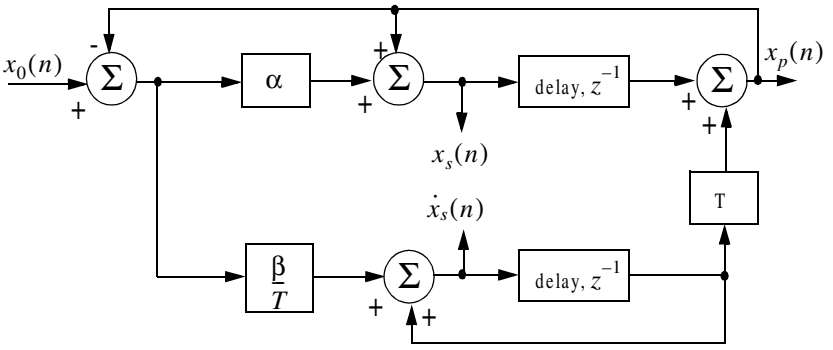

Figure 11.20. An implementation for an $\alpha\beta$ tracker.

A general form for the covariance matrix was developed in the previous section, and is given in Eq. (11.75). In general, a second order one-dimensional covariance matrix (in the context of the $\alpha\beta$ filter) can be written as

$$\underline{C}(n|n) = \begin{bmatrix} C_{xx} & C_{x\dot{x}} \\ C_{\dot{x}x} & C_{\dot{x}\dot{x}} \end{bmatrix} \tag{11.87}$$

where, in general, C_{xy} is

$$C_{xy} = E\{xy^t\} \tag{11.88}$$

By inspection, the $\alpha\beta$ filter has

$$\underline{A} = \begin{bmatrix} 1-\alpha & (1-\alpha)T \\ -\beta/T & (1-\beta) \end{bmatrix} \tag{11.89}$$

$$\underline{K} = \begin{bmatrix} \alpha \\ \beta/T \end{bmatrix} \tag{11.90}$$

$$\underline{G} = \begin{bmatrix} 1 & 0 \end{bmatrix} \tag{11.91}$$

$$\underline{\Phi} = \begin{bmatrix} 1 & T \\ 0 & 1 \end{bmatrix} \tag{11.92}$$

Finally, by using Eqs. (11.89) through (11.92) in Eq. (11.72) yields the steady state noise covariance matrix,

$$\underline{C} = \frac{\sigma_v^2}{\alpha(4-2\alpha-\beta)} \begin{bmatrix} 2\alpha^2 - 3\alpha\beta + 2\beta & \dfrac{\beta(2\alpha-\beta)}{T} \\ \dfrac{\beta(2\alpha-\beta)}{T} & \dfrac{2\beta^2}{T^2} \end{bmatrix} \tag{11.93}$$

It follows that the position and velocity VRR ratios are, respectively, given by

$$(VRR)_x = C_{xx}/\sigma_v^2 = \frac{2\alpha^2 - 3\alpha\beta + 2\beta}{\alpha(4-2\alpha-\beta)} \tag{11.94}$$

$$(VRR)_{\dot{x}} = C_{\dot{x}\dot{x}}/\sigma_v^2 = \frac{1}{T^2}\ \frac{2\beta^2}{\alpha(4-2\alpha-\beta)} \tag{11.95}$$

The stability of the $\alpha\beta$ filter is determined from its system transfer functions. For this purpose, compute the roots for Eq. (11.80) with $\underline{A}$ from Eq. (11.89),

$$\left|\underline{I} - \underline{A}z^{-1}\right| = 1 - (2-\alpha-\beta)z^{-1} + (1-\alpha)z^{-2} = 0 \tag{11.96}$$

Solving Eq. (11.96) for z yields

$$z_{1,2} = 1 - \frac{\alpha+\beta}{2} \pm \frac{1}{2}\sqrt{(\alpha-\beta)^2 - 4\beta} \tag{11.97}$$

and in order to guarantee stability

$$\left|z_{1,2}\right| < 1 \tag{11.98}$$

Two cases are analyzed. First, $z_{1,2}$ are real. In this case (the details are left as an exercise),

$$\beta > 0 \qquad ;\ \alpha > -\beta \tag{11.99}$$

The second case is when the roots are complex; in this case we find

$$\alpha > 0 \tag{11.100}$$

The system transfer functions can be derived by using Eqs. (11.79), (11.89), and (11.90),

$$\begin{bmatrix} h_x(z) \\ h_{\dot{x}}(z) \end{bmatrix} = \frac{1}{z^2 - z(2-\alpha-\beta) + (1-\alpha)} \begin{bmatrix} \alpha z\left(z - \dfrac{(\alpha-\beta)}{\alpha}\right) \\ \dfrac{\beta z(z-1)}{T} \end{bmatrix} \tag{11.101}$$

Up to this point all relevant relations concerning the $\alpha\beta$ filter were made with no regard to how to choose the gain coefficients (α and β). Before considering the methodology of selecting these coefficients, consider the main objective behind using this filter. The purpose of the $\alpha\beta$ tracker can be described twofold:

1. *The tracker must reduce the measurement noise as much as possible.*
2. *The filter must be able to track maneuvering targets, with as little residual (tracking error) as possible.*

The reduction of measurement noise reduction is normally determined by the VRR ratios. However, the maneuverability performance of the filter depends heavily on the choice of the parameters α and β.

A special variation of the $\alpha\beta$ filter was developed by Benedict and Bordner[1], and is often referred to as the Benedict-Bordner filter. The main advantage of the Benedict-Bordner is reducing the transient errors associated with the $\alpha\beta$ tracker. This filter uses both the position and velocity VRR ratios as measure of performance. It computes the sum of the squared differences between the input (position) and the output when the input has a unit step velocity at time zero. Additionally, it computes the squared differences between the real velocity and the velocity output when the input is as described earlier. Both error differences are minimized when

$$\beta = \frac{\alpha^2}{2-\alpha} \tag{11.102}$$

In this case, the position and velocity VRR ratios are, respectively, given by

$$(VRR)_x = \frac{\alpha(6-5\alpha)}{\alpha^2 - 8\alpha + 8} \tag{11.103}$$

$$(VRR)_{\dot{x}} = \frac{2}{T^2}\,\frac{\alpha^3/(2-\alpha)}{\alpha^2 - 8\alpha + 8} \tag{11.104}$$

Another important sub-class of the $\alpha\beta$ tracker is the critically damped filter, often called the fading memory filter. In this case, the filter coefficients are chosen on the basis of a smoothing factor ξ, where $0 \le \xi \le 1$. The gain coefficients are given by

$$\alpha = 1 - \xi^2 \tag{11.105}$$

---

1. Benedict, T. R. and Bordner, G. W., Synthesis of an Optimal Set of Radar Track-While-Scan Smoothing Equations. *IRE Transaction on Automatic Control, AC-7*. July 1962, pp. 27-32.

$$\beta = (1-\xi)^2 \tag{11.106}$$

Heavy smoothing means $\xi \to 1$ and little smoothing means $\xi \to 0$. The elements of the covariance matrix for a fading memory filter are

$$C_{xx} = \frac{1-\xi}{(1+\xi)^3}\ (1+4\xi+5\xi^2)\ \sigma_v^2 \tag{11.107}$$

$$C_{x\dot{x}} = C_{\dot{x}x} = \frac{1}{T}\ \frac{1-\xi}{(1+\xi)^3}\ (1+2\xi+3\xi^2)\ \sigma_v^2 \tag{11.108}$$

$$C_{\dot{x}\dot{x}} = \frac{2}{T^2}\ \frac{1-\xi}{(1+\xi)^3}\ (1-\xi)^2\ \sigma_v^2 \tag{11.109}$$

11.8.2. The αβγ Filter

The αβγ tracker produces, for the nth observation, smoothed estimates of position, velocity, and acceleration. It also produces predicted position and velocity for the $(n+1)th$ observation. An implementation of the αβγ tracker is shown in Fig. 11.21.

The αβγ tracker will follow an input whose acceleration is constant with no steady state errors. Again, in order to reduce the error at the output of the tracker, a weighted difference between the measured and predicted values is used in estimating the smoothed position, velocity, and acceleration as follows:

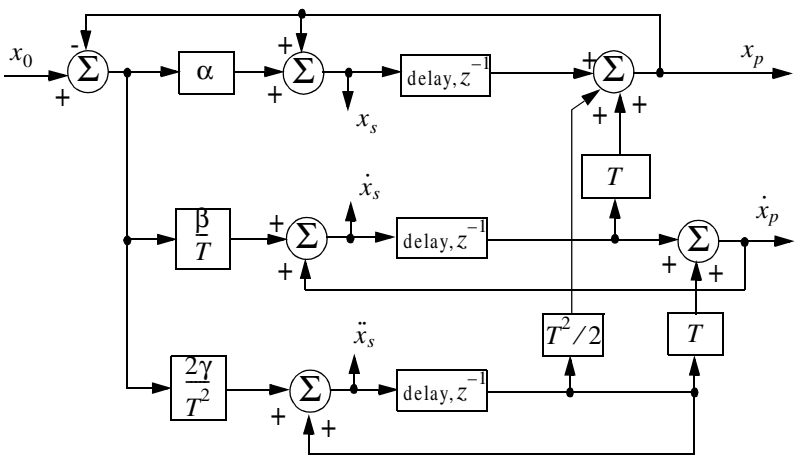

Figure 11.21. An implementation for an αβγ tracker.

$$x_s(n) = x_p(n) + \alpha(x_0(n) - x_p(n)) \tag{11.110}$$

$$\dot{x}_s(n) = \dot{x}_s(n-1) + T\ddot{x}_s(n-1) + \frac{\beta}{T}\ (x_0(n) - x_p(n)) \tag{11.111}$$

$$\ddot{x}_s(n) = \ddot{x}_s(n-1) + \frac{2\gamma}{T^2}\ (x_0(n) - x_p(n)) \tag{11.112}$$

$$x_p(n+1) = x_s(n) + T\ \dot{x}_s(n) + \frac{T^2}{2}\ \ddot{x}_s(n) \tag{11.113}$$

and the initialization process is

$$x_s(1) = x_p(2) = x_0(1)$$

$$\dot{x}_s(1) = \ddot{x}_s(1) = \ddot{x}_s(2) = 0$$

$$\dot{x}_s(2) = \frac{x_0(2) - x_0(1)}{T}$$

$$\ddot{x}_s(3) = \frac{x_0(3) + x_0(1) - 2x_0(2)}{T^2}$$

Using Eq. (11.63) the state transition matrix for the $\alpha\beta\gamma$ filter is

$$\underline{\Phi} = \begin{bmatrix} 1 & T & \frac{T^2}{2} \\ 0 & 1 & T \\ 0 & 0 & 1 \end{bmatrix} \tag{11.114}$$

The covariance matrix (which is symmetric) can be computed from Eq. (11.76). For this purpose, note that

$$\underline{K} = \begin{bmatrix} \alpha \\ \beta/T \\ \gamma/T^2 \end{bmatrix} \tag{11.115}$$

$$\underline{G} = \begin{bmatrix} 1 & 0 & 0 \end{bmatrix} \tag{11.116}$$

and

$$\underline{A} = (\underline{I} - \underline{K}\underline{G})\underline{\Phi} = \begin{bmatrix} 1-\alpha & (1-\alpha)T & (1-\alpha)T^2/2 \\ -\beta/T & -\beta+1 & (1-\beta/2)T \\ -2\gamma/T^2 & -2\gamma/T & (1-\gamma) \end{bmatrix} \tag{11.117}$$

Substituting Eq. (11.117) into (11.76) and collecting terms the VRR ratios are computed as

$$(VRR)_x = \frac{2\beta(2\alpha^2 + 2\beta - 3\alpha\beta) - \alpha\gamma(4 - 2\alpha - \beta)}{(4 - 2\alpha - \beta)(2\alpha\beta + \alpha\gamma - 2\gamma)} \tag{11.118}$$

$$(VRR)_{\dot{x}} = \frac{4\beta^3 - 4\beta^2\gamma + 2\gamma^2(2 - \alpha)}{T^2(4 - 2\alpha - \beta)(2\alpha\beta + \alpha\gamma - 2\gamma)} \tag{11.119}$$

$$(VRR)_{\ddot{x}} = \frac{4\beta\gamma^2}{T^4(4 - 2\alpha - \beta)(2\alpha\beta + \alpha\gamma - 2\gamma)} \tag{11.120}$$

As in the case of any discrete time system, this filter will be stable if and only if all of its poles fall within the unit circle in the z-plane.

The $\alpha\beta\gamma$ characteristic equation is computed by setting

$$\left|\underline{I} - \underline{A}z^{-1}\right| = 0 \tag{11.121}$$

Substituting Eq. (11.117) into (11.121) and collecting terms yield the following characteristic function:

$$f(z) = z^3 + (-3\alpha + \beta + \gamma)z^2 + (3 - \beta - 2\alpha + \gamma)z - (1 - \alpha) \tag{11.122}$$

The $\alpha\beta\gamma$ becomes a Benedict-Bordner filter when

$$2\beta - \alpha\left(\alpha + \beta + \frac{\gamma}{2}\right) = 0 \tag{11.123}$$

Note that for $\gamma = 0$ Eq. (11.123) reduces to Eq. (11.102). For a critically damped filter the gain coefficients are

$$\alpha = 1 - \xi^3 \tag{11.124}$$

$$\beta = 1.5(1 - \xi^2)(1 - \xi) = 1.5(1 - \xi)^2(1 + \xi) \tag{11.125}$$

$$\gamma = (1 - \xi)^3 \tag{11.126}$$

Note that heavy smoothing takes place when $\xi \to 1$, while $\xi = 0$ means that no smoothing is present.

MATLAB Function "ghk_tracker.m"

The function *"ghk_tracker.m"*[1] implements the steady state $\alpha\beta\gamma$ filter. It is given in Listing 11.2 in Section 11.10. The syntax is as follows:

[residual, estimate] = ghk_tracker (X0, smoocof, inp, npts, T, nvar)

where

Symbol	Description	Status
X0	*initial state vector*	*input*
smoocof	*desired smoothing coefficient*	*input*
inp	*array of position measurements*	*input*
npts	*number of points in input position*	*input*
T	*sampling interval*	*input*
nvar	*desired noise variance*	*input*
residual	*array of position error (residual)*	*output*
estimate	*array of predicted position*	*output*

Note that *"ghk_tracker.m"* uses MATLAB's function *"normrnd.m"* to generate zero mean Gaussian noise, which is part of MATLAB's Statistics Toolbox. If this toolbox is not available to the user, then *"ghk_tracker.m"* function-call must be modified to

[residual, estimate] = ghk_tracker1 (X0, smoocof, inp, npts, T)

which is also part of Listing 11.2. In this case, noise measurements are either to be considered unavailable or are part of the position input array.

To illustrate how to use the functions *ghk_tracker.m* and *ghk_tracker.m1,* consider the inputs shown in Figs. 11.22 and 11.23. Fig. 11.22 assumes an input with lazy maneuvering, while Fig. 11.23 assumes an aggressive maneuvering case. For this purpose, the program called *"fig11_21.m"* was written. It is given in Listing 11.3 in Section 11.10.

Figs. 11.24 and 11.25 show the residual error and predicted position corresponding (generated using the program *"fig11_21.m")* to Fig. 11.22 for two cases: heavy smoothing and little smoothing with and without noise. The noise is white Gaussian with zero mean and variance of $\sigma_v^2 = 0.05$. Figs. 11. 26 and 11.27 show the residual error and predicted position corresponding (generated using the program *"fig11_20.m")* to Fig. 11.23 with and without noise.

1. This function was written by Mr. Edward Shamsi of COLSA Corporation in Huntsville, AL.

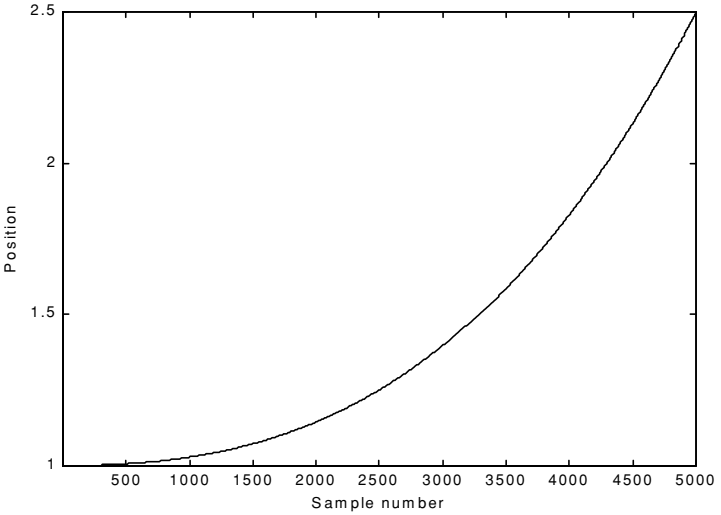

Figure 11.22. Position (truth-data); lazy maneuvering.

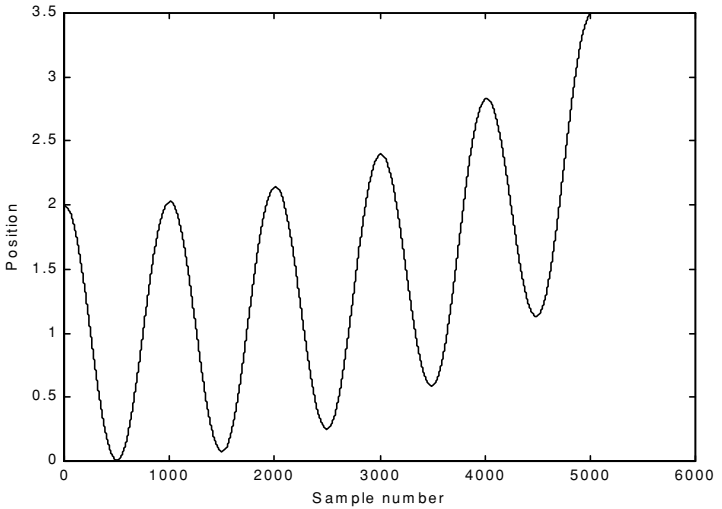

Figure 11.23. Position (truth-data); aggresive maneuvering.

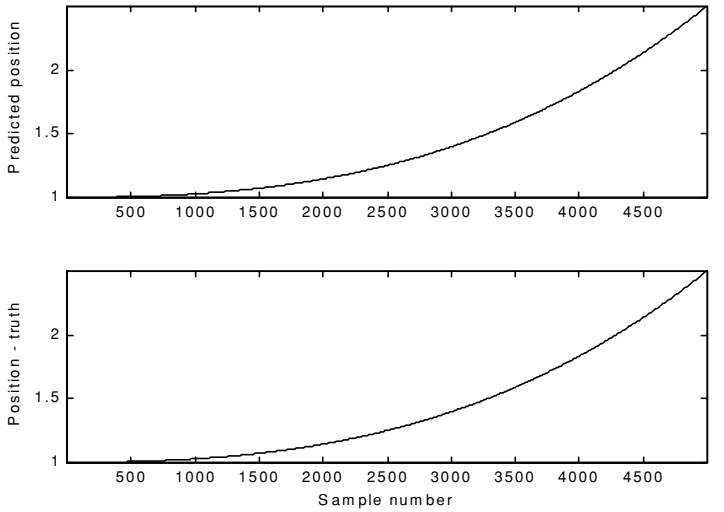

Figure 11.24a-1. Predicted and true position. $\xi = 0.1$ (i.e., large gain coefficients). No noise present.

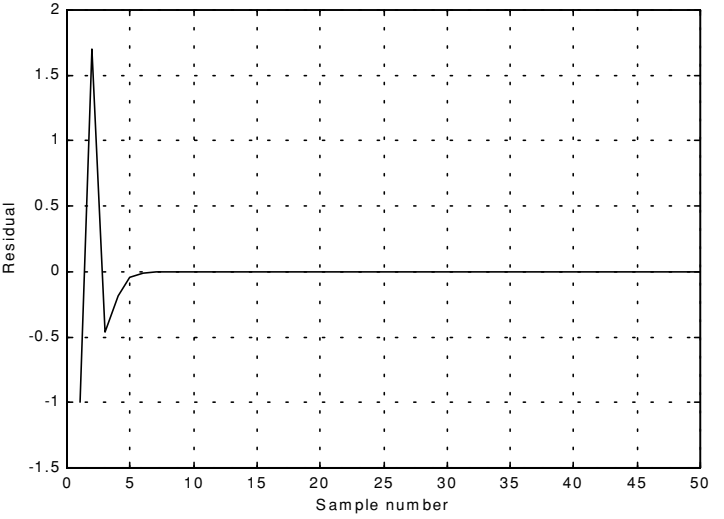

Figure 11.24a-2. Position residual (error). Large gain coefficients. No noise. The error settles to zero fairly quickly.

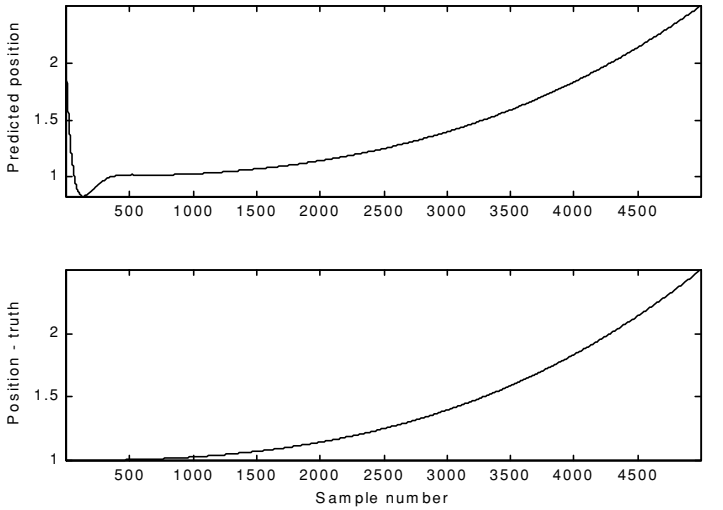

Figure 11.24b-1. Predicted and true position. $\xi = 0.9$ (i.e., small gain coefficients). No noise present.

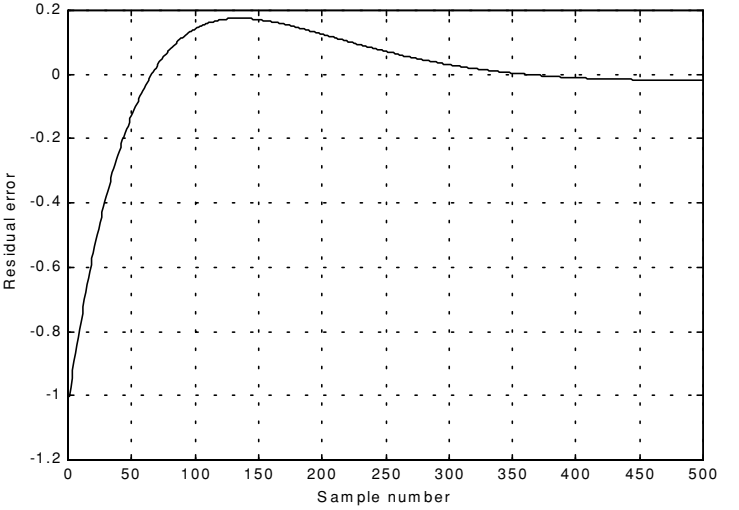

Figure 11.24b-2. Position residual (error). Small gain coefficients. No noise. It takes the filter longer time for the error to settle down.

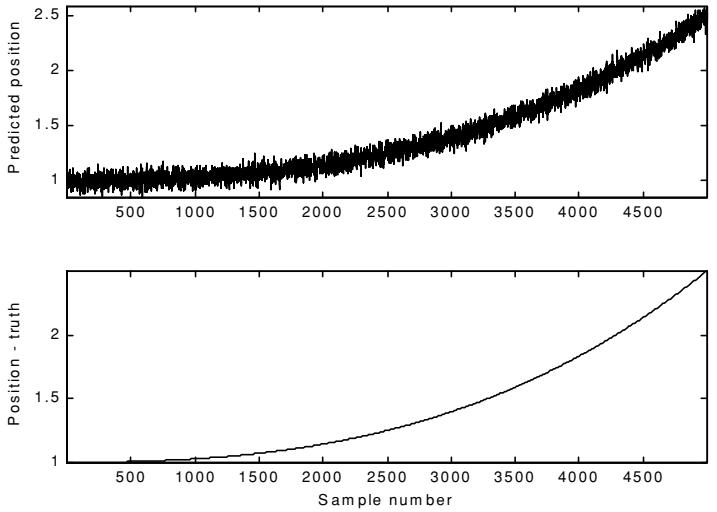

Figure 11.25a-1. Predicted and true position. $\xi = 0.1$ (i.e., large gain coefficients). Noise is present.

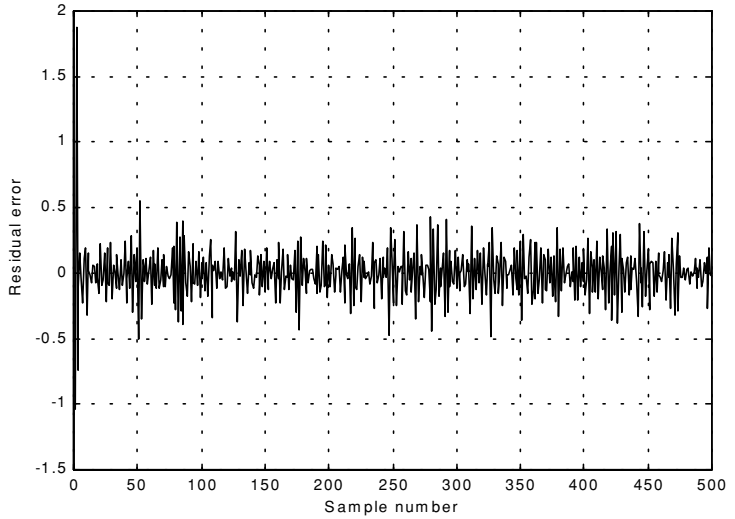

Figure 11.25a-2. Position residual (error). Large gain coefficients. Noise present. The error settles down quickly. The variation is due to noise.

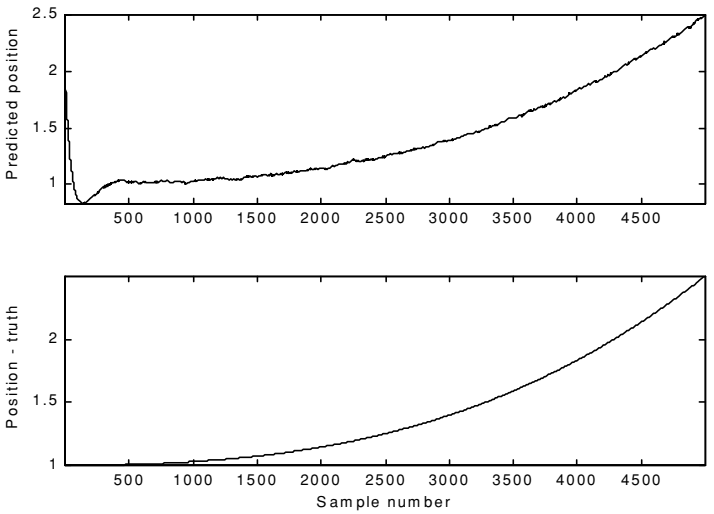

Figure 11.25b-1. Predicted and true position. $\xi = 0.9$ (i.e., small gain coefficients). Noise is present.

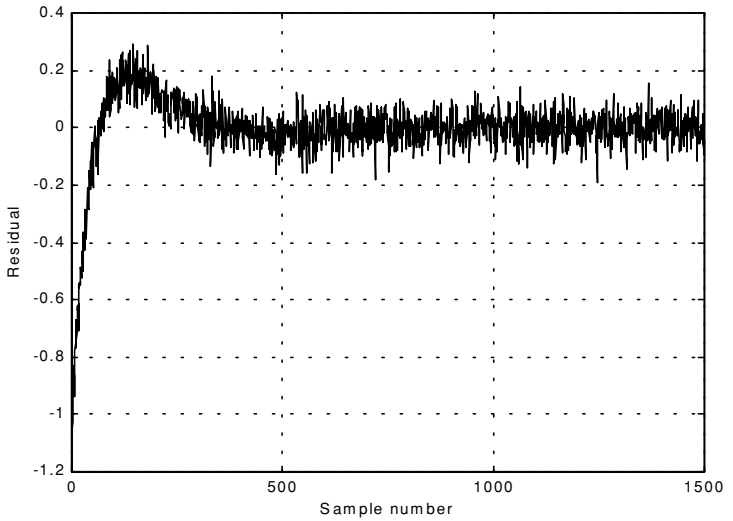

Figure 11.25b-2. Position residual (error). Small gain coefficients. Noise present. The error requires more time before settling down. The variation is due to noise.

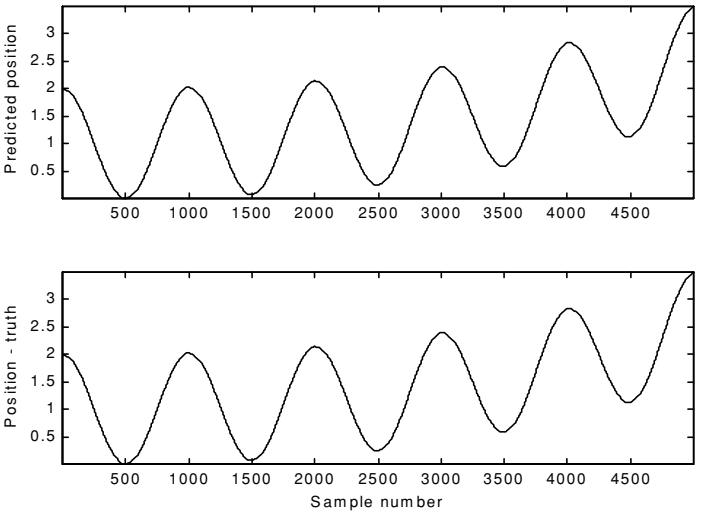

Figure 11.26a. Predicted and true position. $\xi = 0.1$ (i.e., large gain coefficients). Noise is present.

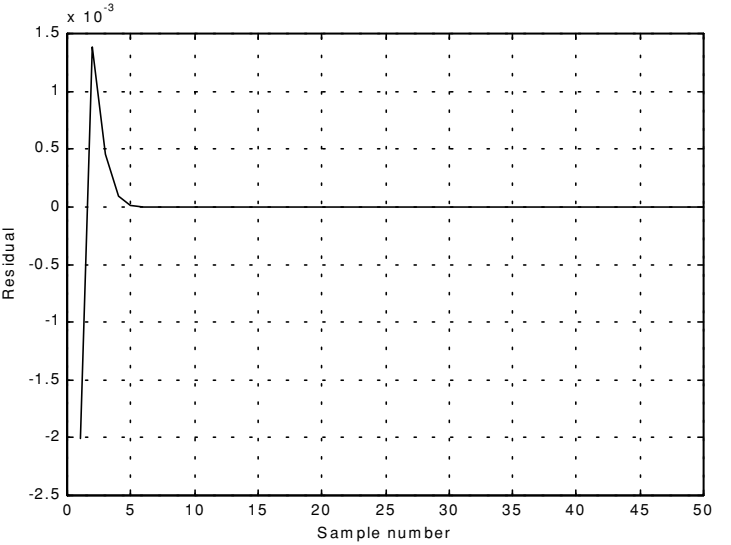

Figure 11.26b. Position residual (error). Large gain coefficients. No noise. The error settles down quickly.

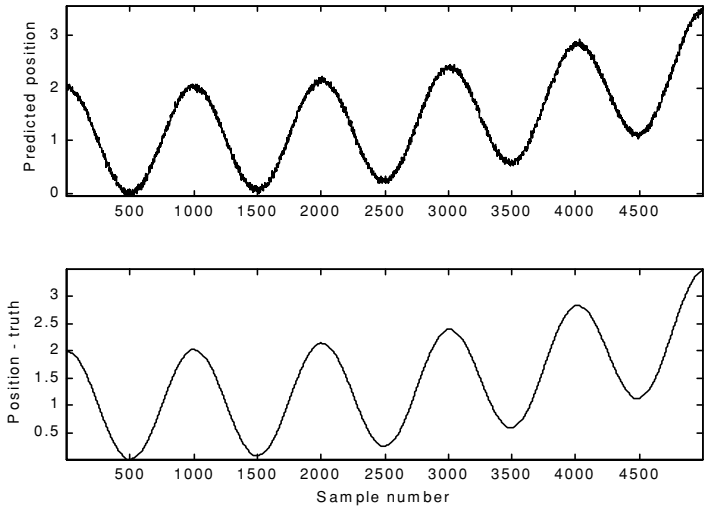

Figure 11.27a. Predicted and true position. $\xi = 0.8$ (i.e., small gain coefficients). Noise is present.

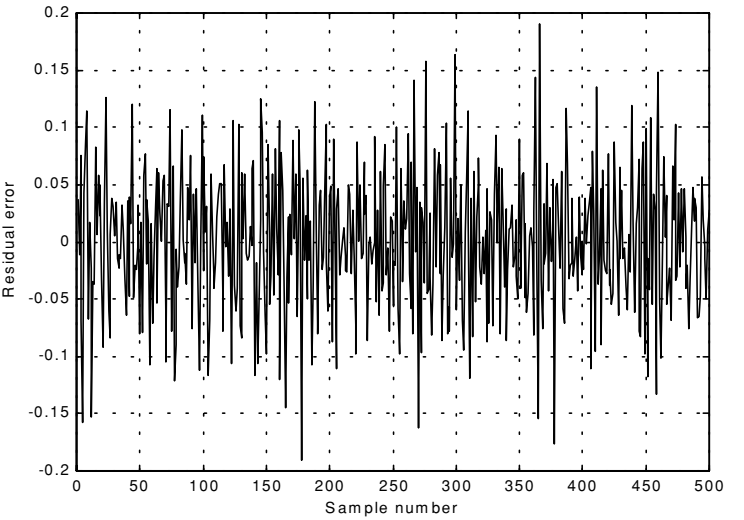

Figure 11.27b. Position residual (error). Small gain coefficients. Noise present. The error stays fairly large; however, its average is around zero. The variation is due to noise.

11.9. The Kalman Filter

The Kalman filter is a linear estimator that minimizes the mean squared error as long as the target dynamics are modeled accurately. All other recursive filters, such as the $\alpha\beta\gamma$ and the Benedict-Bordner filters, are special cases of the general solution provided by the Kalman filter for the mean squared estimation problem. Additionally, the Kalman filter has the following advantages:

1. *The gain coefficients are computed dynamically. This means that the same filter can be used for a variety of maneuvering target environments.*
2. *The Kalman filter gain computation adapts to varying detection histories, including missed detections.*
3. *The Kalman filter provides an accurate measure of the covariance matrix. This allows for better implementation of the gating and association processes.*
4. *The Kalman filter makes it possible to partially compensate for the effects of miss-correlation and miss-association.*

Many derivations of the Kalman filter exist in the literature; only results are provided in this chapter. Fig. 11.28 shows a block diagram for the Kalman filter. The Kalman filter equations can be deduced from Fig. 11.28. The filtering equation is

$$\underline{x}(n|n) = \underline{x}_s(n) = \underline{x}(n|n-1) + K(n)[\underline{y}(n) - \underline{\underline{G}}\,\underline{x}(n|n-1)] \qquad \textbf{(11.127)}$$

The measurement vector is

$$\underline{y}(n) = \underline{\underline{G}}\,\underline{x}(n) + \underline{v}(n) \qquad \textbf{(11.128)}$$

where $\underline{v}(n)$ is zero mean, white Gaussian noise with covariance $\Re_c$,

$$\Re_c = E\{\underline{y}(n)\ \underline{y}^t(n)\} \qquad \textbf{(11.129)}$$

The gain (weights) vector is dynamically computed as

$$\underline{K}(n) = \underline{P}(n|n-1)\underline{G}^t[\underline{\underline{G}}\,\underline{\underline{P}}(n|n-1)\underline{G}^t + \Re_c]^{-1} \qquad \textbf{(11.130)}$$

where the measurement noise matrix $\underline{P}$ represents the predictor covariance matrix, and is equal to

$$\underline{P}(n+1|n) = E\{\underline{x}_s(n+1)\underline{x}^*{}_s(n)\} = \underline{\Phi}\,\underline{P}(n|n)\underline{\Phi}^t + \underline{Q} \qquad \textbf{(11.131)}$$

where $\underline{Q}$ is the covariance matrix for the input $\underline{u}$,

$$\underline{\underline{Q}} = E\{\underline{u}(n)\ \underline{u}^t(n)\} \tag{11.132}$$

The corrector equation (covariance of the smoothed estimate) is

$$\underline{\underline{P}}(n|n) = [\underline{\underline{I}} - \underline{\underline{K}}(n)\underline{\underline{G}}]\underline{\underline{P}}(n|n-1) \tag{11.133}$$

Finally, the predictor equation is

$$\underline{x}(n+1|n) = \underline{\underline{\Phi}}\underline{x}(n|n) \tag{11.134}$$

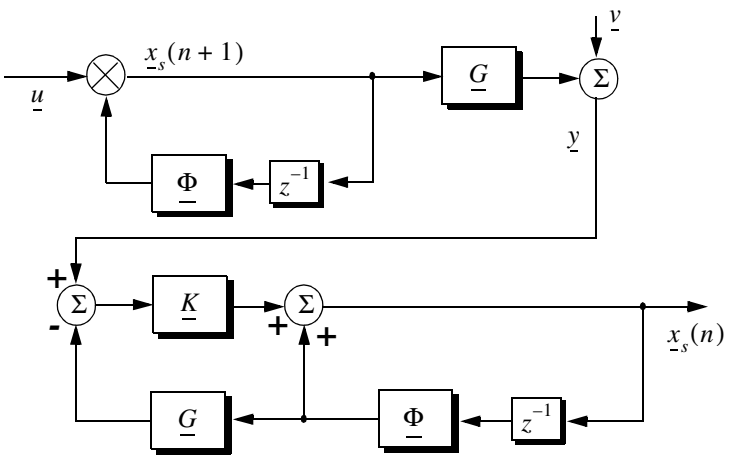

Figure 11.28. Structure of the Kalman filter.

11.9.1. The Singer αβγ-Kalman Filter

The Singer[1] filter is a special case of the Kalman where the filter is governed by a specified target dynamic model whose acceleration is a random process with autocorrelation function given by

$$E\{\ddot{x}(t)\ \ddot{x}(t+t_1)\} = \sigma_a^2\ e^{-\frac{|t_1|}{\tau_m}} \tag{11.135}$$

1. Singer, R. A., Estimating Optimal Tracking Filter Performance for Manned Maneuvering Targets, *IEEE Transaction on aerospace and Electronics, AES-5*, July, 1970. pp. 473-483.

where τ_m is the correlation time of the acceleration due to target maneuver or atmospheric turbulence. The correlation time τ_m may vary from as low as 10 seconds for aggressive maneuvering to as large as 60 seconds for lazy maneuver cases.

Singer defined the random target acceleration model by a first order Markov process given by

$$\ddot{x}(n+1) = \rho_m \ \ddot{x}(n) + \sqrt{1-\rho_m^2} \ \sigma_m \ w(n) \tag{11.136}$$

where $w(n)$ is a zero mean, Gaussian random variable with unity variance, σ_m is the maneuver standard deviation, and the maneuvering correlation coefficient ρ_m is given by

$$\rho_m = e^{-\frac{T}{\tau_m}} \tag{11.137}$$

The continuous time domain system that corresponds to these conditions is as the Wiener-Kolmogorov whitening filter which is defined by the differential equation

$$\frac{d}{dt}v(t) = -\beta_m v(t) + w(t) \tag{11.138}$$

where β_m is equal to $1/\tau_m$. The maneuvering variance using Singer's model is given by

$$\sigma_m^2 = \frac{A_{max}^2}{3}[1 + 4P_{max} - P_0] \tag{11.139}$$

A_{max} is the maximum target acceleration with probability P_{max} and the term P_0 defines the probability that the target has no acceleration.

The transition matrix that corresponds to the Singer filter is given by

$$\underline{\Phi} = \begin{bmatrix} 1 & T & \frac{1}{\beta_m^2}(-1 + \beta_m T + \rho_m) \\ 0 & 1 & \frac{1}{\beta_m}(1 - \rho_m) \\ 0 & 0 & \rho_m \end{bmatrix} \tag{11.140}$$

Note that when $T\beta_m = T/\tau_m$ is small (the target has constant acceleration), then Eq. (11.140) reduces to Eq. (11.114). Typically, the sampling interval T is much less than the maneuver time constant τ_m; hence, Eq. (11.140) can be accurately replaced by its second order approximation. More precisely,

$$\underline{\Phi} = \begin{bmatrix} 1 & T & T^2/2 \\ 0 & 1 & T(1-T/2\tau_m) \\ 0 & 0 & \rho_m \end{bmatrix} \tag{11.141}$$

The covariance matrix was derived by Singer, and it is equal to

$$\underline{C} = \frac{2\sigma_m^2}{\tau_m} \begin{bmatrix} C_{11} & C_{12} & C_{13} \\ C_{21} & C_{22} & C_{23} \\ C_{31} & C_{32} & C_{33} \end{bmatrix} \tag{11.142}$$

where

$$C_{11} = \sigma_x^2 = \frac{1}{2\beta_m^5}\left[1 - e^{-2\beta_m T} + 2\beta_m T + \frac{2\beta_m^3 T^3}{3} - 2\beta_m^2 T^2 - 4\beta_m T e^{-\beta_m T}\right] \tag{11.143}$$

$$C_{12} = C_{21} = \frac{1}{2\beta_m^4}[e^{-2\beta_m T} + 1 - 2e^{-\beta_m T} + 2\beta_m T e^{-\beta_m T} - 2\beta_m T + \beta_m^2 T^2] \tag{11.144}$$

$$C_{13} = C_{31} = \frac{1}{2\beta_m^3}[1 - e^{-2\beta_m T} - 2\beta_m T e^{-\beta_m T}] \tag{11.145}$$

$$C_{22} = \frac{1}{2\beta_m^3}[4e^{-\beta_m T} - 3 - e^{-2\beta_m T} + 2\beta_m T] \tag{11.146}$$

$$C_{23} = C_{32} = \frac{1}{2\beta_m^2}[e^{-2\beta_m T} + 1 - 2e^{-\beta_m T}] \tag{11.147}$$

$$C_{33} = \frac{1}{2\beta_m}[1 - e^{-2\beta_m T}] \tag{11.148}$$

Two limiting cases are of interest:

1. *The short sampling interval case ($T \ll \tau_m$),*

$$\lim_{\beta_m T \to 0} \underline{C} = \frac{2\sigma_m^2}{\tau_m} \begin{bmatrix} T^5/20 & T^4/8 & T^3/6 \\ T^4/8 & T^3/3 & T^2/2 \\ T^3/6 & T^2/2 & T \end{bmatrix} \tag{11.149}$$

and the state transition matrix is computed from Eq. (11.141) as

$$\lim_{\beta_m T \to 0} \underline{\Phi} = \begin{bmatrix} 1 & T & T^2/2 \\ 0 & 1 & T \\ 0 & 0 & 1 \end{bmatrix} \tag{11.150}$$

which is the same as the case for the $\alpha\beta\gamma$ filter (constant acceleration).

2. *The long sampling interval ($T \gg \tau_m$). This condition represents the case when acceleration is a white noise process. The corresponding covariance and transition matrices are, respectively, given by*

$$\lim_{\beta_m T \to \infty} \underline{C} = \sigma_m^2 \begin{bmatrix} \dfrac{2T^3\tau_m}{3} & T^2\tau_m & \tau_m^2 \\ T^2\tau_m & 2T\tau_m & \tau_m \\ \tau_m^2 & \tau_m & 1 \end{bmatrix} \tag{11.151}$$

$$\lim_{\beta_m T \to \infty} \underline{\Phi} = \begin{bmatrix} 1 & T & T\tau_m \\ 0 & 1 & \tau_m \\ 0 & 0 & 0 \end{bmatrix} \tag{11.152}$$

Note that under the condition that $T \gg \tau_m$, the cross correlation terms C_{13} and C_{23} become very small. It follows that estimates of acceleration are no longer available, and thus a two state filter model can be used to replace the three state model. In this case,

$$\underline{C} = 2\sigma_m^2\tau_m \begin{bmatrix} T^3/3 & T^2/2 \\ T^2/2 & T \end{bmatrix} \tag{11.153}$$

$$\underline{\Phi} = \begin{bmatrix} 1 & T \\ 0 & 1 \end{bmatrix} \tag{11.154}$$

11.9.2. Relationship between Kalman and $\alpha\beta\gamma$ Filters

The relationship between the Kalman filter and the $\alpha\beta\gamma$ filters can be easily obtained by using the appropriate state transition matrix $\underline{\Phi}$, and gain vector $\underline{K}$ corresponding to the $\alpha\beta\gamma$ in Eq. (11.127). Thus,

$$\begin{bmatrix} x(n|n) \\ \dot{x}(n|n) \\ \ddot{x}(n|n) \end{bmatrix} = \begin{bmatrix} x(n|n-1) \\ \dot{x}(n|n-1) \\ \ddot{x}(n|n-1) \end{bmatrix} + \begin{bmatrix} k_1(n) \\ k_2(n) \\ k_3(n) \end{bmatrix} [x_0(n) - x(n|n-1)] \tag{11.155}$$

with (see Fig. 11.21)

$$x(n|n-1) = x_s(n-1) + T\ \dot{x}_s(n-1) + \frac{T^2}{2}\ \ddot{x}_s(n-1) \tag{11.156}$$

$$\dot{x}(n|n-1) = \dot{x}_s(n-1) + T\ \ddot{x}_s(n-1) \tag{11.157}$$

$$\ddot{x}(n|n-1) = \ddot{x}_s(n-1) \tag{11.158}$$

Comparing the previous three equations with the $\alpha\beta\gamma$ filter equations yields,

$$\begin{bmatrix} \alpha \\ \beta \\ \frac{\beta}{T} \\ \frac{\gamma}{T^2} \end{bmatrix} = \begin{bmatrix} k_1 \\ k_2 \\ k_3 \end{bmatrix} \tag{11.159}$$

Additionally, the covariance matrix elements are related to the gain coefficients by

$$\begin{bmatrix} k_1 \\ k_2 \\ k_3 \end{bmatrix} = \frac{1}{C_{11} + \sigma_v^2} \begin{bmatrix} C_{11} \\ C_{12} \\ C_{13} \end{bmatrix} \tag{11.160}$$

Eq. (11.160) indicates that the first gain coefficient depends on the estimation error variance to the total residual variance, while the other two gain coefficients are calculated through the covariances between the second and third states and the first observed state.

MATLAB Function "kalman_filter.m"

The function *"kalman_filter.m"*[1] implements the Singer-$\alpha\beta\gamma$ Kalman filter. It is given in Listing 11.4 in Section 11.10. The syntax is as follows:

[residual, estimate] = kalman_filter(npts, T, X0, inp, R, nvar)

1. This function was written by Mr. Edward Shamsi of COLSA Corporation in Huntsville, AL.

where

Symbol	Description	Status
npts	*number of points in input position*	*input*
T	*sampling interval*	*input*
X0	*initial state vector*	*input*
inp	*input array*	*input*
R	*noise variance see Eq. (11-129)*	*input*
nvar	*desired state noise variance*	*input*
residual	*array of position error (residual)*	*output*
estimate	*array of predicted position*	*output*

Note that *"kalman_filter.m"* uses MATLAB's function *"normrnd.m"* to generate zero mean Gaussian noise, which is part of MATLAB's Statistics Toolbox.

To illustrate how to use the functions "*kalman_filter.m",* consider the inputs shown in Figs. 11.22 and 11.23. Figs. 11.29 and 11.30 show the residual error and predicted position corresponding to Figs. 11.22 and 11.23. These plots can be reproduced using the program *"fig11_28.m"* given in Listing 11.5 in Section 11.10.

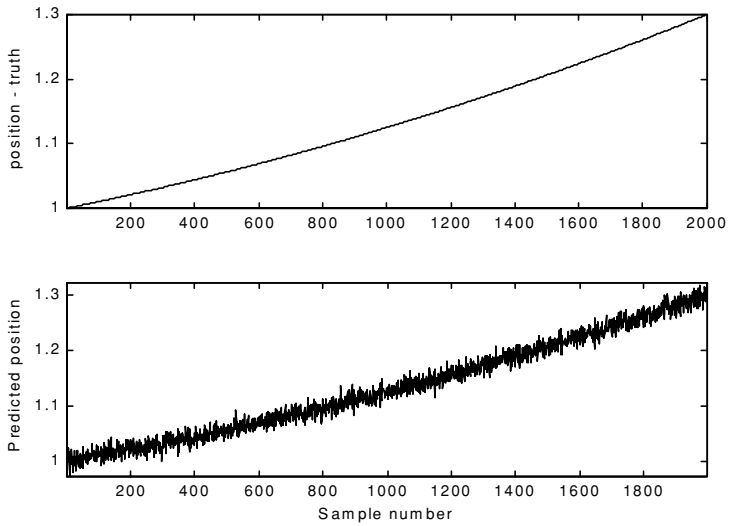

Figure 11.29a. True and predicted positions. Lazy maneuvering. Plot produced using the function *"kalman_filter.m".*

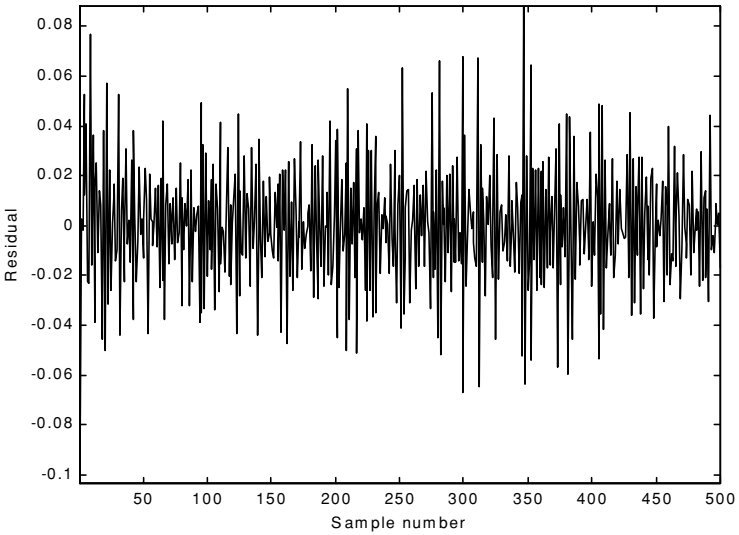

Figure 11.29b. Residual corresponding to Fig. 11.29a.

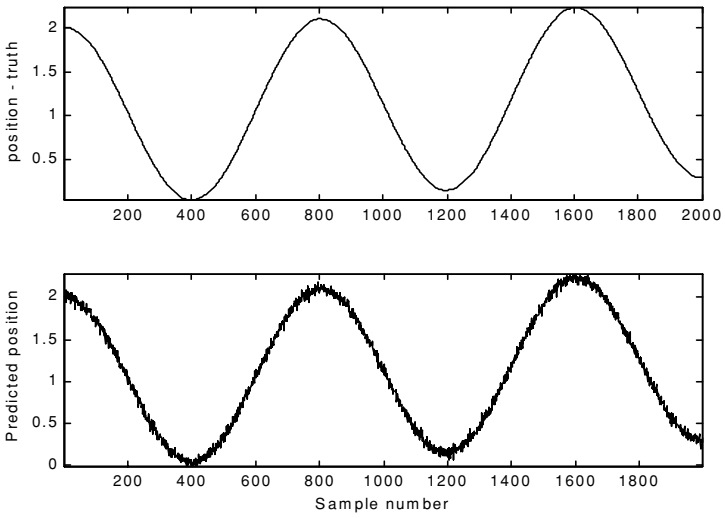

Figure 11.30a. True and predicted positions. Aggressive maneuvering. Plot produced using the function *"kalman_filter.m"*.

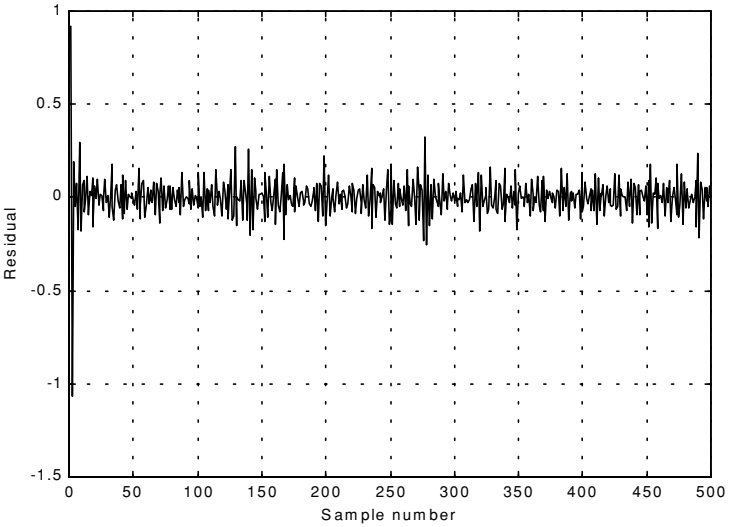

Figure 11.30b. Residual corresponding to Fig. 11.30a.

11.10. MATLAB Programs and Functions

This section contains listings of all MATLAB programs and functions used in this chapter. Users are encouraged to rerun these codes with different inputs in order to enhance their understanding of the theory.

Listing 11.1. MATLAB Function "mono_pulse.m"

```
function mono_pulse(phi0)
eps = 0.0000001;
angle = -pi:0.01:pi;
y1 = sinc(angle + phi0);
y2 = sinc((angle - phi0));
ysum = y1 + y2;
ydif = -y1 + y2;
figure (1)
plot (angle,y1,'k',angle,y2,'k');
grid;
xlabel ('Angle - radians')
ylabel ('Squinted patterns')
figure (2)
plot(angle,ysum,'k');
```

```
grid;
xlabel ('Angle - radians')
ylabel ('Sum pattern')
figure (3)
plot (angle,ydif,'k');
grid;
xlabel ('Angle - radians')
ylabel ('Difference pattern')
angle = -pi/4:0.01:pi/4;
y1 = sinc(angle + phi0);
y2 = sinc((angle - phi0));
ydif = -y1 + y2;
ysum = y1 + y2;
dovrs = ydif ./ ysum;
figure(4)
plot (angle,dovrs,'k');
grid;
xlabel ('Angle - radians')
ylabel ('voltage gain')
```

Listing 11.2. MATLAB Function "ghk_tracker.m"

```
function [residual, estimate] = ghk_tracker (X0, smoocof, inp, npts, T, nvar)
rn = 1.;
% read the initial estimate for the state vector
X = X0;
theta = smoocof;
%compute values for alpha, beta, gamma
w1 = 1. - (theta^3);
w2 = 1.5 * (1. + theta) * ((1. - theta)^2) / T;
w3 = ((1. - theta)^3) / (T^2);
% setup the transition matrix PHI
PHI = [1. T (T^2)/2.;0. 1. T;0. 0. 1.];
while rn < npts ;
  %use the transition matrix to predict the next state
  XN = PHI * X;
  error = (inp(rn) + normrnd(0,nvar)) - XN(1);
  residual(rn) = error;
  tmp1 = w1 * error;
  tmp2 = w2 * error;
  tmp3 = w3 * error;
  % compute the next state
  X(1) = XN(1) + tmp1;
  X(2) = XN(2) + tmp2;
  X(3) = XN(3) + tmp3;
  estimate(rn) = X(1);
  rn = rn + 1.;
end
```

return

MATLAB Function "ghk_traker1.m"

```
function [residual, estimate] = ghk_tracker1 (X0, smoocof, inp, npts, T)
rn = 1.;
% read the initial estimate for the state vector
X = X0;
theta = smoocof;
%compute values for alpha, beta, gamma
w1 = 1. - (theta^3);
w2 = 1.5 * (1. + theta) * ((1. - theta)^2) / T;
w3 = ((1. - theta)^3) / (T^2);
% setup the transition matrix PHI
PHI = [1. T (T^2)/2.;0. 1. T;0. 0. 1.];
while rn < npts ;
  %use the transition matrix to predict the next state
  XN = PHI * X;
  error = inp(rn)  - XN(1);
  residual(rn) = error;
  tmp1 = w1 * error;
  tmp2 = w2 * error;
  tmp3 = w3 * error;
  % compute the next state
  X(1) = XN(1) + tmp1;
  X(2) = XN(2) + tmp2;
  X(3) = XN(3) + tmp3;
  estimate(rn) = X(1);
  rn = rn + 1.;
end
return
```

Listing 11.3. MATLAB Program "fig11_21.m"

```
clear all
eps = 0.0000001;
npts = 5000;
del = 1./ 5000.;
t = 0. : del : 1.;
% generate input sequence
inp = 1.+ t.^3 + .5 .*t.^2 + cos(2.*pi*10 .* t) ;
% read the initial estimate for the state vector
X0 = [2,.1,.01]';
% this is the update interval in seconds
T = 100. * del;
% this is the value of the smoothing coefficient
xi = .91;
[residual, estimate] = ghk_tracker (X0, xi, inp, npts, T, .01);
```

```
figure(1)
plot (residual(1:500))
xlabel ('Sample number')
ylabel ('Residual error')
grid
figure(2)
NN = 4999.;
n = 1:NN;
plot (n,estimate(1:NN),'b',n,inp(1:NN),'r')
xlabel ('Sample number')
ylabel ('Position')
legend ('Estimated','Input')
```

Listing 11.4. MATLAB Function "kalman_filter.m"

```
function [residual, estimate] = kalman_filter(npts, T, X0, inp, R, nvar)
N = npts;
rn=1;
% read the initial estimate for the state vector
X = X0;
% it is assumed that the measurmeny vector H=[1,0,0]
% this is the state noise variance
VAR = nvar;
% setup the initial value for the predication covariance.
S = [1. 1. 1.; 1. 1. 1.; 1. 1. 1.];
% setup the transition matrix PHI
PHI = [1. T (T^2)/2.; 0. 1. T; 0. 0. 1.];
% setup the state noise covariance matrix
Q(1,1) = (VAR * (T^5)) / 20.;
Q(1,2) = (VAR * (T^4)) / 8.;
Q(1,3) = (VAR * (T^3)) / 6.;
Q(2,1) = Q(1,2);
Q(2,2) = (VAR * (T^3)) / 3.;
Q(2,3) = (VAR * (T^2)) / 2.;
Q(3,1) = Q(1,3);
Q(3,2) = Q(2,3);
Q(3,3) = VAR * T;
while rn < N ;
  %use the transition matrix to predict the next state
  XN = PHI * X;
  % Perform error covariance extrapolation
  S = PHI * S * PHI' + Q;
  % compute the Kalman gains
  ak(1) = S(1,1) / (S(1,1) + R);
  ak(2) = S(1,2) / (S(1,1) + R);
  ak(3) = S(1,3) / (S(1,1) + R);
  %perform state estimate update:
  error = inp(rn) + normrnd(0,R) - XN(1);
```

```
  residual(rn) = error;
  tmp1 = ak(1) * error;
  tmp2 = ak(2) * error;
  tmp3 = ak(3) * error;
  X(1) = XN(1) + tmp1;
  X(2) = XN(2) + tmp2;
  X(3) = XN(3) + tmp3;
  estimate(rn) = X(1);
  % update the error covariance
  S(1,1) = S(1,1) * (1. -ak(1));
  S(1,2) = S(1,2) * (1. -ak(1));
  S(1,3) = S(1,3) * (1. -ak(1));
  S(2,1) = S(1,2);
  S(2,2) = -ak(2) * S(1,2) + S(2,2);
  S(2,3) = -ak(2) * S(1,3) + S(2,3);
  S(3,1) = S(1,3);
  S(3,3) = -ak(3) * S(1,3) + S(3,3);
  rn = rn + 1.;
end
```

Listing 11.5. MATLAB Program "fig11_28.m"

```
clear all
npts = 2000;
del = 1/2000;
t = 0:del:1;
inp = (1+.2 .* t + .1 .*t.^2) + cos(2. * pi * 2.5 .* t);
X0 = [1,.1,.01]';
% it is assumed that the measurmeny vector H=[1,0,0]
% this is the update interval in seconds
T = 1.;
% enter the measurement noise variance
R = .035;
% this is the state noise variance
nvar = .5;
[residual, estimate] = kalman_filter(npts, T, X0, inp, R, nvar);
figure(1)
plot(residual)
xlabel ('Sample number')
ylabel ('Residual')
figure(2)
subplot(2,1,1)
plot(inp)
axis tight
ylabel ('position - truth')
subplot(2,1,2)
plot(estimate)
axis tight
```

```
xlabel ('Sample number')
ylabel ('Predicted position')
```

Problems

11.1. Show that in order to be able to quickly achieve changing the beam position the error signal needs to be a linear function of the deviation angle.

11.2. Prepare a short report on the vulnerability of conical scan to amplitude modulation jamming. In particular consider the self-protecting technique called "Gain Inversion."

11.3. Consider a conical scan radar. The pulse repetition interval is $10\mu s$. Calculate the scan rate so that at least ten pulses are emitted within one scan.

11.4. Consider a conical scan antenna whose rotation around the tracking axis is completed in 4 seconds. If during this time 20 pulses are emitted and received, calculate the radar PRF and the unambiguous range.

11.5. Reproduce Fig. 11.11 for $\varphi_0 = 0.05, 0.1, 0.15$ radians.

11.6. Reproduce Fig. 11.13 for the squint angles defined in the previous problem.

11.7. Derive Eq. (11.33) and Eq. (11.34).

11.8. Consider a monopulse radar where the input signal is comprised of both target return and additive white Gaussian noise. Develop an expression for the complex ratio Σ/Δ.

11.9. Consider the sum and difference signals defined in Eqs. (11.7) and (11.8). What is the squint angle φ_0 that maximizes $\Sigma(\varphi = 0)$?

11.10. A certain system is defined by the following difference equation:

$$y(n) + 4y(n-1) + 2y(n-2) = w(n)$$

Find the solution to this system for $n > 0$ and $w = \delta$.

11.11. Prove the state transition matrix properties (i.e., Eqs. (11.30) through (11.36)).

11.12. Suppose that the state equations for a certain discrete time LTI system are

$$\begin{bmatrix} x_1(n+1) \\ x_2(n+1) \end{bmatrix} = \begin{bmatrix} 0 & 1 \\ -2 & -3 \end{bmatrix} \begin{bmatrix} x_1(n) \\ x_2(n) \end{bmatrix} + \begin{bmatrix} 0 \\ 1 \end{bmatrix} w(n)$$

If $y(0) = y(1) = 1$, find $y(n)$ when the input is a step function.

11.13. Derive Eq. (11.55).

11.14. Derive Eq. (11.75).

11.15. Using Eq. (11.83), compute a general expression (in terms of the transfer function) for the steady state errors when the input sequence is:

$$u1 = \{0, 1, 1, 1, 1, \ldots\}$$

$$u2 = \{0, 1, 2, 3, \ldots\}$$

$$u3 = \{0, 1^2, 2^2, 3^2, \ldots\}$$

$$u4 = \{0, 1^3, 2^3, 3^3, \ldots\}$$

11.16. Verify the results in Eqs. (11.99) and (11.100).

11.17. Develop an expression for the steady state error transfer function for an $\alpha\beta$ tracker.

11.18. Using the result of the previous problem and Eq. (11.83), compute the steady-state errors for the $\alpha\beta$ tracker with the inputs defined in Problem 11.13.

11.19. Design a critically damped $\alpha\beta$, when the measurement noise variance associated with position is $\sigma_v^2 = 50m$ and when the desired standard deviation of the filter prediction error is $5.5m$.

11.20. Derive Eqs. (11.118) through (11.120).

11.21. Derive Eq. (11.122).

11.22. Consider a $\alpha\beta\gamma$ filter. We can define six transfer functions: $H_1(z)$, $H_2(z)$, $H_3(z)$, $H_4(z)$, $H_5(z)$, and $H_6(z)$ (predicted position, predicted velocity, predicted acceleration, smoothed position, smoothed velocity, and smoothed acceleration). Each transfer function has the form

$$H(z) = \frac{a_3 + a_2 z^{-1} + a_1 z^{-2}}{1 + b_2 z^{-1} + b_1 z^{-2} + b_0 z^{-3}}$$

The denominator remains the same for all six transfer functions. Compute all the relevant coefficients for each transfer function.

11.23. Verify the results obtained for the two limiting cases of the Singer-Kalman filter.

11.24. Verify Eq. (11.160).

Chapter 12 *Synthetic Aperture Radar*

12.1. Introduction

Modern airborne radar systems are designed to perform a large number of functions which range from detection and discrimination of targets to mapping large areas of ground terrain. This mapping can be performed by the Synthetic Aperture Radar (SAR). Through illuminating the ground with coherent radiation and measuring the echo signals, SAR can produce high resolution two-dimensional (and in some cases three-dimensional) imagery of the ground surface. The quality of ground maps generated by SAR is determined by the size of the resolution cell. A resolution cell is specified by range and azimuth resolutions of the system. Other factors affecting the size of the resolution cells are (1) size of the processed map and the amount of signal processing involved; (2) cost consideration; and (3) size of the objects that need to be resolved in the map. For example, mapping gross features of cities and coastlines does not require as much resolution when compared to resolving houses, vehicles, and streets.

SAR systems can produce maps of reflectivity versus range and Doppler (cross range). Range resolution is accomplished through range gating. Fine range resolution can be accomplished by using pulse compression techniques. The azimuth resolution depends on antenna size and radar wavelength. Fine azimuth resolution is enhanced by taking advantage of the radar motion in order to synthesize a larger antenna aperture. Let N_r denote the number of range bins and let N_a denote the number of azimuth cells. It follows that the total number of resolution cells in the map is $N_r N_a$. SAR systems that are

generally concerned with improving azimuth resolution are often referred to as Doppler Beam-Sharpening (DBS) SARs. In this case, each range bin is processed to resolve targets in Doppler which correspond to azimuth. This chapter is presented in the context of DBS.

Due to the large amount of signal processing required in SAR imagery, the early SAR designs implemented optical processing techniques. Although such optical processors can produce high quality radar images, they have several shortcomings. They can be very costly and are, in general, limited to making strip maps. Motion compensation is not easy to implement for radars that utilize optical processors. With the recent advances in solid state electronics and Very Large Scale Integration (VLSI) technologies, digital signal processing in real time has been made possible in SAR systems.

12.2. Real Versus Synthetic Arrays

A linear array of size N, element spacing d, isotropic elements, and wavelength λ is shown in Fig. 12.1. A synthetic linear array is formed by linear motion of a single element, transmitting and receiving from distinct positions that correspond to the element locations in a real array. Thus, synthetic array geometry is similar to that of a real array, with the exception that the array exists only at a single element position at a time.

The two-way radiation pattern (in the direction-sine $\sin\beta$) for a real linear array was developed in Chapter 10; it is repeated here as Eq. (12.1):

$$G(\sin\beta) = \left(\frac{\sin((Nkd\sin\beta)/2)}{\sin((kd\sin\beta)/2)}\right)^2 \tag{12.1}$$

Since a synthetic array exists only at a single location at a time, the array transmission is sequential with only one element receiving. Therefore, the returns received by the successive array positions differ in phase by $\delta = k\Delta r$, where $k = 2\pi/\lambda$, and $\Delta r = 2d\sin\beta$ is the round-trip path difference between contiguous element positions. The two-way array pattern for a synthetic array is the coherent sum of the returns at all the array positions.

Thus, the overall two-way electric field for the synthetic array is

$$E(\sin\beta) = 1 + e^{-j2\delta} + e^{-j4\delta} + \ldots + e^{-j2(N-1)\delta} = \sum_{n=1}^{N} e^{-j2(N-1)kd\sin\beta} \tag{12.2}$$

By using similar analysis as in Section 10.4, the two-way electric field for a synthetic array can be expressed as

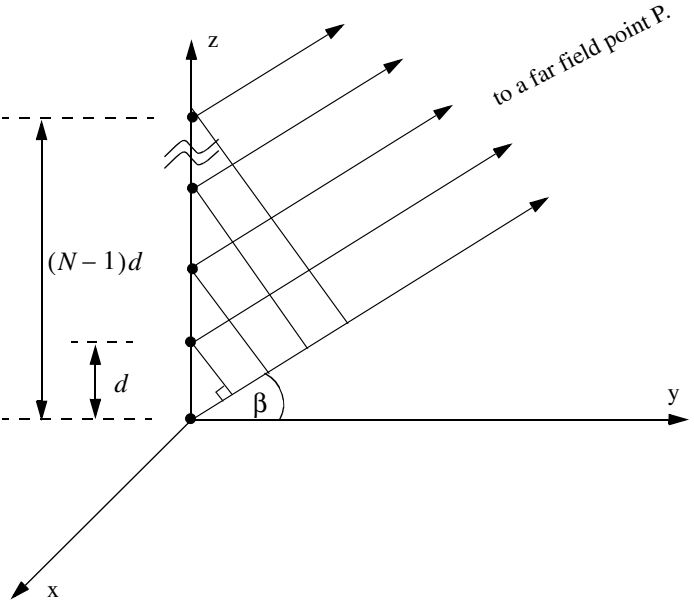

Figure 12.1. Geometry of real or synthetic array.

$$E(\sin\beta) = \frac{\sin(Nkd\sin\beta)}{\sin(kd\sin\beta)} \tag{12.3}$$

and the two-way radiation pattern is

$$G(\sin\beta) = |E(\sin\beta)| = \left|\frac{\sin(Nkd\sin\beta)}{\sin(kd\sin\beta)}\right| \tag{12.4}$$

Comparison of Eq. (12.4) and Eq. (12.1) indicates that the two-way radiation pattern for a real array is of the form $(\sin\theta/\theta)^2$, while it is of the form $\sin 2\theta/2\theta$ for the synthetic array. Consequently, for the same size aperture, the main beam of the synthetic array is twice as narrow as that for the real array. Or equivalently, the resolution of a synthetic array of length L (aperture size) is equal to that of a real array with twice the aperture size $(2L)$, as illustrated in Fig. 12.2.

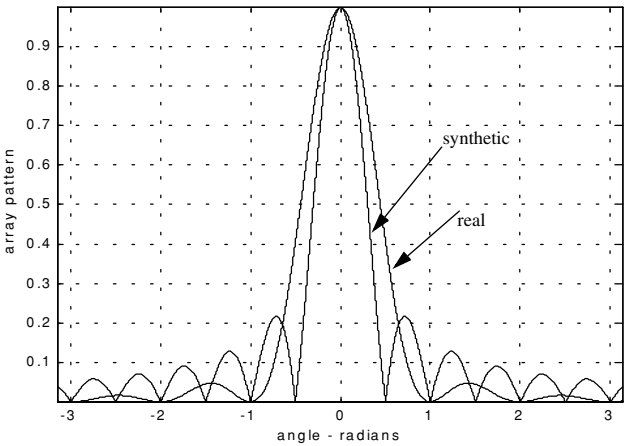

Figure 12.2. Pattern difference between real and synthetic arrays. This plot can be reproduced using MATLAB program *"fig12_2.m"* given in Listing 12.1 in Section 12.12.

12.3. Side Looking SAR Geometry

Fig. 12.3 shows the geometry for the standard side looking SAR. We will assume that the platform carrying the radar maintains both fixed altitude h and velocity v. The antenna $3dB$ beam width is θ, and the elevation angle (measured from the z-axis to the antenna axis) is β. The intersection of the antenna beam with the ground defines a footprint. As the platform moves, the footprint scans a swath on the ground.

The radar position with respect to the absolute origin $\vec{O} = (0, 0, 0)$, at any time is the vector $\vec{a}(t)$. The velocity vector $\vec{a}'(t)$ is

$$\vec{a}'(t) = 0 \times \hat{a}_x + v \times \hat{a}_y + 0 \times \hat{a}_z \qquad \textbf{(12.5)}$$

The Line of Sight (LOS) for the current footprint centered at $\vec{q}(t_c)$ is defined by the vector $\vec{R}(t_c)$, where t_c denotes the central time of the observation interval T_{ob} (coherent integration interval). More precisely,

$$(t = t_a + t_c) \;\; ; \;\; -\frac{T_{ob}}{2} \le t \le \frac{T_{ob}}{2} \qquad \textbf{(12.6)}$$

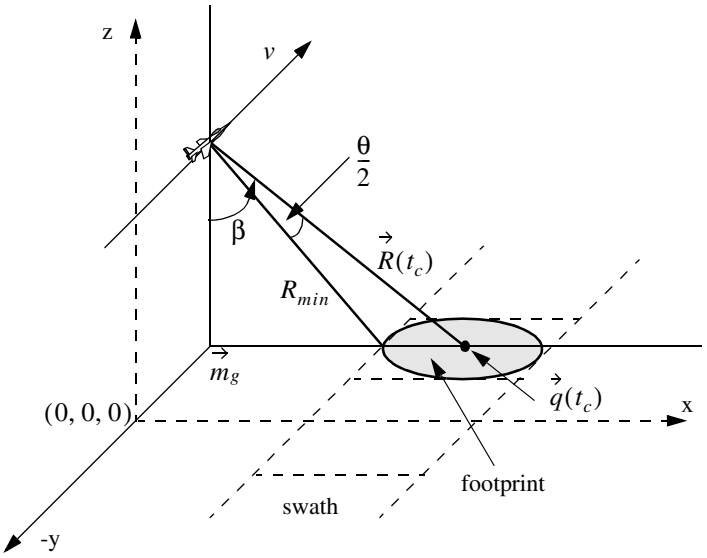

(a)

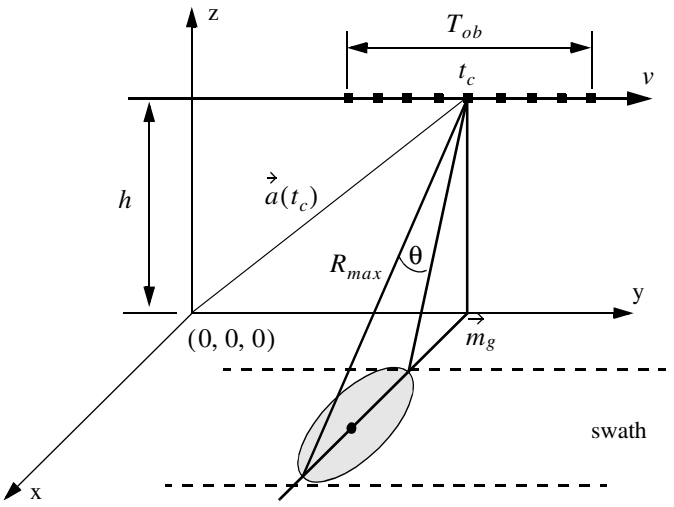

(b)

Figure 12.3. Side looking SAR geometry.

where t_a and t are the absolute and relative times, respectively. The vector $\vec{m}_g$ defines the ground projection of the antenna at central time. The minimum slant range to the swath is R_{min}, and the maximum range is denoted R_{max}, as illustrated by Fig. 12.4. It follows that

$$\begin{aligned} R_{min} &= h/\cos(\beta - \theta/2) \\ R_{max} &= h/\cos(\beta + \theta/2) \\ \left|\vec{R}(t_c)\right| &= h/\cos\beta \end{aligned} \tag{12.7}$$

Notice that the elevation angle β is equal to

$$\beta = 90 - \psi_g \tag{12.8}$$

where ψ_g is the grazing angle. The size of the footprint is a function of the grazing angle and the antenna beam width, as illustrated in Fig. 12.5. The SAR geometry described in this section is referred to as SAR "strip mode" of operation. Another SAR mode of operation, which will not be discussed in this chapter, is called "spot-light mode," where the antenna is steered (mechanically or electronically) to continuously illuminate one spot (footprint) on the ground. In this case, one high resolution image of the current footprint is generated during an observation interval.

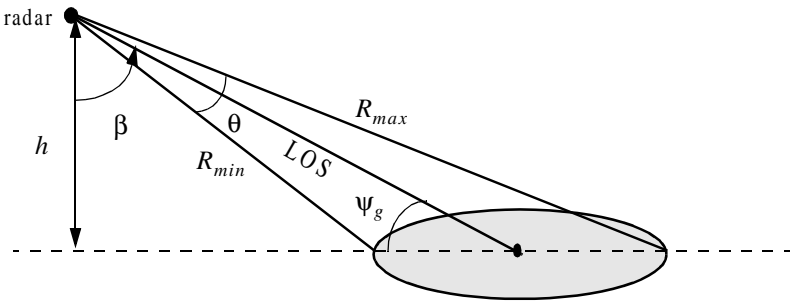

Figure 12.4. Definition of minimum and maximum range.

12.4. SAR Design Considerations

The quality of SAR images is heavily dependent on the size of the map resolution cell shown in Fig. 12.6. The range resolution, ΔR, is computed on the beam LOS, and is given by

$$\Delta R = (c\tau)/2 \tag{12.9}$$

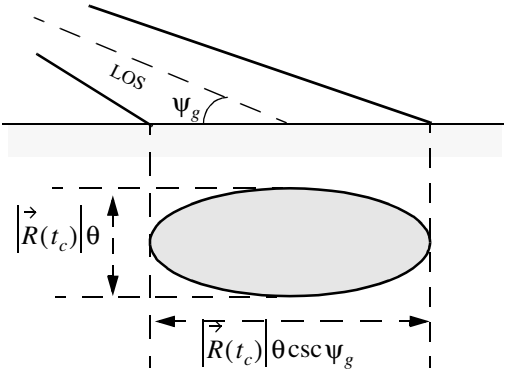

Figure 12.5. Footprint definition.

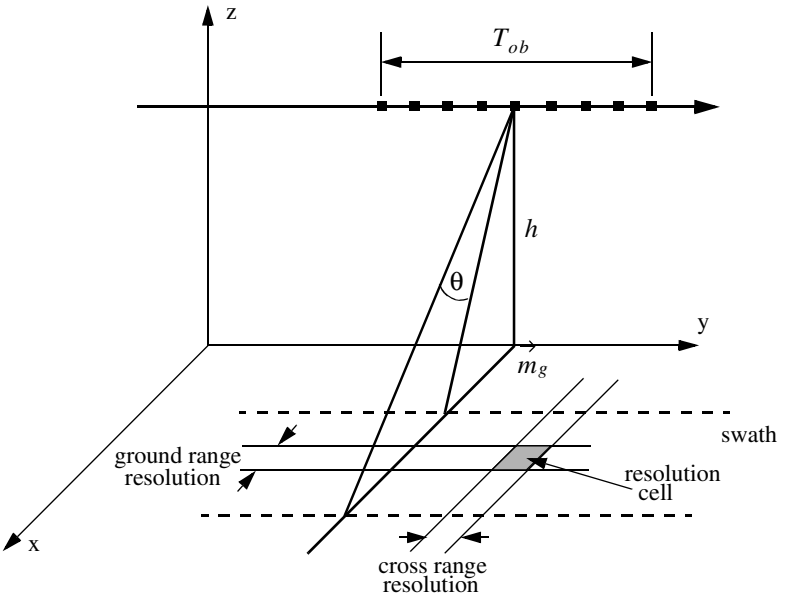

Figure 12.6. Definition of a resolution cell.

where τ is the pulse width. From the geometry in Fig. 12.7 the extent of the range cell ground projection ΔR_g is computed as

$$\Delta R_g = \frac{c\tau}{2} \sec \psi_g \tag{12.10}$$

The azimuth or cross range resolution for a real antenna with a $3dB$ beam width θ (radians) at range R is

$$\Delta A_r = \theta R \tag{12.11}$$

However, the antenna beam width is proportional to the aperture size,

$$\theta \approx \frac{\lambda}{L} \tag{12.12}$$

where λ is the wavelength and L is the aperture length. It follows that

$$\Delta A_r = \frac{\lambda R}{L} \tag{12.13}$$

And since the effective synthetic aperture size is twice that of a real array, the azimuth resolution for a synthetic array is then given by

$$\Delta A = \frac{\lambda R}{2L} \tag{12.14}$$

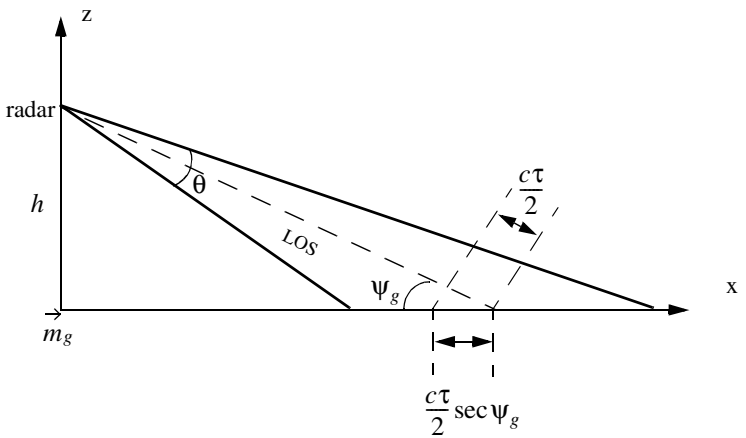

Figure 12.7. Definition of a range cell on the ground.

Furthermore, since the synthetic aperture length L is equal to vT_{ob}, Eq. (12.14) can be rewritten as

$$\Delta A = \frac{\lambda R}{2vT_{ob}} \tag{12.15}$$

The azimuth resolution can be greatly improved by taking advantage of the Doppler variation within a footprint (or a beam). As the radar travels along its flight path the radial velocity to a ground scatterer (point target) within a footprint varies as a function of the radar radial velocity in the direction of that scatterer. The variation of Doppler frequency for a certain scatterer is called the "Doppler history."

Let $R(t)$ denote range to a scatterer at time t, and v_r be the corresponding radial velocity; thus the Doppler shift is

$$f_d = -\frac{2R'(t)}{\lambda} = \frac{2v_r}{\lambda} \tag{12.16}$$

where $R'(t)$ is the range rate to the scatterer. Let t_1 and t_2 be the times when the scatterer enters and leaves the radar beam, respectively, and let t_c be the time that corresponds to minimum range. Fig. 12.8 shows a sketch of the corresponding $R(t)$ (see Eq. (12.16)). Since the radial velocity can be computed as the derivative of $R(t)$ with respect to time, one can clearly see that Doppler frequency is maximum at t_1, zero at t_c, and minimum at t_2, as illustrated in Fig. 12.9.

In general, the radar maximum PRF, $f_{r_{max}}$, must be low enough to avoid range ambiguity. Alternatively, the minimum PRF, $f_{r_{min}}$, must be high enough to avoid Doppler ambiguity. SAR unambiguous range must be at least as wide as the extent of a footprint. More precisely, since target returns from maximum range due to the current pulse must be received by the radar before the next pulse is transmitted, it follows that SAR unambiguous range is given by

$$R_u = R_{max} - R_{min} \tag{12.17}$$

An expression for unambiguous range was derived in Chapter 1, and is repeated here as Eq. (12.18),

$$R_u = \frac{c}{2f_r} \tag{12.18}$$

Combining Eq. (12.18) and Eq. (12.17) yields

$$f_{r_{max}} \leq \frac{c}{2(R_{max} - R_{min})} \tag{12.19}$$

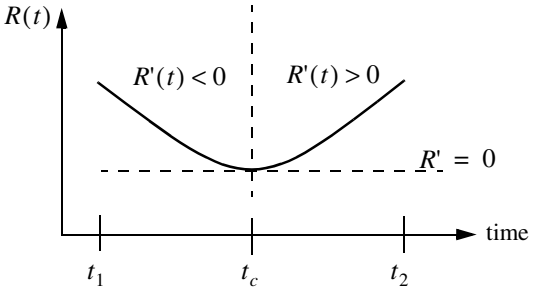

Figure 12.8. Sketch of range versus time for a scatterer.

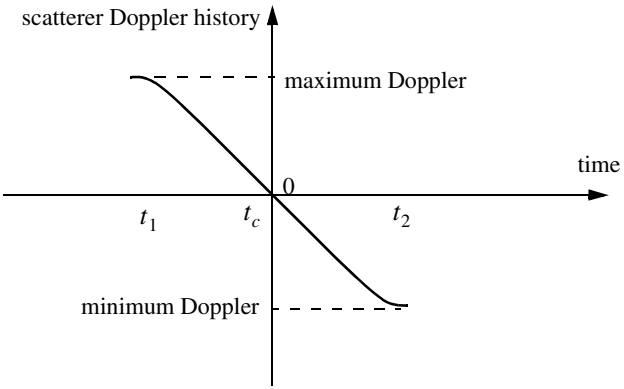

Figure 12.9. Point scatterer Doppler history.

SAR minimum PRF, $f_{r_{min}}$, is selected so that Doppler ambiguity is avoided. In other words, $f_{r_{min}}$ must be greater than the maximum expected Doppler spread within a footprint. From the geometry of Fig. 12.10, the maximum and minimum Doppler frequencies are, respectively, given by

$$\left(f_{d_{max}} = \frac{2v}{\lambda} \cos\left(90 - \frac{\theta}{2}\right)\sin\beta\right) \; ; \; at \;\; t_1 \qquad \textbf{(12.20)}$$

$$\left(f_{d_{min}} = \frac{2v}{\lambda} \cos\left(90 + \frac{\theta}{2}\right)\sin\beta\right) \; ; \; at \;\; t_2 \qquad \textbf{(12.21)}$$

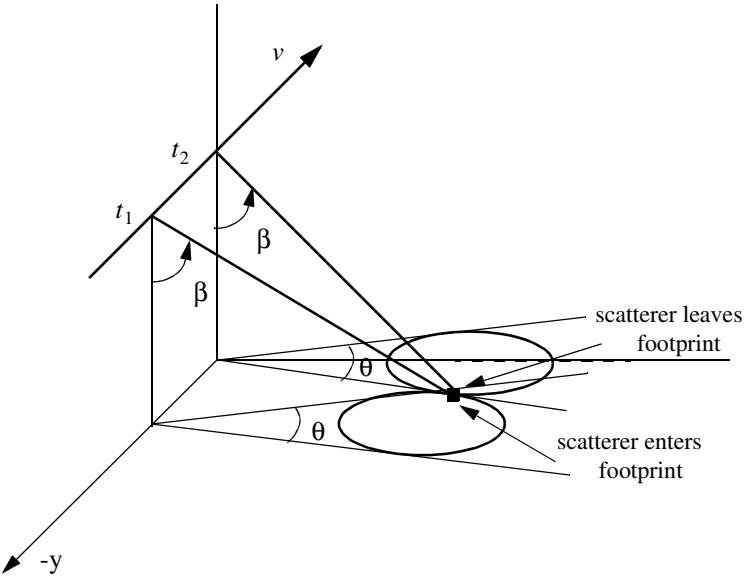

(a)

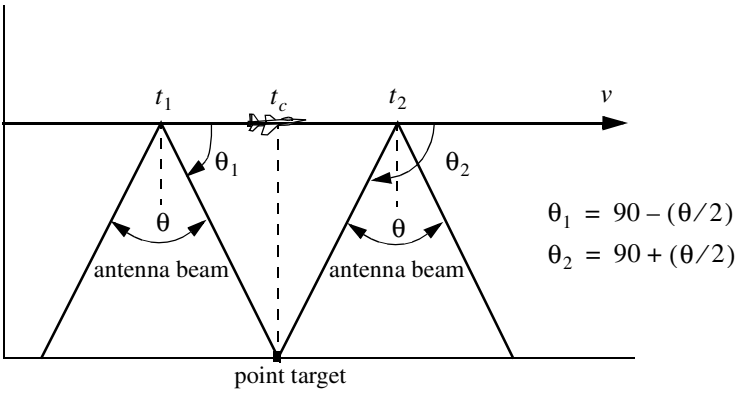

(b)

Figure 12.10. Doppler history computation. (a) Full view; (b) top view.

It follows that the maximum Doppler spread is

$$\Delta f_d = f_{d_{max}} - f_{d_{min}} \tag{12.22}$$

Substituting Eqs. (11.20) and (11.21) into Eq. (12.22) and applying the proper trigonometric identities yield

$$\Delta f_d = \frac{4v}{\lambda} \sin\frac{\theta}{2} \sin\beta \tag{12.23}$$

Finally, by using the small angle approximation we get

$$\Delta f_d \approx \frac{4v}{\lambda} \frac{\theta}{2} \sin\beta = \frac{2v}{\lambda} \theta \sin\beta \tag{12.24}$$

Therefore, the minimum PRF is

$$f_{r_{min}} \geq \frac{2v}{\lambda} \theta \sin\beta \tag{12.25}$$

Combining Eqs. (11.19) and (11.25) we get

$$\frac{c}{2(R_{max} - R_{min})} \geq f_r \geq \frac{2v}{\lambda} \theta \sin\beta \tag{12.26}$$

It is possible to resolve adjacent scatterers at the same range within a footprint based only on the difference of their Doppler histories. For this purpose, assume that the two scatterers are within the kth range bin. Denote their angular displacement as $\Delta\theta$, and let $\Delta f_{d_{min}}$ be the minimum Doppler spread between the two scatterers such that they will appear in two distinct Doppler filters. Using the same methodology that led to Eq. (12.24) we get

$$\Delta f_{d_{min}} = \frac{2v}{\lambda} \Delta\theta \sin\beta_k \tag{12.27}$$

where β_k is the elevation angle corresponding to the kth range bin.

The bandwidth of the individual Doppler filters must be equal to the inverse of the coherent integration interval T_{ob} (i.e., $\Delta f_{d_{min}} = 1/T_{ob}$). It follows that

$$\Delta\theta = \frac{\lambda}{2vT_{ob}\sin\beta_k} \tag{12.28}$$

Substituting L for vT_{ob} yields

$$\Delta\theta = \frac{\lambda}{2L\sin\beta_k} \tag{12.29}$$

Therefore, the SAR azimuth resolution (within the kth range bin) is

$$\Delta A_g = \Delta\theta R_k = R_k \frac{\lambda}{2L\sin\beta_k} \tag{12.30}$$

Note that when $\beta_k = 90°$, Eq. (12.30) is identical to Eq. (12.14).

12.5. SAR Radar Equation

The single pulse radar equation was derived in Chapter 1, and is repeated here as Eq. (12.31),

$$SNR = \frac{P_t G^2 \lambda^2 \sigma}{(4\pi)^3 R_k^4 k T_0 B L_{Loss}} \tag{12.31}$$

where: P_t is peak power; G is antenna gain; λ is wavelength; σ is radar cross section; R_k is radar slant range to the kth range bin; k is Boltzman's constant; T_0 is receiver noise temperature; B is receiver bandwidth; and L_{Loss} is radar losses. The radar cross section is a function of the radar resolution cell and terrain reflectivity. More precisely,

$$\sigma = \sigma^0 \Delta R_g \Delta A_g = \sigma^0 \Delta A_g \frac{c\tau}{2} \sec\psi_g \tag{12.32}$$

where σ^0 is the clutter scattering coefficient, ΔA_g is the azimuth resolution, and Eq. (12.10) was used to replace the ground range resolution. The number of coherently integrated pulses within an observation interval is

$$n = f_r T_{ob} = \frac{f_r L}{v} \tag{12.33}$$

where L is the synthetic aperture size. Using Eq. (12.30) in Eq. (12.33) and rearranging terms yield

$$n = \frac{\lambda R f_r}{2\Delta A_g v} \csc\beta_k \tag{12.34}$$

The radar average power over the observation interval is

$$P_{av} = (P_t / B) f_r \tag{12.35}$$

The SNR for n coherently integrated pulses is then

$$(SNR)_n = nSNR = n \frac{P_t G^2 \lambda^2 \sigma}{(4\pi)^3 R_k^4 k T_0 B L_{Loss}} \tag{12.36}$$

Substituting Eqs. (11.35), (11.34), and (11.32) into Eq. (12.36) and performing some algebraic manipulations give the SAR radar equation,

$$(SNR)_n = \frac{P_{av} G^2 \lambda^3 \sigma^0}{(4\pi)^3 R_k^3 k T_0 L_{Loss}} \frac{\Delta R_g}{2v} \csc\beta_k \tag{12.37}$$

Eq. (12.37) leads to the conclusion that in SAR systems the SNR is (1) inversely proportional to the third power of range; (2) independent of azimuth resolution; (3) function of the ground range resolution; (4) inversely proportional to the velocity v; and (5) proportional to the third power of wavelength.

12.6. SAR Signal Processing

There are two signal processing techniques to sequentially produce a SAR map or image; they are line-by-line processing and Doppler processing. The concept of SAR line-by-line processing is as follows. Through the radar linear motion a synthetic array is formed, where the elements of the current synthetic array correspond to the position of the antenna transmissions during the last observation interval. Azimuth resolution is obtained by forming narrow synthetic beams through combination of the last observation interval returns. Fine range resolution is accomplished in real time by utilizing range gating and pulse compression. For each range bin and each of the transmitted pulses during the last observation interval, the returns are recorded in a two-dimensional array of data that is updated for every pulse. Denote the two-dimensional array of data as MAP.

To further illustrate the concept of line-by-line processing, consider the case where a map of size $N_a \times N_r$ is to be produced, N_a is the number of azimuth cells, and N_r is the number of range bins. Hence, MAP is of size $N_a \times N_r$, where the columns refer to range bins, and the rows refer to azimuth cells. For each transmitted pulse, the echoes from consecutive range bins are recorded sequentially in the first row of MAP. Once the first row is completely filled (i.e., returns from all range bins have been received), all data (in all rows) are shifted downward one row before the next pulse is transmitted. Thus, one row of MAP is generated for every transmitted pulse. Consequently, for the current observation interval, returns from the first transmitted pulse will be located in the bottom row of MAP, and returns from the last transmitted pulse will be in the first row of MAP.

In SAR Doppler processing, the array MAP is updated once every N pulses so that a block of N columns is generated simultaneously. In this case, N refers to the number of transmissions during an observation interval (i.e., size of the synthetic array). From an antenna point of view, this is equivalent to having N adjacent synthetic beams formed in parallel through electronic steering.

12.7. Side Looking SAR Doppler Processing

Consider the geometry shown in Fig. 12.11, and assume that the scatterer C_i is located within the kth range bin. The scatterer azimuth and elevation angles are μ_i and β_i, respectively. The scatterer elevation angle β_i is assumed to be equal to β_k, the range bin elevation angle. This assumption is true if the ground range resolution, ΔR_g, is small; otherwise, $\beta_i = \beta_k + \varepsilon_i$ for some small ε_i; in this chapter $\varepsilon_i = 0$.

The normalized transmitted signal can be represented by

$$s(t) = \cos(2\pi f_0 t - \xi_0) \tag{12.38}$$

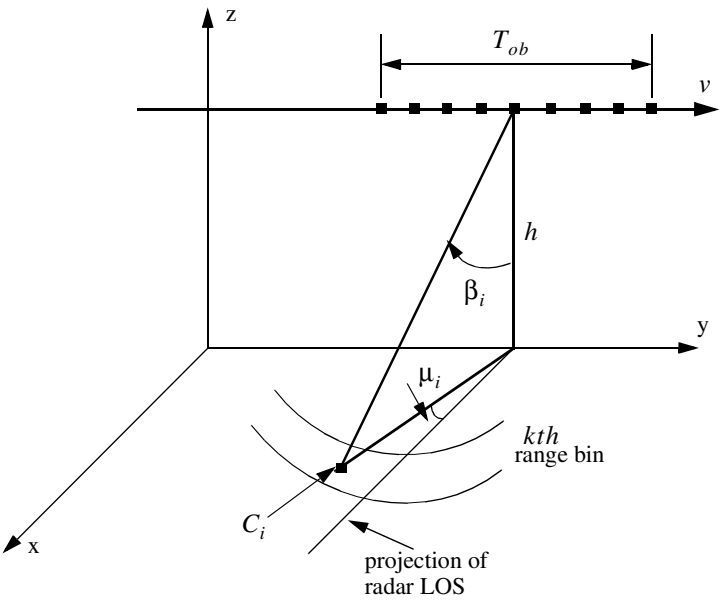

Figure 12.11. A scatterer C_i within the kth range bin.

where f_0 is the radar operating frequency, and ξ_0 denotes the transmitter phase. The returned radar signal from C_i is then equal to

$$s_i(t, \mu_i) = A_i \cos[2\pi f_0(t - \tau_i(t, \mu_i)) - \xi_0] \tag{12.39}$$

where $\tau_i(t, \mu_i)$ is the round-trip delay to the scatterer, and A_i includes scatterer strength, range attenuation, and antenna gain. The round-trip delay is

$$\tau_i(t, \mu_i) = \frac{2r_i(t, \mu_i)}{c} \tag{12.40}$$

where c is the speed of light and $r_i(t, \mu_i)$ is the scatterer slant range. From the geometry in Fig. 12.11, one can write the expression for the slant range to the ith scatterer within the kth range bin as

$$r_i(t, \mu_i) = \frac{h}{\cos\beta_i}\sqrt{1 - \frac{2vt}{h}\cos\beta_i\cos\mu_i\sin\beta_i + \left(\frac{vt}{h}\cos\beta_i\right)^2} \tag{12.41}$$

And by using Eq. (12.40) the round-trip delay can be written as

$$\tau_i(t, \mu_i) = \frac{2}{c}\frac{h}{\cos\beta_i}\sqrt{1 - \frac{2vt}{h}\cos\beta_i\cos\mu_i\sin\beta_i + \left(\frac{vt}{h}\cos\beta_i\right)^2} \tag{12.42}$$

The round-trip delay can be approximated using a two-dimensional second order Taylor series expansion about the reference state $(t, \mu) = (0, 0)$. Performing this Taylor series expansion yields

$$\tau_i(t, \mu_i) \approx \bar{\tau} + \bar{\tau}_{t\mu}\ \mu_i t + \bar{\tau}_{tt}\ \frac{t^2}{2} \tag{12.43}$$

where the over-bar indicates evaluation at the state $(0, 0)$, and the subscripts denote partial derivatives. For example, $\tau_{t\mu}$ means

$$\bar{\tau}_{t\mu} = \frac{\partial^2}{\partial t \partial \mu}\tau_i(t, \mu_i)\Big|_{(t, \mu) = (0, 0)} \tag{12.44}$$

The Taylor series coefficients are (see Problem 11.6)

$$\bar{\tau} = \left(\frac{2h}{c}\right)\frac{1}{\cos\beta_i} \tag{12.45}$$

$$\bar{\tau}_{t\mu} = \left(\frac{2v}{c}\right)\sin\beta_i \tag{12.46}$$

$$\bar{\tau}_{tt} = \left(\frac{2v^2}{hc}\right)\cos\beta_i \tag{12.47}$$

Note that other Taylor series coefficients are either zeros or very small, hence they are neglected. Finally, by substituting Eqs. (12.45) through (12.47) into Eq. (12.43), we can rewrite the returned radar signal as

$$\begin{aligned} s_i(t, \mu_i) &= A_i \cos[\psi_i(t, \mu_i) - \xi_0] \\ \hat{\psi}_i(t, \mu_i) &= 2\pi f_0\left[(1 - \bar{\tau}_{t\mu}\mu_i)t - \bar{\tau} - \bar{\tau}_{tt}\frac{t^2}{2}\right] \end{aligned} \tag{12.48}$$

Observation of Eq. (12.48) indicates that the instantaneous frequency for the ith scatterer varies as a linear function of time due to the second order phase term $2\pi f_0(\bar{\tau}_{tt}t^2/2)$ (this confirms the result we concluded about a scatterer Doppler history). Furthermore, since this phase term is range-bin dependent and not scatterer dependent, all scatterers within the same range bin produce this exact second order phase term. It follows that scatterers within a range bin have identical Doppler histories. These Doppler histories are separated by the time delay required to fly between them, as illustrated in Fig. 12.12.

Suppose that there are I scatterers within the kth range bin. In this case, the combined returns for this cell are the sum of the individual returns due to each scatterer as defined by Eq. (12.48). In other words, superposition holds, and the overall echo signal is

$$s_r(t) = \sum_{i=1}^{I} s_i(t, \mu_i) \tag{12.49}$$

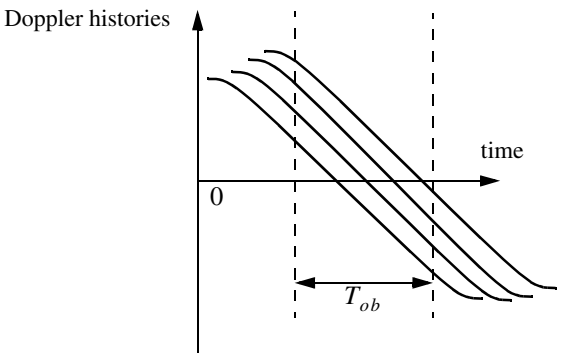

Figure 12.12. Doppler histories for several scatterers within the same range bin.

A signal processing block diagram for the kth range bin is illustrated in Fig. 12.13. It consists of the following steps. First, heterodyning with carrier frequency is performed to extract the quadrature components.

This is followed by LP filtering and A/D conversion. Next, deramping or focusing to remove the second order phase term of the quadrature components is carried out using a phase rotation matrix. The last stage of the processing includes windowing, performing FFT on the windowed quadrature components, and scaling of the amplitude spectrum to account for range attenuation and antenna gain.

The discrete quadrature components are

$$\begin{aligned} \tilde{x}_I(t_n) &= \tilde{x}_I(n) = A_i \cos[\tilde{\psi}_i(t_n, \mu_i) - \xi_0] \\ \tilde{x}_Q(t_n) &= \tilde{x}_Q(n) = A_i \sin[\tilde{\psi}_i(t_n, \mu_i) - \xi_0] \end{aligned} \tag{12.50}$$

$$\tilde{\psi}_i(t_n, \mu_i) = \hat{\psi}_i(t_n, \mu_i) - 2\pi f_0 t_n \tag{12.51}$$

and t_n denotes the nth sampling time (remember that $-T_{ob}/2 \le t_n \le T_{ob}/2$). The quadrature components after deramping (i.e., removal of the phase $\psi = -\pi f_0 \bar{\tau}_{tt} t_n^2$) are given by

$$\begin{bmatrix} x_I(n) \\ x_Q(n) \end{bmatrix} = \begin{bmatrix} \cos\psi & -\sin\psi \\ \sin\psi & \cos\psi \end{bmatrix} \begin{bmatrix} \tilde{x}_I(n) \\ \tilde{x}_Q(n) \end{bmatrix} \tag{12.52}$$

12.8. SAR Imaging Using Doppler Processing

It was mentioned earlier that SAR imaging is performed using two orthogonal dimensions (range and azimuth). Range resolution is controlled by the receiver bandwidth and pulse compression. Azimuth resolution is limited by the antenna beam width. A one-to-one correspondence between the FFT bins and the azimuth resolution cells can be established by utilizing the signal model described in the previous section. Therefore, the problem of target detection is transformed into a spectral analysis problem, where detection is based on the amplitude spectrum of the returned signal. The FFT frequency resolution Δf is equal to the inverse of the observation interval T_{ob}. It follows that a peak in the amplitude spectrum at $k_1 \Delta f$ indicates the presence of a scatterer at frequency $f_{d1} = k_1 \Delta f$.

For an example, consider the scatterer C_i within the kth range bin. The instantaneous frequency f_{di} corresponding to this scatterer is

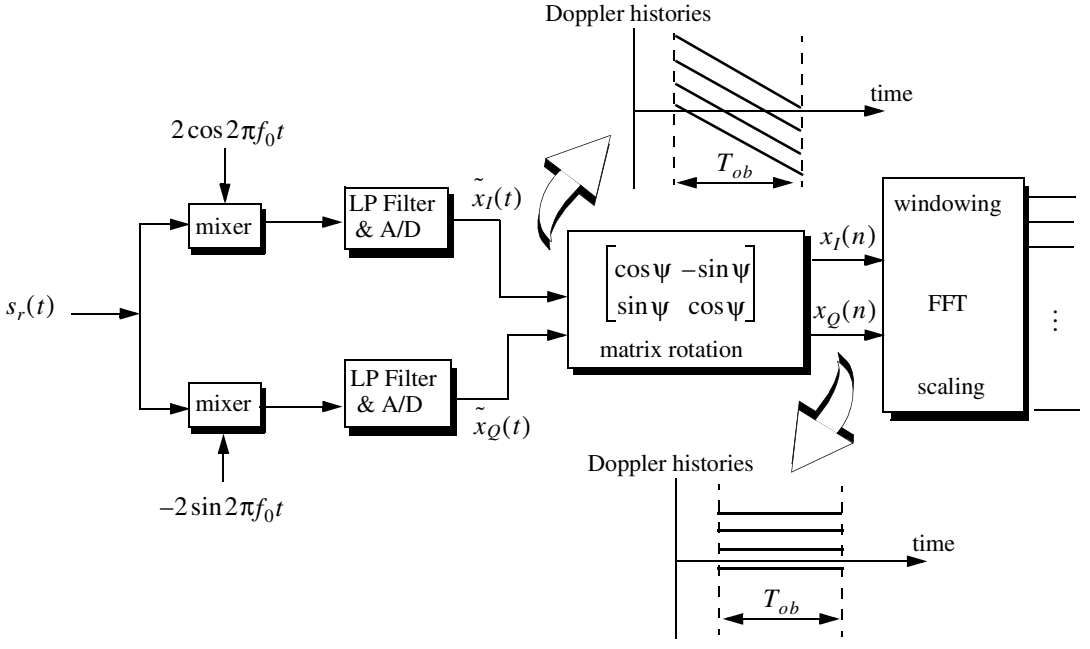

Figure 12.13. Signal processing block diagram for the *kth* range bin.

$$f_{di} = \frac{1}{2\pi}\frac{d\psi}{dt} = f_0\bar{\tau}_{t\mu}\mu_i = \frac{2v}{\lambda}\sin\beta_i\mu_i \tag{12.53}$$

which is the same result derived in Eq. (12. 27), where $\mu_i = \Delta\theta$. Therefore, the scatterers separated in Doppler by a frequency greater than Δf can then be resolved.

12.9. Range Walk

As shown earlier SAR Doppler processing is achieved in two steps: first, range gating and second, azimuth compression within each bin at the end of the observation interval. For this purpose, azimuth compression assumes that each scatterer remains within the same range bin during the observation interval. However, since the range gates are defined with respect to a radar that is moving, the range gate grid is also moving relative to the ground. As a result a scatterer appears to be moving within its range bin. This phenomenon is known as range walk. A small amount of range walk does not bother Doppler processing as long as the scatterer remains within the same range bin. However, range walk over several range bins can constitute serious problems, where in this case Doppler processing is meaningless.

12.10. Case Study

Table 12.1 lists the selected design system parameters. The 3 dB element beamwidth is $\theta = 63.75\ milliradians$. The maximum range interval spanned by the central footprint is

$$R_{span} = R_{mx} - R_{mn} \tag{12.54}$$

$$R_{mx} = h/\cos(\beta^* + \theta/2) \tag{12.55}$$

$$R_{mn} = h/\cos(\beta^* - \theta/2) \tag{12.56}$$

Substituting the proper values from Table 12.1 into Eqs. (12.54), (12.55), and (12.56) yields

$$\{R_{span}, R_{mx}, R_{mn}\} = \{81.448, 1315.538, 1234.090\}m \tag{12.57}$$

which indicates that the system should have a total of 82 range bins. Doppler shift over the footprint is proportional to the radial velocity. It is given by

$$\frac{2v}{\lambda}\cos(90 + \theta/2)\sin\beta^* < f < \frac{2v}{\lambda}\cos(90 - \theta/2)\sin\beta^* \tag{12.58}$$

For this example, f_d is

TABLE 12.1. List of selected system parameters.

Parameter	Symbol	Value
# subintervals	M	64
size of array	N	32
wavelength	λ	$3.19mm$
element spacing	d	16λ
velocity	v	$65m/s$
height	h	$900m$
elevation angle	β^*	35°
range resolution	d_r	$1m$
observation interval	D_{ob}	$20ms$

$$-1489.88Hz < f_d < 1489.88Hz \tag{12.59}$$

To avoid range and Doppler ambiguities the Pulse Repetition Frequency (PRF) should be

$$\frac{2v}{\lambda}\theta \le PRF \le \frac{c}{2R_{span}} \tag{12.60}$$

Using the system parameters defined in Table 12.1, we find $5.995KHz \le PRF \le 1.31579MHz$. The DFT frequency resolution Δf is computed as the inverse of the observation interval, and it is equal to $50Hz$. The size of the DFT, denoted as $NFFT$, is equal to the number of positions the antenna takes on along the flight path. The maximum Doppler variation resolved by this DFT is less than or equal to $\Delta f \times NFFT/2$.

12.11. Arrays in Sequential Mode Operation

Standard Synthetic Aperture Radar (SAR) imaging systems are generally used to generate high resolution two-dimensional (2-D) images of ground terrain. Range gating determines resolution along the first dimension. Pulse compression techniques are usually used to achieve fine range resolution. Such techniques require the use of wide band receiver and display devices in order to resolve the time structure in the returned signals. The width of azimuth cells

provides resolution along the other dimension. Azimuth resolution is limited by the duration of the observation interval.

An approach for multiple target detection using linear arrays operated in sequential mode was previously presented by Mahafza. This technique is based on Discrete Fourier Transform (DFT) processing of equiphase data collected in sequential mode (DFTSQM). DFTSQM processing was also developed for 2-D real and synthetic arrays to include applications such as SAR imaging. The Field of View (FOV) of an array utilizing DFTSQM operation and signal processing is defined by the 3 dB beamwidth of a single element. Advantages of DFTSQM are (1) simultaneous detection of targets within the array's FOV without using any phase shifting hardware; and (2) the two-way array pattern is improved due to the coherent integration of equiphase returns. More specifically, the main lobe resolution is doubled while achieving a 27 dB sidelobe attenuation. However, the time required for transmission and processing may become a limitation when using this technique. A brief description of DFTSQM is presented in the next section.

12.11.1. Linear Arrays

Consider a linear array of size N, uniform element spacing d, and wavelength λ. Assume a far field scatterer P located at direction-sine $\sin\beta_l$. DFTSQM operation for this array can be described as follows. The elements are fired sequentially, one at a time, while all elements receive in parallel. The echoes are collected and integrated coherently on the basis of equal phase to compute a complex information sequence $\{b(m); m = 0, 2N-1\}$. The x-coordinates, in d-units, of the x_n^{th} element with respect to the center of the array are

$$x_n = \left(-\frac{N-1}{2} + n\right);\ n = 0, N-1 . \tag{12.61}$$

The electric field received by the x_2^{th} element due to the firing of the x_1^{th}, and reflection by the l^{th} far field scatterer P is

$$E(x_1, x_2; s_l) = G^2(s_l)\left(\frac{R_0}{R}\right)^4 \sqrt{\sigma_l}\ \ exp(j\phi(x_1, x_2; s_l)) \tag{12.62}$$

$$\phi(x_1, x_2; s_l) = \frac{2\pi}{\lambda}(x_1 + x_2)(s_l) \tag{12.63}$$

$$s_l = \sin\beta_l \tag{12.64}$$

where $\sqrt{\sigma_l}$ is the target cross section, $G^2(s_l)$ is the two-way element gain, and $(R_0/R)^4$ is the range attenuation with respect to reference range R_0. The scatterer phase is assumed to be zero, however it could be easily included.

Assuming multiple scatterers in the array's FOV, the cumulative electric field in the path $x_1 \Rightarrow x_2$ due to reflection from all scatterers is

$$E(x_1, x_2) = \sum_{all\ l} [E_I(x_1, x_2; s_l) + jE_Q(x_1, x_2; s_l)] \tag{12.65}$$

where the subscripts (I, Q) denote the quadrature components. Note that the variable part of the phase given in Eq. (12.63) is proportional to the integers resulting from the sums $\{(x_{n1} + x_{n2});\ (n1, n2) = 0, N-1\}$. In the far field operation there are a total of $(2N-1)$ distinct $(x_{n1} + x_{n2})$ sums. Therefore, the electric fields with paths of the same $(x_{n1} + x_{n2})$ sums can be collected coherently. In this manner the information sequence $\{b(m); m = 0, 2N-1\}$ is computed, where $b(2N-1)$ is set to equal zero. At the same time one forms the sequence $\{c(m); m = 0, 2N-2\}$ which keeps track of the number of returns that have the same $(x_{n1} + x_{n2})$ sum. More precisely, for $m = n1 + n2;\ (n1, n2) = 0, N-1$

$$b(m) = b(m) + E(x_{n1}, x_{n2}) \tag{12.66}$$

$$c(m) = c(m) + 1 \tag{12.67}$$

It follows that

$$\{c(m); m = 0, 2N-2\} = \begin{Bmatrix} m+1 & ;\ m = 0, N-2 \\ N & ;\ m = N-1 \\ 2N-1-m & \quad m = N, 2N-2 \end{Bmatrix} \tag{12.68}$$

which is a triangular shape sequence.

The processing of the sequence $\{b(m)\}$ is performed as follows: (1) the weighting takes the sequence $\{c(m)\}$ into account; (2) the complex sequence $\{b(m)\}$ is extended to size N_F, a power integer of two, by zero padding; (3) the DFT of the extended sequence $\{b'(m); m = 0, N_F - 1\}$ is computed,

$$B(q) = \sum_{m=0}^{N_F - 1} b'(m) \cdot exp\left(-j\frac{2\pi qm}{N_F}\right);\ q = 0, N_F - 1 \tag{12.69}$$

and (4) after compensation for antenna gain and range attenuation, scatterers are detected as peaks in the amplitude spectrum $|B(q)|$. Note that step (4) is true only when

$$\sin\beta_q = \frac{\lambda q}{2Nd} \quad ; \; q = 0, 2N-1 \tag{12.70}$$

where $\sin\beta_q$ denotes the direction-sine of the q^{th} scatterer, and $N_F = 2N$ is implied in Eq. (12.70).

The classical approach to multiple target detection is to use a phased array antenna with phase shifting and tapering hardware. The array beamwidth is proportional to (λ/Nd), and the first sidelobe is at about -13 dB. On the other hand, multiple target detection using DFTSQM provides a beamwidth proportional to $(\lambda/2Nd)$ as indicated by Eq. (12.70), which has the effect of doubling the array's resolution. The first sidelobe is at about -27 dB due the triangular sequence $\{c(m)\}$. Additionally, no phase shifting hardware is required for detection of targets within a single element field of view.

12.11.2. Rectangular Arrays

DFTSQM operation and signal processing for 2-D arrays can be described as follows. Consider an $N_x \times N_y$ rectangular array. All N_xN_y elements are fired sequentially, one at a time; after each firing, all the N_xN_y array elements receive in parallel. Thus, N_xN_y samples of the quadrature components are collected after each firing, and a total of $(N_xN_y)^2$ samples will be collected. However, in the far field operation, there are only $(2N_x-1)\times(2N_y-1)$ distinct equiphase returns. Therefore, the collected data can be added coherently to form a 2-D information array of size $(2N_x-1)\times(2N_y-1)$. The two-way radiation pattern is computed as the modulus of the 2-D amplitude spectrum of the information array. The processing includes 2-D windowing, 2-D Discrete Fourier Transformation, antenna gain, and range attenuation compensation. The field of view of the 2-D array is determined by the 3 dB pattern of a single element. All the scatterers within this field will be detected simultaneously as peaks in the amplitude spectrum.

Consider a rectangular array of size $N \times N$, with uniform element spacing $d_x = d_y = d$, and wavelength λ. The coordinates of the n^{th} element, in d-units, are

$$x_n = \left(-\frac{N-1}{2} + n\right) \quad ; \; n = 0, N-1 \tag{12.71}$$

$$y_n = \left(-\frac{N-1}{2} + n\right) \quad ; \; n = 0, N-1 \tag{12.72}$$

Assume a far field point P defined by the azimuth and elevation angles (α, β). In this case, the one-way geometric phase for an element is

$$\varphi'(x, y) = \frac{2\pi}{\lambda}[x \sin\beta \cos\alpha + y \sin\beta \sin\alpha] \tag{12.73}$$

Therefore, the two-way geometric phase between the (x_1, y_1) and (x_2, y_2) elements is

$$\varphi(x_1, y_1, x_2, y_2) = \frac{2\pi}{\lambda} \sin\beta[(x_1 + x_2)\cos\alpha + (y_1 + y_2)\sin\alpha] \tag{12.74}$$

The two-way electric field for the l^{th} scatterer at (α_l, β_l) is

$$E(x_1, x_2, y_1, y_2; \alpha_l, \beta_l) = G^2(\beta_l)\left(\frac{R_0}{R}\right)^4 \sqrt{\sigma_l}\ \ exp[j(\varphi(x_1, y_1, x_2, y_2))] \tag{12.75}$$

Assuming multiple scatterers within the array's FOV, then the cumulative electric field for the two-way path $(x_1, y_1) \Rightarrow (x_2, y_2)$ is given by

$$E(x_1, x_2, y_1, y_2) = \sum_{all\ \ scatterers} E(x_1, x_2, y_1, y_2; \alpha_l, \beta_l) \tag{12.76}$$

All formulas for the 2-D case reduce to those of a linear array case by setting $N_y = 1$ and $\alpha = 0$.

The variable part of the phase given in Eq. (12.74) is proportional to the integers $(x_1 + x_2)$ and (y_1, y_2). Therefore, after completion of the sequential firing, electric fields with paths of the same (i, j) sums, where

$$\{i = x_{n1} + x_{n2}; i = -(N-1), (N-1)\} \tag{12.77}$$

$$\{j = y_{n1} + y_{n2}; j = -(N-1), (N-1)\} \tag{12.78}$$

can be collected coherently. In this manner the 2-D information array $\{b(m_x, m_y); (m_x, m_y) = 0, 2N-1\}$ is computed. The coefficient sequence $\{c(m_x, m_y); (m_x, m_y) = 0, 2N-2\}$ is also computed. More precisely,

$$\begin{aligned} &for\ \ m_x = n1 + n2\ \ and\ \ m_y = n1 + n2; \\ &n1 = 0, N-1\ \ ,\ \ and\ \ n2 = 0, N-1 \end{aligned} \tag{12.79}$$

$$b(m_x, m_y) = b(m_x, m_y) + E(x_{n1}, y_{n1}, x_{n2}, y_{n2}) \tag{12.80}$$

It follows that

$$c(m_x, m_y) = (N_x - |m_x - (N_x - 1)|) \times (N_y - |m_y - (N_y - 1)|) \quad \textbf{(12.81)}$$

The processing of the complex 2-D information array $\{b(m_x, m_y)\}$ is similar to that of the linear case with the exception that one should use a 2-D DFT. After antenna gain and range attenuation compensation, scatterers are detected as peaks in the 2-D amplitude spectrum of the information array. A scatterer located at angles (α_l, β_l) will produce a peak in the amplitude spectrum at DFT indexes (p_l, q_l), where

$$\alpha_l = \text{atan}\left(\frac{q_l}{p_l}\right) \quad \textbf{(12.82)}$$

$$\sin\beta_l = \frac{\lambda p_l}{2Nd\cos\alpha_l} = \frac{\lambda q_l}{2Nd\sin\alpha_l} \quad \textbf{(12.83)}$$

In order to prove Eq. (12.82), consider a rectangular array of size $N \times N$, with uniform element spacing $d_x = d_y = d$, and wavelength λ. Assume sequential mode operation where elements are fired sequentially, one at a time, while all elements receive in parallel. Assuming far field observation defined by azimuth and elevation angles (α, β). The unit vector $\hat{u}$ on the line of sight, with respect to $\overrightarrow{O}$, is given by

$$\hat{u} = \sin\beta\cos\alpha\ \hat{a}_x + \sin\beta\sin\alpha\ \hat{a}_y + \cos\beta\ \hat{a}_z \quad \textbf{(12.84)}$$

The $(n_x, n_y)^{th}$ element of the array can be defined by the vector

$$\hat{e}(n_x, n_y) = \left(n_x - \frac{N-1}{2}\right)d\ \hat{a}_x + \left(n_y - \frac{N-1}{2}\right)d\ \hat{a}_y \quad \textbf{(12.85)}$$

where $(n_x, n_y = 0, N-1)$. The one-way geometric phase for this element is

$$\varphi'(n_x, n_y) = k(\hat{u} \bullet \hat{e}(n_x, n_y)) \quad \textbf{(12.86)}$$

where $k = 2\pi/\lambda$ is the wave-number, and the operator $(\ \bullet\ )$ indicates dot product. Therefore, the two-way geometric phase between the (n_{x1}, n_{y1}) and (n_{x2}, n_{y2}) elements is

$$\varphi(n_{x1}, n_{y1}, n_{x2}, n_{y2}) = k[\hat{u} \bullet \{\hat{e}(n_{x1}, n_{y1}) + \hat{e}(n_{x2}, n_{y2})\}] \quad \textbf{(12.87)}$$

The cumulative two-way normalized electric due to all transmissions in the direction (α, β) is

$$E(\hat{u}) = E_t(\hat{u})E_r(\hat{u}) \quad \textbf{(12.88)}$$

where the subscripts t and r, respectively, refer to the transmitted and received electric fields. More precisely,

$$E_t(\hat{\vec{u}}) = \sum_{n_{xt}=0}^{N-1} \sum_{n_{yt}=0}^{N-1} w(n_{xt}, n_{yt}) exp[jk\{\hat{\vec{u}} \bullet \hat{\vec{e}}(n_{xt}, n_{yt})\}] \quad \textbf{(12.89)}$$

$$E_r(\hat{\vec{u}}) = \sum_{n_{xr}=0}^{N-1} \sum_{n_{yr}=0}^{N-1} w(n_{xr}, n_{yr}) exp[jk\{\hat{\vec{u}} \bullet \hat{\vec{e}}(n_{xr}, n_{yr})\}] \quad \textbf{(12.90)}$$

In this case, $w(n_x, n_y)$ denotes the tapering sequence. Substituting Eqs. (12.87), (12.89), and (12.90) into Eq. (12.88) and grouping all fields with the same two-way geometric phase yield

$$E(\hat{\vec{u}}) = e^{j\delta} \sum_{m=0}^{N_a-1} \sum_{n=0}^{N_a-1} w'(m, n) exp[jkd \sin\beta(m\cos\alpha + n\sin\alpha)] \quad \textbf{(12.91)}$$

$$N_a = 2N - 1 \quad \textbf{(12.92)}$$

$$m = n_{xt} + n_{xr}; m = 0, 2N - 2 \quad \textbf{(12.93)}$$

$$n = n_{yt} + n_{yr}; n = 0, 2N - 2 \quad \textbf{(12.94)}$$

$$\delta = \left(\frac{-d\sin\beta}{2}\right)(N-1)(\cos\alpha + \sin\alpha) \quad \textbf{(12.95)}$$

The two-way array pattern is then computed as

$$\left|E(\hat{\vec{u}})\right| = \left| \sum_{m=0}^{N_a-1} \sum_{n=0}^{N_a-1} w'(m, n) exp[jkd \sin\beta(m\cos\alpha + n\sin\alpha)] \right| \quad \textbf{(12.96)}$$

Consider the two-dimensional DFT transform, $W'(p, q)$, of the array $w'(n_x, n_y)$

$$W'(p, q) = \sum_{m=0}^{N_a-1} \sum_{n=0}^{N_a-1} w'(m, n) e^{-j\frac{2\pi}{N_a}(pm + qn)} \quad ; \ (p, q) = 0, N_a - 1 \quad \textbf{(12.97)}$$

Comparison of Eq. (12.96) and (12.97) indicates that $|E(\hat{u})|$ is equal to $|W'(p, q)|$ if

$$-\left(\frac{2\pi}{N_a}\right)p = \frac{2\pi}{\lambda}d\sin\beta\cos\alpha \tag{12.98}$$

$$-\left(\frac{2\pi}{N_a}\right)q = \frac{2\pi}{\lambda}d\sin\beta\sin\alpha \tag{12.99}$$

It follows that

$$\alpha = \tan^{-1}\left(\frac{q}{p}\right) \tag{12.100}$$

which is the same as Eq. (12.82).

12.12. MATLAB Programs

This section contains the MATLAB programs used in this chapter.

Listing 12.1. MATLAB Program "fig12_2.m"

```
clear all
var = -pi:0.001:pi;
y1 = (sinc(var)) .^2;
y2 = abs(sinc(2.0 * var));
plot (var,y1,var,y2);
axis tight
grid;
xlabel ('angle - radians');
ylabel ('array pattern');
```

Problems

12.1. A side looking SAR is traveling at an altitude of $15Km$; the elevation angle is $\beta = 15°$. If the aperture length is $L = 5m$, the pulse width is $\tau = 20\mu s$ and the wavelength is $\lambda = 3.5cm$. (a) Calculate the azimuth resolution. (b) Calculate the range and ground range resolutions.

12.2. A MMW side looking SAR has the following specifications: radar velocity $v = 70m/s$, elevation angle $\beta = 35°$, operating frequency $f_0 = 94GHz$, and antenna 3dB beam width $\theta_{3dB} = 65mrad$. (a) Calculate

the footprint dimensions. (b) Compute the minimum and maximum ranges. (c) Compute the Doppler frequency span across the footprint. (d) Calculate the minimum and maximum PRFs.

12.3. A side looking SAR takes on eight positions within an observation interval. In each position the radar transmits and receives one pulse. Let the distance between any two consecutive antenna positions be d, and define $\delta = 2\pi\frac{d}{\lambda}(\sin\beta - \sin\beta_0)$ to be the one-way phase difference for a beam steered at angle β_0. (a) In each of the eight positions a sample of the phase pattern is obtained after heterodyning. List the phase samples. (b) How will you process the sequence of samples using an FFT (do not forget windowing)? (c) Give a formula for the angle between the grating lobes.

12.4. Consider a synthetic aperture radar. You are given the following Doppler history for a scatterer: $\{1000Hz, 0, -1000HZ\}$ which corresponds to times $\{-10ms, 0, 10ms\}$. Assume that the observation interval is $T_{ob} = 20ms$, and a platform velocity $v = 200m/s$. (a) Show the Doppler history for another scatterer which is identical to the first one except that it is located in azimuth $1m$ earlier. (b) How will you perform deramping on the quadrature components (show only the general approach)? (c) Show the Doppler history for both scatterers after deramping.

12.5. You want to design a side looking synthetic aperture Ultrasonic radar operating at $f_0 = 60KHz$ and peak power $P_t = 2W$. The antenna beam is conical with 3dB beam width $\theta_{3dB} = 5°$. The maximum gain is 16. The radar is at a constant altitude $h = 15m$ and is moving at a velocity of $10m/s$. The elevation angle defining the footprint is $\beta = 45°$. (a) Give an expression for the antenna gain assuming a Gaussian pattern. (b) Compute the pulse width corresponding to range resolution of $10mm$. (c) What are the footprint dimensions? (d) Compute and plot the Doppler history for a scatterer located on the central range bin. (e) Calculate the minimum and maximum PRFs; do you need to use more than one PRF? (f) How will you design the system in order to achieve an azimuth resolution of $10mm$?

12.6. Derive Eq. (12.45) through Eq. (12.47).

12.7. In Section 12.7 we assumed the elevation angle increment ε is equal to zero. Develop an equivalent to Eq. (12.43) for the case when $\varepsilon \neq 0$. You need to use a third order three-dimensional Taylor series expansion about the state $(t, \mu, \varepsilon) = (0, 0, 0)$ in order to compute the new round-trip delay expression.

Chapter 13 *Signal Processing*

13.1. Signal and System Classifications

In general, electrical signals can represent either current or voltage, and may be classified into two main categories: energy signals and power signals. Energy signals can be deterministic or random, while power signals can be periodic or random. A signal is said to be random if it is a function of a random parameter (such as random phase or random amplitude). Additionally, signals may be divided into low pass or band pass signals. Signals that contain very low frequencies (close to DC) are called low pass signals; otherwise they are referred to as band pass signals. Through modulation, low pass signals can be mapped into band pass signals.

The average power P for the current or voltage signal $x(t)$ over the interval (t_1, t_2) across a $1\,\Omega$ resistor is

$$P = \frac{1}{t_2 - t_1} \int_{t_1}^{t_2} |x(t)|^2 \, dt \tag{13.1}$$

The signal $x(t)$ is said to be a power signal over a very large interval $T = t_2 - t_1$, if and only if it has finite power; it must satisfy the following relation:

$$0 < \lim_{T \to \infty} \frac{1}{T} \int_{-T/2}^{T/2} |x(t)|^2 \, dt < \infty \tag{13.2}$$

Using Parseval's theorem, the energy E dissipated by the current or voltage signal $x(t)$ across a 1Ω resistor, over the interval (t_1, t_2), is

$$E = \int_{t_1}^{t_2} |x(t)|^2 \, dt \tag{13.3}$$

The signal $x(t)$ is said to be an energy signal if and only if it has finite energy,

$$E = \int_{-\infty}^{\infty} |x(t)|^2 \, dt \quad < \infty \tag{13.4}$$

A signal $x(t)$ is said to be periodic with period T if and only if

$$x(t) = x(t + nT) \qquad for \ all \ t \tag{13.5}$$

where n is an integer.

Example 13.1: Classify each of the following signals as an energy signal, as a power signal, or as neither. All signals are defined over the interval $(-\infty < t < \infty)$*:* $x_1(t) = \cos t + \cos 2t$, $x_2(t) = \exp(-\alpha^2 t^2)$.

Solution:

$$P_{x_1} = \frac{1}{T} \int_{-T/2}^{T/2} (\cos t + \cos 2t)^2 dt = 1 \Rightarrow \ power \ signal$$

Note that since the cosine function is periodic, the limit is not necessary.

$$E_{x_2} = \int_{-\infty}^{\infty} (e^{-\alpha^2 t^2})^2 dt = 2\int_{0}^{\infty} e^{-2\alpha^2 t^2} dt = 2\frac{\sqrt{\pi}}{2\sqrt{2}\alpha} = \frac{1}{\alpha}\sqrt{\frac{\pi}{2}} \ \Rightarrow \ energy \ signal.$$

Electrical systems can be linear or nonlinear. Furthermore, linear systems may be divided into continuous or discrete. A system is linear if the input signal $x_1(t)$ produces $y_1(t)$ and $x_2(t)$ produces $y_2(t)$; then for some arbitrary constants a_1 and a_2 the input signal $a_1x_1(t) + a_2x_2(t)$ produces the output $a_1y_1(t) + a_2y_2(t)$. A linear system is said to be shift invariant (or time invariant) if a time shift at its input produces the same shift at its output. More precisely, if the input signal $x(t)$ produces $y(t)$ then the delayed signal $x(t - t_0)$ produces the output $y(t - t_0)$. The impulse response of a Linear Time Invariant (LTI) system, $h(t)$, is defined to be the system's output when the input is an impulse (delta function).

13.2. The Fourier Transform

The Fourier Transform (FT) of the signal $x(t)$ is

$$F\{x(t)\} = X(\omega) = \int_{-\infty}^{\infty} x(t)e^{-j\omega t}\, dt \tag{13.6}$$

or

$$F\{x(t)\} = X(f) = \int_{-\infty}^{\infty} x(t)e^{-j2\pi ft}\, dt \tag{13.7}$$

and the Inverse Fourier Transform (IFT) is

$$F^{-1}\{X(\omega)\} = x(t) = \frac{1}{2\pi}\int_{-\infty}^{\infty} X(\omega)e^{j\omega t}\, d\omega \tag{13.8}$$

or

$$F^{-1}\{X(f)\} = x(t) = \int_{-\infty}^{\infty} X(f)e^{j2\pi ft}\, df \tag{13.9}$$

where, in general, t represents time, while $\omega = 2\pi f$ and f represent frequency in radians per second and Hertz, respectively. In this book we will use both notations for the transform, as appropriate (i.e., $X(\omega)$ and $X(f)$).

A detailed table of the FT pairs is listed in Appendix C. The FT properties are (the proofs are left as an exercise):

1. *Linearity:*

$$F\{a_1x_1(t) + a_2x_2(t)\} = a_1X_1(\omega) + a_2X_2(\omega) \tag{13.10}$$

2. *Symmetry: If* $F\{x(t)\} = X(\omega)$ *then*

$$2\pi X(-\omega) = \int_{-\infty}^{\infty} X(t)e^{-j\omega t}dt \tag{13.11}$$

3. *Shifting: For any real time* t_0

$$F\{x(t \pm t_0)\} = e^{\pm j\omega t_0} X(\omega) \tag{13.12}$$

4. *Scaling: If* $F\{x(t)\} = X(\omega)$ *then*

$$F\{x(at)\} = \frac{1}{|a|} X\left(\frac{\omega}{a}\right) \tag{13.13}$$

5. *Central Ordinate:*

$$X(0) = \int_{-\infty}^{\infty} x(t)dt \tag{13.14}$$

$$x(0) = \frac{1}{2\pi} \int_{-\infty}^{\infty} X(\omega)d\omega \tag{13.15}$$

6. *Frequency Shift: If* $F\{x(t)\} = X(\omega)$ *then*

$$F\{e^{\pm\omega_0 t} x(t)\} = X(\omega \mp \omega_0) \tag{13.16}$$

7. *Modulation: If* $F\{x(t)\} = X(\omega)$ *then*

$$F\{x(t)\cos\omega_0 t\} = \frac{1}{2}[X(\omega + \omega_0) + X(\omega - \omega_0)] \tag{13.17}$$

$$F\{x(t)\sin(\omega_0 t)\} = \frac{1}{2j}[X(\omega - \omega_0) - X(\omega + \omega_0)] \tag{13.18}$$

8. *Derivatives:*

$$F\left\{\frac{d^n}{dt^n}(x(t))\right\} = (j\omega)^n X(\omega) \tag{13.19}$$

9. *Time Convolution: if* $x(t)$ *and* $h(t)$ *have Fourier transforms* $X(\omega)$ *and* $H(\omega)$*, respectively, then*

$$F\left\{\int_{-\infty}^{\infty} x(\tau)h(t-\tau)d\tau\right\} = X(\omega)H(\omega) \tag{13.20}$$

10. *Frequency Convolution:*

$$F\{x(t)h(t)\} = \frac{1}{2\pi}\int_{-\infty}^{\infty} X(\tau)H(\omega-\tau)d\tau \tag{13.21}$$

11. *Autocorrelation:*

$$F\left\{\int_{-\infty}^{\infty} x(\tau)x^*(\tau-t)d\tau\right\} = X(\omega)X^*(\omega) = |X(\omega)|^2 \tag{13.22}$$

12. *Parseval's Theoerem: The energy associated with the signal $x(t)$ is*

$$E = \int_{-\infty}^{\infty} |x(t)^2|dt = \int_{-\infty}^{\infty} |X(\omega)|^2 d\omega \tag{13.23}$$

13. *Moments: The nth moment is*

$$m_n = \int_0^{\infty} t^n x(t)dt = \frac{d^n}{d\omega^n}X(\omega)\Big|_{\omega=0} \tag{13.24}$$

13.3. The Fourier Series

A set of functions $S = \{\varphi_n(t)\ ;\ n = 1, \ldots, N\}$ is said to be orthogonal over the interval (t_1, t_2) if and only if

$$\int_{t_1}^{t_2} \varphi_i^*(t)\varphi_j(t)dt = \int_{t_1}^{t_2} \varphi_i(t)\varphi_j^*(t)dt = \begin{cases} 0 & i \neq j \\ \lambda_i & i = j \end{cases} \tag{13.25}$$

where the asterisk indicates complex conjugate, and λ_i are constants. If $\lambda_i = 1$ for all i, then the set S is said to be an orthonormal set.

An electrical signal $x(t)$ can be expressed over the interval (t_1, t_2) as a weighted sum of a set of orthogonal functions as

$$x(t) \approx \sum_{n=1}^{N} X_n \varphi_n(t) \tag{13.26}$$

where X_n are, in general, complex constants, and the orthogonal functions $\varphi_n(t)$ are called basis functions. If the integral-square error over the interval (t_1, t_2) is equal to zero as N approaches infinity, i.e.,

$$\lim_{N \to \infty} \int_{t_1}^{t_2} \left| x(t) - \sum_{n=1}^{N} X_n \varphi_n(t) \right|^2 dt = 0 \tag{13.27}$$

then the set $S = \{\varphi_n(t)\}$ is said to be complete, and Eq. (13.12) becomes an equality. The constants X_n are computed as

$$X_n = \frac{\int_{t_1}^{t_2} x(t)\varphi_n^*(t)dt}{\int_{t_1}^{t_2} |\varphi_n(t)|^2 dt} \tag{13.28}$$

Let the signal $x(t)$ be periodic with period T, and let the complete orthogonal set S be

$$S = \left\{ e^{\frac{j2\pi nt}{T}} \; ; \; n = -\infty, \infty \right\} \tag{13.29}$$

Then the complex exponential Fourier series of $x(t)$ is

$$x(t) = \sum_{n=-\infty}^{\infty} X_n e^{\frac{j2\pi nt}{T}} \tag{13.30}$$

Using Eq. (13.28) yields

$$X_n = \frac{1}{T} \int_{-T/2}^{T/2} x(t) e^{\frac{-j2\pi nt}{T}} dt \tag{13.31}$$

The FT of Eq. (13.30) is given by

$$X(\omega) = 2\pi \sum_{n=-\infty}^{\infty} X_n \delta\left(\omega - \frac{2\pi n}{T}\right) \tag{13.32}$$

where $\delta(\cdot)$ is delta function. When the signal $x(t)$ is real we can compute its trigonometric Fourier series from Eq. (13.30) as

$$x(t) = a_0 + \sum_{n=1}^{\infty} a_n \cos\left(\frac{2\pi nt}{T}\right) + \sum_{n=1}^{\infty} b_n \sin\left(\frac{2\pi nt}{T}\right) \tag{13.33}$$

$$\begin{aligned} a_0 &= X_0 \\ a_n &= \frac{1}{T}\int_{-T/2}^{T/2} x(t)\cos\left(\frac{2\pi nt}{T}\right)dt \\ b_n &= \frac{1}{T}\int_{-T/2}^{T/2} x(t)\sin\left(\frac{2\pi nt}{T}\right)dt \end{aligned} \tag{13.34}$$

The coefficients a_n are all zeros when the signal $x(t)$ is an odd function of time. Alternatively, when the signal is an even function of time, then all b_n are equal to zero.

Consider the periodic energy signal defined in Eq. (13.33). The total energy associated with this signal is then given by

$$E = \frac{1}{T}\int_{t_0}^{t+T} |x(t)|^2 dt = \frac{a_0^2}{4} + \sum_{n=1}^{\infty}\left(\frac{a_n^2}{2} + \frac{b_n^2}{2}\right) \tag{13.35}$$

13.4. Convolution and Correlation Integrals

The convolution $\phi_{xh}(t)$ between the signals $x(t)$ and $h(t)$ is defined by

$$\phi_{xh}(t) = x(t) \bullet h(t) = \int_{-\infty}^{\infty} x(\tau)h(t-\tau)d\tau \tag{13.36}$$

where τ is a dummy variable, and the operator $\bullet$ is used to symbolically describe the convolution integral. Convolution is commutative, associative, and distributive. More precisely,

$$\begin{aligned} x(t) \bullet h(t) &= h(t) \bullet x(t) \\ x(t) \bullet h(t) \bullet g(t) &= (x(t) \bullet h(t)) \bullet g(t) = x(t) \bullet (h(t) \bullet g(t)) \end{aligned} \tag{13.37}$$

For the convolution integral to be finite at least one of the two signals must be an energy signal. The convolution between two signals can be computed using the FT

$$\phi_{xh}(t) = F^{-1}\{X(\omega)H(\omega)\} \tag{13.38}$$

Consider an LTI system with impulse response $h(t)$ and input signal $x(t)$. It follows that the output signal $y(t)$ is equal to the convolution between the input signal and the system impulse response,

$$y(t) = \int_{-\infty}^{\infty} x(\tau)h(t-\tau)d\tau = \int_{-\infty}^{\infty} h(\tau)x(t-\tau)d\tau \tag{13.39}$$

The cross-correlation function between the signals $x(t)$ and $g(t)$ is defined as

$$R_{xg}(t) = \int_{-\infty}^{\infty} x^*(\tau)g(t+\tau)d\tau \tag{13.40}$$

Again, at least one of the two signals should be an energy signal for the correlation integral to be finite. The cross-correlation function measures the similarity between the two signals. The peak value of $R_{xg}(t)$ and its spread around this peak are an indication of how good this similarity is. The cross-correlation integral can be computed as

$$R_{xg}(t) = F^{-1}\{X^*(\omega)G(\omega)\} \tag{13.41}$$

When $x(t) = g(t)$ we get the autocorrelation integral,

$$R_x(t) = \int_{-\infty}^{\infty} x^*(\tau)x(t+\tau)d\tau \tag{13.42}$$

Note that the autocorrelation function is denoted by $R_x(t)$ rather than $R_{xx}(t)$. When the signals $x(t)$ and $g(t)$ are power signals, the correlation integral becomes infinite and thus, time averaging must be included. More precisely,

$$\bar{R}_{xg}(t) = \lim_{T\to\infty} \frac{1}{T} \int_{-T/2}^{T/2} x^*(\tau)g(t+\tau)d\tau \tag{13.43}$$

13.5. Energy and Power Spectrum Densities

Consider an energy signal $x(t)$. From Parseval's theorem, the total energy associated with this signal is

$$E = \int_{-\infty}^{\infty} |x(t)|^2 dt = \frac{1}{2\pi} \int_{-\infty}^{\infty} |X(\omega)|^2 d\omega \tag{13.44}$$

When $x(t)$ is a voltage signal, the amount of energy dissipated by this signal when applied across a network of resistance R is

$$E = \frac{1}{R} \int_{-\infty}^{\infty} |x(t)|^2 dt = \frac{1}{2\pi R} \int_{-\infty}^{\infty} |X(\omega)|^2 d\omega \tag{13.45}$$

Alternatively, when $x(t)$ is a current signal we get

$$E = R \int_{-\infty}^{\infty} |x(t)|^2 dt = \frac{R}{2\pi} \int_{-\infty}^{\infty} |X(\omega)|^2 d\omega \tag{13.46}$$

The quantity $\int |X(\omega)|^2 d\omega$ represents the amount of energy spread per unit frequency across a 1Ω resistor; therefore, the Energy Spectrum Density (ESD) function for the energy signal $x(t)$ is defined as

$$ESD = |X(\omega)|^2 \tag{13.47}$$

The ESD at the output of an LTI system when $x(t)$ is at its input is

$$|Y(\omega)|^2 = |X(\omega)|^2 |H(\omega)|^2 \tag{13.48}$$

where $H(\omega)$ is the FT of the system impulse response, $h(t)$. It follows that the energy present at the output of the system is

$$E_y = \frac{1}{2\pi} \int_{-\infty}^{\infty} |X(\omega)|^2 |H(\omega)|^2 d\omega \tag{13.49}$$

Example 13.2: The voltage signal $x(t) = e^{-5t}$; $t \geq 0$ *is applied to the input of a low pass LTI system. The system bandwidth is* $5Hz$, *and its input resistance is* 5Ω. *If* $H(\omega) = 1$ *over the interval* $(-10\pi < \omega < 10\pi)$ *and zero elsewhere, compute the energy at the output.*

Solution: From Eqs. (13.45) and (13.49) we get

$$E_y = \frac{1}{2\pi R} \int_{\omega = -10\pi}^{10\pi} |X(\omega)|^2 |H(\omega)|^2 d\omega$$

Using Fourier transform tables and substituting $R = 5$ *yield*

$$E_y = \frac{1}{5\pi}\int_0^{10\pi} \frac{1}{\omega^2 + 25} d\omega$$

Completing the integration yields

$$E_y = \frac{1}{25\pi}[\text{atanh}(2\pi) - \text{atanh}(0)] = 0.01799 \ \ Joules$$

Note that an infinite bandwidth would give $E_y = 0.02$, *only 11% larger.*

The total power associated with a power signal $g(t)$ is

$$P = \lim_{T\to\infty} \frac{1}{T}\int_{-T/2}^{T/2} |g(t)|^2 dt \qquad \textbf{(13.50)}$$

Define the Power Spectrum Density (PSD) function for the signal $g(t)$ as $S_g(\omega)$, where

$$P = \lim_{T\to\infty} \frac{1}{T}\int_{-T/2}^{T/2} |g(t)|^2 dt = \frac{1}{2\pi}\int_{-\infty}^{\infty} S_g(\omega) d\omega \qquad \textbf{(13.51)}$$

It can be shown that (see Problem 1.13)

$$S_g(\omega) = \lim_{T\to\infty} \frac{|G(\omega)|^2}{T} \qquad \textbf{(13.52)}$$

Let the signals $x(t)$ and $g(t)$ be two periodic signals with period T. The complex exponential Fourier series expansions for those signals are, respectively, given by

$$x(t) = \sum_{n=-\infty}^{\infty} X_n e^{\frac{j2\pi nt}{T}} \qquad \textbf{(13.53)}$$

$$g(t) = \sum_{m=-\infty}^{\infty} G_m e^{\frac{j2\pi mt}{T}} \qquad \textbf{(13.54)}$$

The power cross-correlation function $\overline{R}_{gx}(t)$ was given in Eq. (13.43), and is repeated here as Eq. (13.55),

$$\bar{R}_{gx}(t) = \frac{1}{T}\int_{-T/2}^{T/2} g^*(\tau)x(t+\tau)d\tau \tag{13.55}$$

Note that because both signals are periodic the limit is no longer necessary. Substituting Eqs. (13.53) and (13.54) into Eq. (13.55), collecting terms, and using the definition of orthogonality, we get

$$\bar{R}_{gx}(t) = \sum_{n=-\infty}^{\infty} G_n^* X_n e^{\frac{j2n\pi t}{T}} \tag{13.56}$$

When $x(t) = g(t)$, Eq. (13.56) becomes the power autocorrelation function,

$$\bar{R}_x(t) = \sum_{n=-\infty}^{\infty} |X_n|^2 e^{\frac{j2n\pi t}{T}} = |X_0|^2 + 2\sum_{n=1}^{\infty} |X_n|^2 e^{\frac{j2n\pi t}{T}} \tag{13.57}$$

The power spectrum and cross-power spectrum density functions are then computed as the FT of Eqs. (13.57) and (13.56), respectively. More precisely,

$$\begin{aligned} \bar{S}_x(\omega) &= 2\pi \sum_{n=-\infty}^{\infty} |X_n|^2 \delta\left(\omega - \frac{2n\pi}{T}\right) \\ \bar{S}_{gx}(\omega) &= 2\pi \sum_{n=-\infty}^{\infty} G_n^* X_n \delta\left(\omega - \frac{2n\pi}{T}\right) \end{aligned} \tag{13.58}$$

The line (or discrete) power spectrum is defined as the plot of $|X_n|^2$ versus n, where the lines are $\Delta f = 1/T$ apart. The DC power is $|X_0|^2$, and the total power is $\sum_{n=-\infty}^{\infty} |X_n|^2$.

13.6. Random Variables

Consider an experiment with outcomes defined by a certain sample space. The rule or functional relationship that maps each point in this sample space into a real number is called "random variable." Random variables are designated by capital letters (e.g., *X*, *Y*, …), and a particular value of a random variable is denoted by a lowercase letter (e.g., *x*, *y*, …).

The Cumulative Distribution Function (*cdf*) associated with the random variable X is denoted as $F_X(x)$, and is interpreted as the total probability that the random variable X is less or equal to the value x. More precisely,

$$F_X(x) = Pr\{X \leq x\} \tag{13.59}$$

The probability that the random variable X is in the interval (x_1, x_2) is then given by

$$F_X(x_2) - F_X(x_1) = Pr\{x_1 \leq X \leq x_2\} \tag{13.60}$$

The *cdf* has the following properties:

$$\begin{gathered} 0 \leq F_X(x) \leq 1 \\ F_X(-\infty) = 0 \\ F_X(\infty) = 1 \\ F_X(x_1) \leq F_X(x_2) \Leftrightarrow x_1 \leq x_2 \end{gathered} \tag{13.61}$$

It is often practical to describe a random variable by the derivative of its *cdf*, which is called the Probability Density Function *(pdf).* The *pdf* of the random variable X *is*

$$f_X(x) = \frac{d}{dx} F_X(x) \tag{13.62}$$

or, equivalently,

$$F_X(x) = Pr\{X \leq x\} = \int_{-\infty}^{x} f_X(\lambda) d\lambda \tag{13.63}$$

The probability that a random variable X has values in the interval (x_1, x_2) is

$$F_X(x_2) - F_X(x_1) = Pr\{x_1 \leq X \leq x_2\} = \int_{x_1}^{x_2} f_X(x) dx \tag{13.64}$$

Define the nth moment for the random variable X as

$$E[X^n] = \overline{X^n} = \int_{-\infty}^{\infty} x^n f_X(x) dx \tag{13.65}$$

The first moment, $E[X]$, is called the mean value, while the second moment, $E[X^2]$, is called the mean squared value. When the random variable X

represents an electrical signal across a 1Ω resistor, then $E[X]$ is the DC component, and $E[X^2]$ is the total average power.

The nth central moment is defined as

$$E[(X-\bar{X})^n] = \overline{(X-\bar{X})^n} = \int_{-\infty}^{\infty} (x-\bar{x})^n f_X(x)dx \tag{13.66}$$

and thus, the first central moment is zero. The second central moment is called the variance and is denoted by the symbol σ_X^2,

$$\sigma_X^2 = \overline{(X-\bar{X})^2} \tag{13.67}$$

Appendix E has some common *pdf*s and their means and variances.

In practice, the random nature of an electrical signal may need to be described by more than one random variable. In this case, the joint *cdf* and *pdf* functions need to be considered. The joint *cdf* and *pdf* for the two random variables X and Y are, respectively, defined by

$$F_{XY}(x, y) = Pr\{X \le x; Y \le y\} \tag{13.68}$$

$$f_{XY}(x, y) = \frac{\partial^2}{\partial x \partial y} F_{XY}(x, y) \tag{13.69}$$

The marginal *cdf*s are obtained as follows:

$$\begin{aligned} F_X(x) &= \int_{-\infty}^{\infty}\int_{-\infty}^{x} f_{UV}(u, v)dudv = F_{XY}(x, \infty) \\ F_Y(y) &= \int_{-\infty}^{\infty}\int_{-\infty}^{y} f_{UV}(u, v)dvdu = F_{XY}(\infty, y) \end{aligned} \tag{13.70}$$

If the two random variables are statistically independent, then the joint *cdf*s and *pdf*s are, respectively, given by

$$F_{XY}(x, y) = F_X(x)F_Y(y) \tag{13.71}$$

$$f_{XY}(x, y) = f_X(x)f_Y(y) \tag{13.72}$$

Let us now consider a case when the two random variables X and Y are mapped into two new variables U and V through some transformations T_1 and T_2 defined by

$$U = T_1(X, Y)$$
$$V = T_2(X, Y) \tag{13.73}$$

The joint *pdf*, $f_{UV}(u, v)$, may be computed based on the invariance of probability under the transformation. One must first compute the matrix of derivatives; then the new joint *pdf* is computed as

$$f_{UV}(u, v) = f_{XY}(x, y)|J| \tag{13.74}$$

$$|J| = \begin{vmatrix} \frac{\partial x}{\partial u} & \frac{\partial x}{\partial v} \\ \frac{\partial y}{\partial u} & \frac{\partial y}{\partial v} \end{vmatrix} \tag{13.75}$$

where the determinant of the matrix of derivatives $|J|$ is called the Jacobian.

The characteristic function for the random variable X is defined as

$$C_X(\omega) = E[e^{j\omega X}] = \int_{-\infty}^{\infty} f_X(x) e^{j\omega x} dx \tag{13.76}$$

The characteristic function can be used to compute the *pdf* for a sum of independent random variables. More precisely, let the random variable Y be equal to

$$Y = X_1 + X_2 + \ldots + X_N \tag{13.77}$$

where $\{X_i \ ; \ i = 1, \ldots N\}$ is a set of independent random variables. It can be shown that

$$C_Y(\omega) = C_{X_1}(\omega) C_{X_2}(\omega) \ldots C_{X_N}(\omega) \tag{13.78}$$

and the *pdf* $f_Y(y)$ is computed as the inverse Fourier transform of $C_Y(\omega)$ (with the sign of y reversed),

$$f_Y(y) = \frac{1}{2\pi} \int_{-\infty}^{\infty} C_Y(\omega) e^{-j\omega y} d\omega \tag{13.79}$$

The characteristic function may also be used to compute the nth moment for the random variable X as

$$E[X^n] = (-j)^n \frac{d^n}{d\omega^n} C_X(\omega)\bigg|_{\omega = 0} \tag{13.80}$$

13.7. Multivariate Gaussian Distribution

Consider a joint probability for m random variables, $X_1, X_2, \ldots, X_m$. These variables can be represented as components of an $m \times 1$ random column vector, $\underline{X}$. More precisely,

$$\underline{X}^t = \left[X_1 \; X_2 \; \ldots \; X_m\right] \tag{13.81}$$

where the superscript indicates the transpose operation. The joint *pdf* for the vector $\underline{X}$ is

$$f_{\underline{X}}(\underline{x}) = f_{x_1, x_2, \ldots, x_m}(x_1, x_2, \ldots, x_m) \tag{13.82}$$

The mean vector is defined as

$$\mu_x = \left[E[X_1] \; E[X_2] \; \ldots \; E[X_m]\right]^t \tag{13.83}$$

and the covariance is an $m \times m$ matrix given by

$$C_x = E[\underline{X} \; \underline{X}^t] - \mu_x \; \mu_x^t \tag{13.84}$$

Note that if the elements of the vector $\underline{X}$ are independent, then the covariance matrix is a diagonal matrix.

By definition a random vector $\underline{X}$ is multivariate Gaussian if its *pdf* has the form

$$f_{\underline{x}}(\underline{x}) = \left[(2\pi)^{m/2} \left|C_x\right|^{1/2}\right]^{-1} \exp\left(-\frac{1}{2}(\underline{x} - \mu_x)^t C_x^{-1} (\underline{x} - \mu_x)\right) \tag{13.85}$$

where μ_x is the mean vector, C_x is the covariance matrix, C_x^{-1} is inverse of the covariance matrix and $\left|C_x\right|$ is its determinant, and $\underline{X}$ is of dimension m. If $\underline{A}$ is a $k \times m$ matrix of rank k, then the random vector $\underline{Y} = \underline{A}\underline{X}$ is a k-variate Gaussian vector with

$$\mu_y = \underline{A}\mu_x \tag{13.86}$$

and

$$C_y = \underline{A} C_x \underline{A}^t \tag{13.87}$$

The characteristic function for a multivariate Guassian *pdf* is defined by

$$C_{\underline{X}} = E[\exp\{j(\omega_1 X_1 + \omega_2 X_2 + \ldots + \omega_m X_m)\}] = \quad \textbf{(13.88)}$$

$$\exp\left\{j\underline{\mu}_x^t\underline{\omega} - \frac{1}{2}\underline{\omega}^t C_x \underline{\omega}\right\}$$

Then the moments for the joint distribution can be obtained by partial differentiation. For example,

$$E[X_1X_2X_3] = \frac{\partial^3}{\partial\omega_1\partial\omega_2\partial\omega_3} C_{\underline{X}}(\omega_1, \omega_2, \omega_3) \qquad at \quad \underline{\omega} = \underline{0} \qquad \textbf{(13.89)}$$

Example 13.3: The vector $\underline{X}$ is a 4-variate Gaussian with

$$\mu_x = \begin{bmatrix} 2 & 1 & 1 & 0 \end{bmatrix}^t$$

$$C_x = \begin{bmatrix} 6 & 3 & 2 & 1 \\ 3 & 4 & 3 & 2 \\ 2 & 3 & 4 & 3 \\ 1 & 2 & 3 & 3 \end{bmatrix}$$

Define

$$\underline{X}_1 = \begin{bmatrix} X_1 \\ X_2 \end{bmatrix} \qquad \underline{X}_2 = \begin{bmatrix} X_3 \\ X_4 \end{bmatrix}$$

Find the distribution of $\underline{X}_1$ and the distibution of

$$\underline{Y} = \begin{bmatrix} 2X_1 \\ X_1 + 2X_2 \\ X_3 + X_4 \end{bmatrix}$$

Solution:

$\underline{X}_1$ has a bivariate Gaussian distribution with

$$\mu_{x_1} = \begin{bmatrix} 2 \\ 1 \end{bmatrix} \qquad C_{x_1} = \begin{bmatrix} 6 & 3 \\ 3 & 4 \end{bmatrix}$$

The vector $\underline{Y}$ can be expressed as

$$\underline{Y} = \begin{bmatrix} 2 & 0 & 0 & 0 \\ 1 & 2 & 0 & 0 \\ 0 & 0 & 1 & 1 \end{bmatrix} \begin{bmatrix} X_1 \\ X_2 \\ X_3 \\ X_4 \end{bmatrix} = \underline{A}\underline{X}$$

It follows that

$$\mu_y = \underline{A}\mu_x = \begin{bmatrix} 4 & 4 & 1 \end{bmatrix}^t$$

$$C_y = \underline{A}C_x\underline{A}^t = \begin{bmatrix} 24 & 24 & 6 \\ 24 & 34 & 13 \\ 6 & 13 & 13 \end{bmatrix}$$

13.8. Random Processes

A random variable X is by definition a mapping of all possible outcomes of a random experiment to numbers. When the random variable becomes a function of both the outcomes of the experiment as well as time, it is called a random process and is denoted by $X(t)$. Thus, one can view a random process as an ensemble of time domain functions that are the outcome of a certain random experiment, as compared to single real numbers in the case of a random variable.

Since the *cdf* and *pdf* of a random process are time dependent, we will denote them as $F_X(x;t)$ and $f_X(x;t)$, respectively. The nth moment for the random process $X(t)$ is

$$E[X^n(t)] = \int_{-\infty}^{\infty} x^n f_X(x;t)dx \qquad \textbf{(13.90)}$$

A random process $X(t)$ is referred to as stationary to order one if all its statistical properties do not change with time. Consequently, $E[X(t)] = \overline{X}$, where $\overline{X}$ is a constant. A random process $X(t)$ is called stationary to order two (or wide sense stationary) if

$$f_X(x_1, x_2;t_1, t_2) = f_X(x_1, x_2;t_1 + \Delta t, t_2 + \Delta t) \qquad \textbf{(13.91)}$$

for all t_1, t_2 and Δt.

Define the statistical autocorrelation function for the random process $X(t)$ as

$$\Re_X(t_1, t_2) = E[X(t_1)X(t_2)] \tag{13.92}$$

The correlation $E[X(t_1)X(t_2)]$ is, in general, a function of (t_1, t_2). As a consequence of the wide sense stationary definition, the autocorrelation function depends on the time difference $\tau = t_2 - t_1$, rather than on absolute time; and thus, for a wide sense stationary process we have

$$\begin{aligned} E[X(t)] &= \overline{X} \\ \Re_X(\tau) &= E[X(t)X(t+\tau)] \end{aligned} \tag{13.93}$$

If the time average and time correlation functions are equal to the statistical average and statistical correlation functions, the random process is referred to as an ergodic random process. The following is true for an ergodic process:

$$\lim_{T\to\infty} \frac{1}{T} \int_{-T/2}^{T/2} x(t)dt = E[X(t)] = \overline{X} \tag{13.94}$$

$$\lim_{T\to\infty} \frac{1}{T} \int_{-T/2}^{T/2} x^*(t)x(t+\tau)dt = \Re_X(\tau) \tag{13.95}$$

The covariance of two random processes $X(t)$ and $Y(t)$ is defined by

$$C_{XY}(t, t+\tau) = E[\{X(t) - E[X(t)]\}\{Y(t+\tau) - E[Y(t+\tau)]\}] \tag{13.96}$$

which can be written as

$$C_{XY}(t, t+\tau) = \Re_{XY}(\tau) - \overline{X}\,\overline{Y} \tag{13.97}$$

13.9. Sampling Theorem

Most modern communication and radar systems are designed to process discrete samples of signals bearing information. In general, we would like to determine the necessary condition such that a signal can be fully reconstructed from its samples by filtering, or data processing in general. The answer to this question lies in the sampling theorem which may be stated as follows: let the signal $x(t)$ be real-valued and band-limited with bandwidth B; this signal can be fully reconstructed from its samples if the time interval between samples is no greater than $1/(2B)$.

Fig. 13.1 illustrates the sampling process concept. The sampling signal $p(t)$ is periodic with period T_s, which is called the sampling interval. The Fourier series expansion of $p(t)$ is

$$p(t) = \sum_{n=-\infty}^{\infty} P_n e^{\frac{j2\pi nt}{T_s}} \tag{13.98}$$

The sampled signal $x_s(t)$ is then given by

$$x_s(t) = \sum_{n=-\infty}^{\infty} x(t) P_n e^{\frac{j2\pi nt}{T_s}} \tag{13.99}$$

Taking the FT of Eq. (13.99) yields

$$X_s(\omega) = \sum_{n=-\infty}^{\infty} P_n \, X\left(\omega - \frac{2\pi n}{T_s}\right) = P_0 X(\omega) + \sum_{\substack{n=-\infty \\ n \neq 0}}^{\infty} P_n \, X\left(\omega - \frac{2\pi n}{T_s}\right) \tag{13.100}$$

where $X(\omega)$ is the FT of $x(t)$.

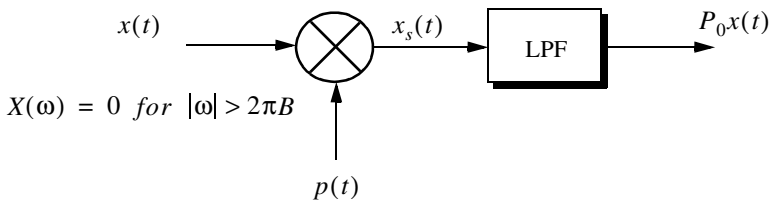

Figure 13.1. Concept of sampling.

Therefore, we conclude that the spectral density, $X_s(\omega)$, consists of replicas of $X(\omega)$ spaced $(2\pi/T_s)$ apart and scaled by the Fourier series coefficients P_n. A Low Pass Filter (LPF) of bandwidth B can then be used to recover the original signal $x(t)$.

When the sampling rate is increased (i.e., T_s decreases), the replicas of $X(\omega)$ move farther apart from each other. Alternatively, when the sampling rate is decreased (i.e., T_s increases), the replicas get closer to one another. The value of T_s such that the replicas are tangent to one another defines the minimum required sampling rate so that $x(t)$ can be recovered from its samples by using an LPF. It follows that

$$\frac{2\pi}{T_s} = 2\pi(2B) \Leftrightarrow T_s = \frac{1}{2B} \tag{13.101}$$

The sampling rate defined by Eq. (13.101) is known as the Nyquist sampling rate. When $T_s > (1/2B)$, the replicas of $X(\omega)$ overlap and thus, $x(t)$ cannot be recovered cleanly from its samples. This is known as aliasing. In practice, ideal LPF cannot be implemented; hence, practical systems tend to over-sample in order to avoid aliasing.

Example 13.4: Assume that the sampling signal $p(t)$ is given by

$$p(t) = \sum_{n=-\infty}^{\infty} \delta(t - nT_s)$$

Compute an expression for $X_s(\omega)$.

Solution: The signal $p(t)$ is called the Comb function. Its exponential Fourier series is

$$p(t) = \sum_{n=-\infty}^{\infty} \frac{1}{T_s} e^{\frac{2\pi n t}{T_s}}$$

It follows that

$$x_s(t) = \sum_{n=-\infty}^{\infty} x(t) \frac{1}{T_s} e^{\frac{2\pi n t}{T_s}}$$

Taking the Fourier transform of this equation yields

$$X_s(\omega) = \frac{2\pi}{T_s} \sum_{n=-\infty}^{\infty} X\left(\omega - \frac{2\pi n}{T_s}\right).$$

Before proceeding to the next section, we will establish the following notation: samples of the signal $x(t)$ are denoted by $x(n)$ and referred to as a discrete time domain sequence, or simply a sequence. If the signal $x(t)$ is periodic, we will denote its sample by the periodic sequence $x(n)$.

13.10. The Z-Transform

The Z-transform is a transformation that maps samples of a discrete time domain sequence into a new domain known as the z-domain. It is defined as

$$Z\{x(n)\} = X(z) = \sum_{n=-\infty}^{\infty} x(n)z^{-n} \tag{13.102}$$

where $z = re^{j\omega}$, and for most cases, $r = 1$. It follows that Eq. (13.102) can be rewritten as

$$X(e^{j\omega}) = \sum_{n=-\infty}^{\infty} x(n)e^{-jn\omega} \tag{13.103}$$

In the z-domain, the region over which $X(z)$ is finite is called the Region of Convergence (ROC). Appendix D has a list of most common Z-transform pairs. The Z-transform properties are (the proofs are left as an exercise):

1. *Linearity:*

$$Z\{ax_1(n) + bx_2(n)\} = aX_1(z) + bX_2(z) \tag{13.104}$$

2. *Right-Shifting Property:*

$$Z\{x(n-k)\} = z^{-k}X(z) \tag{13.105}$$

3. *Left-Shifting Property:*

$$Z\{x(n+k)\} = z^{k}X(z) - \sum_{n=0}^{k-1} x(n)z^{k-n} \tag{13.106}$$

4. *Time Scaling:*

$$Z\{a^n x(n)\} = X(a^{-1}z) = \sum_{n=0}^{\infty} (a^{-1}z)^{-n} x(n) \tag{13.107}$$

5. *Periodic Sequences:*

$$Z\{x(n)\} = \frac{z^N}{z^N - 1} Z\{x(n)\} \tag{13.108}$$

where N is the period.

6. *Multiplication by n :*

$$Z\{nx(n)\} = -z\frac{d}{dz}X(z) \tag{13.109}$$

7. *Division by n + a ; a is a real number:*

$$Z\left\{\frac{x(n)}{n+a}\right\} = \sum_{n=0}^{\infty} x(n) z^a \left(-\int_0^z u^{-k-a-1} du\right) \tag{13.110}$$

8. *Initial Value:*

$$x(n_0) = z^{n_0} X(z)\Big|_{z \to \infty} \tag{13.111}$$

9. *Final Value:*

$$\lim_{n \to \infty} x(n) = \lim_{z \to 1} (1 - z^{-1}) X(z) \tag{13.112}$$

10. *Convolution:*

$$Z\left\{\sum_{k=0}^{\infty} h(n-k)x(k)\right\} = H(z)X(z) \tag{13.113}$$

11. *Bilateral Convolution:*

$$Z\left\{\sum_{k=-\infty}^{\infty} h(n-k)x(k)\right\} = H(z)X(z) \tag{13.114}$$

Example 13.5: Prove Eq. (13.109).

Solution: Starting with the definition of the Z-transform,

$$X(z) = \sum_{n=-\infty}^{\infty} x(n)z^{-n}$$

Taking the derivative, with respect to z, of the above equation yields

$$\frac{d}{dz}X(z) = \sum_{n=-\infty}^{\infty} x(n)(-n)z^{-n-1}$$

$$= (-z^{-1}) \sum_{n=-\infty}^{\infty} nx(n)z^{-n}$$

It follows that

$$Z\{nx(n)\} = (-z)\frac{d}{dz}X(z)$$

In general, a discrete LTI system has a transfer function $H(z)$ which describes how the system operates on its input sequence $x(n)$ in order to produce the output sequence $y(n)$. The output sequence $y(n)$ is computed from the discrete convolution between the sequences $x(n)$ and $h(n)$,

$$y(n) = \sum_{m=-\infty}^{\infty} x(m)h(n-m) \qquad \textbf{(13.115)}$$

However, since practical systems require that the sequence $x(n)$ be of finite length, we can rewrite Eq. (13.115) as

$$y(n) = \sum_{m=0}^{N} x(m)h(n-m) \qquad \textbf{(13.116)}$$

where N denotes the input sequence length. Taking the Z-transform of Eq. (13.116) yields

$$Y(z) = X(z)H(z) \qquad \textbf{(13.117)}$$

and the discrete system transfer function is

$$H(z) = \frac{Y(z)}{X(z)} \qquad \textbf{(13.118)}$$

Finally, the transfer function $H(z)$ can be written as

$$H(z)\Big|_{z = e^{j\omega}} = \left|H(e^{j\omega})\right| e^{\angle H(e^{j\omega})} \tag{13.119}$$

where $\left|H(e^{j\omega})\right|$ is the amplitude response, and $\angle H(e^{j\omega})$ is the phase response.

13.11. The Discrete Fourier Transform

The Discrete Fourier Transform (DFT) is a mathematical operation that transforms a discrete sequence, usually from the time domain into the frequency domain, in order to explicitly determine the spectral information for the sequence. The time domain sequence can be real or complex. The DFT has finite length N, and is periodic with period equal to N.

The discrete Fourier transform for the finite sequence $x(n)$ is defined by

$$\tilde{X}(k) = \sum_{n=0}^{N-1} x(n) e^{-\frac{j2\pi nk}{N}} \quad ; \; k = 0, \ldots, N-1 \tag{13.120}$$

The inverse DFT is given by

$$\tilde{x}(n) = \frac{1}{N} \sum_{k=0}^{N-1} \tilde{X}(k) e^{\frac{j2\pi nk}{N}} \quad ; \; n = 0, \ldots, N-1 \tag{13.121}$$

The Fast Fourier Transform (FFT) is not a new kind of transform different from the DFT. Instead, it is an algorithm used to compute the DFT more efficiently. There are numerous FFT algorithms that can be found in the literature. In this book we will interchangeably use the DFT and the FFT to mean the same. Furthermore, we will assume radix-2 FFT algorithm, where the FFT size is equal to $N = 2^m$ for some integer m.

13.12. Discrete Power Spectrum

Practical discrete systems utilize DFTs of finite length as a means of numerical approximation for the Fourier transform. It follows that input signals must be truncated to a finite duration (denoted by T) before they are sampled. This is necessary so that a finite length sequence is generated prior to signal processing. Unfortunately, this truncation process may cause some serious problems.

To demonstrate this difficulty, consider the time domain signal $x(t) = \sin 2\pi f_0 t$. The spectrum of $x(t)$ consists of two spectral lines at $\pm f_0$. Now, when $x(t)$ is truncated to length T seconds and sampled at a rate $T_s = T/N$, where N is the number of desired samples, we produce the sequence $\{x(n)\ ;\ n = 0, 1, \ldots, N-1\}$. The spectrum of $x(n)$ would still be composed of the same spectral lines if T is an integer multiple of T_s and if the DFT frequency resolution Δf is an integer multiple of f_0. Unfortunately, those two conditions are rarely met and as a consequence, the spectrum of $x(n)$ spreads over several lines (normally the spread may extend up to three lines). This is known as spectral leakage. Since f_0 is normally unknown, this discontinuity caused by an arbitrary choice of T cannot be avoided. Windowing techniques can be used to mitigate the effect of this discontinuity by applying smaller weights to samples close to the edges.

A truncated sequence $x(n)$ can be viewed as one period of some periodic sequence $x(n)$ with period N. The discrete Fourier series expansion of $x(n)$ is

$$x(n) = \sum_{k=0}^{N-1} X_k e^{\frac{j2\pi nk}{N}} \tag{13.122}$$

It can be shown that the coefficients X_k are given by

$$X_k = \frac{1}{N}\sum_{n=0}^{N-1} x(n) e^{\frac{-j2\pi nk}{N}} = \frac{1}{N}X(k) \tag{13.123}$$

where $X(k)$ is the DFT of $x(n)$. Therefore, the Discrete Power Spectrum (DPS) for the band limited sequence $x(n)$ is the plot of $|X_k|^2$ versus k, where the lines are Δf apart,

$$\begin{aligned} P_0 &= \frac{1}{N^2}|X(0)|^2 \\ P_k &= \frac{1}{N^2}\{|X(k)|^2 + |X(N-k)|^2\} \qquad ;\ k = 1, 2, \ldots, \frac{N}{2} - 1 \\ P_{N/2} &= \frac{1}{N^2}|X(N/2)|^2 \end{aligned} \tag{13.124}$$

Before proceeding to the next section, we will show how to select the FFT parameters. For this purpose, consider a band limited signal $x(t)$ with bandwidth B. If the signal is not band limited, a LPF can be used to eliminate

frequencies greater than B. In order to satisfy the sampling theorem, one must choose a sampling frequency $f_s = 1/T_s$, such that

$$f_s \geq 2B \tag{13.125}$$

The truncated sequence duration T and the total number of samples N are related by

$$T = NT_s \tag{13.126}$$

or equivalently,

$$f_s = \frac{N}{T} \tag{13.127}$$

It follows that

$$f_s = \frac{N}{T} \geq 2B \tag{13.128}$$

and the frequency resolution is

$$\Delta f = \frac{1}{NT_s} = \frac{f_s}{N} = \frac{1}{T} \geq \frac{2B}{N} \tag{13.129}$$

13.13. Windowing Techniques

Truncation of the sequence $x(n)$ can be accomplished by computing the product,

$$x_w(n) = x(n)w(n) \tag{13.130}$$

where

$$w(n) = \left\{ \begin{array}{ll} f(n) & ;\ n = 0, 1, \ldots, N-1 \\ 0 & otherwise \end{array} \right\} \tag{13.131}$$

where $f(n) \leq 1$. The finite sequence $w(n)$ is called a windowing sequence, or simply a window. The windowing process should not impact the phase response of the truncated sequence. Consequently, the sequence $w(n)$ must retain linear phase. This can be accomplished by making the window symmetrical with respect to its central point.

If $f(n) = 1$ for all n we have what is known as the rectangular window. It leads to the Gibbs phenomenon which manifests itself as an overshoot and a

ripple before and after a discontinuity. Fig. 13.2 shows the amplitude spectrum of a rectangular window. Note that the first side lobe is about $-13.46dB$ below the main lobe. Windows that place smaller weights on the samples near the edges will have lesser overshoot at the discontinuity points (lower side lobes); hence, they are more desirable than a rectangular window. However, side lobes reduction is offset by a widening of the main lobe (loss of resolution). Therefore, the proper choice of a windowing sequence is continuous trade-off between side lobe reduction and main lobe widening.

The multiplication process defined in Eq. (13.131) is equivalent to cyclic convolution in the frequency domain. It follows that $X_w(k)$ is a smeared (distorted) version of $X(k)$. To minimize this distortion, we would seek windows that have a narrow main lobe and small side lobes. Additionally, using a window other than a rectangular window reduces the power by a factor P_w, where

$$P_w = \frac{1}{N}\sum_{n=0}^{N-1} w^2(n) = \sum_{k=0}^{N-1} |W(k)|^2 \qquad \textbf{(13.132)}$$

It follows that the DPS for the sequence $x_w(n)$ is now given by

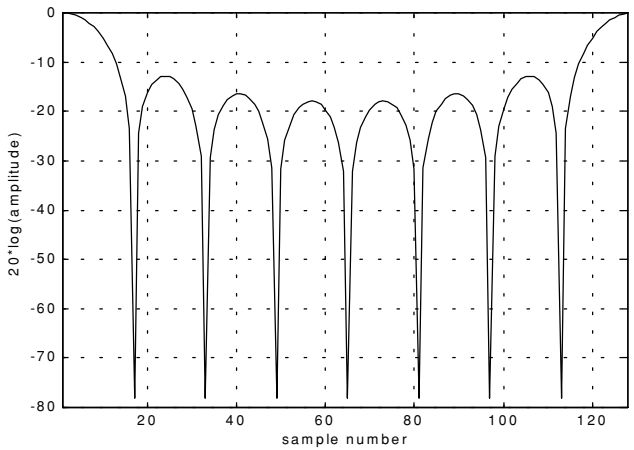

Figure 13.2. Normalized amplitude spectrum for rectangular window.

$$P_0^w = \frac{1}{P_w N^2}|X(0)|^2$$

$$P_k^w = \frac{1}{P_w N^2}\{|X(k)|^2 + |X(N-k)|^2\} \quad ; \; k = 1, 2, \ldots, \frac{N}{2} - 1 \tag{13.133}$$

$$P_{N/2}^w = \frac{1}{P_w N^2}|X(N/2)|^2$$

where P_w is defined in Eq. (13.133). Table 13.1 lists some common windows. Figs. 13.3 through 13.5 show the frequency domain characteristics for these windows.

TABLE 13.1. Some common windows. $n = 0, N-1$.

Window	Expression	First side lobe	Main lobe width
rectangular	$w(n) = 1$	$-13.46dB$	1
Hamming	$w(n) = 0.54 - 0.46\cos\left(\frac{2\pi n}{N-1}\right)$	$-41dB$	2
Hanning	$w(n) = 0.5\left[1 - \cos\left(\frac{2\pi n}{N-1}\right)\right]$	$-32dB$	2
Kaiser	$w(n) = \frac{I_0[\beta\sqrt{1-(2n/N)^2}]}{I_0(\beta)}$ I_0 is the zero-order modified Bessel function of the first kind	$-46dB$ *for* $\beta = 2\pi$	$\sqrt{5}$ *for* $\beta = 2\pi$

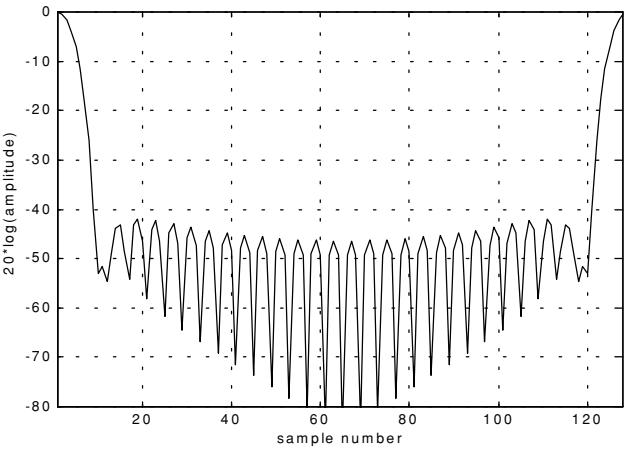

Figure 13.3. Normalized amplitude spectrum for Hamming window.

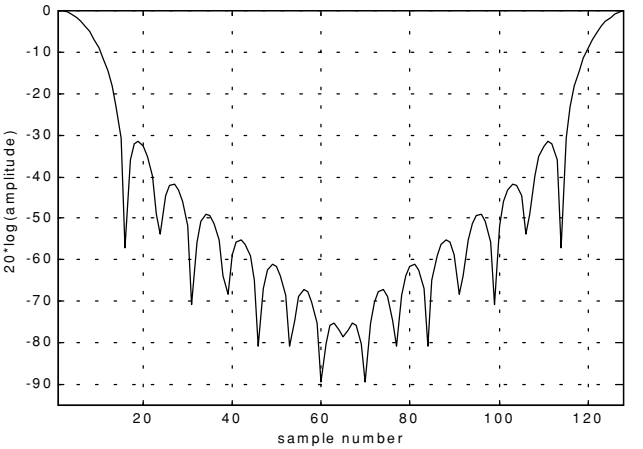

Figure 13.4. Normalized amplitude spectrum for Hanning window.

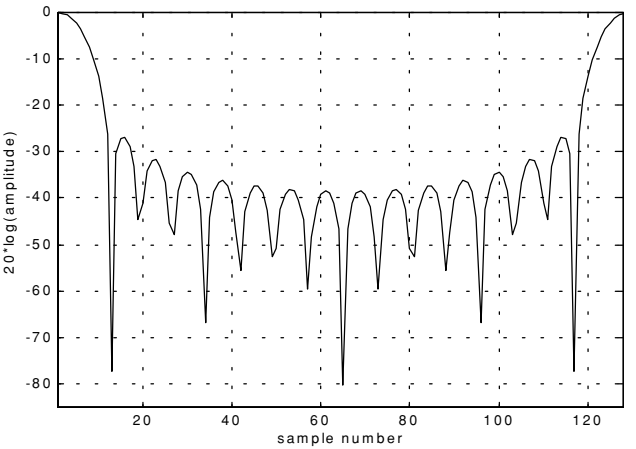

Figure 13.5. Normalized amplitude spectrum for Kaiser window (parameter π).

Problems

13.1. Classify each of the following signals as an energy signal, as a power signal, or as neither. (a) $\exp(0.5t)\ \ (t \geq 0)$; (b) $\exp(-0.5t)\ \ (t \geq 0)$; (c) $\cos t + \cos 2t\ \ (-\infty < t < \infty)$; (d) $e^{-a|t|}\ \ (a > 0)$.

13.2. Compute the energy associated with the signal $x(t) = ARect(t/\tau)$.

13.3. (a) Prove that $\varphi_1(t)$ and $\varphi_2(t)$, shown in Fig. P13.3, are orthogonal over the interval $(-2 \leq t \leq 2)$. (b) Express the signal $x(t) = t$ as a weighted sum of $\varphi_1(t)$ and $\varphi_2(t)$ over the same time interval.

13.4. A periodic signal $x_p(t)$ is formed by repeating the pulse $x(t) = 2\Delta((t-3)/5)$ every 10 seconds. (a) What is the Fourier transform of $x(t)$. (b) Compute the complex Fourier series of $x_p(t)$? (c) Give an expression for the autocorrelation function $\bar{R}_{x_p}(t)$ and the power spectrum density $\bar{S}_{x_p}(\omega)$.

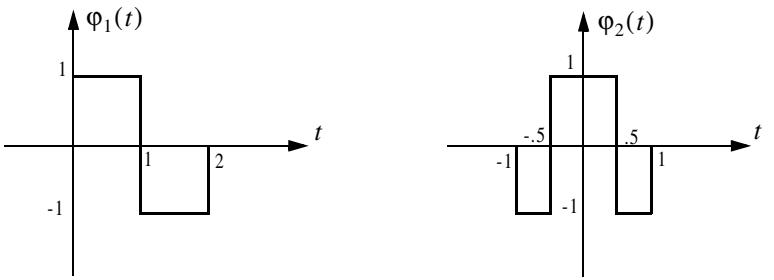

Figure P13.3

13.5. If the Fourier series is

$$x(t) = \sum_{n=-\infty}^{\infty} X_n e^{j2\pi nt/T}$$

define $y(t) = x(t - t_0)$. Compute an expression for the complex Fourier series expansion of $y(t)$.

13.6. Show that (a) $\bar{R}_x(-t) = \bar{R}_x^*(t)$. (b) If $x(t) = f(t) + m_1$ and $y(t) = g(t) + m_2$, then $\bar{R}_{xy}(t) = m_1 m_2$, where the average values for $f(t)$ and $g(t)$ are zeroes.

13.7. What is the power spectral density for the signal

$$x(t) = A\cos(2\pi f_0 t + \theta_0)$$

13.8. A certain radar system uses linear frequency modulated waveforms of the form

$$x(t) = Rect\left(\frac{t}{\tau}\right)\cos\left(\omega_0 t + \mu\frac{t^2}{2}\right)$$

What are the quadrature components? Give an expression for both the modulation and instantaneous frequencies.

13.9. Consider the signal $x(t) = Rect(t/\tau)\cos(\omega_0 t - Bt^2/2\tau)$ and let $\tau = 15\mu s$ and $B = 10MHz$. What are the quadrature components?

13.10. Determine the quadrature components for the signal

$$h(t) = \delta(t) - \left(\frac{\omega_0}{\omega_d}\right)e^{-2t}\sin\omega_0 t \;\; u(t).$$

13.11. If $x(t) = x_1(t) - 2x_1(t-5) + x_1(t-10)$, determine the autocorrelation functions $R_{x_1}(t)$ and $R_x(t)$ when $x_1(t) = \exp(-t^2/2)$.

13.12. Write an expression for the autocorrelation function $R_y(t)$, where

$$y(t) = \sum_{n=1}^{5} Y_n Rect\left(\frac{t-n5}{2}\right)$$

and $\{Y_n\} = \{0.8, 1, 1, 1, 0.8\}$. Give an expression for the density function $S_y(\omega)$.

13.13. Derive Eq. (13.52).

13.14. An LTI system has impulse response

$$h(t) = \begin{Bmatrix} \exp(-2t) & t \geq 0 \\ 0 & t < 0 \end{Bmatrix}$$

(a) Find the autocorrelation function $R_h(\tau)$. (b) Assume the input of this system is $x(t) = 3\cos(100t)$. What is the output?

13.15. Suppose you want to determine an unknown DC voltage v_{dc} in the presence of additive white Gaussian noise $n(t)$ of zero mean and variance σ_n^2. The measured signal is $x(t) = v_{dc} + n(t)$. An estimate of v_{dc} is computed by making three independent measurements of $x(t)$ and computing the arithmetic mean, $\widehat{v_{dc}} \approx (x_1 + x_2 + x_3)/3$. (a) Find the mean and variance of the random variable $\widehat{v_{dc}}$. (b) Does the estimate of v_{dc} get better by using ten measurements instead of three? Why?

13.16. Consider the network shown in Fig. P13.16, where $x(t)$ is a random voltage with zero mean and autocorrelation function $\Re_x(\tau) = 1 + \exp(-a|t|)$. Find the power spectrum $S_x(\omega)$. What is the transfer function? Find the power spectrum $S_v(\omega)$.

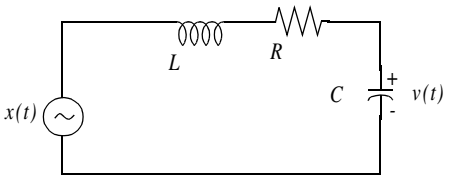

Figure P13.16.

13.17. (a) A random voltage $v(t)$ has an exponential distribution function $f_V(v) = a\exp(-av)$ where $(a > 0); (0 \le v < \infty)$. The expected value $E[V] = 0.5$. Determine $Pr\{V > 0.5\}$.

13.18. Assume the X and Y miss distances of darts thrown at a bulls-eye dart board are Gaussian with zero mean and variance σ^2. (a) Determine the probability that a dart will fall between 0.8σ and 1.2σ. (b) Determine the radius of a circle about the bulls-eye that contains 80% of the darts thrown. (c) Consider a square with side s in the first quadrant of the board. Determine s so that the probability that a dart will fall within the square is 0.07.

13.19. Let $\bar{S}_X(\omega)$ be the PSD function for the stationary random process $X(t)$. Compute an expression for the PSD function of $Y(t) = X(t) - 2X(t-T)$.

13.20. Let X be a random variable with

$$f_X(x) = \begin{Bmatrix} \frac{1}{\sigma} t^3 e^{-t} & t \ge 0 \\ 0 & elsewhere \end{Bmatrix}$$

(a) Determine the characteristic function $C_X(\omega)$. (b) Using $C_X(\omega)$, validate that $f_X(x)$ is a proper *pdf*. (c) Use $C_X(\omega)$ to determine the first two moments of X. (d) Calculate the variance of X.

13.21. Let $X(t)$ be a stationary random process, $E[X(t)] = 1$ and the autocorrelation $\Re_x(\tau) = 3 + \exp(-|\tau|)$. Define a new random variable

$$Y = \int_0^2 x(t)dt$$

Compute $E[Y(t)]$ and σ_Y^2.

13.22. In Fig. 13.1, let

$$p(t) = \sum_{n=-\infty}^{\infty} ARect\left(\frac{t-nT}{\tau}\right)$$

Give an expression for $X_s(\omega)$.

13.23. Compute the Z-transform for

$$\text{(a) } x_1(n) = \frac{1}{n!}u(n)\text{; (b) } x_2(n) = \frac{1}{(-n)!}u(-n).$$

13.24. (a) Write an expression for the Fourier transform of

$$x(t) = Rect(t/3)$$

(b) Assume that you want to compute the modulus of the Fourier transform using a DFT of size 512 with a sampling interval of 1 second. Evaluate the modulus at frequency $(80/512)Hz$. Compare your answer to the theoretical value and compute the error.

13.25. A certain band-limited signal has bandwidth $B = 20KHz$. Find the FFT size required so that the frequency resolution is $\Delta f = 50Hz$. Assume radix 2 FFT and record length of 1 second.

13.26. Assume that a certain sequence is determined by its FFT. If the record length is $2ms$ and the sampling frequency is $f_s = 10KHz$, find N.

Bibliography

Abramowitz, M. and Stegun, I. A., Editors, *Handbook of Mathematical Functions, with Formulas, Graphs, and Mathematical Tables*, Dover Publications, 1970.

Balanis, C. A., *Antenna Theory, Analysis and Design*, Harper & Row, New York, 1982.

Barkat, M., *Signal Detection and Estimation*, Artech House, Norwood, MA, 1991.

Barton, D. K., *Modern Radar System Analysis*, Artech House, Norwood, MA, 1988.

Benedict, T. and Bordner, G., Synthesis of an Optimal set of Radar Track-While-Scan Smoothing Equations, *IRE Transaction on Automatic Control, Ac-7*. July 1962, pp. 27-32.

Beyer, W. H., *CRC Standard Mathematical Tables*, 26th edition, CRC Press, Boca Raton, FL, 1981.

Billetter, D. R., *Multifunction Array Radar*, Artech House, Norwood, MA, 1989.

Blackman, S. S., *Multiple-Target Tracking with Radar Application*, Artech House, Norwood, MA, 1986.

Blake, L. V., *A Guide to Basic Pulse-Radar Maximum Range Calculation Part-I Equations, Definitions, and Aids to Calculation*, Naval Res. Lab. Report 5868, 1969.

Blake, L. V., *Radar-Range Performance Analysis*, Lexington Books, Lexington, MA, 1980.

Boothe, R. R., *A Digital Computer Program for Determining the Performance of an Acquisition Radar Through Application of Radar Detection Probability Theory*, U.S. Army Missile Command: Report No. RD-TR-64-2. Redstone Arsenal, Alabama, 1964.

Brookner, E., Editor, *Aspects of Modern Radar*, Artech House, Norwood, MA, 1988.

Brookner, E., Editor, *Practical Phased Array Antenna System*, Artech House, Norwood, MA, 1991.

Brookner, E., *Radar Technology*, Lexington Books, Lexington, MA, 1996.

Burdic, W. S., *Radar Signal Analysis*, Prentice-Hall, Englewood Cliffs, NJ, 1968.

Brookner, E., *Tracking and Kalman Filtering Made Easy*, John Wiley & Sons, New York, 1998.

Cadzow, J. A., *Discrete-Time Systems, an Introduction with Interdisciplinary Applications*, Prentice-Hall, Englewood Cliffs, NJ, 1973.

Carlson, A. B., *Communication Systems, An Introduction to Signals and Noise in Electrical Communication*, 3rd edition, McGraw-Hill, New York, 1986.

Carpentier, M. H., *Principles of Modern Radar Systems*, Artech House, Norwood, MA, 1988.

Compton, R. T., *Adaptive Antennas*, Prentice-Hall, Englewood Cliffs, NJ, 1988.

Costas, J. P., A Study of a Class of Detection Waveforms Having Nearly Ideal Range-Doppler Ambiguity Properties, *Proc. IEEE 72*, 1984, pp. 996-1009.

DiFranco, J. V. and Rubin, W. L., *Radar Detection*. Artech House, Norwood, MA, 1980.

Dillard, R. A. and Dillard, G. M., *Detectability of Spread-Spectrum Signals*, Artech House, Norwood, MA, 1989.

Edde, B., *Radar - Principles, Technology, Applications*, Prentice-Hall, Englewood Cliffs, NJ, 1993.

Fielding, J. E. and Reynolds, G. D., *VCCALC: Vertical Coverage Calculation Software and Users Manual*, Artech House, Norwood, MA, 1988.

Gabriel, W. F., Spectral Analysis and Adaptive Array Superresolution Techniques, *Proc. IEEE*, Vol. 68, June 1980, pp. 654-666.

Gelb, A., Editor, *Applied Optimal Estimation*, MIT Press, Cambridge, MA, 1974.

Hamming, R. W., *Digital Filters*, 2nd edition, Prentice-Hall, Englewood Cliffs, NJ, 1983.

Hanselman, D. and Littlefield, B., *Mastering Matlab 5, A Complete Tutorial and Reference,* Malab Curriculum Series, Prentice-Hall, Englewood Cliffs, NJ, 1998.

Hirsch, H. L. and Grove, D. C., *Practical Simulation of Radar Antennas and Radomes*, Artech House, Norwood, MA, 1987.

Hovanessian, S. A., *Radar System Design and Analysis*, Artech House, Norwood, MA, 1984.

James, D. A., *Radar Homing Guidance for Tactical Missiles*, John Wiley & Sons, New York, 1986.

Klauder, J. R., Price, A. C., Darlington, S., and Albershiem, W. J., The Theory and Design of Chirp Radars, *The Bell System Technical Journal*, Vol. 39, No. 4, 1960.

Knott, E. F., Shaeffer, J. F., and Tuley, M. T., *Radar Cross Section*, 2nd edition, Artech House, Norwood, MA, 1993.

Lativa, J., Low-Angle Tracking Using Multifrequency Sampled Aperture Radar, *IEEE - AES Trans.*, Vol. 27, No. 5, September 1991, pp.797-805.

Levanon, N., *Radar Principles*, John Wiley & Sons, New York, 1988.

Lewis, B. L., Kretschmer, Jr., F. F., and Shelton, W. W., *Aspects of Radar Signal Processing*, Artech House, Norwood, MA, 1986.

Long, M. W., *Radar Reflectivity of Land and Sea*, Artech House, Norwood, MA, 1983.

Lothes, R. N., Szymanski, M. B., and Wiley, R. G., *Radar Vulnerability to Jamming*, Artech House, Norwood, MA, 1990.

Mahafza, B. R. and Polge, R. J., Multiple Target Detection Through DFT Processing in a Sequential Mode Operation of Real Two-Dimensional Arrays, *Proc. of the IEEE Southeast Conf. '90*, New Orleans, LA, April 1990, pp. 168-170.

Mahafza, B. R., Heifner, L.A., and Gracchi, V. C., Multitarget Detection Using Synthetic Sampled Aperture Radars (SSAMAR), *IEEE - AES Trans.*, Vol. 31, No. 3, July 1995, pp. 1127-1132.

Mahafza, B. R. and Sajjadi, M., Three-Dimensional SAR Imaging Using a Linear Array in Transverse Motion, *IEEE - AES Trans.*, Vol. 32, No. 1, January 1996, pp. 499-510.

Mahafza, B. R., *Introduction to Radar Analysis*, CRC Press, Boca Raton, FL, 1998.

Marchand, P., *Graphics and GUIs with Matlab*, 2nd edition, CRC Press, Boca Raton, FL, 1999.

Marcum, J. I., A Statistical Theory of Target Detection by Pulsed Radar, Mathematical Appendix, *IRE Trans.*, Vol. IT-6, April 1960, pp. 145-267.

Meeks, M. L., *Radar Propagation at Low Altitudes*, Artech House, Norwood, MA, 1982.

Melsa, J. L. and Cohn, D. L., *Decision and Estimation Theory*, McGraw-Hill, New York, 1978.

Mensa, D. L., *High Resolution Radar Imaging*, Artech House, Norwood, MA, 1984.

Meyer, D. P. and Mayer, H. A., *Radar Target Detection: Handbook of Theory and Practice*, Academic Press, New York, 1973.

Monzingo, R. A. and Miller, T. W., *Introduction to Adaptive Arrays,* John Wiley & Sons, New York, 1980.

Morchin, W., *Radar Engineer's Sourcebook*, Artech House, Norwood, MA, 1993.

Morris, G. V., Airborne Pulsed Doppler Radar, Artech House, Norwood, MA, 1988.

Nathanson, F. E., *Radar Design Principles*, 2nd edition, McGraw-Hill, New York, 1991.

Navarro, Jr., A. M., *General Properties of Alpha Beta, and Alpha Beta Gamma Tracking Filters*, Physics Laboratory of the National Defense Research Organization TNO, Report PHL 1977-92, January 1977.

North, D. O., An Analysis of the Factors which Determine Signal/Noise Discrimination in Pulsed Carrier Systems, *Proc. IEEE 51*, No. 7, July 1963, pp. 1015-1027.

Oppenheim, A. V. and Schafer, R. W., *Discrete-Time Signal Processing*, Prentice-Hall, Englewood Cliffs, NJ, 1989.

Oppenheim, A. V., Willsky, A. S., and Young, I. T., *Signals and Systems*, Prentice-Hall, Englewood Cliffs, NJ, 1983.

Orfanidis, S. J., *Optimum Signal Processing, an Introduction*, 2nd edition, McGraw-Hill, New York, 1988.

Papoulis, A., *Probability, Random Variables, and Stochastic Processes*, second edition, McGraw-Hill, New York, 1984.

Parl, S. A., New Method of Calculating the Generalized Q Function, *IEEE Trans. Information Theory,* Vol. IT-26, No. 1, January 1980, pp. 121-124.

Peebles, Jr., P. Z., *Probability, Random Variables, and Random Signal Principles*, McGraw-Hill, New York, 1987.

Peebles, Jr., P. Z., *Radar Principles*, John Wiley & Sons, New York, 1998.

Pettit, R. H., *ECM and ECCM Techniques for Digital Communication Systems*, Lifetime Learning Publications, New York, 1982.

Polge, R. J., Mahafza, B. R., and Kim, J. G., *Extension and Updating of the Computer Simulation of Range Relative Doppler Processing for MM Wave Seekers*, Interim Technical Report, Vol. I, prepared for the U.S. Army Missile Command, Redstone Arsenal, Alabama, January 1989.

Polge, R. J., Mahafza, B. R., and Kim, J. G., Multiple Target Detection Through DFT Processing in a Sequential Mode Operation of Real or Synthetic Arrays, *IEEE 21th Southeastern Symposium on System Theory*, Tallahassee, FL, 1989, pp. 264-267.

Poularikas, A. and Seely, S., *Signals and Systems*, PWS Publishers, Boston, MA, 1984.

Rihaczek, A. W., *Principles of High Resolution Radars*, McGraw-Hill, New York, 1969.

Ross, R. A., Radar Cross Section of Rectangular Flat Plate as a Function of Aspect Angle, *IEEE Trans*. AP-14:320, 1966.

Ruck, G. T., Barrick, D. E., Stuart, W. D., and Krichbaum, C. K., *Radar Cross Section Handbook*, Volume 1, Plenum Press, New York, 1970.

Ruck, G. T., Barrick, D. E., Stuart, W. D., and Krichbaum, C. K., *Radar Cross Section Handbook*, Volume 2, Plenum Press, New York, 1970.

Rulf, B. and Robertshaw, G. A., *Understanding Antennas for Radar, Communications, and Avionics*, Van Nostrand Reinhold, 1987.

Scanlan, M.J., Editor, *Modern Radar Techniques*, Macmillan, New York, 1987.

Scheer, J. A. and Kurtz, J. L., Editors, *Coherent Radar Performance Estimation*, Artech House, Norwood, MA, 1993.

Shanmugan, K. S. and Breipohl, A. M., *Random Signals: Detection, Estimation and Data Analysis*, John Wiley & Sons, New York, 1988.

Singer, R. A., Estimating Optimal Tracking Filter Performance for Manned Maneuvering Targets, *IEEE Transaction on Aerospace and Electronics, AES-5*, July 1970, pp. 473-483.

Skillman, W. A., *DETPROB: Probability of Detection Calculation Software and User's Manual*, Artech House, Norwood, MA, 1991.

Skolnik, M. I., *Introduction to Radar Systems*, McGraw-Hill, New York, 1982.
Skolnik, M. I., Editor, *Radar Handbook*, 2nd edition, McGraw-Hill, New York, 1990.
Stearns, S. D. and David, R. A., *Signal Processing Algorithms*, Prentice-Hall, Englewood Cliffs, NJ, 1988.
Stimson, G. W., *Introduction to Airborne Radar*, Hughes Aircaft Company, El Segundo, CA, 1983.
Stratton, J. A., *Electromagnetic Theory*, McGraw-Hill, New York, 1941.
Stremler, F. G., *Introduction to Communication Systems*, 3rd edition, Addison-Wesley, New York, 1990.
Tzannes, N. S., *Communication and Radar Systems*, Prentice-Hall, Englewood Cliffs, NJ, 1985.
Urkowtiz, H., *Signal Theory and Random Processes*, Artech House, Norwood, MA, 1983.
Urkowitz, H., *Decision and Detection Theory*, Unpublished Lecture Notes, Lockheed Martin Co., Moorestown, NJ.
Vaughn, C. R., Birds and Insects as Radar Targets: A Review, *Proc. IEEE*, Vol. 73, No. 2, February 1985, pp. 205-227.
Wehner, D. R., *High Resolution Radar*, Artech House, Norwood, MA, 1987.
White, J. E., Mueller, D. D., and Bate, R. R., *Fundamentals of Astrodynamics*, Dover Publications, 1971.
Ziemer, R. E. and Tranter, W. H., *Principles of Communications, Systems, Modulation, and Noise,* 2nd edition, Houghton Mifflin, Boston, MA, 1985.

Appendix A *Noise Figure*

Any signal other than the target returns in the radar receiver is considered as noise. This includes interfering signals from outside the radar and thermal noise generated within the receiver itself. Thermal noise (thermal agitation of electrons) and shot noise (variation in carrier density of a semiconductor) are the two main internal noise sources within a radar receiver.

The power spectral density of thermal noise is given by

$$S_n(\omega) = \frac{|\omega| h}{\pi\left[\exp\left(\frac{|\omega| h}{2\pi kT}\right) - 1\right]} \tag{A.1}$$

where $|\omega|$ is the absolute value of the frequency in radians per second, T is temperature of the conducting medium in degrees Kelvin, k is Boltzman's constant, and h is Plank's constant ($h = 6.625 \times 10^{-34}\ joule\ \text{sec}onds$). When the condition $|\omega| \ll 2\pi kT/h$ is true, it can be shown that Eq. (A.1) is approximated by

$$S_n(\omega) \approx 2kT \tag{A.2}$$

This approximation is widely accepted, since, in practice, radar systems operate at frequencies less than $100\ GHz$; and, for example, if $T = 290K$, then $2\pi kT/h \approx 6000\ GHz$.

The mean square noise voltage (noise power) generated across a $1\ ohm$ resistance is then

$$\langle n^2 \rangle = \frac{1}{2\pi} \int_{-2\pi B}^{2\pi B} 2kT \quad d\omega = 4kTB \tag{A.3}$$

where B is the system bandwidth in hertz.

Any electrical system containing thermal noise and having input resistance R_{in} can be replaced by an equivalent noiseless system with a series combination of a noise equivalent voltage source and a noiseless input resistor R_{in} added at its input. This is illustrated in Fig. A.1.

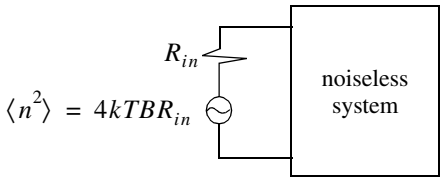

Figure A.1. Noiseless system with an input noise voltage source.

The amount of noise power that can physically be extracted from $\langle n^2 \rangle$ is one fourth the value computed in Eq. (A.3). The proof is left as an exercise.

Consider a noisy system with power gain A_P, as shown in Fig. A.2.

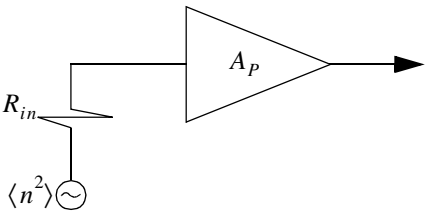

Figure A.2. Noisy amplifier replaced by its noiseless equivalent and an input voltage source in series with a resistor.

The noise figure is defined by

$$F_{dB} = 10 \log \frac{total\ \ noise\ \ power\ \ out}{noise\ \ power\ \ out\ \ due\ \ to\ \ R_{in}\ \ alone} \tag{A.4}$$

More precisely,

$$F_{dB} = 10 \log \frac{N_o}{N_i\ A_p} \tag{A.5}$$

where N_o and N_i are, respectively, the noise power at the output and input of the system.

If we define the input and output signal power by S_i and S_o, respectively, then the power gain is

$$A_P = \frac{S_o}{S_i} \tag{A.6}$$

It follows that

$$F_{dB} = 10\log\left(\frac{S_i/Ni}{S_o/N_o}\right) = \left(\frac{S_i}{N_i}\right)_{dB} - \left(\frac{S_o}{N_o}\right)_{dB} \tag{A.7}$$

where

$$\left(\frac{S_i}{N_i}\right)_{dB} > \left(\frac{S_o}{N_o}\right)_{dB} \tag{A.8}$$

Thus, it can be said that the noise figure is the loss in the signal-to-noise ratio due to the added thermal noise of the amplifier $((SNR)_o = (SNR)_i - F \ \ in \ \ dB)$.

We can also express the noise figure in terms of the system's effective temperature T_e. Consider the amplifier shown in Fig. A.2, and let its effective temperature be T_e. Assume the input noise temperature is T_o. Thus, the input noise power is

$$N_i = kT_oB \tag{A.9}$$

and the output noise power is

$$N_o = kT_oB \ \ A_p + kT_eB \ \ A_p \tag{A.10}$$

where the first term on the right-hand side of Eq. (A.10) corresponds to the input noise, and the latter term is due to thermal noise generated inside the system. It follows that the noise figure can be expressed as

$$F = \frac{(SNR)_i}{(SNR)_o} = \frac{S_i}{kT_oB} \ \ kBA_p \ \ \frac{T_o + T_e}{S_o} = 1 + \frac{T_e}{T_o} \tag{A.11}$$

Equivalently, we can write

$$T_e = (F-1)T_o \tag{A.12}$$

Example A.1: An amplifier has a 4dB noise figure; the bandwidth is $B = 500 \ \ KHz$. *Calculate the input signal power that yields a unity SNR at the output. Assume* $T_o = 290$ *degree Kelvin and an input resistance of one ohm.*

Solution: The input noise power is

$$kT_oB = 1.38 \times 10^{-23} \times 290 \times 500 \times 10^3 = 2.0 \times 10^{-15} w$$

Assuming a voltage signal, then the input noise mean squared voltage is

$$\langle n_i^2 \rangle = kT_oB = 2.0 \times 10^{-15} \quad v^2$$

$$F = 10^{0.4} = 2.51$$

From the noise figure definition we get

$$\frac{S_i}{N_i} = F\left(\frac{S_o}{N_o}\right) = F$$

and

$$\langle s_i^2 \rangle = F\langle n_i^2 \rangle = 2.51 \times 2.0 \times 10^{-15} = 5.02 \times 10^{-15} \quad v^2$$

Finally,

$$\sqrt{\langle s_i^2 \rangle} = 70.852nv$$

Consider a cascaded system as in Fig. A.3. Network 1 is defined by noise figure F_1, power gain G_1, bandwidth B, and temperature T_{e1}. Similarly, network 2 is defined by F_2, G_2, B, and T_{e2}. Assume the input noise has temperature T_0.

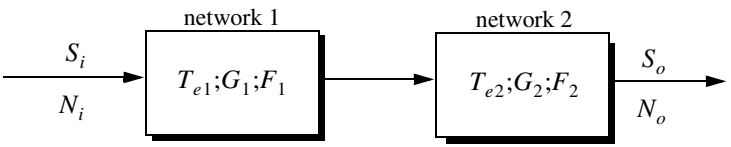

Figure A.3. Cascaded linear system.

The output signal power is

$$S_o = S_iG_1G_2 \tag{A.13}$$

The input and output noise powers are, respectively, given by

$$N_i = kT_oB \tag{A.14}$$

$$N_o = kT_0BG_1G_2 + kT_{e1}BG_1G_2 + kT_{e2}BG_2 \quad \textbf{(A.15)}$$

where the three terms on the right-hand side of Eq. (A.15), respectively, correspond to the input noise power, thermal noise generated inside network 1, and thermal noise generated inside network 2.

Now if we use the relation $T_e = (F-1)T_0$ along with Eq. (A.13) and Eq. (A.14), we can express the overall output noise power as

$$N_o = F_1N_iG_1G_2 + (F_2-1)NiG_2 \quad \textbf{(A.16)}$$

It follows that the overall noise figure for the cascaded system is

$$F = \frac{(S_i/N_i)}{(S_o/N_o)} = F_1 + \frac{F_2-1}{G_1} \quad \textbf{(A.17)}$$

In general, for an n-stage system we get

$$F = F_1 + \frac{F_2-1}{G_1} + \frac{F_3-1}{G_1G_2} + \cdots + \frac{F_n-1}{G_1G_2G_3\cdots G_{n-1}} \quad \textbf{(A.18)}$$

Also, the n-stage system effective temperatures can be computed as

$$T_e = T_{e1} + \frac{T_{e2}}{G_1} + \frac{T_{e3}}{G_1G_2} + \cdots + \frac{T_{en}}{G_1G_2G_3\cdots G_{n-1}} \quad \textbf{(A.19)}$$

As suggested by Eq. (A.18) and Eq. (A.19), the overall noise figure is mainly dominated by the first stage. Thus, radar receivers employ low noise power amplifiers in the first stage in order to minimize the overall receiver noise figure. However, for radar systems that are built for low RCS operations every stage should be included in the analysis.

Example A.2: A radar receiver consists of an antenna with cable loss $L = 1dB = F_1$, *an RF amplifier with* $F_2 = 6dB$, *and gain* $G_2 = 20dB$, *followed by a mixer whose noise figure is* $F_3 = 10dB$ *and conversion loss* $L = 8dB$, *and finally, an integrated circuit IF amplifier with* $F_4 = 6dB$ *and gain* $G_4 = 60dB$. *Find the overall noise figure.*

Solution:

From Eq. (A.18) we have

$$F = F_1 + \frac{F_2-1}{G_1} + \frac{F_3-1}{G_1G_2} + \frac{F_4-1}{G_1G_2G_3}$$

G_1	G_2	G_3	G_4	F_1	F_2	F_3	F_4
$-1dB$	$20dB$	$-8dB$	$60dB$	$1dB$	$6dB$	$10dB$	$6dB$
0.7943	100	0.1585	10^6	1.2589	3.9811	10	3.9811

It follows that

$$F = 1.2589 + \frac{3.9811 - 1}{0.7943} + \frac{10 - 1}{100 \times 0.7943} + \frac{3.9811 - 1}{0.158 \times 1000.7943} = 5.3628$$

$$F = 10\log(5.3628) = 7.294dB$$

Problems

A.1. A source with equivalent temperature $T_e = 500K$ is followed by three amplifiers with specifications shown in the table below.

Amplifier	**F, *dB***	**G, *dB***	$\mathbf{T_e}$
1	You must compute	12	350
2	10	22	
3	15	35	

Assume a bandwidth of $150KHz$. (a) Compute the noise figure for the three cascaded amplifiers. (b) Compute the effective temperature for the three cascaded amplifiers. (c) Compute the overall system noise figure.

A.2. Derive Eq. (A.19).

Appendix B *Decibel Arithmetic*

The decibel, often called dB, is widely used in radar system analysis and design. It is a way of representing the radar parameters and relevant quantities in terms of logarithms. The unit dB is named after Alexander Graham Bell, who originated the unit as a measure of power attenuation in telephone lines. By Bell's definition, a unit of Bell gain is

$$\log\left(\frac{P_0}{P_i}\right) \tag{B.1}$$

where the logarithm operation is base 10, P_0 is the output power of a standard telephone line (almost one mile long), and P_i is the input power to the line. If voltage (or current) ratios were used instead of the power ratio, then a unit Bell gain is defined as

$$\log\left(\frac{V_0}{V_i}\right)^2 \qquad or \quad \log\left(\frac{I_0}{I_i}\right)^2 \tag{B.2}$$

A decibel, dB, is $1/10$ of a Bell (the prefix "deci" means 10^{-1}). It follows that a dB is defined as

$$10\log\left(\frac{P_0}{P_i}\right) = 10\log\left(\frac{V_0}{V_i}\right)^2 = 10\log\left(\frac{I_0}{I_i}\right)^2 \tag{B.3}$$

The inverse dB is computed from the relations

$$\begin{aligned} P_0/P_i &= 10^{dB/10} \\ V_0/V_i &= 10^{dB/20} \\ I_0/I_i &= 10^{dB/20} \end{aligned} \tag{B.4}$$

Decibels are widely used by radar designers and users for several reasons. Perhaps the most important of them all is that utilizing dBs drastically reduces the dynamic range that a designer or a user has to use. For example, an incoming radar signal may be as weak as $0.000000001V$, which can be expressed in dBs as $10\log(0.000000001) = -90dB$. Alternatively, a target may be located at range $R = 1000000m = 1000Km$ which can be expressed in dBs as $60dB$.

Another advantage of using dB in radar analysis is to facilitate the arithmetic associated with calculating the different radar parameters. The reason for this is the following: when using logarithms, multiplication of two numbers is equivalent to adding their corresponding dBs, and their division is equivalent to subtraction of dBs. For example,

$$\frac{250 \times 0.0001}{455} = \tag{B.5}$$

$$[10\log(250) + 10\log(0.0001) - 10\log(455)]dB = -42.6dB$$

In general,

$$10\log\left(\frac{A \times B}{C}\right) = 10\log A + 10\log B - 10\log C \tag{B.6}$$

$$10\log A^q = q \times 10\log A \tag{B.7}$$

Other dB ratios that are often used in radar analysis include the dBsm (dB - squared meters). This definition is very important when referring to target RCS, whose units are in squared meters. More precisely, a target whose RCS is $\sigma\ m^2$ can be expressed in dBsm as $10\log(\sigma\ m^2)$. For example, a $10m^2$ target is often referred to as $10dBsm$ target, and a target with RCS $0.01m^2$ is equivalent to a $-20dBsm$.

Finally, the units dBm and dBW are power ratios of dBs with reference to one milliwatt and one Watt, respectively.

$$dBm = 10\log\left(\frac{P}{1mW}\right) \tag{B.8}$$

$$dBW = 10\log\left(\frac{P}{1W}\right) \tag{B.9}$$

To find dBm from dBW, add 30 dB, and to find dBW from dBm, subtract 30 dB.

Appendix C

Fourier Transform Table

$x(t)$	$X(\omega)$
$ARect(t/\tau)$; rectangular pulse	$A\tau Sinc(\omega\tau/2)$
$A\Delta(t/\tau)$; triangular pulse	$A\frac{\tau}{2}Sinc^2(\tau\omega/4)$
$\frac{1}{\sqrt{2\pi}\sigma}\exp\left(-\frac{t^2}{2\sigma^2}\right)$; Gaussian pulse	$\exp\left(-\frac{\sigma^2\omega^2}{2}\right)$
$e^{-at}u(t)$	$1/(a+j\omega)$
$e^{-a\|t\|}$	$\frac{2a}{a^2+\omega^2}$
$e^{-at}\sin\omega_0 t \;\; u(t)$	$\frac{\omega_0}{\omega_0^2+(a+j\omega)^2}$
$e^{-at}\cos\omega_0 t \;\; u(t)$	$\frac{a+j\omega}{\omega_0^2+(a+j\omega)^2}$
$\delta(t)$	1
1	$2\pi\delta(\omega)$
$u(t)$	$\pi\delta(\omega)+\frac{1}{j\omega}$
$\mathrm{sgn}(t)$	$\frac{2}{j\omega}$

$x(t)$	$X(\omega)$
$\cos \omega_0 t$	$\pi[\delta(\omega - \omega_0) + \delta(\omega + \omega_0)]$
$\sin \omega_0 t$	$j\pi[\delta(\omega + \omega_0) - \delta(\omega - \omega_0)]$
$u(t) \cos \omega_0 t$	$\frac{\pi}{2}[\delta(\omega - \omega_0) + \delta(\omega + \omega_0)] + \frac{j\omega}{\omega_0^2 - \omega^2}$
$u(t) \sin \omega_0 t$	$\frac{\pi}{2j}[\delta(\omega + \omega_0) - \delta(\omega - \omega_0)] + \frac{\omega_0}{\omega_0^2 - \omega^2}$
$\lvert t \rvert$	$\frac{-2}{\omega^2}$

Appendix D

Some Common Probability Densities

Chi-Square with N degrees of freedom

$$f_X(x) = \frac{x^{(N/2)-1}}{2^{N/2}\Gamma(N/2)} \exp\left\{\frac{-x}{2}\right\} \; ; \; x > 0$$

$$\bar{X} = N \; ; \; \sigma_X^2 = 2N$$

$$gamma\ function = \Gamma(z) = \int_0^\infty \lambda^{z-1} e^{-\lambda} d\lambda \; ; \; Re\{z\} > 0$$

Exponential

$$(f_X(x) = a \exp\{-ax\}) \; ; \; x > 0$$

$$\bar{X} = \frac{1}{a} \; ; \; \sigma_X^2 = \frac{1}{a^2}$$

Gaussian

$$f_X(x) = \frac{1}{\sqrt{2\pi}\sigma} \exp\left\{-\frac{1}{2}\left(\frac{x - x_m}{\sigma}\right)^2\right\}; \; \bar{X} = x_m \; ; \; \sigma_X^2 = \sigma^2$$

Laplace

$$f_X(x) = \frac{\sigma}{2} \exp\{-\sigma|x - x_m|\}$$

$$\bar{X} = x_m \;\; ; \;\; \sigma_X^2 = \frac{2}{\sigma^2}$$

Log-Normal

$$f_X(x) = \frac{1}{x\sigma\sqrt{2\pi}} \exp\left(- \frac{(\ln x - \ln x_m)^2}{2\sigma^2} \right) \;\; ; \;\; x > 0$$

$$\bar{X} = \exp\left\{ \ln x_m + \frac{\sigma^2}{2} \right\} \;\; ; \;\; \sigma_X^2 = [\exp\{2\ln x_m + \sigma^2\}][\exp\{\sigma^2\} - 1]$$

Rayleigh

$$f_X(x) = \frac{x}{\sigma^2} \exp\left\{ \frac{-x^2}{2\sigma^2} \right\} \;\; ; \;\; x \geq 0$$

$$\bar{X} = \sqrt{\frac{\pi}{2}}\sigma \;\; ; \;\; \sigma_X^2 = \frac{\sigma^2}{2}(4 - \pi)$$

Uniform

$$f_X(x) = \frac{1}{b - a} \;\; ; \;\; a < b \quad ; \quad \bar{X} = \frac{a + b}{2} \;\; ; \;\; \sigma_X^2 = \frac{(b - a)^2}{12}$$

Weibull

$$f_X(x) = \frac{b x^{b-1}}{\bar{\sigma}_0} \exp\left(-\frac{(x)^b}{\bar{\sigma}_0} \right) \;\; ; \;\; (x, b, \bar{\sigma}_0) \geq 0$$

$$\bar{X} = \frac{\Gamma(1 + b^{-1})}{1/(\sqrt[b]{\bar{\sigma}_0})} \;\; ; \;\; \sigma_X^2 = \frac{\Gamma(1 + 2b^{-1}) - [\Gamma(1 + b^{-1})]^2}{1/[\sqrt[b]{(\bar{\sigma}_0)^2}]}$$

Appendix E *Z - Transform Table*

$x(n);\ n \geq 0$	$X(z)$	**ROC;** $\lvert z \rvert > R$
$\delta(n)$	1	0
1	$\dfrac{z}{z-1}$	1
n	$\dfrac{z}{(z-1)^2}$	1
n^2	$\dfrac{z(z+1)}{(z-1)^3}$	1
a^n	$\dfrac{z}{z-a}$	$\lvert a \rvert$
na^n	$\dfrac{az}{(z-a)^2}$	$\lvert a \rvert$
$\dfrac{a^n}{n!}$	$e^{a/z}$	0
$(n+1)a^n$	$\dfrac{z^2}{(z-a)^2}$	$\lvert a \rvert$
$\sin n\omega T$	$\dfrac{z\sin\omega T}{z^2 - 2z\cos\omega T + 1}$	1
$\cos n\omega T$	$\dfrac{z(z-\cos\omega T)}{z^2 - 2z\cos\omega T + 1}$	1

$x(n);\ n \geq 0$	$X(z)$	**ROC;** $\lvert z \rvert > R$
$a^n \sin n\omega T$	$\dfrac{az \sin \omega T}{z^2 - 2az \cos \omega T + a^2}$	$\dfrac{1}{\lvert a \rvert}$
$a^n \cos n\omega T$	$\dfrac{z(z - a^2 \cos \omega T)}{z^2 - 2az \cos \omega T + a^2}$	$\dfrac{1}{\lvert a \rvert}$
$\dfrac{n(n-1)}{2!}$	$\dfrac{z}{(z-1)^3}$	1
$\dfrac{n(n-1)(n-2)}{3!}$	$\dfrac{z}{(z-1)^4}$	1
$\dfrac{(n+1)(n+2)a^n}{2!}$	$\dfrac{z^3}{(z-a)^3}$	$\lvert a \rvert$
$\dfrac{(n+1)(n+2)\ldots(n+m)a^n}{m!}$	$\dfrac{z^{m+1}}{(z-a)^{m+1}}$	$\lvert a \rvert$

Appendix F *MATLAB Program and Function Name List*

A MATLAB program and function[1] name list is provided in this appendix on a per-chapter basis. Programs and functions that have associated MATLAB GUI are identified. All these programs and functions can be downloaded from CRC Press Web site (*www.crcpress.com*). For this purpose, create the following directory in your C-drive: *C:\RSA*. Copy all programs into this directory. The path tree should be as shown in Fig. F.1. Users can execute a certain function / program GUI by typing: *file_name_driver*, where file names are as indicated in the left columns of the tables listed in this appendix.

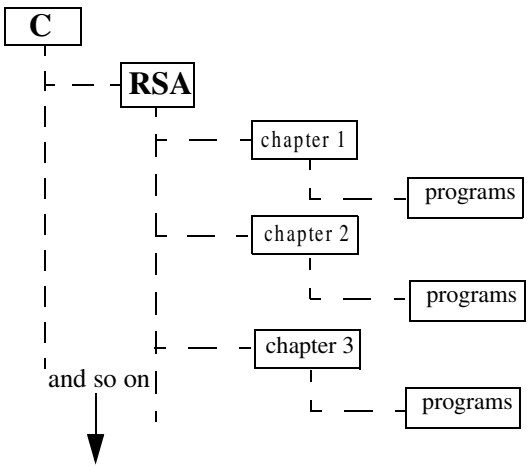

Figure F.1. Path tree.

1. All MATLAB programs and functions provided in this book were developed using MATLAB 5.0 - R11 with the Signal Processing Toolbox, on a PC with Windows 98 operating system.

Chapter 1:

Name	Purpose
pulse_train	compute duty cycle, average power, pulse energy
range_resolution	compute range resolution
doppler_frequency	compute Doppler frequency
radar_equation	implement the radar equation - with GUI
lprf_req	implement the LPRF radar equation - with GUI
hprf_req	implement the HPRF radar equation - with GUI
power_aperture	implement the surveillance radar equation - with GUI
ssj_req	implement self-screening jammer radar equation - with GUI
soj_req	implement the stand-off jammer radar equation - with GUI
range_red_fac	compute and plot the range reduction factor associated with ECM - with GUI

Chapter 2:

Name	Purpose (all functions have associated GUI)
rcs_aspect	compute and plot RCS dependency on aspect angle
rcs_frequency	compute and plot RCS dependency on frequency
rcs_sphere	compute and plot RCS of a sphere
rcs_ellipsoid	compute and plot RCS of an ellipsoid
rcs_circ_plate	compute and plot RCS of a circular flat plate
rcs_frustum	compute and plot RCS of a truncated cone
rcs_cylinder	compute and plot RCS of a cylinder
rcs_rect_plate	compute and plot RCS of a rectangular flat plate
rcs_isoceles	compute and plot RCS of a triangular flat plate
rcs_cylinder_complex	reproduce Fig. 2.22
swerlin_models	reproduce Fig. 2.24

Chapter 3:

Name	Purpose
range_calc	perform radar range equation calculation - with MATLAB-based GUI

Chapter 4:

Name	Purpose
marcumsq	compute and plot single pulse probability of detection versus SNR
improv_fac	compute and plot non-coherent integration improvement factor
incomplete_gamma	compute and plot Incomplete Gamma function
threshold	compute appropriate threshold for probability of detection calculation
pd_swerling5	compute and plot probability of detection for Swerling 5 targets
pd_swerling1	compute and plot probability of detection for Swerling 1 targets
pd_swerling2	compute and plot probability of detection for Swerling 2 targets
pd_swerling3	compute and plot probability of detection for Swerling 3 targets
pd_swerling4	compute and plot probability of detection for Swerling 4 targets

Chapter 5:

Name	Purpose
fresnel	compute and plot Fresnel functions
hrr_profile	compute and plot High Range Resolution Profiles associated with Stepped Frequency waveforms

Chapter 6:

Name	Purpose
single_pulse_ambg	compute and plot single ambiguity function
fig6_3	reproduce Fig. 6.3
fig6_5	reproduce Fig. 6.5
lfm_ambg	compute and plot LFM ambiguity function, with GUI
fig6_6	reproduce Fig. 6.6
fig6_7	reproduce Fig. 6.7
train_ambg	compute and plot ambiguity function for a coherent pulse train
fig6-9a	reproduce Fig. 6.9a

Chapter 7:

Name	Purpose
matched_filter	Compute and plot compressed output from a matched filter
stretch	implements stretch pulse compression
fig7_10	reproduce Fig. 7.10

Chapter 8:

Name	Purpose
ref_coef	compute and plot reflection coefficient - vertical and horizontal

Chapter 9:

Name	Purpose
single_canceler	plot output from a single delay line canceler
double_canceler	plot output from a double delay line canceler
fig9_15	reproduce Fig. 9.15
fig9_16	reproduce Fig. 9.16
fig9_17	reproduce Fig. 9.17

Chapter 10:

Name	Purpose
circ_aperture	compute and plot antenna radiation pattern for a circular aperture, including 3-D
fig10_5	reproduce Fig. 10.5
fig10_10	reproduce Fig. 10.10
linear_array	compute and plot radiation pattern for a linear phased array
rect_array	compute and plot radiation pattern for a rectangular array

Chapter 11:

Name	Purpose
mono_pulse	compute and plot sum and difference patterns for monopulse antenna
ghk_tracker	implement ghk 3-state tracker
fig11_21	reproduce Fig. 11.21
kalaman_filter	implement a 3-state Kalman filter
fig11_28	reproduce Fig. 11.28

Chapter 12:

Name	Purpose
fig12_2	reproduce Fig. 12.2